

Stellingen bij het proefschrift van Kees Wisse

1. Het interpreteren van schokbuisexperimenten met behulp van een theorie die alleen de axiale verplaatsingen modelleert is geoorloofd indien de spleet tussen het gesteentemonster en de schokbuiswand minstens twee ordes van grootte kleiner is dan de schokbuisdiameter. Het invoeren van effectieve parameters in geval van grotere spleetbreedtes kan beschouwd worden als een noodoplossing.

Dit proefschrift.

2. Partiële verzadiging kan een sterke frequentieafhankelijkheid veroorzaken van de golfsnelheden. Schokbuismetingen in het frequentiedomein kunnen nieuwe perspectieven bieden om dit probleem te analyseren.

Dit proefschrift.

SMEULDERS, D.M.J., & M.E.H. VAN DONGEN. 1997. Wave propagation in porous media containing a dilute gas- liquid mixture: theory and experiments. *J. Fluid. Mech.* **343**:351-373.

3. Een nauwkeurige beschrijving van golfvoortplanting in een poreus medium zoals gegeven door Biot impliceert een groot aantal materiaalparameters. In verband met toepassing in inversieprocedures is het aan te bevelen om vereenvoudigde modellen te ontwikkelen en te verifiëren met behulp van het model van Biot.

TANG, X.M., & C.H. CHENG, & M.N. TOKSÖZ. 1991. Dynamic permeability and borehole Stoneley waves: A simplified Biot-Rosenbaum model. *J. Acous. Soc. Am.* **90**:1632-1646.

4. Huidige technisch-wetenschappelijke publicaties geven geen beschrijving van de emoties die optreden tijdens het verkrijgen van de beschreven resultaten. In zekere zin is dit een vorm van geschiedvervalsing.

n.a.v. A. VAN DEN BEUKEL. 1990. De dingen hebben hun geheim. *Ten Have, Baarn.*

5. Het gebruik van understatements is één van de weinige toegestane vormen van humor in technisch-wetenschappelijke teksten. Het toepassen van meerdere vormen van humor zou het lezen en schrijven van deze publicaties zeer veraangename.
6. De uitspraak 'men mag niet meten met twee maten' betekent niet dat men geen vrienden mag zijn met collega's.
7. Wie de Bijbel leest als ware het een computerprogramma verstaat niet hetgeen hij of zij leest.

8. Een atheïst die vloekt bezigt een taalgebruik dat niet consistent is met zijn wereldbeeld.
9. In discussies over authentieke uitvoeringen van de muziek van Bach wordt doorgaans geen rekening gehouden met het verschil in perceptie tussen tijdgenoten van Bach en de hedendaagse luisteraars.
10. Een streng compositiesysteem is alleen vruchtbaar voor geniale componisten.
11. Een componist die citeert uit het werk van collega's wordt geacht de geleende noten in een andere context te plaatsen, dit in tegenstelling tot een wetenschapper die rekenschap moet geven van het juiste gebruik van het geciteerde materiaal. Een overeenkomst tussen beiden is dat plagiaat verboden is.

710657

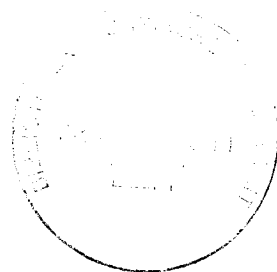
3242

TR3336

ON FREQUENCY DEPENDENCE
OF
ACOUSTIC WAVES
IN POROUS CYLINDERS

ON FREQUENCY DEPENDENCE
OF
ACOUSTIC WAVES
IN POROUS CYLINDERS

Proefschrift



ter verkrijging van de graad van doctor
aan de Technische Universiteit Delft,
op gezag van de Rector Magnificus prof.ir. K. Wakker,
in het openbaar te verdedigen ten overstaan van een commissie,
door het College voor Promoties aangewezen,

op dinsdag 18 mei 1999 te 16.00 uur
door Cornelis Johannes WISSE
werktuigkundig ingenieur
geboren te Mariekerke.

Dit proefschrift is goedgekeurd door de promotoren:

Prof.ir. M. Peeters

Prof.dr.ir. M.E.H. van Dongen

Samenstelling promotiecommissie:

Rector Magnificus, voorzitter

Prof.ir. M. Peeters, TU Delft, promotor

Prof.dr.ir. M.E.H. van Dongen, TU Eindhoven, promotor

Prof.dr.ir. J.T. Fokkema, TU Delft

Prof.dr.ir. F.B.J. Barends, TU Delft

Dr. S.W. Rienstra, TU Eindhoven

Dr. ir. D.M.J. Smeulders, TU Delft

Prof.ir. C.P.J.W. van Kruijsdijk, TU Delft, reservelid

Dr. ir. D.M.J. Smeulders heeft als begeleider in belangrijke mate aan het totstandkomen van het proefschrift bijgedragen.

This research was funded by the Netherlands Technology foundation (STW), Grant No. DMB33.3070, Shell IEP RTS Rijswijk, and Baker Atlas. This support is gratefully acknowledged.

Omslagontwerp: Ben Mobach/Joachim Tempelaars

Druk: Universiteitsdrukkerij TU Eindhoven

ISBN 90-9012596-5

Copyright ©1999 by C.J. Wisse, Delft University of Technology

All rights reserved. No part of the material protected by this copyright notice may be reproduced or utilized in any form or by any means, electronic or mechanical, including photocopying, recording or by any information storage and retrieval system, without written permission from the author.

Contents

Summary	9
Samenvatting	11
1 Introduction	15
1.1 Background and problem statement	15
1.2 Approach and thesis outline	17
1.3 Literature survey	19
1.3.1 Waves in porous media	19
1.3.2 Borehole Stoneley waves and parameter dependence	21
1.3.3 Surface waves and flat interfaces.	22
1.3.4 Wave modes in poroelastic waveguides	22
2 Constitutive relations and momentum equations	25
2.1 Continuum theory	25
2.1.1 Stresses and strains	26
2.1.2 Stress-strain relations	27
2.2 'Gedanken' experiments	28
2.2.1 'Jacketed' test	29
2.2.2 'Unjacketed' test	30
2.2.3 Relation to measurable quantities	30
2.3 Momentum equations	32
2.4 Rigid frame limit	33
2.5 Dynamic permeability	35
3 Wave phenomena	37
3.1 Equations of motion using potentials	37
3.1.1 Compressional waves	38
3.1.2 Shear waves	39
3.2 Low- and high-frequency limits	40
3.2.1 Low-frequency limit	40
3.2.2 High-frequency limit	41
3.3 Stiff frame	42
3.3.1 Low-frequency limit (stiff frame)	42
3.3.2 High-frequency limit (stiff frame)	42
3.4 Bulk properties and boundary conditions	43

4	One-dimensional wave propagation	47
4.1	1-D waves in porous materials	47
4.2	Liquid-loaded porous half-space	48
4.3	Multiple layers	51
5	Shock tube experiments	55
5.1	Shock tube	55
5.2	Results water-saturated samples	56
5.2.1	Large gap experiments	57
5.2.2	Small gap experiments	59
5.2.3	Comparison of Biot's theory and the Wyllie equation	59
5.3	Results air-filled pores	62
5.3.1	Wave behaviour	62
5.3.2	Diffusion behaviour	65
5.3.3	Concluding remarks air-filled pores	67
6	Two-dimensional phenomena	69
6.1	Surface waves and elastic solids	69
6.1.1	Free surface of an elastic half space	70
6.1.2	Liquid-solid interface	72
6.2	Surface waves and porous solids	76
6.2.1	Potentials	76
6.2.2	Lossless porous medium	79
6.2.3	Lossy media	83
7	Wave modes in elastic cylinders	87
7.1	Pochhammer equation	88
7.2	Computational results wave modes	91
7.2.1	Undamped modes	91
7.2.2	Damped modes	95
8	Wave modes in the shock tube	97
8.1	Rigid shock tube wall	97
8.1.1	Frequency-wavenumber equation	97
8.1.2	Computational results	101
8.2	Full modelling fast formation	114
8.3	Parameter study	118
8.3.1	Compressible grains	118
8.3.2	Gap effects	120
8.3.3	Permeability effects	124
8.3.4	Shear effects	127
8.3.5	Slow formation	127
8.4	Summary	130

9 Prony's method	133
9.1 Noiseless signals	134
9.2 Least squares Prony's methods	136
9.2.1 Singular value decomposition	137
9.2.2 Implementation	139
9.2.3 Forward and backward prediction	140
9.3 Discussion and conclusions	141
10 Experimental results in the frequency domain	143
10.1 Modification of the conventional shock tube	143
10.2 Reflection measurements	145
10.2.1 Phase velocities	148
10.2.2 Reflection coefficients	150
10.3 Transmission experiments	150
10.3.1 Editing the large gap experiment for Bentheimer sandstone	152
10.3.2 Comparison with theory	155
10.3.3 Small gap experiments for Bentheimer sandstone	155
10.3.4 Large gap experiments for synthetic rock	156
10.4 Discussion and conclusions	158
11 Conclusions	161
A Basic relations cartesian and cylindrical coordinates	163
A.1 Cartesian coordinaters	163
A.2 Cylindrical coordinates	165
B Bessel functions	167
C Riemann sheets	169
D Zero-search routines	173
D.1 Phase contour lines	173
D.2 Newton-Raphson iteration	173
E Parameters of porous samples.	177
E.1 Porosity and grain density	177
E.2 Permeability	177
E.3 Tortuosity	179
E.4 Elastic parameters	181
E.5 Parameters	184
Bibliography	186
Dankwoord	197
Curriculum vitae	199

Summary

For the interpretation of acoustic borehole logs a thorough understanding of the effects of rock properties on acoustic wave propagation is required. Examples of these properties are the porosity, permeability, lithology, and hydrocarbon saturation. For comparison of seismic data with wireline logging data the frequency dependence of wave velocities and damping coefficients is an important topic. In conventional acoustic borehole logging the first arrival of the acoustic wave train can be used to determine porosity. The full wave train is applied to determine mechanical properties, while one of the late arrivals, the Stoneley wave, is used to obtain permeability data.

In this thesis acoustic wave propagation in porous cylinders is investigated both experimentally and theoretically. The frequency and rock property dependence of both wave velocities and damping coefficients were studied, together with surface waves.

In our experiments a shock tube was used. In the shock tube a pressure step with a broad frequency content is generated in the test section in which the porous cylinder is mounted. Between the porous cylinder and the wall of the shock tube a gap exists. Using a large ratio of gap width to sample radius, it is possible to excite the Stoneley wave. Furthermore, a unique modification of the classical shock tube configuration was developed. With aid of a screw gear unit the equivalent of a large series of pressure transducers was realized, while in the classical shock tube experiment only a limited number of pressure signals could be recorded. The large number of pressure signals enabled us to apply a special signal processing technique, the Prony's method. In this way phase velocities, damping and reflection coefficients in the 1-120 kHz frequency range were derived from the experiments.

The Biot theory is the basis for describing wave propagation. We reviewed the Biot theory and a numerical code was developed which models one-dimensional wave propagation in the shock tube, including internal reflections. The main part of our theoretical work is concerned with the modelling of two-dimensional effects, including surface waves. To obtain a thorough understanding of two-dimensional phenomena we studied flat interfaces between elastic solids and fluids, and poroelastic solids and fluids. Due to the presence of the slow Biot wave three types of surface waves occur. We extended the surface wave model of Feng and Johnson (1983) for lossless media to lossy media, and as a result we obtained a better description for the attenuation of surface waves.

Finally, we studied the theory of guided wave modes in solid elastic cylinders. This theory was applied to the porous cylinder in the shock tube. Some of the wave modes that occur in the porous cylinder in the shock tube are equivalent to the ones in a solid elastic cylinder. A surface mode occurs at the interface between the porous cylinder and a relatively large water-filled gap. At high frequencies this wave is related to the pseudo-Stoneley wave in case of a Bentheimer sandstone cylinder, which is a fast formation. For

one specific synthetic slow formation we found that this wave corresponds to the true Stoneley wave. An extra bulk wave mode type occurs due to the presence of the slow Biot wave. The damping of the higher-order slow wave modes is at least as high as the damping of the slow wave itself.

The surface mode is sensitive to both the permeability and the shear velocity. Because this conclusion is valid both for our shock tube set-up and also for the borehole configuration, it has important implications for the analysis of permeability estimation from acoustic logging data.

Experimental results were obtained for both air-filled and water-saturated pores. For air-filled pores the transition from wave-like behaviour to diffusion-like behaviour of the slow wave was demonstrated. For very high permeabilities (> 500 D) the shock wave character is preserved and is detected at the end of the sample. For lower permeabilities the diffusion effect dominates. The non-linear diffusion process is described by Forchheimer's equation.

We investigated water-saturated samples extensively. Two configurations were used, the so-called small gap and large gap experiment. Using the small gap experiment we performed a large measurement series for samples with a wide range of properties. The velocities calculated with Biot's theory and derived from Wyllie's equation were compared with the experimental results. It was concluded that if the porosity is entered into Wyllie's equation, this model can be used as a first guess for the fast wave velocity.

In the frequency domain we measured reflection coefficients in the 1-100 kHz range. Generally, agreement was found with the Biot theory. Phase velocities were determined in the 1-120 kHz frequency range for natural and synthetic rocks. For the large gap experiment the surface mode in Bentheimer sandstone was observed, as well as a number of bulk modes. This is noteworthy, as most laboratory experiments either succeed in generating multiple wave modes over a small frequency range, or in generating only one wave mode over a broad frequency range. Agreement was found with the full modeling of the shock tube configuration for the surface mode and the lowest-order bulk mode. The comparison between the experiments and theory is based on parameters which were determined independently on core samples. For high Signal-to-Noise ratio's reasonable results for the damping coefficients can be obtained. Qualitative agreement between experimental and theoretical attenuation data was found for synthetic rock.

Our experiments confirm the predictive power of Biot's theory of wave propagation in cylindrical configurations. Despite the geometrical differences with the borehole configuration our results lead to a better understanding of borehole wave phenomena. Future work should concentrate on different boundary conditions in order to investigate the influence of the mud cake.

Samenvatting

Goed begrip van de invloed van gesteenteparameters op voortplanting van akoestische golven is van groot belang voor de interpretatie van akoestische loggingdata. Enkele voorbeelden van deze parameters zijn de porositeit, permeabiliteit, lithologie en de verzadigingsgraad. Om seismische data te kunnen vergelijken met loggingdata is het tevens belangrijk om goed inzicht te hebben in de frequentieafhankelijkheid van golfsnelheden en dempingsfactoren. In de traditionele loggingpraktijk werd de eerste aankomst gebruikt om de porositeit te bepalen. Het volledige signaal kan worden toegepast om de mechanische eigenschappen te bepalen. De zogenaamde Stoneleygolf is één van de golven die het laatst gedetecteerd wordt. Met behulp van deze golf is het mogelijk om de permeabiliteit te bepalen.

In dit proefschrift is voortplanting van akoestische golven in een poreuze cilinder onderwerp van studie. Het onderzoek bestaat uit een experimenteel en een theoretisch gedeelte. Er wordt aandacht besteed aan zowel de frequentieafhankelijkheid als de parameterafhankelijkheid van golfsnelheden en dempingscoëfficiënten. Tevens komen oppervlaktegolven aan de orde.

In de experimenten is gebruik gemaakt van een schokbuis. In de schokbuis wordt een drukstap met een brede frequentieband gegenereerd. In de testsectie is een poreuze cilinder aangebracht en tussen deze cilinder en de schokbuiswand bevindt zich een spleet. Indien de spleet groot is ten opzichte van de inwendige diameter van de schokbuis is het mogelijk de Stoneleygolf te exciteren. Gedurende het onderzoek is de klassieke schokbuisconfiguratie op unieke wijze aangepast. Met behulp van een schroefspindel is het equivalent van een groot aantal drukopnemers bereikt. In de klassieke schokbuisconfiguratie was slechts een beperkt aantal drukopnemers beschikbaar. Door het grote aantal drukopnemers was het mogelijk een speciale signaalverwerkingstechniek toe te passen: de zogenaamde Prony's methode. Op deze manier zijn fasesnelheden, dempingsfactoren en reflectiecoëfficiënten verkregen in de range van 1 tot 120 kHz.

Voor de beschrijving van de golfvoortplanting werd gebruik gemaakt van het model van Biot. In dit proefschrift wordt de theorie van Biot samengevat en becommentarieerd. Een computerprogramma wordt beschreven dat de ééndimensionale golfvoortplanting modelleert in de schokbuis, inclusief de interne reflecties. Het belangrijkste deel van de theorie behandelt tweedimensionale effecten, tevens met betrekking tot oppervlaktegolven. Om een goed beeld te krijgen van de tweedimensionale effecten zijn eerst grensvlakken bestudeerd tussen elastische vaste stoffen en vloeistoffen. Vervolgens zijn ook grensvlakken tussen poreuze media en vloeistoffen onderzocht. Tengevolge van de aanwezigheid van de langzame golf zoals voorspeld door Biot treden er drie typen oppervlaktegolven op. Het oppervlaktegolfmodel van Feng en Johnson (1983) is uitgebreid van verliesvrije me-

dia naar materialen inclusief demping. Het resultaat is een betere beschrijving van de demping van oppervlaktegolven.

Het laatste deel van de theoretische analyse behandelt golfmodes in een cilinder die bestaat uit een elastische vaste stof. Deze theorie is vervolgens toegepast op een poreuze cilinder in de schokbuis. Enkele van de golfmodes die voorkomen in de poreuze cilinder zijn vergelijkbaar met de modes in een elastische cilinder. Op het grensvlak van de poreuze cilinder en een relatief grote vloeistofge vulde spleet treedt een oppervlaktegolfmode op. Voor een cilinder die bestaat uit Bentheimer zandsteen is bij hoge frequenties de laatstgenoemde golf gerelateerd aan de pseudo-Stoneleygolf. Voor één specifieke synthetische steensoort is de oppervlaktegolf bij hoge frequenties gerelateerd aan de true-Stoneleygolf. Bentheimer zandsteen is een zogenaamde 'fast formation', terwijl het synthetische steen correspondeert met een 'slow formation'. Tengevolge van de langzame Biotgolf treedt er een extra type golfmode op. De demping van deze hogere-orde langzame-golfmodes is minstens even groot als de demping van de langzame Biotgolf zelf.

Zowel de permeabiliteit als de snelheid van de schuifgolf beïnvloeden de eigenschappen van de oppervlaktegolf in de schokbuis. Ze beïnvloeden tevens de oppervlaktegolf in een boorgat, met als gevolg dat analyse van de schokbuisresultaten van belang is voor de bepaling van de permeabiliteit uit akoestische loggingdata.

Experimentele resultaten werden verkregen voor monsters met luchtgevulde poriën en voor waterverzadigde monsters. Voor monsters met luchtgevulde poriën is de overgang van golfgedrag naar diffusiegedrag zichtbaar gemaakt. Voor hoge permeabiliteiten (> 500 D) is het schokgolfgedrag nog steeds aanwezig in het poreuze monster. Aan het eind van het monster is het schokgolfgedrag gedetecteerd. Voor lagere permeabiliteiten is het diffusie-effect dominant. Het niet-lineaire diffusieproces kan beschreven worden met behulp van de Forchheimervergelijking.

Waterverzadigde monsters zijn uitgebreid bestudeerd. Er werd gebruik gemaakt van twee configuraties: het kleine-spleetexperiment en het grote-spleetexperiment. Met behulp van de kleine-spleetconfiguratie werd een groot aantal experimenten uitgevoerd met monsters met een breed scala aan gesteente-eigenschappen. De golfsnelheden zoals voorspeld door de theorie van Biot en door de vergelijking van Wyllie zijn beide vergeleken met de experimentele resultaten. Op grond van de resultaten werd geconcludeerd dat de vergelijking van Wyllie met gebruik van de porositeit toegepast kan worden als een eerste-orde benadering voor de snelheid van de snelle Biotgolf.

In de range van 1 tot 100 kHz zijn reflectiecoëfficiënten gemeten. Behoudens enkele afwijkingen was er goede overeenkomst met de theorie van Biot. Voor zowel natuurlijk zandsteen als synthetisch gesteente zijn golfsnelheden bepaald in de range van 1 tot 120 kHz. In het geval van de grote-spleetconfiguratie zijn de oppervlaktegolfmode en een aantal hogere-orde golfmodes waargenomen. Dit is een belangrijk resultaat omdat in veel laboratoriumexperimenten men er in slaagt slechts één golfmode over een brede frequentieband waar te nemen. In geval van meerdere golfmodes is de frequentieband vaak smal. De experimentele resultaten zijn in overeenstemming met de volledige modellering van de schokbuisconfiguratie met betrekking tot de oppervlakte-mode en de laagste-orde bulkmode. De vergelijking tussen de experimenten en de theorie was gebaseerd op gesteent-

teparameters die onafhankelijk bepaald werden met behulp van kleine samples. Voor hoge signaal-ruisverhoudingen bleek het mogelijk om aanvaardbare resultaten te behalen voor de dempingsfactoren. Voor het synthetische gesteente was er kwalitatieve overeenkomst tussen de theorie van Biot en de experimenten.

De huidige experimenten bevestigen de voorspellende kracht van de theorie van Biot voor golfvoortplanting in cilindrische configuraties. Ondanks verschillen tussen de schokbuisgeometrie en de boorgatconfiguratie leiden de resultaten van dit proefschrift tot een beter begrip van golfverschijnselen in boorgaten. Het is aan te bevelen in de toekomst aandacht te schenken aan de verschillende randvoorwaarden, dit in verband met de invloed van de zogenaamde mud cake.

Chapter 1

Introduction

1.1 Background and problem statement

Acoustic wave propagation is very important for the oil industry to determine the different properties of an oil reservoir. The storage space (porosity), hydraulic conductivity (permeability), and lithology (rock type), and hydrocarbon saturation are properties of interest. Several subsurface interpretation techniques are involved with acoustic wave propagation: surface seismic, borehole seismic, acoustic borehole logging and borehole imaging. For an introduction to these techniques we refer to Ellis (1987). The common aim of these techniques is to deduce the rock properties from the wave velocities, amplitudes, damping and reflection coefficients. This is performed via a so-called inversion procedure, for which a model is required that describes wave propagation and reflection in (porous) rock. However, each of the mentioned techniques operates in a different frequency range. The frequency ranges vary from about 100 Hz for seismic applications to the MHz region in case of borehole imaging. Frequency dependence of wave velocities, damping and reflection coefficients has to be understood in order to compare the data of the different disciplines.

Theoretically, wave propagation and reflection characteristics were investigated for each particular frequency range. However, laboratory experiments that cover a broad frequency range are scarce. Most experiments were performed in the ultrasonic frequency range (0.5-5 MHz), while many applications use much lower frequencies. In this thesis we study the frequency dependence of the wave velocities, damping and reflection coefficients in the 1-120 kHz range, both experimentally and theoretically. This frequency range is relevant for acoustic borehole logging. Therefore, we give a short introduction to the principles of this technique.

Acoustic-logging probes such as illustrated in Fig. 1.1 measure the signal transmitted from a source T via the borehole fluid and through rock along the borehole wall to a set of receivers R located at some distance away. A typical diameter of the borehole is 30 cm, while a typical value for the tool diameter is 10 cm. The transmitter-receiver distance is about 1 m. The centre frequency of the acoustic pulses is around 20 kHz for conventional tools. A typical example of the recorded wavetrain is given in Fig. 1.2. The first arrival is the compressional head wave, while the second wave to arrive is the shear head wave. The third wave to arrive has a large amplitude and corresponds to the Stoneley wave,

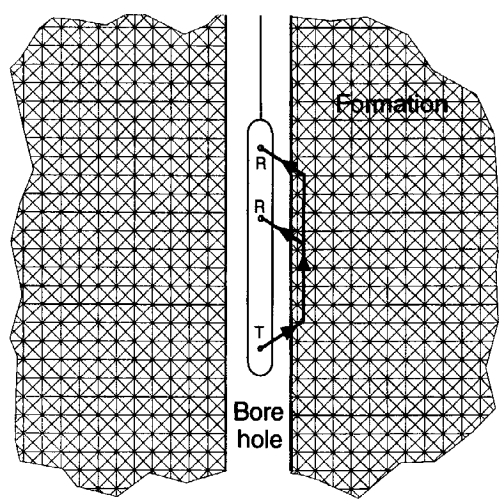


Figure 1.1: *Basic configuration acoustic logging.*

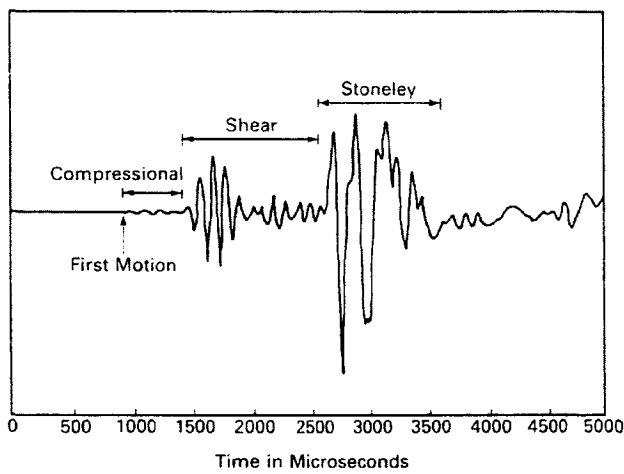


Figure 1.2: *Typical example of the received signal in a borehole (Ellis 1987)*

which is also called the tube wave. The velocity of the compressional wave is determined with the first arrivals of the wave train at the two receivers. Subsequently, Wyllie's equation (Wyllie *et al.* 1956, Wyllie *et al.* 1958) can be used to relate the compressional wave velocity to the porosity. New techniques have been developed to exploit the full wave train for the determination of the shear velocity and permeability. For estimation of the shear velocity in slow formations (shear velocity < compressional borehole fluid velocity), dipole and multiple sources are used. The permeability is estimated from the Stoneley wave (Tang and Cheng 1996, Tang 1998). An overview of these techniques and its applications can be found in the work of Paillet *et al.* (1991, 1992).

A literature survey of the studies concerned with the relation between the Stoneley wave and the permeability is given below. Experimental and theoretical evidence was found for the relation between the Stoneley wave properties and the permeability. The presence of the mud-cake and anisotropy remain however a problem. The mud-cake changes the boundary conditions at the wall of the borehole such that the Stoneley wave is less affected by the permeability. Furthermore, the interpretation of the full wave train is complicated by the presence of the logging tool and/or diameter variations of the borehole. These problems were covered by theoretical studies, but laboratory experiments are scarce in the frequency range which is relevant for acoustic logging.

As mentioned above frequency dependence of the wave velocities, damping and reflection coefficients are subject of research. More specifically, we investigated frequency-dependent wave propagation in a liquid-loaded porous cylinder. Both bulk and surface waves were considered for several diameters of the cylinder, and a wide range of rock properties. We concentrated on the effect of the permeability and the shear modulus on wave propagation parameters such as velocity and attenuation. An analogy for the presence of the logging tool in a borehole was obtained by using different values for the diameter of the porous cylinder.

We limited ourselves to the description of the rock property and frequency dependence of the phase velocities and damping coefficients. The inversion process itself was not considered. It is important to note that the approach of the inversion process is different from the modelling. In the inversion process the recorded acoustic signals are used to predict the reservoir properties. The predicted results can be validated by data of other wireline logging techniques or core samples. In the modelling the rock properties together with a wave propagation model are used to predict the acoustic signals. The predicted signals are compared with signals recorded during laboratory experiments.

1.2 Approach and thesis outline

In our experimental set-up, a so-called shock tube, it is possible to measure the progress of a pressure stepfunction through a water-saturated porous cylinder (Fig. 1.3). A shock wave in air is generated, which is transmitted into the water column on top of the sample. The step wave in the water partially reflects, partially transmits into the sample. Several pressure transducers are mounted in the wall of the shock tube. Between the porous cylinder and the wall of the shock tube a gap exists. Using a large value for the ratio of gap width to sample radius it is possible to excite both Stoneley and bulk waves. We performed a large series of measurements on samples with a wide range of porosi-

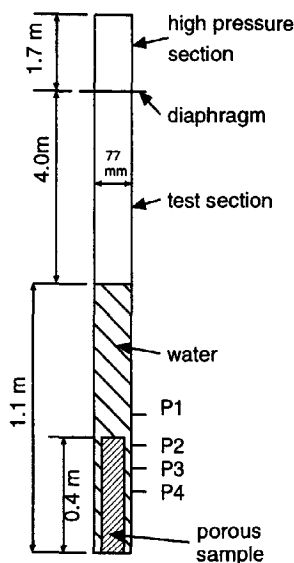


Figure 1.3: Shock tube configuration. P1, P2, P3 and P4 indicate the positions of the pressure transducers.

ties, permeabilities and lithologies. Furthermore, we modified the classical shock tube configuration in such a way that data were obtained in the frequency domain.

With our shock tube it is possible to study also non-linear phenomena. For these studies we used an air-filled test section, and also the pores were filled with air. Due to the high velocities of air flow in the pores, non-linear effects occur, and Darcy's law is not valid any more. Different permeabilities were used to investigate the limits of Darcy's law.

In our theoretical considerations we analyzed Biot's theory on waves in porous media. As surface waves play an important role in our research project, we first investigated the surface wave phenomena on flat interfaces between elastic solid formations and liquids. Following Feng and Johnson (1983), we extended this theory to a lossless poroelastic solid, and finally we applied the full Biot model, including damping.

The Stoneley wave can be modelled using the theory of wave modes. We started by giving an analysis of the wave mode theory for an elastic cylinder, after which we incorporated also the poroelastic effects. In our final model of the wave motion in porous cylinder, the liquid-filled gap and the elastic wall of the shock tube were taken into account. We present the afore mentioned topics in the following way:

- In the Chapter 2 and 3 Biot's theory of wave propagation in porous media is discussed. Equations of motion are given, as well as the boundary conditions.
- In Chapter 4 we discuss one-dimensional wave propagation in multiple layers as function of the different boundary conditions. In this way we can understand the

basic features of Biot's theory. The fundamentals of a numerical code are presented. With this numerical code we can analyze one-dimensional wave propagation in the shock tube configuration.

- In Chapter 5 the principle of the shock tube measurements is explained. Using a large measurement series on water-saturated samples we evaluated both Biot's theory and Wyllie's equation. For air-filled pores results for samples with different permeabilities are presented, together with an evaluation of Darcy's law and a non-linear model, the Forchheimer equation.
- Surface wave phenomena are discussed in Chapter 6 for elastic and poroelastic media. The theory of elastic wave guides is given in Chapter 7. Both topics are used in Chapter 8 to explain the theory of wave modes in the porous cylinder in the shock tube. The analysis is based on both the wave mode theory and Biot's theory. Finally, the parameter dependence of the Stoneley mode is analysed.
- An advanced signal processing technique, the so-called Prony's method is used to obtain phase velocities and damping coefficients in the frequency domain. The main properties of this theory are discussed in Chapter 9.
- Experimental results for the phase velocities and damping coefficients of the Stoneley mode and higher-order modes are presented in Chapter 10. Both natural and synthetic rock are considered. The results are compared with the theoretical model of Chapter 8.

1.3 Literature survey

First, we give a short review of the models which are commonly used in field and laboratory studies, the Wyllie equation and the Biot model. Subsequently, we focus on the relation between the borehole Stoneley wave and the rock properties, after which a more general consideration of surface waves is given. Our last topic in this survey is formed by the theoretical and experimental results for poroelastic waveguides.

1.3.1 Waves in porous media

As mentioned above Wyllie's equation can be used for porosity evaluation. The velocity of the compressional wave is based on an averaging of the inverse sound velocities of the grains and the saturant fluid, where the porosity is used as the weighting factor. The model is based on a system of solid parallel plates with different properties. It is therefore a simplified model of wave propagation in a porous solid, but it can easily be implemented in an inversion procedure. Wyllie *et al.* (1956, 1958) observed good agreement between their model and their experiments for pressurised sandstone samples.

A more complete theory to describe wave propagation through porous media was given by Biot (Biot 1956a, Biot 1956b). He presented his theory around the same time as Wyllie, but his theory is less popular in field applications. The complexity of the equations and the large number of rock parameters that are required produce a very complicated inversion procedure.

Theory

The most striking feature of Biot's theory is that it predicts two compressional waves and a shear wave in a poroelastic solid. This is in contrast to an elastic solid, where only one compressional wave and a shear wave occur. The first wave of a wave train to arrive in a poroelastic solid is called the fast wave, and corresponds to the in-phase motion of the solid and the fluid. The second compressional wave is called the slow wave, and corresponds to out-of-phase motion of the solid and the fluid. The latter is characterized by a high damping coefficient and diffusive behaviour in the low-frequency limit. The first experimental observation of the slow wave was reported by Plona (1980). Independently of Biot, De Josselin de Jong (1956) described acoustic wave propagation through porous sandstone saturated with water, and he also predicted the occurrence of two compressional waves and a shear wave.

In the frequency domain Biot's theory contains two limiting cases, the high-frequency and the low-frequency limit. In the high-frequency limit inertia forces play a dominant role and both the fast and the slow compressional wave are propagatory. In the low-frequency limit the viscous forces in the fluid dominate the inertia forces and the slow wave shows diffusive behaviour. This limit is also called the Biot-Gassmann result (Gassmann 1951). Boundary conditions for poroelastic media were given by Deresiewicz and Skalak (1963). They proposed the so-called open pore and sealed pore conditions as two limiting cases and introduced the concept of interface permeability.

An important contribution to Biot's theory was given by Johnson *et al.* (1987). They developed the model for the dynamic permeability. In between the low-frequency and the high-frequency limit both inertia and viscous forces play an important role. With their proposal Johnson *et al.* incorporated these two effects in one model, which satisfied both limits. They derived their results using energy considerations. Smeulders *et al.* (1992) derived the same results from the micro-structural approach.

Wave propagation in porous media is strongly influenced by the fluid saturation. Partially saturated pores were studied by Smeulders and Van Dongen (1997). Air-filled pores were investigated by several authors (Attenborough 1987, Allard 1993, van Dongen *et al.* 1995). Deviations from Darcy's law for this case were observed by Van de Grinten *et al.* (1985) and Wilson *et al.* (1988).

Laboratory experiments

Experimental results show the strong predictive power of Biot's theory. As already mentioned, Plona (1980) reported the first observations of the slow wave. Using a spectral ratio technique and synthetic rock samples Johnson and Plona (1994) measured phase velocities of the three Biot waves and damping coefficients of the slow wave in the 0.1 - 1 MHz frequency range. Kelder (1998) used a similar experimental technique, but presents also data on natural rock samples. Experiments to measure dynamic permeability were presented by Johnson *et al.* (1994), Smeulders *et al.* (1992) and Kelder (1998).

Shock tube experiments provide data in a lower frequency range due to the low frequency content of a step wave. Van der Grinten *et al.* (1985, 1987), Sniekers *et al.* (1989), and Smeulders and Van Dongen (1997) performed shock tube experiments on water-saturated, partially saturated, and dry samples. Nakoryakov *et al.* (1989) studied

the propagation of both step waves and bell-shaped waves in a shock tube configuration. Up to now shock tube data were presented in the time domain, while the frequency dependence is an important point of interest. In this thesis we present a technique to obtain phase velocities and damping coefficients in the frequency domain, using a shock tube. The initial results were reported earlier (Wisse *et al.* 1998).

Van der Grinten *et al.* (1985) report also shock tube experiments on air-filled porous media. Due to the strong shock wave, in that configuration, non-linear effects were observed, which were described by Forchheimer's equation. For other experiments on air-filled pores, we refer to Allard (1993) and Nagy and Adler (1990). They reported measurements of reflection coefficients and tortuosity factors.

In this short review of the models of porous media we have concentrated on Wyllie's equation and Biot's model. For more extensive reviews and other available models we refer to Stoll (1974), Bourbié *et al.* (1987) and Allard (1993).

1.3.2 Borehole Stoneley waves and parameter dependence

Acoustic wave trains in a borehole were studied with Biot's theory by Rosenbaum *et al.* (1974). He was one of the first authors to indicate the relation between the Stoneley wave and the permeability effects. Williams *et al.* (1984) used field data to show a correlation between the core-measured permeability, the Stoneley wave velocity and the Stoneley wave amplitude. The data of Williams *et al.* were evaluated with Biot's theory by Cheng *et al.* (1987), who confirmed the correlation between the permeability and Stoneley wave properties. They did, however, not take into account the variations of the elasticity. Burns *et al.* (1988) incorporated the variations of the shear modulus and obtained a better correlation. Theoretically, Schmitt *et al.* (1988a, 1988b) and Winkler *et al.* (1989) investigated the relation between the Stoneley wave properties and the permeability. Schmitt *et al.* also mentioned the influence of the shear wave velocity on the Stoneley wave. Hence, a good estimation of the shear modulus is needed to obtain a reliable permeability evaluation. Burns and Cheng (1987) reported a method to obtain shear attenuation values from guided waves such as the Stoneley wave. In slow formations, where no shear wave arrival is observed, the Stoneley wave is used to obtain the shear velocity.

Simplified models are needed to perform the inversion process. White (1983) and Hsui and Toksöz (1986) derived a low-frequency model for the tube wave. Chang *et al.* (1988) compared the White approximation with the full modelling with Biot's theory. Tang *et al.* (1991) developed a simplified expression for the Stoneley wave, and showed a comparison between their model and the full Biot modeling. Agreement was found with the laboratory data of Winkler *et al.* (1989). Tang *et al.* (1995) presented a processing technique for the estimation of the formation shear velocity from Stoneley waveforms. The simplified model for the Stoneley wave was incorporated in an inversion procedure (Tang *et al.* 1995, Tang and Cheng 1996), from which the permeability could be obtained using the Stoneley wave. In this inversion procedure the influence of the shear velocity on the Stoneley wave was also taken into account. The results clearly demonstrate a successful use of the Stoneley wave for permeability estimation.

The permeability estimation from the Stoneley wave can be disturbed by mud particles in the borehole fluid. The first problem caused by the mud is that the viscous effects of

the borehole fluid cannot be neglected (Burns 1988). Furthermore, it is not entirely clear which boundary conditions have to be applied. This is due to the mud-cake, which is an aggregate of mud particles that collect on the borehole surface. Recently, Liu and Johnson (1997) proposed a set of boundary conditions for the mud-cake. They also analysed the influence of these boundary conditions on the Stoneley mode.

1.3.3 Surface waves and flat interfaces.

The Stoneley wave on the borehole wall corresponds at high frequencies (above 10 kHz) to a surface wave, while at low frequencies (below 1 kHz) it corresponds to the so-called 'water-hammer'. The acoustic pressure of a surface wave falls off exponentially as it departs from the boundary. For a general treatment of surface waves in acoustics, we refer to Uberall (1973), Viktorov (1967) and Brekhovskikh (1980). The surface wave at a flat interface between an elastic half space and a vacuum is the well-known Rayleigh wave. On a flat liquid-solid interface not only the Stoneley wave is present, but also the pseudo-Rayleigh wave. (Uberall 1973). The velocity of the Stoneley wave is lower than the liquid sound velocity, while the velocity of the pseudo-Rayleigh wave is in between the liquid sound velocity and the shear velocity of the elastic formation. It should be noted that there is a difference between this pseudo-Rayleigh wave and the so-called pseudo-Rayleigh modes in a borehole. The latter are higher-order borehole modes (Paillet and Cheng 1991), which are strongly dispersive, and the high-frequency limit of the phase velocity is the shear velocity. Below a certain frequency they are cut off.

The theory of surface waves and pseudo-surface waves for elastic media has been extended to poroelastic media by Feng and Johnson (1983). Their analysis was based on the high-frequency limit of Biot's theory. The viscous dissipation was not taken into account and a lossless medium was considered. In the case of a fast formation three types of surface waves exist: the true Stoneley wave, the pseudo-Stoneley wave and the pseudo-Rayleigh wave. The true Stoneley wave has a phase velocity which is lower than the slow wave velocity, and is therefore lower than all the bulk velocities in the system. The velocity of the pseudo-Stoneley wave is in between the slow wave velocity and the liquid velocity, while the pseudo-Rayleigh wave velocity is in between the liquid velocity and the shear wave velocity. The pseudo-Stoneley wave is the wave which is related to the permeability. Generally, in borehole applications this wave is called the Stoneley wave.

1.3.4 Wave modes in poroelastic waveguides

A review of the wave mode theory in boreholes is given by Paillet and Cheng (1991). In this subsection we focus on the wave mode theory in cylinders. Waves in elastic cylinders have been investigated by many authors. The research was already started by Pochhammer in 1876, but due to the complexity of the equations it took half a century to obtain computational results. For details of the historic development we refer to Onoe *et al.* (1962) and Meeker and Meitzler (1964). Experimental data on this subject were provided by Fox *et al.* (1958) and Zemanek (1971). The main result of the Pochhammer theory is that a finite number of undamped modes occur, which have the shear velocity

as their high-frequency limit and are cut off below a certain frequency. The lowest-order mode is propagatory over the entire frequency range and its low-frequency limit is called the 'bar'-velocity.

Theory

The theory of wave modes in elastic cylinders can be used together with Biot's theory for the modelling of porous cylinders. From a theoretical point of view an interesting question is whether the slow Biot wave gives rise to an extra wave mode type. This is indeed the case, as indicated by several authors. We summarize their results chronologically. Gardner (1962) was the first to apply the wave mode theory to porous cylinders. He used the long-wavelength approximation together with the low-frequency limit of Biot's theory. He studied the case of an isolated porous cylinder, i.e. the pressure of the surrounding medium is zero. He predicted the presence of two types of wave modes, one due to the fast wave and one due to the slow wave. Because of the approximations in the theory, his expression for the second wave type is not generally valid. Berryman (1983) used the full Biot theory to study the wave modes in an isolated cylinder. For the open pore conditions he presented three wave modes of the same type which are similar to the elastic wave modes. For the open pore conditions he did not find the slow wave mode type. For the sealed pores he found such a wave type with a phase velocity lower than the slow wave. It was suggested that this wave type is related to the true surface wave which was discussed by Feng and Johnson (1983). Liu (1988) analysed the wave modes in the configuration of Winkler *et al.* (1989) which is drawn in Fig. 1.4 (LHS). In this configuration the borehole in the porous cylinder is filled with liquid. The porous cylinder is saturated with liquid and immersed in liquid. Liu (1988) found two wave mode types, one due to the fast wave, and one due to the slow compressional wave. The existence of a second mode type is also confirmed by the results of Hsu *et al.*, who modelled the configuration as given in Fig. 1.4 (RHS). Further work on porous cylinders has been carried out by Johnson and Kostek (1995), that provided a comparison between the approximation of Gardner and the full Biot theory for the first mode type.

Laboratory experiments

Laboratory data on wave modes which cover a broad frequency range are scarce. The quasi-static experiments in the 0.2-200 Hz range of Dunn (1986, 1987) are difficult to interpret due to boundary effects. Resonant bar techniques on rod shaped rock samples provide data in the 1-20 kHz range, but these data are limited to the lowest-order wave mode. Due to the long-wavelength approximation it is difficult to operate this technique above 20 kHz (White 1983, Tang 1993). Furthermore, the interpretation is also complicated by boundary effects. Tang (1993) used a waveform inversion technique for an elastic solid cylinder. He obtained data in the 10-150 kHz frequency range for the lowest-order mode. His technique is also applicable to porous cylinders.

Winkler *et al.* (1989) reported experiments on Stoneley waves in both artificial and natural (Berea sandstone) samples in the 10-90 kHz frequency range. We explain their experiment in more detail because of the similarities with our experimental technique. Their set-up is shown in Fig. 1.4 (LHS). A monopole source is placed in the borehole

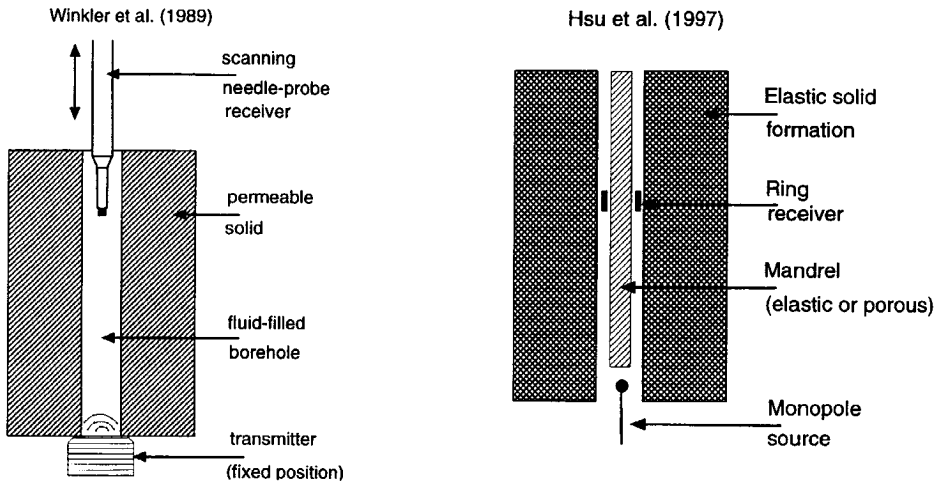


Figure 1.4: *Experimental configurations of Winkler et al. (1989) and Hsu et al. (1997)*

which penetrates a porous cylinder. The receiver is moved vertically in one centimeter increments, and a waveform is recorded at each position. A typical scan contains 15 to 20 waveforms, of which each is the average of 100 waveforms per station. Using Prony's method (Marple 1987, Lang *et al.* 1987) Winkler *et al.* obtained phase velocities and damping coefficients of the Stoneley wave. Excellent agreement was found between modelling and experimental results. The model parameters for the compressional and shear waves were measured under saturated conditions. They only report data of the Stoneley wave, most likely because other mode types were weakly excited.

Recently Hsu *et al.* (1997) investigated the characteristics of tube waves in an elastic solid formation, with and without a cylindrical mandrel (Fig. 1.4 (RHS)). Porous and elastic mandrels were used. In case of a porous mandrel, this configuration is very similar to ours. Using synthetic porous samples, they found excellent agreement with their modelling for the phase velocity of the tube wave in the 10-100 kHz frequency range. Between 50 and 90 kHz a bulk mode could be recorded. Due to the way they set up the experiment only the modes with appreciable energy in the fluid annulus could be detected. The dimension of the fluid annulus that they used was quite large, the ratio of the diameter of the mandrel to the diameter of the borehole is equal to 0.6. Attenuation data were also presented, but the scatter is such that it is difficult to compare the results to their modelling.

Summarizing these laboratory experiments, we may say that they either succeed in generating multiple wave modes over a small frequency range, or in generating only one wave mode over a broad frequency range.

Chapter 2

Constitutive relations and momentum equations

In next two chapters we discuss the main features of Biot's theory of wave propagation in porous media. Developed by Biot (Biot 1956a, Biot 1956b) some forty years ago, it is widely used now in the field of porous media. The experimental observation of the predicted second compressional wave by Plona (1980), the re-derivation of the equations from the microstructure by Burridge and Keller (1983) and the concept of dynamic permeability, developed by Johnson *et al.* (1987) contributed to the acceptance of Biot's theory.

The approach of this chapter is as follows. First, we discuss definitions and assumptions followed by the stress-strain relations for a porous solid. Subsequently, the elasticity coefficients occurring in the constitutive relations are related to measurable quantities. To obtain a thorough insight in the phenomena described by Biot's theory we discuss the so-called rigid frame limit, which is followed by the introduction of the concept of dynamic permeability.

2.1 Continuum theory

Considering a fluid-filled elastic skeleton with a statistical distribution of interconnected pores, the porosity can be expressed by:

$$\phi = \frac{V_f}{V_b}, \quad (2.1)$$

where V_f is the volume occupied by the fluid and V_b is the total volume. For a statistically isotropic porous material this is equal to the ratio of the surfaces A_f and A_b (Fig. 2.1). In this definition only interconnected pores contribute to the porosity. The closed pores are considered as part of the solid. For long-wavelength disturbances ($\lambda \gg a$, where a is a typical pore size and λ is the wavelength) propagating through such a porous medium, it makes sense to define average values of the (local) displacements in the solid and in the fluid. For further discussions on the relation between the microscopic and the macroscopic level, the reader is referred to the publications of Burridge and Keller (1983), Smeulders (1992), and Kelder (1998). In this chapter we use macroscopic properties, and if necessary

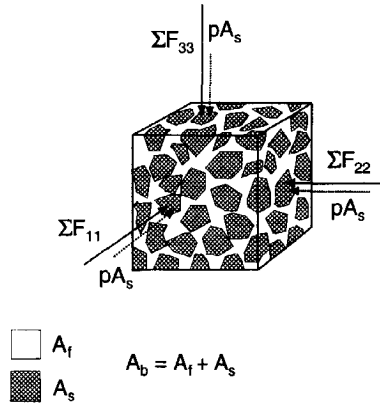


Figure 2.1: Cube of unit size. The intergranular forces are denoted by F_{ij} , the pore pressure by p .

a link shall be made to the microscopic structure. Furthermore, we make the following assumptions in this chapter:

- The displacements of both the fluid and solid phases are assumed to be small. The equations are presented in their linearized form.
- The fluid neither transmits nor reacts to a shear force in the solid. This is in accordance with the assumption that the fluid has no shear strength.
- The matrix is assumed to be elastic and isotropic, and dissipation related to the matrix is neglected. Only dissipation due to the interaction between the solid and the fluid is taken into account.
- The absence of thermo-elastic and chemical reaction effects is assumed.

2.1.1 Stresses and strains

The average displacement vector for the solid frame is \mathbf{u}_s , while that for the pore fluid is \mathbf{u}_f . Within the restrictions of the linearized theory the strains e_{ij} for the solid and ϵ_{ij} for the fluid can be described as follows:

$$e_{ij} = \frac{1}{2} \left(\frac{\partial u_{si}}{\partial x_j} + \frac{\partial u_{sj}}{\partial x_i} \right), \quad (2.2)$$

$$\epsilon_{ij} = \frac{1}{2} \left(\frac{\partial u_{fi}}{\partial x_j} + \frac{\partial u_{fj}}{\partial x_i} \right). \quad (2.3)$$

When defining the stress tensor in a porous medium one has to be strict on notation. This is especially important when the work of several authors is compared. The total

stress tensor of the porous material can be written in the following way:

$$\begin{pmatrix} \tau_{11} + \tau & \tau_{12} & \tau_{13} \\ \tau_{21} & \tau_{22} + \tau & \tau_{23} \\ \tau_{31} & \tau_{32} & \tau_{33} + \tau \end{pmatrix}, \quad (2.4)$$

with the symmetry property $\tau_{ij} = \tau_{ji}$. If a cube of unit size of the bulk material is considered (Fig. 2.1), τ represents the total normal tension force per unit bulk area A_b applied to the fluid part of the faces of the cube. Denoting by p the pressure of the fluid in the pores we may write:

$$\tau = -\frac{pA_f}{A_b} = -\phi p. \quad (2.5)$$

The remaining components τ_{ij} of the total stress tensor are the forces per unit bulk area A_b applied to that portion of the cube faces occupied by the solid. Both the intergranular forces F_{ij} and the pressure p contribute to the stress τ_{ij} :

$$\tau_{ij}A_b = -\sum F_{ij} - pA_s\delta_{ij}, \quad (2.6)$$

where the Kronecker symbol δ_{ij} is introduced because the pore fluid cannot exert nor sustain any shear forces on the macroscopic scale. With the intergranular stress $\sigma_{ij} = \sum F_{ij}/A_b$ we write:

$$\tau_{ij} = -\sigma_{ij} - (1 - \phi)p\delta_{ij}. \quad (2.7)$$

We notice that the additional intergranular stresses σ_{ij} are defined negative in tension. They are referred to as 'additional' because they add up to the fluid pressure-induced stresses in the solid. From these considerations it follows that the total stress tensor for the porous material may be written as:

$$\begin{pmatrix} -\sigma_{11} - p & -\sigma_{12} & -\sigma_{13} \\ -\sigma_{21} & -\sigma_{22} - p & -\sigma_{23} \\ -\sigma_{31} & -\sigma_{32} & -\sigma_{33} - p \end{pmatrix}. \quad (2.8)$$

The formulation of the total stress tensor is also given by Verruijt (1982); it must however be noted that he denotes the total stress tensor by σ_{ij} and the intergranular stress by $\bar{\sigma}_{ij}$.

2.1.2 Stress-strain relations

We now proceed to establish the relation between the stress and strain components of the porous medium as defined before. Biot (1955) developed the stress-strain relationships by generalization of the procedure followed in the classical theory of elasticity (Love 1944). In a previous paper (Biot 1941), the relations were derived for an isotropic solid using a kind of 'gedanken' experiment. In this section we summarize the derivation presented in the paper of 1955. The elastic potential energy V of the porous system can be written as:

$$2V = \tau_{11}e_{11} + \tau_{22}e_{22} + \tau_{33}e_{33} + 2\tau_{12}e_{12} + 2\tau_{13}e_{13} + 2\tau_{23}e_{23} + \tau\epsilon, \quad (2.9)$$

with $\epsilon = \epsilon_{11} + \epsilon_{22} + \epsilon_{33}$. If it is assumed that the seven stress components are linear functions of the seven strain components, the expression $2V$ is a homogeneous quadratic function of the strain. This function is a positive definite form with 49 coefficients. Due to the symmetry of the seven-by-seven matrix of elasticity coefficients the number of distinct coefficients equals 28:

$$\begin{pmatrix} \tau_{11} \\ \tau_{22} \\ \tau_{33} \\ \tau_{12} \\ \tau_{13} \\ \tau_{23} \\ \tau \end{pmatrix} = \begin{pmatrix} c_{11} & c_{12} & c_{13} & c_{14} & c_{15} & c_{16} & c_{17} \\ & c_{22} & c_{23} & c_{24} & c_{25} & c_{26} & c_{27} \\ & & c_{33} & c_{34} & c_{35} & c_{36} & c_{37} \\ & & & c_{44} & c_{45} & c_{46} & c_{47} \\ & & & & c_{55} & c_{56} & c_{57} \\ & & & & & c_{66} & c_{67} \\ & & & & & & c_{77} \end{pmatrix} \begin{pmatrix} e_{11} \\ e_{22} \\ e_{33} \\ 2e_{12} \\ 2e_{13} \\ 2e_{23} \\ \epsilon_{kk} \end{pmatrix}, \quad (2.10)$$

with the symmetry property $c_{ij} = c_{ji}$. In case of complete isotropy the function V becomes invariant for all transformations from one set of orthogonal axes to another. Then the problem is simplified and the number of elasticity coefficients reduces to four. The stress components are given by the partial derivatives of V as follows:

$$\frac{\partial V}{\partial e_{11}} = \tau_{11}, \quad \frac{\partial V}{\partial e_{22}} = \tau_{22}, \quad \frac{\partial V}{\partial e_{33}} = \tau_{33}. \quad (2.11)$$

$$\frac{\partial V}{\partial e_{12}} = 2\tau_{12}, \quad \frac{\partial V}{\partial e_{13}} = 2\tau_{13}, \quad \frac{\partial V}{\partial e_{23}} = 2\tau_{23}. \quad (2.12)$$

$$\frac{\partial V}{\partial \epsilon} = \tau. \quad (2.13)$$

For the isotropic case, the stress-strain relations read as follows (Biot 1955):

$$\tau_{ij} = A e_{kk} \delta_{ij} + Q \epsilon_{kk} \delta_{ij} + 2G e_{ij}, \quad (2.14)$$

$$\tau = -\phi p = Q e_{kk} + R \epsilon_{kk}, \quad (2.15)$$

where the elasticity coefficients A , Q , R and G have been introduced and $e_{kk} = e_{11} + e_{22} + e_{33}$. Using Equation (2.5) and (2.7) we write for the intergranular stress:

$$\sigma_{ij} = - \left[A - \frac{(1-\phi)}{\phi} Q \right] e_{kk} \delta_{ij} - \left[Q - \frac{(1-\phi)}{\phi} R \right] \epsilon_{kk} \delta_{ij} - 2G e_{ij}. \quad (2.16)$$

2.2 'Gedanken' experiments

The so-called 'gedanken' experiments can be used to relate the elasticity coefficients A , Q , R and G to measureable quantities. The coefficient G corresponds to the shear modulus of the solid skeleton, and can be determined by a shear test. The relations of the coefficients A , Q and R to measureable quantities, however, are complicated. The 'gedanken' experiments presented in this section have been developed by Biot and Willis (1957) and were used by Geertsma and Smit (1961), Berryman (1981), Johnson and Plona (1986), Smeulders (1992) and Kelder (1998).

2.2.1 'Jacketed' test

In the first 'gedanken' experiment, the so-called 'jacketed' test, the influence of the intergranular stress is studied. There are no shear forces acting on the sample and the second (pressure) term on the RHS of Equation (2.7) is equal to zero. This result is obtained in the following way. A saturated porous sample is jacketed and fully submerged in a watertank (pressure change dp') and the inside of the jacket is allowed to communicate with the atmosphere via a tube to ensure constant internal fluid pressure. Using Equation (2.7) with $p = 0$, we may write for the stress tensor:

$$\begin{aligned}\tau_{ij} &= -dp' \delta_{ij}, \\ \tau &= 0.\end{aligned}\tag{2.17}$$

From Equations (2.14) and (2.15) we obtain:

$$-dp' = A - \frac{Q^2}{R} e_{kk} + \frac{2}{3} G e_{kk},\tag{2.18}$$

and

$$\epsilon_{kk} = -\frac{Q e_{kk}}{R}.\tag{2.19}$$

As there are no changes of the pore pressure, the jacketed test measures the influence of a change of the intergranular stress on the bulk volume of the sample. The matrix bulk modulus K_b is defined in the following way:

$$\frac{1}{K_b} = -\frac{1}{V_b} \frac{dV_b}{dp'},\tag{2.20}$$

which gives the opportunity to write the dilatation of the solid as:

$$e_{kk} = -\frac{dp'}{K_b}.\tag{2.21}$$

We then obtain the following expression for the bulk modulus K_b :

$$K_b = A - \frac{Q^2}{R} + \frac{2}{3} G,\tag{2.22}$$

which shows a similarity to the elastic case, where the well-known Lamé coefficients λ and μ are related to the bulk modulus as follows (Achenbach 1973):

$$K_b = \lambda + \frac{2}{3} \mu.\tag{2.23}$$

The quantity $A - Q^2/R$ is therefore equivalent to the Lamé coefficient λ of the porous material under conditions of constant pore pressure.

2.2.2 'Unjacketed' test

In the second 'gedanken' experiment the influence of a pore pressure change is studied. Then the first (stress) term on the RHS of Equation (2.7) is kept equal to zero. In this test, called the unjacketed test, the porous sample is immersed in a watertank, while a pressure change dp' is applied, and the sample is assumed to be fully water-saturated. Then it is clear that the fluid pressure must be continuous over the interface ($dp = dp'$) and the intergranular stresses are equal to zero. Then we may write for the stress tensor:

$$\begin{aligned}\tau_{ij} &= -(1 - \phi)dp'\delta_{ij}, \\ \tau &= -\phi dp'.\end{aligned}\tag{2.24}$$

In this unjacketed test the influence of pore pressure changes on the volumes of both the solid and the fluid are studied. In the homogeneous case the application of an incremental pressure dp' means applying this increment both to the outer and inner pore surface, which leads to a linear mapping and does not change the porosity ϕ . Therefore the change of the volume of the solid as well as the change of the bulk volume can be related to the bulk modulus of the single grains K_s in the following way:

$$\frac{1}{K_s} = \frac{-1}{V_b} \frac{dV_b}{dp'} = \frac{-1}{V_s} \frac{dV_s}{dp'}.\tag{2.25}$$

The pore fluid is compressed only due to the increase of pressure dp' and can move freely in and out of the sample at the boundaries of the sample. Therefore, the change of the fluid volume V_f is related to the pressure change dp' via the bulk modulus of the saturant fluid:

$$\frac{1}{K_f} = \frac{-1}{V_f} \frac{dV_f}{dp'}.\tag{2.26}$$

In this way we have obtained expressions for the dilatation of the solid ($e_{kk} = -dp'/K_s$) and the dilatation of the fluid ($e_{kk} = -dp'/K_f$). These relations can be substituted in the stress-strain Equations (2.14) and (2.15). Together with the expressions for the stresses of Equation (2.24) we obtain two additional equations for the coefficients A , Q , R and G :

$$\phi = \frac{R}{K_f} + \frac{Q}{K_s},\tag{2.27}$$

$$1 - \phi = \frac{A}{K_s} + \frac{Q}{K_f} + \frac{2}{3} \frac{G}{K_s}.\tag{2.28}$$

Note that these relations are only valid for the homogeneous case. For the non-homogeneous case the reader is referred to Biot and Willis (1957) and Kelder (1998).

2.2.3 Relation to measurable quantities

After some algebraic manipulation of the results of the jacketed test (Equation (2.22)) and the unjacketed test (Equations (2.27) and (2.28)), we can write the coefficients A , Q

and R explicitly as function of the measurable quantities K_b , K_s and K_f :

$$A = \frac{K_f \left((1 - \phi) \left((1 - \phi) - \frac{K_b}{K_s} \right) + \phi K_b \right)}{\beta} - \frac{2}{3}G, \quad (2.29)$$

$$Q = \frac{\phi K_f \left((1 - \phi) - \frac{K_b}{K_s} \right)}{\beta}, \quad (2.30)$$

$$R = \frac{\phi^2 K_f}{\beta}, \quad (2.31)$$

where

$$\beta = \phi + \frac{K_f}{K_s} \left((1 - \phi) - \frac{K_b}{K_s} \right). \quad (2.32)$$

Kelder (1998) derived these expressions from continuity and constitutive relations based on the work of Verruijt (1982). If we assume that the matrix and pore fluid are much more compressible than the grains themselves ($K_b/K_s \ll (1 - \phi)$ and $K_f/K_s \ll \phi$), we may write

$$A = \frac{(1 - \phi)^2}{\phi} K_f + K_b - \frac{2}{3}G, \quad (2.33)$$

$$Q = K_f(1 - \phi), \quad (2.34)$$

$$R = \phi K_f. \quad (2.35)$$

In Appendix E the measurement methods of K_b and G is discussed. Then it is assumed that the saturant fluid does not influence the values of K_b and G . This implies that the measurements can be performed on dry samples, which facilitates their determination. For the incompressible grain approximation the stress-strain relations simplify. Substituting Equations (2.33), (2.34), and (2.35) in Equations (2.15) and (2.16), we obtain:

$$\sigma_{ij} = -(K_b - \frac{2}{3}G)e_{kk}\delta_{ij} - 2Ge_{ij}, \quad (2.36)$$

and

$$p = -\frac{\tau}{\phi} = -\frac{K_f(1 - \phi)e_{kk}}{\phi} - K_f\epsilon_{kk}. \quad (2.37)$$

2.3 Momentum equations

The momentum equations for a porous medium have been derived from Lagrangian mechanics by Biot in his paper of 1956. Using a two-space method of homogenization Burridge and Keller (1983) arrived at the same results for the case that the viscosity of the saturant liquid is low. In this section we follow the derivation of Biot.

From Lagrange's equations (Davies 1988) including dissipation it can be derived that

$$\frac{\partial}{\partial t} \left(\frac{\partial T}{\partial \dot{u}_{si}} \right) + \frac{\partial D}{\partial \dot{u}_{si}} = F_{si}, \quad (2.38)$$

and

$$\frac{\partial}{\partial t} \left(\frac{\partial T}{\partial \dot{u}_{fi}} \right) + \frac{\partial D}{\partial \dot{u}_{fi}} = F_{fi}. \quad (2.39)$$

In these equations T is the kinetic energy per unit volume of the porous system, F_{si} the force acting on the solid per unit volume, and F_{fi} the force acting on the fluid per unit volume. The dissipation function is denoted by D . Time derivatives are denoted by dots above the variables. The expression for the kinetic energy reads as follows:

$$2T = \rho_{11} \dot{u}_{si} \dot{u}_{si} + 2\rho_{12} \dot{u}_{si} \dot{u}_{fi} + \rho_{22} \dot{u}_{fi} \dot{u}_{fi}, \quad (2.40)$$

where the summation convention must be invoked. In this expression the densities ρ_{11} and ρ_{22} are related to the density of the solid ρ_s and the density of the fluid ρ_f by

$$\rho_{11} = (1 - \phi)\rho_s - \rho_{12}, \quad (2.41)$$

$$\rho_{22} = \phi\rho_f - \rho_{12}. \quad (2.42)$$

The coefficient ρ_{12} represents a mass coupling parameter between the solid and the fluid and is related to the fluid density in the following way:

$$\rho_{12} = -(\alpha_\infty - 1)\phi\rho_f, \quad (2.43)$$

where the parameter α_∞ is referred to as the tortuosity ($\alpha_\infty \geq 1$). We discuss this term more extensively in the next section. Dissipation depends only on the relative motion between the fluid and the solid. Introducing the concept of the dissipation function, we may write this function as a homogeneous quadratic form with the six velocities \dot{u}_{si} and \dot{u}_{fi} . The dissipation vanishes when there is no relative motion of the fluid and the solid. The dissipation function D for the isotropic case is therefore (Biot 1956b):

$$2D = b_0(\dot{u}_{si} - \dot{u}_{fi})(\dot{u}_{si} - \dot{u}_{fi}), \quad (2.44)$$

where the coefficient b_0 is related to the Darcy's coefficient of permeability k_0 by

$$b_0 = \frac{\phi^2 \eta}{k_0}. \quad (2.45)$$

The dynamic viscosity of the saturant liquid is denoted by η . For anisotropic solids the permeability depends on the direction and is expressed by a tensor. In the next section, the relation between Darcy's law and the dissipation function is clarified using simplified cases. The force components F_{si} and F_{fi} are related to the stresses in the following way:

$$F_{si} = \frac{\partial \tau_{ij}}{\partial x_j}, \quad (2.46)$$

and

$$F_{fi} = \frac{\partial \tau}{\partial x_i}. \quad (2.47)$$

Using the expressions for the stress tensor we can write for the dynamic equations:

$$\frac{\partial \tau_{ij}}{\partial x_j} = \rho_{11} \ddot{u}_{si} + \rho_{12} \ddot{u}_{fi} + b_0(\dot{u}_{si} - \dot{u}_{fi}), \quad (2.48)$$

$$\frac{\partial \tau}{\partial x_i} = \rho_{12} \ddot{u}_{si} + \rho_{22} \ddot{u}_{fi} - b_0(\dot{u}_{si} - \dot{u}_{fi}). \quad (2.49)$$

The equations of motion are obtained by substituting the stress-strain relations (2.14) and (2.15) into the dynamic relations (2.48) and (2.49). The equations of motion read then as follows:

$$G \nabla^2 \mathbf{u}_s + (A + G) \nabla \nabla \cdot \mathbf{u}_s + Q \nabla \nabla \cdot \mathbf{u}_f = \rho_{11} \ddot{\mathbf{u}}_s + \rho_{12} \ddot{\mathbf{u}}_f + b(\dot{\mathbf{u}}_s - \dot{\mathbf{u}}_f), \quad (2.50)$$

$$Q \nabla \nabla \cdot \mathbf{u}_s + R \nabla \nabla \cdot \mathbf{u}_f = \rho_{12} \ddot{\mathbf{u}}_s + \rho_{22} \ddot{\mathbf{u}}_f - b(\dot{\mathbf{u}}_s - \dot{\mathbf{u}}_f). \quad (2.51)$$

2.4 Rigid frame limit

As an illustration, we proceed with the discussion of the rigid frame limit. The rigid frame limit clarifies the role of dissipation term and the background of the added mass term ρ_{12} . We can also incorporate the dynamic-permeability concept, which means that the b coefficient in the dissipation function is modified because of the frequency dependence of the dissipation process.

We obtain for the dynamic relations for the fluid from Equation (2.49):

$$-\phi \frac{\partial p}{\partial x_i} = \rho_{22} \ddot{u}_{fi} + b_0 \dot{u}_{fi}. \quad (2.52)$$

Subsequently, we can study the low- and high-frequency limit of this equation. For low frequencies the acceleration vanishes and viscous forces are dominant. We obtain the well-known Darcy's law:

$$\frac{\partial p}{\partial x_i} = -\frac{b_0}{\phi} \dot{u}_{fi} = -\frac{\eta \phi}{k_0} \dot{u}_{fi}. \quad (2.53)$$

In the high-frequency limit the inertia terms become dominant over the viscosity terms. Using the expression for the densities ρ_{22} and ρ_{12} of Equation (2.42) and Equation (2.43) we simply obtain

$$\alpha_{\infty} \phi \rho_f \ddot{u}_{fi} = -\phi \frac{\partial p}{\partial x_i}. \quad (2.54)$$

In this equation the tortuosity α_{∞} appears as a modification of the acceleration term of the fluid. To understand this phenomenon, it is important to realize that we are dealing with a macroscopic theory. The macroscopic lengthscale is related to the wavelength λ , a scale at which measurable, continuous and differentiable quantities may be identified and boundary value problems can be stated and solved. The microstructure of a random porous medium is generally characterized by a lengthscale proportional to the pore size (Smeulders *et al.* 1992). The direction of the acceleration on a micro-scale may very well differ from the macroscopic acceleration direction, as indicated in Fig. 2.2, where the macroscopic flow is assumed to be one-dimensional, while the microscopic flow is at least two-dimensional. Smeulders *et al.* (1992) relate the microscopic flow field to the macroscopic flow field using an averaging technique of homogenization. Then they obtain the following result in the high frequency limit:

$$\alpha_{\infty} = \frac{\langle |\mathbf{u}_p|^2 \rangle}{|\mathbf{v}_0|^2}. \quad (2.55)$$

In this expression, \mathbf{u}_p is the microscopic potential flow solution and \mathbf{v}_0 is the macroscopic velocity of the fluid while $\langle \rangle$ denotes the averaging operator (Smeulders *et al.* 1992). In

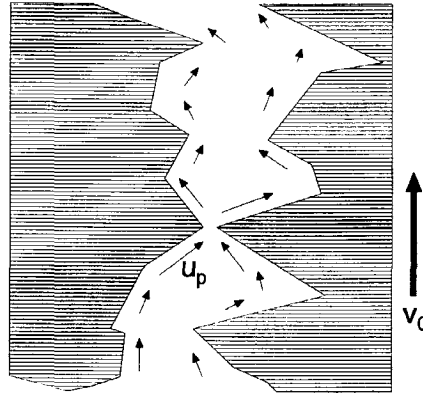


Figure 2.2: Sketch of the microscopic flow of the fluid

this way, it can be imagined that the local variations of the flow (see Fig. 2.2) contribute to the one-dimensional inertia term on the macroscopic level. In a cylindrical duct the averaged microscopic velocity is the same as the macroscopic velocity, which results in a tortuosity equal to 1.

2.5 Dynamic permeability

Equation (2.52) shows the momentum equation of the fluid as a superposition of the low-frequency and the high-frequency limit as described above. This is, however, a simplified model of the dissipation process. A more realistic model can be obtained by assuming a frequency dependence of the factor b_0 . Hence, b_0 is replaced by $b(\omega)$. A model for $b(\omega)$ has been developed by Johnson *et al.* (1987), which satisfies the high-frequency and the low-frequency limit. For the intermediate frequency range a model is proposed based on the ratio of the $\delta = \sqrt{2\eta/\omega\rho_f}$ and the characteristic lengthscale of the pore size, denoted by Λ . Johnson *et al.* arrive at the following expression:

$$\frac{b(\omega)}{b_0} = \sqrt{1 + \frac{iM}{2} \frac{\omega}{\omega_c}}, \quad (2.56)$$

where

$$\omega_c = \frac{\eta\phi}{k_0\alpha_\infty\rho_f}, \quad (2.57)$$

and

$$M = \frac{8\alpha_\infty k_0}{\phi\Lambda^2}. \quad (2.58)$$

The rollover frequency ω_c denotes the frequency where the inertia effects and the viscous effects are of the same magnitude. The factor M is a universal scaling parameter for all porous media, which is assumed to be equal to 1. Allard *et al.* (1998) report measurements of M , where indeed M is of that order of magnitude. Smeulders *et al.* (1994) discuss the validity of the assumption $M \approx 1$ for sharp-edged porous media and Kelder (1998) uses a model of tubes with different radii to investigate M . They conclude that the dynamic permeability of smooth porous media can be described very well by $M \approx 1$. For a further background of this model we refer to Johnson *et al.* (1987) and Smeulders *et al.* (1992).

Previously, Biot (1956b) proposed a model for $b(\omega)/b_0$ based on an oscillating flow in a circular tube. He suggested:

$$\frac{b(\omega)}{b_0} = \frac{1}{4} i\kappa^2 \frac{J_1(i^{3/2}\kappa)}{i^{3/2}\kappa J_0(i^{3/2}\kappa) - 2J_1(i^{3/2}\kappa)}, \quad (2.59)$$

where $\kappa = R_{eff}\sqrt{\omega\rho_f/\eta}$ and J_1 and J_0 are Bessel functions. For the effective radius R_{eff} the characteristic lengthscale Λ as defined by Equation (2.58) can be used. Kelder (1998) provides a comparison between these two models and concludes that the two functions essentially display the same behaviour. The models for the dynamic permeability can be incorporated in the equations of motion for deformable porous materials simply by substituting the coefficient b_0 by $b(\omega)$ (Biot 1956b).

Chapter 3

Wave phenomena

In this chapter we discuss the general characteristics of waves in porous media using Biot's model, including the concept of dynamic permeability as summarized in the previous chapter. The displacements of the fluid and the solid are described by a number of potentials, which is advantageous in case of cylindrical coordinates. Results are obtained for the phase velocities and damping coefficients for several wave types. Again we pay attention to the high- and low- frequency behaviour of the rigid frame limit. The last section is concerned with acoustic bulk properties and boundary conditions. Part of the analysis is performed in the frequency-wavenumber domain. We use the following sign conventions for the temporal and spatial Fourier transform:

$$\hat{f}(\mathbf{x}, \omega) = \frac{1}{2\pi} \int_{-\infty}^{\infty} f(\mathbf{x}, t) e^{-i\omega t} dt, \quad (3.1)$$

$$f(\mathbf{x}, t) = \int_{-\infty}^{\infty} \hat{f}(\mathbf{x}, \omega) e^{i\omega t} d\omega, \quad (3.2)$$

and

$$\tilde{f}(\mathbf{k}, \omega) = \frac{1}{(2\pi)^3} \int_{-\infty}^{\infty} \hat{f}(\mathbf{x}, \omega) e^{i\mathbf{k} \cdot \mathbf{x}} d\mathbf{x}, \quad (3.3)$$

$$\hat{f}(\mathbf{x}, \omega) = \int_{-\infty}^{\infty} \tilde{f}(\mathbf{k}, \omega) e^{-i\mathbf{k} \cdot \mathbf{x}} d\mathbf{k}, \quad (3.4)$$

where \mathbf{x} is the three-dimensional position vector, \mathbf{k} is the three-dimensional wavenumber vector, t denotes the time, and ω is the angular frequency.

3.1 Equations of motion using potentials

Following Deresiewicz (1960) and Berryman (1983) we use the following decomposition, which is similar to the Lamé solution in the elastic case (Miklowitz 1978):

$$\begin{aligned} \mathbf{u}_s &= \nabla \varphi_s + \nabla \times \boldsymbol{\psi}_s, \\ \mathbf{u}_f &= \nabla \varphi_f + \nabla \times \boldsymbol{\psi}_f. \end{aligned} \quad (3.5)$$

Substituting these equations in the equations of motion (2.50) and (2.51), we obtain the following equations

$$\begin{aligned} \nabla \left[(A + 2G) \nabla^2 \varphi_s + Q \nabla^2 \varphi_f - \rho_{11} \ddot{\varphi}_s - \rho_{12} \ddot{\varphi}_f - b(\dot{\varphi}_s - \dot{\varphi}_f) \right] \\ + \nabla \times \left[G \nabla^2 \psi_s - \rho_{11} \ddot{\psi}_s - \rho_{12} \ddot{\psi}_f - b(\dot{\psi}_s - \dot{\psi}_f) \right] = 0, \end{aligned} \quad (3.6)$$

and

$$\begin{aligned} \nabla \left[Q \nabla^2 \varphi_s + R \nabla^2 \varphi_f - \rho_{12} \ddot{\varphi}_s - \rho_{22} \ddot{\varphi}_f - b(\dot{\varphi}_f - \dot{\varphi}_s) \right] \\ - \nabla \times \left[\rho_{12} \ddot{\psi}_s + \rho_{22} \ddot{\psi}_f + b(\dot{\psi}_f - \dot{\psi}_s) \right] = 0. \end{aligned} \quad (3.7)$$

These equations are satisfied if the terms between the square brackets are equal to zero.¹

3.1.1 Compressional waves

For the temporal Fourier transform of the potentials $\hat{\varphi}_s$ and $\hat{\varphi}_f$, which correspond to the compressional waves, we can now write (Allard 1993):

$$\begin{pmatrix} P & Q \\ Q & R \end{pmatrix} \begin{pmatrix} \nabla^2 \hat{\varphi}_s \\ \nabla^2 \hat{\varphi}_f \end{pmatrix} = \begin{pmatrix} -\tilde{\rho}_{11} & -\tilde{\rho}_{12} \\ -\tilde{\rho}_{12} & -\tilde{\rho}_{22} \end{pmatrix} \omega^2 \begin{pmatrix} \hat{\varphi}_s \\ \hat{\varphi}_f \end{pmatrix}, \quad (3.8)$$

where $P = A + 2G$, $\tilde{\rho}_{11} = \rho_{11} - ib/\omega$, $\tilde{\rho}_{12} = \rho_{12} + ib/\omega$ and $\tilde{\rho}_{22} = \rho_{22} - ib/\omega$. This can also be written as:

$$\begin{pmatrix} \nabla^2 \hat{\varphi}_s \\ \nabla^2 \hat{\varphi}_f \end{pmatrix} = -\omega^2 \mathbf{M} \begin{pmatrix} \hat{\varphi}_s \\ \hat{\varphi}_f \end{pmatrix}, \quad (3.9)$$

where

$$\mathbf{M} = \frac{1}{PR - Q^2} \begin{pmatrix} \tilde{\rho}_{11}R - \tilde{\rho}_{12}Q & \tilde{\rho}_{12}R - \tilde{\rho}_{22}Q \\ \tilde{\rho}_{12}P - \tilde{\rho}_{11}Q & \tilde{\rho}_{22}P - \tilde{\rho}_{12}Q \end{pmatrix}. \quad (3.10)$$

Using the spatial Fourier transform we obtain the following eigenvalue problem:

$$\mathbf{M} \begin{pmatrix} \tilde{\varphi}_s \\ \tilde{\varphi}_f \end{pmatrix} = \frac{\mathbf{k} \cdot \mathbf{k}}{\omega^2} \begin{pmatrix} \tilde{\varphi}_s \\ \tilde{\varphi}_f \end{pmatrix} = \zeta \begin{pmatrix} \tilde{\varphi}_s \\ \tilde{\varphi}_f \end{pmatrix}. \quad (3.11)$$

The characteristic polynomial of this matrix is defined as $|\mathbf{M} - \zeta \mathbf{I}| = 0$, where \mathbf{I} denotes the unity matrix, and $|\cdot|$ denotes the determinant. After some algebraic manipulation, we find:

$$d_2 \zeta^2 + d_1 \zeta + d_0 = 0, \quad (3.12)$$

where

$$\begin{aligned} d_2 &= PR - Q^2, \\ d_1 &= -(P\tilde{\rho}_{22} + R\tilde{\rho}_{11} - 2Q\tilde{\rho}_{12}), \\ d_0 &= \tilde{\rho}_{11}\tilde{\rho}_{22} - \tilde{\rho}_{12}^2. \end{aligned} \quad (3.13)$$

¹In the elastic case, a proof of completeness of Lamé's solution can be given. Deresiewicz (1960) was the first to apply this decomposition on Biot's equations for the non-dissipative case. His remark on the completeness: 'It is not unlikely that the present solution, too, is complete'.

Equation (3.12) has two complex roots ζ_{c1} and ζ_{c2} , which means that two damped dilatational waves exist. For ζ_{c1} , and ζ_{c2} we write:

$$\zeta_{c1,c2} = \frac{-d_1 \pm d_1 \sqrt{1 - 4 \frac{d_2 d_0}{d_1^2}}}{2d_2}. \quad (3.14)$$

The eigenvalue ζ is equivalent to the inverse squared wave velocities: $\zeta = |\mathbf{k}|^2/\omega^2$ where \mathbf{k} is the free-field wavenumber. The properties of the two waves were illustrated by Biot (1956a), who showed that the fluid and the skeletal velocities have the same sign for one root, and have opposite signs for the other root. This means that there is one wave in which fluid and skeletal velocities are in phase, and another in which they are in opposite phase. In the same paper, it is also shown that the wave which propagates fastest has in-phase fluid and skeletal velocities, whereas the slower propagating wave has those velocities in opposite phase. As a matter of definition the wave which propagates fastest will be denoted as the fast wave (subscript c1), while the other one will be denoted as the slow wave (subscript c2).² It can be imagined that the slow wave is damped more strongly than the fast wave because the out-of-phase character of the slow wave represents a highly effective dissipation mechanism.

The scalar potential $\tilde{\varphi}_s$ consists of contributions of the fast and the slow compressional wave $\tilde{\varphi}_{sc1}$ and $\tilde{\varphi}_{sc2}$:

$$\tilde{\varphi}_s = \tilde{\varphi}_{sc1} + \tilde{\varphi}_{sc2}. \quad (3.15)$$

The potentials of the fluid $\tilde{\varphi}_{f(c1,c2)}$ are related to the potentials of the solid $\tilde{\varphi}_{s(c1,c2)}$ via a linear relationship. Equation (3.8) can be used to show that

$$\beta_{c1,c2} = \frac{\tilde{\varphi}_{fc1,fc2}}{\tilde{\varphi}_{sc1,sc2}} = \frac{\tilde{\rho}_{11} - P\zeta_{c1,c2}}{Q\zeta_{c1,c2} - \tilde{\rho}_{12}}. \quad (3.16)$$

Therefore we may write for the potential of the fluid $\tilde{\varphi}_f$:

$$\tilde{\varphi}_f = \beta_{c1}\tilde{\varphi}_{sc1} + \beta_{c2}\tilde{\varphi}_{sc2}. \quad (3.17)$$

3.1.2 Shear waves

The vector potentials ψ_s and ψ_f describe the displacements of the solid and the fluid due to transverse waves. Using the equations (3.6) and (3.7), we obtain:

$$G\nabla^2 \hat{\psi}_s = -\tilde{\rho}_{11}\omega^2 \hat{\psi}_s - \tilde{\rho}_{12}\omega^2 \hat{\psi}_f, \quad (3.18)$$

$$0 = -\omega^2 \tilde{\rho}_{12} \hat{\psi}_s - \omega^2 \rho_{22} \hat{\psi}_f. \quad (3.19)$$

²This nomenclature applies for the porous media which are investigated in this thesis. For a further comment we refer to Bardot (1996).

The latter expression provides the relation β_{sh} between the fluid vector potential and the solid vector potential:

$$\hat{\psi}_f = \beta_{sh} \hat{\psi}_s, \quad (3.20)$$

where

$$\beta_{sh} = -\frac{\tilde{\rho}_{12}}{\tilde{\rho}_{22}}. \quad (3.21)$$

For ζ_{sh} we find:

$$\frac{1}{\zeta_{sh}} = \frac{\omega^2}{|\mathbf{k}_{sh}|^2} = \frac{G\tilde{\rho}_{22}}{\tilde{\rho}_{11}\tilde{\rho}_{22} - \tilde{\rho}_{12}^2}. \quad (3.22)$$

3.2 Low- and high-frequency limits

We shall discuss now some limiting cases for the complex wave velocities as formulated in Equations (3.14) and (3.22). We start with the low-frequency limit for which the viscous effects in the fluid dominate the inertial effects. The slow wave will become diffusive and the fast wave will remain propagatory.

3.2.1 Low-frequency limit

For $\omega \rightarrow 0$ the square root in Equation (3.14) can be replaced by the first term of the Taylor series expansion, and hence we obtain:

$$\zeta_{c1,c2} \approx \frac{-d_1 \pm d_1(1 - 2\frac{d_2 d_0}{d_1^2})}{2d_2}. \quad (3.23)$$

For fast wave we can write:

$$\lim_{\omega \rightarrow 0} \frac{1}{\zeta_{c1}} = -\frac{d_1}{d_0} = \frac{P + R + 2Q}{\rho} = \frac{H}{\rho}, \quad (3.24)$$

where $\rho = \rho_{11} + 2\rho_{12} + \rho_{22}$. The effective modulus H was originally derived by Gassmann (1951) in an article which predates the Biot theory, and therefore this low-frequency limit is often called the Biot-Gassmann result. According to Equation (3.16), the corresponding value β_{c1} is equal to 1. This means that the fluid motion is locked-on to the solid's. The relative velocity of the fluid ($\mathbf{u}_f - \mathbf{u}_s$) is then equal to zero, so no damping will be observed. This is in agreement with the phase velocity which is real-valued according to Equation (3.24).

For the slow wave we find that:

$$\lim_{\omega \rightarrow 0} \frac{1}{\zeta_{c2}} = -\frac{d_2}{d_1} = -\frac{\omega(PR - Q^2)}{ib_0(P + R + 2Q)}. \quad (3.25)$$

This solution shows that the slow wave is described by a diffusion equation rather than a wave equation in the low-frequency limit, because the squared wavenumber $|\mathbf{k}|^2$ is the eigenvalue of the diffusion equation

$$\frac{\partial^2 \chi}{\partial x^2} = \frac{\chi i \omega}{c_D}, \quad (3.26)$$

where χ can be any relevant variable (p , ρ_f etc.) and

$$c_D = \frac{PR - Q^2}{b_0(P + R + 2Q)}. \quad (3.27)$$

The ratio of fluid and the solid potential β_{c2} in this case can be calculated using Equation (3.16):

$$\beta_{c2} = -\frac{Q + P}{Q + R}. \quad (3.28)$$

In the low-frequency limit the expression for the transverse wave is simplified also. It is straightforward to derive that

$$\zeta_{sh} = \frac{\rho}{G}, \quad (3.29)$$

where $\rho = \phi \rho_f + (1 - \phi) \rho_s$. The motion of the fluid is also locked-on to the solid for this case. The low-frequency limit of β_{sh} is equal to 1 and the phase velocity is also real-valued, according to Equation (3.29).

3.2.2 High-frequency limit

In the high-frequency limit the inertia effects dominate the viscous ones which results in real-valued density terms $\tilde{\rho}_{11}$, $\tilde{\rho}_{12}$, and $\tilde{\rho}_{22}$. The coefficients of Equation (3.12) become for $\omega \rightarrow \infty$:

$$\begin{aligned} d_2 &= PR - Q^2, \\ d_1 &= -(P\rho_{22} + R\rho_{11} - 2Q\rho_{12}), \\ d_0 &= \rho_{11}\rho_{22} - \rho_{12}^2. \end{aligned} \quad (3.30)$$

Consequently, both waves become propagatory. For the inverse squared phase velocity of the shear wave we find:

$$\zeta_{sh} = \frac{(1 - \phi)\rho_s + \phi(1 - 1/\alpha_\infty)\rho_f}{G}. \quad (3.31)$$

Despite the fact that the fluid cannot sustain shear forces on the macroscopic scale the fluid contributes to the shear wave velocity due to the tortuosity factor. It follows that $\beta_{sh} = -\rho_{12}/\rho_{22}$, which is equal to $-(\alpha_\infty - 1)/\alpha_\infty$.

3.3 Stiff frame

A case of special interest for both the low-frequency limit and the high-frequency limit is obtained when it is assumed that the grains are incompressible, and also that: $K_b, G \gg K_f$. This is the so-called stiff frame limit. In this case the coefficient P is equal to $K_b + \frac{4}{3}G$ which is also called the constrained modulus K_p . The wave velocity for the transverse wave is influenced only by the shear modulus and the densities, and hence the shear wave velocity is insensitive to the ratio of the compressibilities. The low-frequency limit of the slow wave was investigated by Chandler (1981), Chandler and Johnson (1981), while Johnson (1980), Nagy *et al.* (1990), and Allard *et al.* (1993, 1998) investigated the high-frequency limit.

3.3.1 Low-frequency limit (stiff frame)

For the rigid-frame limit we obtain an expression for the diffusion coefficient which is decoupled from the elasticity of the solid:

$$c_D = \frac{k_0 K_f}{\eta \phi}. \quad (3.32)$$

For the solution of the fast wave we may write:

$$\frac{1}{\zeta_{c1}} = \frac{P + R + 2Q}{\rho} = \frac{K_p}{(1 - \phi)\rho_s + \phi\rho_f}. \quad (3.33)$$

The phase velocity of the fast wave is related to the elasticity of the solid and decoupled from the fluid modulus. For a density of the fluid much smaller than the solid density the equations reduce further, which can be used in the so-called dry measurements to determine the permeability using c_D , and K_p using ζ_{c1} . The value of β_{c1} remains 1 due to the viscous forces.

3.3.2 High-frequency limit (stiff frame)

For the high-frequency limit we can derive for a stiff frame that:

$$\zeta_{c1} = \frac{(1 - \phi)\rho_s + \phi(1 - 1/\alpha_\infty)\rho_f}{K_p}, \quad (3.34)$$

$$\zeta_{c2} = \frac{\alpha_\infty \rho_f}{K_f} = \frac{\alpha_\infty}{c_{fluid}^2}. \quad (3.35)$$

Johnson (1980) used superfluid ^4He , with zero viscosity, as a saturant fluid to measure the tortuosity parameter α_∞ . Nagy *et al.* (1990) and Allard *et al.* (1998) used ultra-sound on air-filled porous materials to measure the tortuosity. As in the low-frequency case, K_p and G can be deduced from ζ_{c1} and ζ_{sh} .

3.4 Bulk properties and boundary conditions

The complex wavenumbers k_j for $j = c_1, c_2, c_{sh}$ are related to the acoustic bulk properties of the material viz. the phase speed $\omega/|\Re(k_j)|$ and the attenuation $\Im m(k_j)$.³ Using the parameters of water-saturated Bentheimer sandstone (see Table E.1), we calculated the frequency dependence of the phase velocities and the attenuation of the fast, the slow and the shear waves. The results are shown in Fig. 3.1. For the elasticity parameters P , Q and R we used the Equations (2.33), (2.34) and (2.35). For the dynamic permeability the tube model of Biot was used.

It is clear from these results that the phase velocities of the fast wave are almost frequency-independent. The phase velocity of the slow wave, however, shows a transition from a low-frequency diffusion-like behaviour to a high-frequency propagatory behaviour. The phase velocity of the shear wave is in between the fast wave speed and the slow wave speed. The attenuation is frequency-dependent for both the compressional waves and the shear wave. It is shown in Fig. 3.1 that the slow wave attenuation is much higher than the attenuation of the fast and the shear wave. This is a result of the out-of-phase character of the slow wave which explains a highly effective dissipation.

Boundary conditions on porous media were proposed by Deresiewicz and Skalak (1963). These boundary conditions were applied by Rosenbaum (1974) to a cylindrical borehole. In this section we limit ourselves to the boundary between a (saturated) porous solid (subscript a) and a fluid (subscript b). The configuration is given in Fig. 3.2. The normal vector is denoted by \mathbf{n} . The velocities in the normal direction for the solid and the pore fluid are indicated by \dot{u}_{as} and \dot{u}_{af} , respectively. The relevant stress components are the normal stress and the shear stress, which are indicated by σ_{an} and σ_{ash} , respectively. The velocity in the normal direction of the fluid (b) is indicated by \dot{u}_{bf} . For the condition at the interface we discern the so-called 'sealed' and the 'unsealed' case.

In the unsealed case only forces due to the fluid pressure are acting on the grains at the boundary (see Fig. 3.2) so that it can be stated that at the boundary

$$\begin{aligned}\sigma_{an} &= 0, \\ \sigma_{ash} &= 0.\end{aligned}\tag{3.36}$$

The second condition for the 'unsealed' case prescribes the continuity of the fluid pressure:

$$p_a = p_b.\tag{3.37}$$

Continuity of the fluid mass over the boundary moving with the normal velocity of the solid \dot{u}_{as} provides a third boundary condition:

$$\phi \dot{u}_{af} + (1 - \phi) \dot{u}_{as} = \dot{u}_{bf}.\tag{3.38}$$

³An alternative way to present damping properties is to define the specific attenuation $1/Q$. It is defined as:

$$\frac{1}{Q} = 2 \frac{\Im m(k_j)}{\Re(k_j)}.$$

In this thesis the data will be presented using $\Im m(k_j)$.

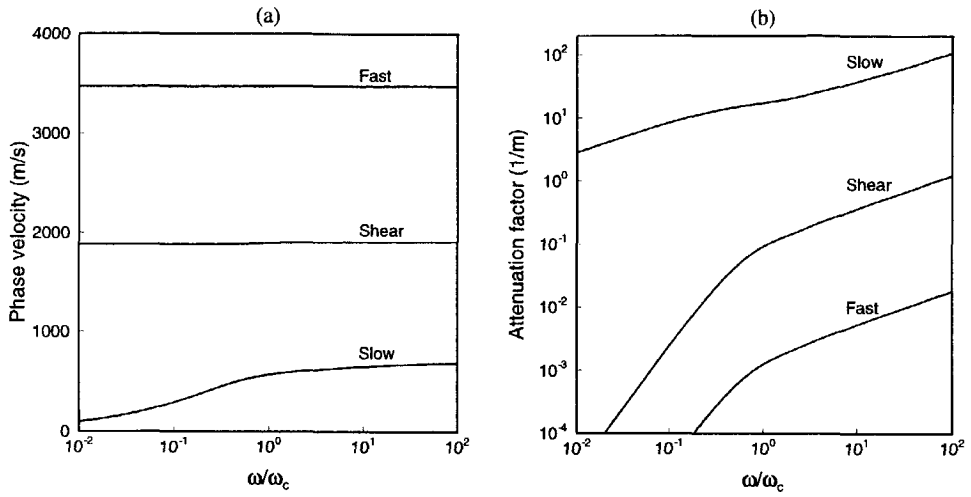


Figure 3.1: Phase velocities and damping of the fast, slow and shear wave for water-saturated Bentheimer sandstone. Parameter values are listed in Table E.1, Appendix E.

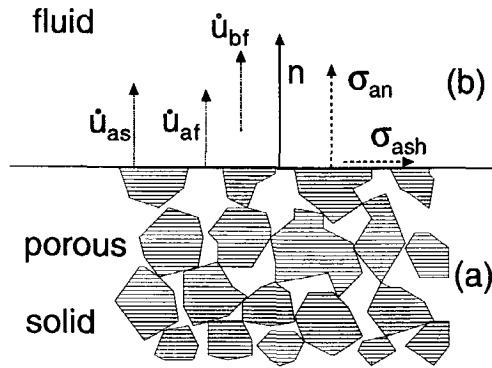


Figure 3.2: Boundary between a fluid and a porous solid. The normal vector is denoted by \mathbf{n} . The velocities in the normal direction for the solid and the pore fluid are indicated by \dot{u}_{as} and \dot{u}_{af} . The stress components are denoted by σ_{an} and σ_{ash} . The velocity in the normal direction of the fluid (b) is indicated by \dot{u}_{bf} .

In the sealed case the relative normal displacement of the fluid of the porous medium is equal to zero at the surface, so that we may write:

$$\dot{u}_{af} = \dot{u}_{as} = \dot{u}_{bf} . \quad (3.39)$$

The following relation applies for the continuity of the stresses:

$$\sigma_{an} + p_a = p_b, \quad (3.40)$$

and

$$\sigma_{ash} = 0. \quad (3.41)$$

In the next chapter, it is shown that a sealed interface suppresses the generation of the slow wave. This can be imagined if we note that in case of a sealed boundary the velocities of the solid and the fluid are equal at the interface. The slow wave, however, is associated with out of phase motion of the fluid and the solid.

Chapter 4

One-dimensional wave propagation

In this chapter we use the Biot theory to study one-dimensional wave propagation in porous materials. The approach of this chapter is an extension of the work of Smeulders (1992), and Van Dongen *et al.* (1995). In combination with concepts of Hölscher (1995) we are able to handle multiple layers consisting of porous materials, elastic materials or fluids.

4.1 1-D waves in porous materials

For one-dimensional wave propagation we assume that the displacements of the solid and the fluid in the y - and x -direction are equal to zero. In case of one-dimensional wave propagation we write for the pore pressure in a porous material:

$$\hat{p}(z, \omega) = \tilde{p}_1^+(k, \omega)e^{-ik_1 z} + \tilde{p}_2^+(k, \omega)e^{-ik_2 z} + \tilde{p}_1^-(k, \omega)e^{ik_1 z} + \tilde{p}_2^-(k, \omega)e^{ik_2 z}. \quad (4.1)$$

In this expression the pressures due to the fast waves travelling in the positive and negative z -directions are superimposed (wavenumbers $\pm k_1$). The same is performed for the slow waves (wavenumbers $\pm k_2$). The intergranular stress can be written in a similar way:

$$\hat{\sigma}_{zz}(z, \omega) = \tilde{\sigma}_{zz1}^+(k, \omega)e^{-ik_1 z} + \tilde{\sigma}_{zz2}^+(k, \omega)e^{-ik_2 z} + \tilde{\sigma}_{zz1}^-(k, \omega)e^{ik_1 z} + \tilde{\sigma}_{zz2}^-(k, \omega)e^{ik_2 z}. \quad (4.2)$$

We can relate the stress amplitudes $\tilde{\sigma}_{zz1}^+, \dots, \tilde{\sigma}_{zz2}^-$ to the pressure amplitudes $\tilde{p}_1^+, \dots, \tilde{p}_2^-$. Using Equation (2.36) the following expression for the time derivative of the one-dimensional intergranular stress can be derived:

$$\frac{\partial \sigma_{zz}}{\partial t} = -(K_b + 4/3G) \frac{\partial v_{sz}}{\partial z} = -K_p \frac{\partial v_{sz}}{\partial z}, \quad (4.3)$$

where v_{sz} is the time derivative of the solid displacement u_{sz} . The time-derivative of the pressure follows from Equation (2.37):¹

$$-\phi \frac{\partial p}{\partial t} = K_f(1 - \phi) \frac{\partial v_{sz}}{\partial z} + \phi K_f \frac{\partial v_{fz}}{\partial z}, \quad (4.4)$$

¹Note that in the linear theory the elasticity coefficients are constant. The porosity in this equation denotes the time-averaged value.

where v_{fz} is the time derivative of the fluid displacement u_{fz} . Using the temporal and 1D spatial Fourier transform we find:

$$-i\omega\tilde{\sigma}_{zz} = -ikK_p\tilde{v}_{sz}, \quad (4.5)$$

and

$$-i\omega\phi\tilde{p} = -ikK_f[(1-\phi)\tilde{v}_{sz} + \phi\beta\tilde{v}_{sz}]. \quad (4.6)$$

In this way we can relate the pressure and the stress amplitudes for the positive z-direction:

$$E_1^+ = \frac{\tilde{\sigma}_{zz1}^+}{\tilde{p}_1^+} = S_1 = \frac{K_p\phi}{K_f[(1-\phi) + \phi\beta_{c1}]}, \quad (4.7)$$

$$E_2^+ = \frac{\tilde{\sigma}_{zz2}^+}{\tilde{p}_2^+} = S_2 = \frac{K_p\phi}{K_f[(1-\phi) + \phi\beta_{c2}]}. \quad (4.8)$$

We can also derive that $E_1^- = E_1^+$, and $E_2^- = E_2^+$. The velocity amplitudes of the solid are related to the pressure amplitudes:

$$D_m^\pm = \frac{\tilde{v}_{szm}}{\tilde{p}_m^\pm} = \frac{S_m c_m^\pm}{K_p}, \quad (4.9)$$

where $m = 1, 2$ denotes the fast and the slow wave respectively, and $c_m^+ = \omega/k_m$ and $c_m^- = -\omega/k_m$. The fluid velocity amplitudes are related to the pressure amplitudes by:

$$F_m^\pm = \frac{\tilde{v}_{fzm}}{\tilde{p}_m^\pm} = \beta_m \frac{S_m c_m^\pm}{K_p}. \quad (4.10)$$

Hence we write:

$$\tilde{\sigma}_{zz}(z, \omega) = E_1^+ \tilde{p}_1^+ e^{-ik_1 z} + E_2^+ \tilde{p}_2^+ e^{-ik_1 z} + E_1^- \tilde{p}_1^- e^{ik_1 z} + E_2^- \tilde{p}_2^- e^{ik_1 z}, \quad (4.11)$$

$$\tilde{v}_{sz}(z, \omega) = D_1^+ \tilde{p}_1^+ e^{-ik_1 z} + D_2^+ \tilde{p}_2^+ e^{-ik_1 z} + D_1^- \tilde{p}_1^- e^{ik_1 z} + D_2^- \tilde{p}_2^- e^{ik_1 z}, \quad (4.12)$$

and

$$\tilde{v}_{fz}(z, \omega) = F_1^+ \tilde{p}_1^+ e^{-ik_1 z} + F_2^+ \tilde{p}_2^+ e^{-ik_1 z} + F_1^- \tilde{p}_1^- e^{ik_1 z} + F_2^- \tilde{p}_2^- e^{ik_1 z}. \quad (4.13)$$

4.2 Liquid-loaded porous half-space

With the techniques as given above we study the one-dimensional impact of a pressure wave on a semi-infinite porous layer, surrounded by a liquid-filled gap. The configuration is given in Fig. 4.1. It may be seen as a 1-D representation of the shock tube set-up presented in Chapter 5. The incident wave with amplitude \tilde{p}_{in} partially reflects, and partially transmits into both the porous sample and the liquid filled gap. The amplitude of the reflected wave is denoted by \tilde{p}_r . Within the porous halfspace, the initial pressure

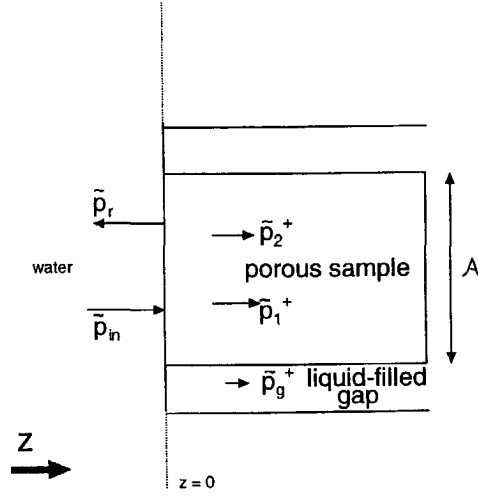


Figure 4.1: Impact of a pressure wave on a semi-infinite porous layer.

disturbance is distributed over the fast and the slow wave. The amplitudes are denoted by \tilde{p}_1^+ and \tilde{p}_2^+ , respectively.

For open-pore boundary conditions (see Section 3.4) the total pressure \tilde{p}_0 is continuous at $z = 0$:

$$\tilde{p}_{in} + \tilde{p}_r = \tilde{p}_1^+ + \tilde{p}_2^+ = \tilde{p}_0. \quad (4.14)$$

Furthermore, the intergranular stress at the interface is zero:

$$\tilde{\sigma}_{zz1} + \tilde{\sigma}_{zz2} = 0, \quad (4.15)$$

which also can be written as

$$E_1^+ \tilde{p}_1^+ + E_2^+ \tilde{p}_2^+ = 0. \quad (4.16)$$

The third boundary condition is given by:

$$\tilde{v}_{fin} + \tilde{v}_{fr} = \mathcal{A} [(1 - \phi)(\tilde{v}_{s1} + \tilde{v}_{s2}) + \phi(\tilde{v}_{f1} + \tilde{v}_{f2})] + (1 - \mathcal{A})\tilde{v}_{fg}, \quad (4.17)$$

where \tilde{v}_{fg} is the fluid velocity in the gap and \mathcal{A} is the surface fraction of the porous column. The pore fluid velocities are denoted by \tilde{v}_{f1} and \tilde{v}_{f2} . The solid velocities are denoted by \tilde{v}_{s1} and \tilde{v}_{s2} . We use $\tilde{v}_{fin} = \tilde{p}_{in}/Z_w$, $\tilde{v}_{fr} = -\tilde{p}_r/Z_w$, $Z_w = \rho_w c_w$, $\tilde{v}_{fg} = \tilde{p}_0/Z_w$, and Equations (4.12) and (4.13) to relate the velocities to the pressures. Hence, we obtain for Equation (4.17):

$$\frac{\tilde{p}_{in}}{Z_w} - \frac{\tilde{p}_r}{Z_w} = \mathcal{A} [(1 - \phi)(D_1^+ \tilde{p}_1^+ + D_2^+ \tilde{p}_2^+) + \phi(F_1^+ \tilde{p}_1^+ + F_2^+ \tilde{p}_2^+)] + (1 - \mathcal{A}) \frac{\tilde{p}_0}{Z_w}, \quad (4.18)$$

where it is assumed that $\tilde{p}_g^+ = \tilde{p}_0$.

Using Equations (4.14) and (4.16) we can now compute the distribution of the total pressure over the transmitted pressures \tilde{p}_1^+ and \tilde{p}_2^+ :

$$\frac{\tilde{p}_1^+}{\tilde{p}_0} = \frac{E_2^+}{E_2^+ - E_1^+} = \frac{S_2}{S_2 - S_1}, \quad (4.19)$$

and

$$\frac{\tilde{p}_2^+}{\tilde{p}_0} = \frac{E_1^+}{E_1^+ - E_2^+} = \frac{S_1}{S_1 - S_2}. \quad (4.20)$$

We can now relate the incident pressure to the total pressure \tilde{p}_0 :

$$\frac{\tilde{p}_{in}}{\tilde{p}_0} = \frac{\tilde{p}_1^+}{\tilde{p}_0} \frac{Z_w \mathcal{A}}{2} [(1 - \phi)D_1^+ + \phi F_1^+] + \frac{\tilde{p}_2^+}{\tilde{p}_0} \frac{Z_w \mathcal{A}}{2} [(1 - \phi)D_2^+ + \phi F_2^+] + \left(1 - \frac{\mathcal{A}}{2}\right). \quad (4.21)$$

Subsequently, the reflection coefficient $r = \tilde{p}_0/\tilde{p}_{in} - 1$ can be computed as a function of frequency. Fig. 4.2 shows the results for $\mathcal{A} = 1$ (no correction) and $\mathcal{A} = 0.95$. The reflection coefficient for the open pore condition decreases as a function of the frequency. For values of \mathcal{A} below 1 the wave is partially transmitted into the liquid-filled gap and the corresponding reflection coefficient is lower over the entire frequency range.

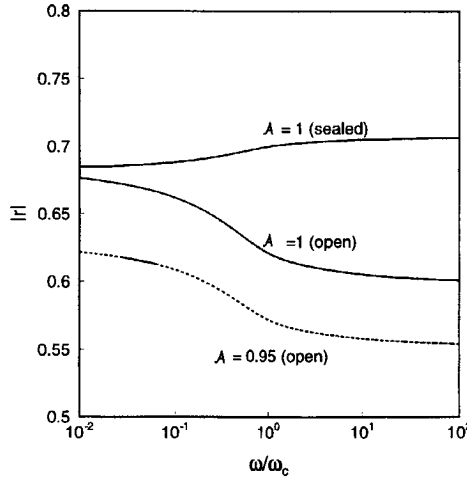


Figure 4.2: Frequency dependence of the reflection coefficient for open pore and sealed pore conditions. For the open pore conditions the result for $\mathcal{A} = 0.95$ is also plotted. The calculations are performed for a Benthim/water interface. Parameter values are given in Table E.1, Appendix E.

For sealed pores we apply the conditions as given in Section 3.4 at $z = 0$ for $\mathcal{A} = 1$. For the continuity of the velocities we obtain:

$$\frac{\tilde{p}_{in}}{Z_w} - \frac{\tilde{p}_r}{Z_w} = D_1^+ \tilde{p}_1^+ + D_2^+ \tilde{p}_2^+ = F_1^+ \tilde{p}_1^+ + F_2^+ \tilde{p}_2^+. \quad (4.22)$$

For the stresses and pressures, we write:

$$\tilde{p}_{in} + \tilde{p}_r = \tilde{p}_1^+(1 + E_1^+) + \tilde{p}_2^+(1 + E_2^+). \quad (4.23)$$

For the ratios $\tilde{p}_1^+/\tilde{p}_0$ and $\tilde{p}_2^+/\tilde{p}_0$, we can derive the following expressions:

$$\frac{\tilde{p}_1^+}{\tilde{p}_0} = \frac{S_2 c_2 (\beta_{c2} - 1)}{(1 + S_1)(\beta_{c2} - 1)S_2 c_2 + S_1 c_1 (1 - \beta_{c1})}, \quad (4.24)$$

and

$$\frac{\tilde{p}_2^+}{\tilde{p}_0} = \frac{S_1 c_1 (1 - \beta_{c1})}{(1 + S_1)S_2 c_2 (\beta_{c2} - 1) + S_1 c_1 (1 - \beta_{c1})}. \quad (4.25)$$

For $\tilde{p}_{in}/\tilde{p}_0$ we obtain

$$\frac{\tilde{p}_{in}}{\tilde{p}_0} = \frac{Z_w}{2} \frac{\tilde{p}_1^+}{\tilde{p}_0} [D_1^+(1 + E_1^+)] + \frac{Z_w}{2} \frac{\tilde{p}_2^+}{\tilde{p}_0} [D_2^+(1 + E_2^+)]. \quad (4.26)$$

The frequency dependence of the reflection coefficient is shown in Fig. 4.2. For this case we observe an increasing value of $|r|$ as a function of frequency. The value of β_{c1} is approximately 1 and from Equation (4.25) we conclude that the slow wave is not generated effectively. The amplitude of the slow wave differs one order in magnitude from the amplitude of the fast wave.

The weak generation of the slow wave for the sealed case is also observed in the time domain. The pressures in the time domain was determined as follows. Using for example a step-wise incident disturbance, we computed the values of \tilde{p}_{in} by means of Fast Fourier Transform. The pressure amplitudes \tilde{p}_1^+ and \tilde{p}_2^+ were calculated at each frequency and Equation (4.1) was used to determine the pressure at position z . The inverse Fast Fourier Transform was used to obtain the pressure signal in the time domain. Fig. 4.3 shows the pressure signals at $z = 7$ cm for both the open pore and sealed pores. The first pressure rise is due to the fast wave, while the second pressure rise for the open pore case is due to the slow wave. For the sealed pores the slow wave is not observed indeed.

4.3 Multiple layers

In our shock tube, reflections in the porous column occur, and the waves in the porous column will be partially transmitted into the end plate (see Chapter 5). Furthermore, it is possible that a shallow water layer exists between the porous sample and the end plate. The one-dimensional model of this configuration is given in Fig. 4.4. In the following the quasi one-dimensional correction for the liquid-filled gap will be omitted.

The open pore boundary conditions at $z = 0$ are the same as in the previous subsection for $\mathcal{A} = 1$. We also include the reflected waves, so that at $z = 0$:

$$\tilde{\sigma}_{zz1}^+ + \tilde{\sigma}_{zz2}^+ + \tilde{\sigma}_{zz1}^- + \tilde{\sigma}_{zz2}^- = 0, \quad (4.27)$$

$$\tilde{p}_{in}^+ + \tilde{p}_r^- = \tilde{p}_1^+ + \tilde{p}_2^+ + \tilde{p}_1^- + \tilde{p}_2^-, \quad (4.28)$$

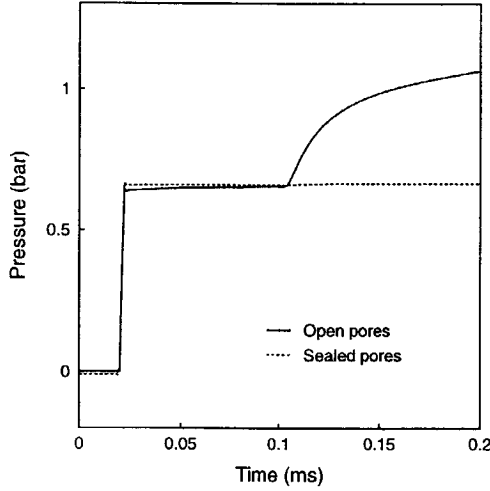


Figure 4.3: Transmitted pressure signal in Bentheimer sandstone at $z = 7$ cm. $\mathcal{A} = 1$. Parameter values are given in Table E.1, Appendix E.

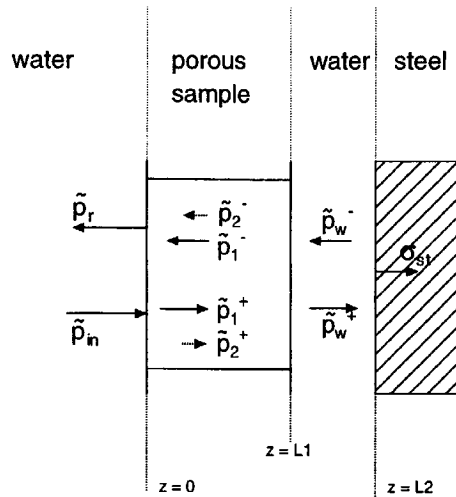


Figure 4.4: Configuration multiple layers: Water-porous medium-water-steel.

$$\tilde{v}_{in}^+ + \tilde{v}_r^- = (1 - \phi) [\tilde{v}_{s1}^+ + \tilde{v}_{s2}^+ + \tilde{v}_{s1}^- + \tilde{v}_{s2}^-] + \phi [\tilde{v}_{f1}^+ + \tilde{v}_{f2}^+ + \tilde{v}_{f1}^- + \tilde{v}_{f2}^-]. \quad (4.29)$$

At $z = L1$ we obtain for open pore conditions:

$$\tilde{\sigma}_{zz1}^+ e^{-ik_1 L1} + \tilde{\sigma}_{zz2}^+ e^{-ik_2 L1} + \tilde{\sigma}_{zz1}^- e^{ik_1 L1} + \tilde{\sigma}_{zz2}^- e^{ik_2 L1} = 0, \quad (4.30)$$

$$\tilde{p}_1^+ e^{-ik_1 L1} + \tilde{p}_2^+ e^{-ik_2 L1} + \tilde{p}_1^- e^{ik_1 L1} + \tilde{p}_2^- e^{ik_2 L1} = \tilde{p}_w^+ e^{-ik_w L1} + \tilde{p}_w^- e^{ik_w L1}, \quad (4.31)$$

$$\begin{aligned} (1 - \phi) [\tilde{v}_{s1}^+ e^{-ik_1 L1} + \tilde{v}_{s2}^+ e^{-ik_2 L1} + \tilde{v}_{s1}^- e^{ik_1 L1} + \tilde{v}_{s2}^- e^{ik_2 L1}] \\ + \phi [\tilde{v}_{f1}^+ e^{-ik_1 L1} + \tilde{v}_{f2}^+ e^{-ik_2 L1} + \tilde{v}_{f1}^- e^{ik_1 L1} + \tilde{v}_{f2}^- e^{ik_2 L1}] \\ = \tilde{v}_w^+ e^{-ik_w L1} + \tilde{v}_w^- e^{ik_w L1}. \end{aligned} \quad (4.32)$$

At $z = L2$ we have continuity of the velocity:

$$\tilde{v}_w^+ e^{-ik_w L2} + \tilde{v}_w^- e^{ik_w L2} = +\tilde{v}_{st}^+ e^{-ik_{st} L2}, \quad (4.33)$$

and continuity of the pressures and stresses:

$$\tilde{p}_w^+ e^{-ik_w L2} + \tilde{p}_w^- e^{ik_w L2} = \tilde{\sigma}_{st}^+ e^{-ik_{st} L2}. \quad (4.34)$$

In these expressions, the wavenumber in the water is denoted by k_w and the wavenumber in the steel by k_{st} . The velocities in the water and the steel are indicated by \tilde{v}_w^+ , \tilde{v}_w^- and \tilde{v}_{st}^+ respectively. The amplitude of the stress is denoted by $\tilde{\sigma}_{st}^+$. Now we have obtained 8 boundary conditions for eight unknown amplitudes \tilde{p}_r , \tilde{p}_1^+ , \tilde{p}_2^+ , \tilde{p}_1^- , \tilde{p}_2^- , \tilde{p}_w^+ , \tilde{p}_w^- , and $\tilde{\sigma}_{st}$. The stress and velocity amplitudes can be related to the pressure amplitudes by the coefficients E_m^\pm , D_m^\pm and F_m^\pm . After these operations we write the system of equations in the following matrix form:

$$\underline{\underline{M}} \begin{pmatrix} \tilde{p}_r & \tilde{p}_1^+ & \tilde{p}_2^+ & \tilde{p}_1^- & \tilde{p}_2^- & \tilde{p}_w^+ & \tilde{p}_w^- & \tilde{\sigma}_{st} \end{pmatrix}^T = \begin{pmatrix} 0 & \tilde{p}_{in} & \tilde{p}_{in} & 0 & 0 & 0 & 0 & 0 \end{pmatrix}^T. \quad (4.35)$$

The matrix elements follow straightforwardly from the boundary conditions as given above. At a given frequency ω we derive \tilde{p}_{in} from the input signal and the system is solved using the routines F07ARF and F07ASF of the Fortran NAG Library (1995).

For the low-frequency limit $\omega = 0$ the wavenumbers k_1 , k_2 , k_w and k_{st} are zero. Due to the zero phase velocity of the slow wave we obtain $D_2^\pm = 0$ and $F_2^\pm = 0$. The boundary conditions at $z = 0$ and $z = L1$ are therefore not independent anymore. Equation (4.27) and (4.30), for example, become identical. However, the variables \tilde{p}_1^+ , \tilde{p}_1^- , and \tilde{p}_2^+ , \tilde{p}_2^- are also not independent. By replacing \tilde{p}_1^+ and \tilde{p}_1^- by $(\tilde{p}_1^+ + \tilde{p}_1^-)$, and \tilde{p}_2^+ and \tilde{p}_2^- by $(\tilde{p}_2^+ + \tilde{p}_2^-)$ we obtain 6 unknown variables and 6 independent boundary conditions, and hence the system of equations can be solved. The pressure signals in the time domain are obtained in the same way as for the case of the fluid-loaded porous half space. Fig. 4.5(a) shows an example of the computed pressure signals in the water layer at $z = -10$ cm (P1) and in the porous rock at $z = 7$ cm (P2). For this case we used $L1 = L2 = 40$ cm in

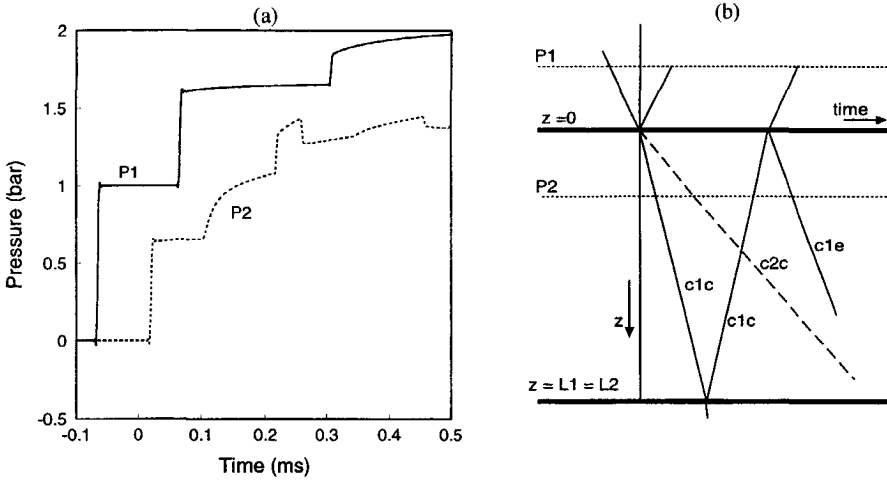


Figure 4.5: Computed pressure signals in the water layer ($P1$, $z = -10$ cm) and in the porous layer ($P2$, $z = 7$ cm) as a function of time (a). The space-time plot is given in (b). The compressional waves are denoted by $c1c$ and $c2c$, the expansion wave by $c1e$. Parameter values are given in Table E.1, Appendix E.

order to obtain a limited number of arrivals. Hence, no water layer exists between the porous medium and the steel. Using the space-time plot of Fig. 4.5(b) we can identify the arrivals of the different waves. At $P1$ the incident step wave arrives at $t = -0.07$ ms. The reflection from the interface at $z = 0$ is recorded at $t = 0.07$ ms. The pressure rise at $t = 0.3$ ms corresponds to the reflection from the interface $L1$. At $P2$, the fast wave and the slow wave arrivals are observed at $t = 0.02$ ms and $t = 0.1$ ms respectively. The reflection from the interface $L1$ is recorded at $t = 0.22$ ms. At $z = 0$ this wave reflects as an expansion wave because of the open pore conditions. The expansion wave is recorded at $P2$ at $t = 0.26$ ms.

Chapter 5

Shock tube experiments

In this chapter we discuss the basics of the shock tube experiments. Both experiments on water-saturated and air-filled pores are covered, but we limit ourselves to the results in the time domain. Phase velocities and damping coefficients in the frequency domain are presented in Chapter 10. In the current chapter the experimental results in the time domain are compared with 1D computations based on Biot's theory and with the results of Wyllie's equations. For air-filled pores we investigate non-linear phenomena which occur due to the high air velocities in the pores.

5.1 Shock tube

The shock tube which we used to perform experiments on porous rocks is shown in Fig. 5.1, where the configuration for water-saturated experiments is shown. The configuration for experiments on air-filled pores is similar, and the details are given in the last section of this chapter. The advantage of our experimental set-up is the capability of generating a simple and reproducible step loading on the pore fluid, which covers a broad band of frequencies. An additional advantage is the possibility to vary the amplitude of the input signal, which enlarges the field of applications to non-linear problems. Van der Grinten *et al.* (1985,1987), Sniekers *et al.* (1989), and Smeulders and Van Dongen (1997) performed shock tube experiments on water-saturated, partially saturated and dry samples. In the current chapter we present an extension of the work of these authors as we performed a large series of experiments on samples with a wide range of properties. Nakoryakov *et al.* (1989) studied the propagation of both step waves and bell-shaped waves in porous media, using a shock tube configuration as well.

The shock tube consists of a high pressure section and a low pressure section, divided by a diaphragm. The length of the shock tube is about 8 m, while the inner diameter of the test section is 77 mm. The test section is this long in order to obtain a fully developed shock wave. The shock tube sections are made out of steel with a wall thickness of 24 mm in order to suppress compliance effects. A porous cylinder is mounted in the test section of the shock tube and carefully saturated with water. The water level is some 66 cm above the top of the sample. For the diameter of the sample two cases have been considered. In the first case a diameter is chosen very close to the inner diameter of the test section: 76.9 mm. This means that the sample-to-tube surface ratio is 0.997. Experiments in this

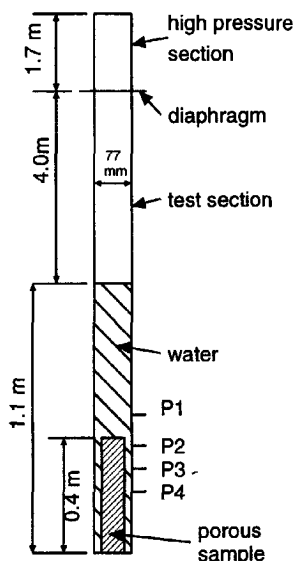


Figure 5.1: Shock tube configuration water-saturated pores. P1, P2, P3 and P4 indicate the positions of the pressure transducers.

configuration are called the small gap experiments. In the second case a diameter of 70.0 mm is used. The surface ratio is then only 0.826 and thus a relatively large water-filled gap exists between the radial surface of the sample and the shock tube wall. These series of experiments are denoted by the large gap experiments.

A wave experiment proceeds as follows. The pressure in the high pressure section is raised to a value in the range of 2-5 bars and by means of an electric current, the diaphragm is forced to rupture. A shock wave in air is generated which is transmitted into the water column on top of the sample. The step wave in the water partially reflects, partially transmits into the sample. Surface waves are generated on the interface between the sample and the liquid filled gap. Because of normal incidence no bulk-type shear waves are induced. The shock tube wall is equipped with four pressure transducers, Kistler 603B, at the positions indicated by P1, P2, P3 and P4. The first transducer P1 is mounted some 15 cm above the top of the cylinder, the second transducer P2 at 0.5 cm below the top. The distance between P2 and P3, and P3 and P4 is 5 cm. The data-acquisition is performed using a Lecroy 6810 waveform recorder.

5.2 Results water-saturated samples

Experiments have been performed with both natural and synthetic rock. The properties of these samples are given in Appendix E. The natural Bentheim sample has a shear velocity higher than the sound velocity of water, a so-called fast formation. Of

the synthetic rock samples (N and G series) some correspond to fast formations, some to slow formations. The shear velocity of a slow formation is lower than the water velocity.

5.2.1 Large gap experiments

An example of the pressure signals recorded for natural Bentheim sandstone with a diameter of 70.0 mm is given in Fig. 5.2 (solid lines). Note that for this case a large water-filled gap exists between the cylinder surface of the sample and the shock tube wall. The results can be interpreted using the space-time plot as given in Fig. 5.3. At P1 the arrival of the step wave is observed at $t = 0.25$ ms followed by its reflection from the top of the sample at $t = 0.43$ ms. The wave which reflected from the top of the porous sample, reflects again from the water-air interface, and returns as an expansion wave which is recorded at $t = 1.1$ ms. The pressure rise at $t = 0.8$ ms is caused by the reflection of the fast wave from the end-plate of the shock tube. At P4 the arrival of the fast compressional wave is recorded at $t = 0.38$ ms, followed by a second pressure rise which probably corresponds to the surface wave.

This is suggested by the results of the one-dimensional theory. Using the computer code as described in Chapter 4 we computed the pressure signals as given in Fig. 5.2 (dashed lines). The parameters are given in Table E.1. The fast wave arrival is predicted at $t = 0.37$ ms, while the slow wave arrival is predicted at $t = 0.53$ ms. Due to the large damping the amplitude of the slow wave arrival is small. The arrival at $t = 0.55$ ms corresponds to the reflection of the fast wave from the end-plate of the shock tube. Therefore, it is unlikely that experimentally observed arrival at $t = 0.45$ ms corresponds to the slow wave arrival. We find that 3-D effects become important for this case. They are modelled in the forthcoming chapters, and we will show that surface wave effects are prominent. Furthermore, the amplitude of the reflected wave in Fig. 5.2 is lower than predicted, but a better match can be obtained by taking into account the quasi 1-D correction as discussed in Section 4.2. This correction, however, does not influence the predicted arrival times.

An example of recorded pressure signals for the synthetic material N5b is given in Fig. 5.4 (solid lines). Again, the diameter of the sample is 70.0 mm. The rock properties of this sample are given in Table E.3. The signal at P1 is similar to the signal of the Bentheim sample. In Fig. 5.4(b) the arrival at $t = 0.4$ ms corresponds to the fast wave, while the pressure rise at $t = 0.68$ ms corresponds to the reflection from the end plate of the shock tube. Again it is suggested that the arrival at $t = 0.56$ ms corresponds to the surface wave. The predicted results, indicated by the dashed lines, are much better in agreement than for the Bentheim case. The amplitude of the reflected wave is too large, but again this can be improved by introducing a quasi 1-D correction. The computed amplitudes at P4 do not predict a slow wave, and hence we conclude that 3-D effects occur.

The conditions for the validity of the 1-D approximation shall be discussed in Chapter 8 where the radial variations of the displacements and stresses are also taken into account.

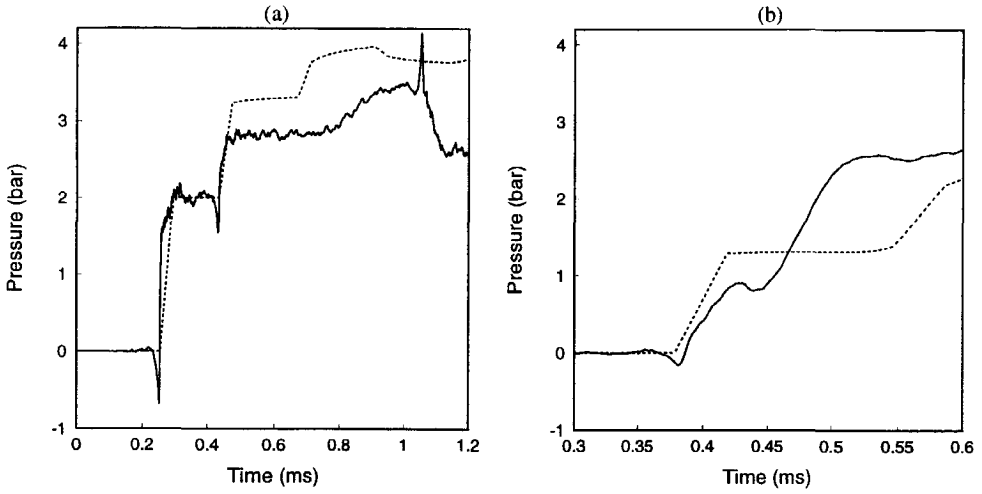


Figure 5.2: Pressure signals at P1 (a) and P4 (b). The experiments were performed on Bentheimer sandstone. Sample diameter: 70 mm. Sample length: 40 cm. P1 is mounted at $z = -133$ mm and P4 at $z = 117$ mm, where $z = 0$ corresponds to the top of the sample. Solid lines refer to the experiments while the dashed lines correspond to 1-D computations based on Biot's theory.

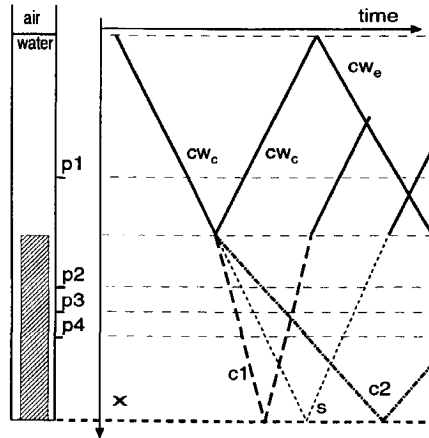


Figure 5.3: Space-time plot of the incident, reflected and transmitted waves. The compressional waves in water are denoted by cw_c , the expansion wave by cw_e . The fast compressional wave is denoted by $c1$, the slow compressional wave by $c2$, and the surface wave by s .

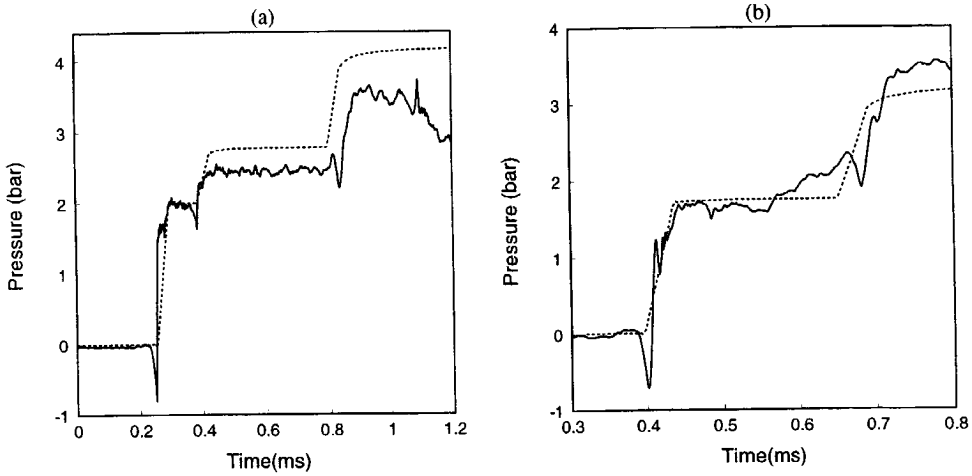


Figure 5.4: Pressure signals at P1 (a) and P4 (b). Sample diameter: 70 mm. Sample length: 40 cm. The experiments were performed on the synthetic material N5b. P1 is mounted at $z = -98$ mm and P4 at $z = 153$ mm, where $z = 0$ corresponds to the top of the sample. Solid lines refer to the experiments while the dashed lines correspond to 1-D computations based on Biot's theory.

5.2.2 Small gap experiments

An example of the recorded signals for a small gap experiment on the synthetic material N5 is shown in Fig. 5.5 (solid lines). The rock properties are given in Table E.3. The diameter is equal to 76.5 mm, while the inner diameter of the shock tube is equal to 77.0 mm. The surface wave is not observed in the small gap experiment and the agreement between the 1-D theory and the experiments is much better. The recorded amplitudes for the reflected and the transmitted waves are in perfect agreement with the predictions. The velocity of the fast wave is somewhat overpredicted as shown by the arrival of the reflection from the end-plate of the shock tube.

Fig. 5.6 shows the results of a similar experiment for the synthetic sample N2. This sample has a permeability one order of magnitude higher than the permeability of N5 and Bentheim (see Table E.3). In addition to the fast wave, the slow compressional wave is also observed with its arrival at $t = 0.78$ ms. The predictions of the 1-D theory show a good agreement with the experimental results. Van der Grinten *et al.* (1987) measured both the pore pressure and the gap pressure. They observed that the registered gap pressure is almost identical to the registered pore pressure. Our experiments confirm the validity of the one-dimensional approximation for small gaps.

5.2.3 Comparison of Biot's theory and the Wyllie equation

We used the small gap configuration for a large measurement series on samples with a wide variety of properties. The parameters were determined in independent laboratory

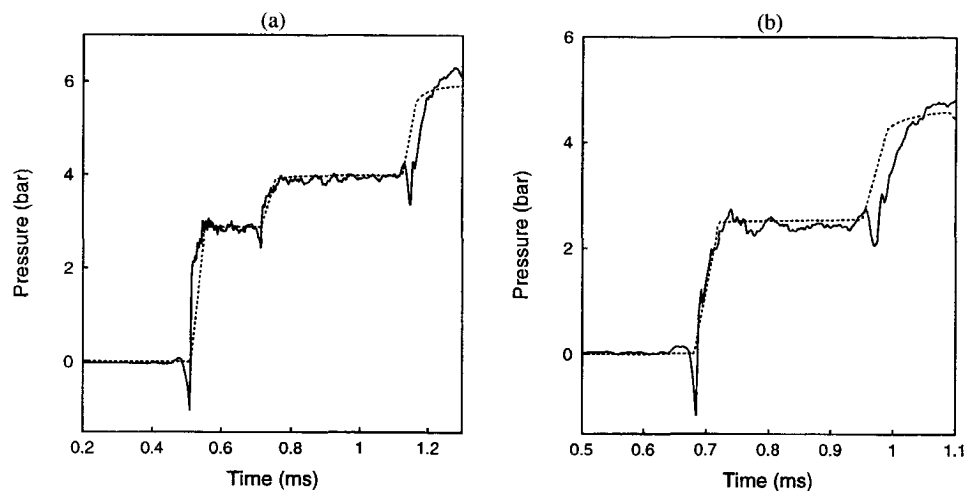


Figure 5.5: Pressure signals at P1 (a) and P4 (b). Sample diameter: 76.9 mm. Sample length: 40 cm. The experiments were performed on the synthetic material N5b. P1 is mounted at $z = -152$ mm and P4 at $z = 136$ mm, where $z = 0$ corresponds to the top of the sample. Solid lines refer to the experiments while the dashed lines correspond to 1-D computations based on Biot's theory.

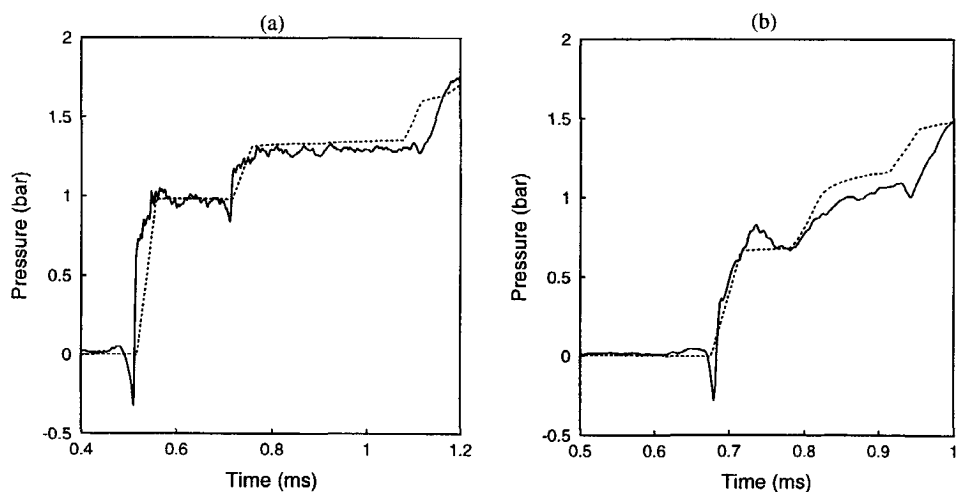


Figure 5.6: Pressure signals at P1 (a) and P4 (b). Sample diameter: 76.9 mm. Sample length: 40 cm. The experiments were performed on the synthetic material N2. P1 is mounted at $z = -152$ mm and P4 at $z = 148$ mm, where $z = 0$ corresponds to the top of the sample. Solid lines refer to the experiments while the dashed lines correspond to 1-D computations based on Biot's theory.

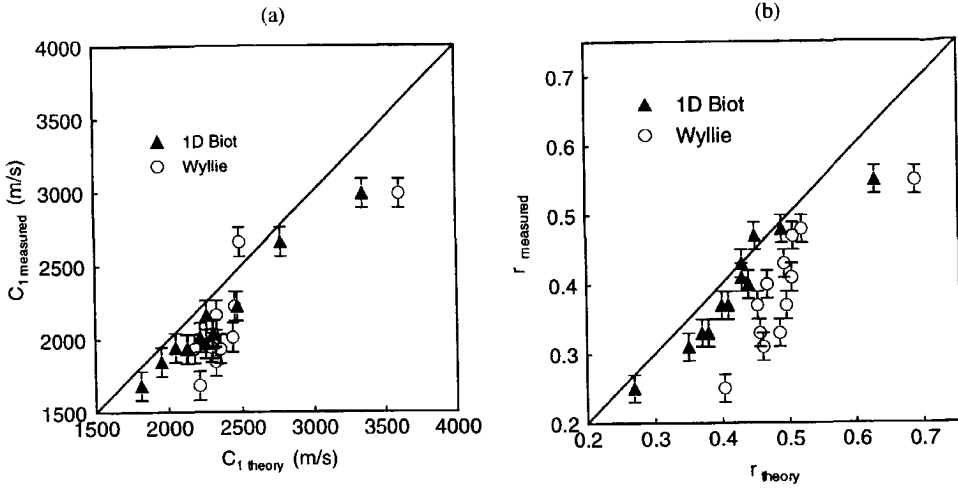


Figure 5.7: Comparison of experimental results with computations based on 1D Biot theory and Wyllie's equation. Phase velocities of the fast wave are given in (a), the reflection coefficients in (b). Error bars indicate the uncertainty in the measurements.

experiments (see Appendix E). Subsequently, we used both Biot's theory and Wyllie's equation to calculate the fast wave velocity and the reflection coefficient. Wyllie's equation (Wyllie *et al.* 1956, Wyllie *et al.* 1958) relates the sound velocity of the porous medium V_{wyl} to the sound velocity of the solid V_s and the sound velocity of the saturant liquid V_l via the following assumption:

$$\frac{1}{V_{wyl}} = \frac{\phi}{V_l} + \frac{1 - \phi}{V_s}. \quad (5.1)$$

For V_l we used the sound velocity of water: $V_l = 1488$ m/s. For V_s we used the sound velocity of silica: $V_s = 5900$ m/s (Wyllie *et al.* 1956). The corresponding reflection coefficients for Wyllie's equation were computed using

$$r = \frac{Z_{wyl} - Z_l}{Z_{wyl} + Z_l}, \quad (5.2)$$

where $Z_{wyl} = (\phi \rho_l + (1 - \phi) \rho_s) V_{wyl}$. The reflection coefficients for the Biot theory are given by the ratios of the amplitudes of the incoming and reflected waves for a semi-infinite cylinder (see Chapter 3).

Fig. 5.7(a) shows the results for the velocity of the fast wave. Twelve different porous samples were used with different porosities and permeabilities. The data represent experiments on the following samples: Bentheimer sandstone, N1B, N2, N3, N4, N4B, N5, N6B, G50A, G30B, G40A, and G20B. The parameters are given in Table E.2 and Table E.3. The experimental fast wave velocities were determined using the arrival time of the minimum of the pressure at P4 ($t = 0.68$ ms in Fig. 5.6). Generally, we observe that prediction of Biot's theory are more accurate than the predictions of Wyllie's equation,

but Wyllie's equation works surprisingly well, considering its ad-hoc character. The deviations between experiments and theory for Wyllie's equation are in agreement with the data of Wyllie (Wyllie *et al.* 1956, Wyllie *et al.* 1958). He observed agreement between his experiments and his equation for porous samples under high pressures. For saturated porous sandstone cores under atmospheric conditions the predicted values were too high.

Fig. 5.7(b) gives the comparison between the experiments and both models for the reflection coefficient. The experimental reflection coefficients were determined using the amplitudes of the incident and reflected waves at P1. Generally, we observe a reasonable agreement between the 1-D Biot theory and the measurements. The predicted values are systematically somewhat too high. Most likely, this is due to the occurrence of 3-D effects. We notice that Wyllie's approach fails here, but we have to keep in mind that it merits lie in the quite accurate predictions of the velocity of the fast compressional wave.

5.3 Results air-filled pores

The configuration for air-filled pores is given in Fig. 5.8. The pressures above the sample are measured by transducers P1 and P2, which are respectively 250 and 150 mm above the lower end plate of the shock tube. Pressure transducer P3 is mounted in the lower end plate of the shock tube. We have performed experiments on samples with a wide range of permeabilities. The physical parameters were determined using the techniques described in Appendix E. We used Bentheimer sandstone and Eindhoven sandstone, as well as two samples which consist of glued glass beads. The glass bead samples are labelled GB1 and GB2. The following size ranges apply: 2.50-3.50 mm for GB1 and 1.16-1.40 mm for GB2. The GB samples were cast in a perspex cylinder in order to prevent radial outflow. For the same reason, the Bentheimer sandstone and the Eindhoven sandstone samples were coated with a two-component epoxy resin. The relevant parameters of the samples are given in Table 5.1. Due to the large difference in compressibility between the solid and the air we can use the rigid frame approximation, and hence the properties of the solid are omitted in Table 5.1. In that case the slow wave properties depend only on the permeability, the tortuosity factor and the properties of the saturant fluid (see Chapter 3). In the high-frequency limit the slow wave is propagatory and its phase velocity is $c_f/\sqrt{\alpha_\infty}$, where c_f is the sound velocity of the fluid. In the low-frequency limit the slow wave shows diffusion-like behaviour with a diffusion coefficient $C_D = K_f k_0/(\eta\phi)$. The cross-over frequency corresponds to a situation in which inertial and viscous forces are of equal importance. Note that the cross-over frequencies ω_c as given in Table 5.1 cover several orders of magnitude.

5.3.1 Wave behaviour

The experimental results for the GB1 sample are shown in Fig. 5.9(a) by the solid lines. The shock wave arrives at the top of the sample at $t = 0$. It is recorded by P2 at $t = -0.24$ ms, and the reflected wave from the sample is recorded at $t = 0.28$ ms. In the porous sample we notice at $t = 0.23$ ms a distinct pressure jump, which corresponds to the arrival of the shock wave at the end plate of the shock tube. From the arrival time we determine the shock wave velocity, which is 243 ± 5 m/s. Since the high-frequency limit of the

	GB1	GB2	Eindhoven sandstone	Bentheimer sandstone
length of the sample (mm)	56	61	152.5	20.5
porosity ϕ	0.32	0.31	0.35	0.23
permeability k (10^{-12}m)	4200	900	122	3.7
Second forchheimer coeff. b_f (mm^{-1})	-	-	75	4990
tortuosity α_∞	2.6	2.7	2.1	2.4
ω_c ($(\text{ms})^{-1}$)	0.4	1.9	18.8	388

Table 5.1: Parameters of the samples which are used in the air-filled pores experiment.

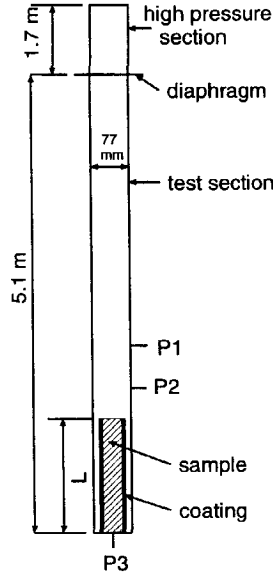


Figure 5.8: Shock tube configuration air-filled pores. P1, P2, P3 indicate the positions of the pressure transducers. P1 and P2 are respectively 250 and 150 mm above the end plate, while P3 is mounted in the end plate of the shock tube.

phase velocity is equal to $c_f/\sqrt{\alpha_\infty}$, which is in this case 211 m/s, the shock wave velocity significantly exceeds the phase velocity. The shock wave is followed by a more gradual diffusive pressure rise. We used the numerical code of Chapter 4 to compute the pressure at the end plate of the shock tube. At P3 we predict the arrival of the slow wave, which is decoupled from the properties of the solid. At $t = 0.8$ ms the first internal reflection of the slow wave arrives, which is an expansion wave due to the free interface at the top of the porous sample. We observe that the qualitative behaviour of the computed pressure signal differs strongly from the experimental pressure curve. The linear theory predicts internal reflections of the slow wave, while the experiments show a diffusive pressure rise.

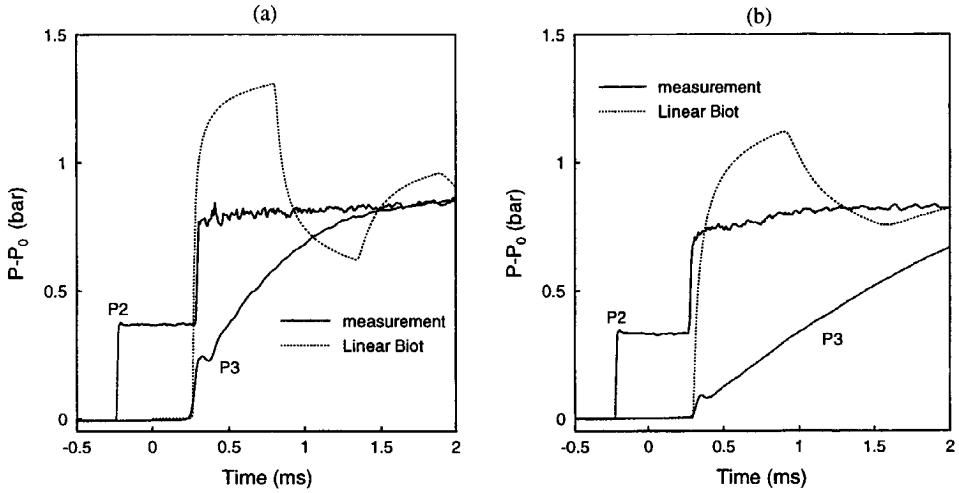


Figure 5.9: Experiments and theory for glass bead sample GB1 (a) and GB2 (b). Solid lines indicate experimental results, while the dashed lines indicate the computational results, which are obtained with the 1-D Biot theory. The atmospheric pressure is denoted by p_0 .

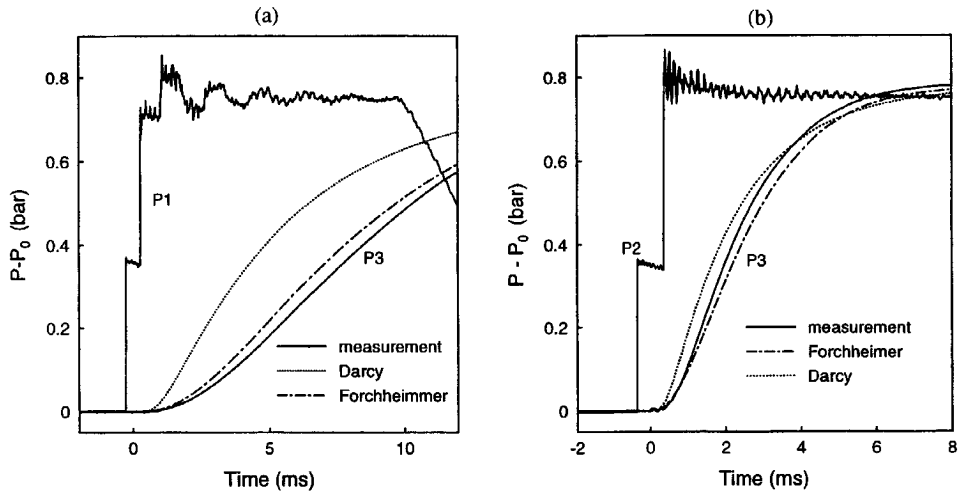


Figure 5.10: Experiments and theory for Eindhoven sandstone (a) and Bentheim sandstone (b). Solid lines indicate the experimental results. The computational results are indicated by the dashed lines and are obtained from the diffusion theory with Darcy's and Forchheimer's equation respectively. The atmospheric pressure is denoted by p_0 .

For the sample GB2 we observe similar phenomena in Fig. 5.9(b), but the amplitude of the shock wave in the porous sample is smaller. Again we observe that the shock wave velocity exceeds the predicted maximum phase velocity. The permeability of this sample is one order lower and the shock wave is strongly damped. We may say that for cross-over frequencies below 10 (ms)^{-1} wave-like behaviour plays an important role. Due to the high-velocities in the pores non-linear effects occur, and the linear Biot theory does not apply. A full description of shock wave propagation in porous media is beyond the scope of this thesis.

5.3.2 Diffusion behaviour

Fig. 5.10(a) shows the experimental results for Eindhoven sandstone. The pressure rise at P3 corresponds to a diffusion-like behaviour. In terms of linear theory we can say that the dominant frequencies in the input signal are far below the cross-over frequency, so that the slow wave is diffusive. As far as wave phenomena occur, they can be neglected because of the strong damping. This gives us the possibility to apply diffusion theory instead of wave theory.

We re-derive the result for the diffusion coefficient C_D of Equation (3.32) using the continuity equation and the momentum balance. The continuity equation for a rigid porous medium reads as follows:

$$\frac{\partial \rho_f}{\partial t} + \nabla(\rho_f \mathbf{v}_f) = 0, \quad (5.3)$$

where ρ_f is the density of the fluid and \mathbf{v}_f the velocity vector of the fluid. Using the ideal gas law and assuming isothermic compression we obtain:

$$\frac{\partial p}{\partial t} + \nabla(p \mathbf{v}_f) = 0, \quad (5.4)$$

where p is the absolute pore pressure. For the momentum equation we use Darcy's law:

$$-\nabla p = \frac{\eta \phi}{k_0} \mathbf{v}_f. \quad (5.5)$$

We substitute Darcy's law in Equation (5.4), and linearize the system using $p = p_0 + p'$, which gives the following result:

$$\frac{\partial p'}{\partial t} = \frac{K_f k_0}{\eta \phi} \nabla^2 p' = C_D \nabla^2 p', \quad (5.6)$$

where K_f is the air bulk modulus. The initial and boundary conditions are given by:

$$\begin{aligned} t = 0 : p' &= 0 \\ t > 0 : p' &= p'_1 \text{ at } x = 0, \quad \frac{\partial p'}{\partial x} = 0 \text{ at } x = L, \end{aligned} \quad (5.7)$$

where L is the length of the sample. Equation (5.6) is a diffusion equation. For the initial and boundary conditions given in Equation (5.7), it can be solved analytically by separation of variables (Carslaw and Jaeger 1986). The following expression results:

$$p'(x, t) = p'_1 + \sum_{n=0}^{\infty} \frac{-4p'_1}{(2n+1)\pi} \exp \left(-C_D \left(\frac{(2n+1)\pi}{2L} \right)^2 t \right) \sin \left(\frac{(2n+1)\pi}{2L} x \right). \quad (5.8)$$

The computational results are given in Fig. 5.10(a) for Eindhoven sandstone and in Fig. 5.10(b) for Bentheimer sandstone. For Eindhoven sandstone we observe a strong deviation between the linear diffusion theory and the experimental results, while for Bentheimer sandstone the agreement is quite reasonable. For Eindhoven sandstone the air velocities in the pores are large so that non-linear effects occur and Darcy's law is not valid any more.

We used Forchheimer's equation to account for the non-linear effects with an extra quadratic term in the velocity (Hannoura and Barends 1981):

$$-\nabla p = \frac{\eta\phi}{k_0} \mathbf{v}_f + \phi^2 b_f \rho_f |\mathbf{v}_f| \mathbf{v}_f. \quad (5.9)$$

Combining Equations (5.4) and (5.9) we obtain a non-linear system which can be solved in different ways. Van der Grinten *et al.* (1985) used a semi-analytical solution based on a transformation of variables. We have applied the Finite Element package SEPRAN, which has the possibility to extend the computations to two or three dimensions. For a discussion of the finite element approach we refer to Cuvelier *et al.* (1986) and Segal (1984). Using the implicit Euler method we obtain for the time-discretization of Equation (5.4):

$$\frac{p^{n+1} - p^n}{\Delta t} + p^{n+1} \nabla \cdot \mathbf{v}_f^{n+1} + \mathbf{v}_f^{n+1} \cdot \nabla p^{n+1} = 0, \quad (5.10)$$

where the superscripts n and $n+1$ denote the properties on $t = t_n$ and $t = t_n + \Delta t$, respectively. Using Forchheimer's equation, we write for the velocity vector:

$$\mathbf{v}_f^{n+1} = \frac{-\nabla p^{n+1}}{a' + b' p^{n+1} |\mathbf{v}_f|^{n+1}}, \quad (5.11)$$

where $a' = \eta\phi/k_0$ and $b' = \phi^2 b_f \rho_0/p_0$. The term $p^{n+1} \nabla \cdot \mathbf{v}_f^{n+1}$ is linearized with a Picard iteration. The value of p^{n+1} denotes the pressure value on step $(i+1)$ during iteration, and p^i denotes the i th value of p^{n+1} . The value of \mathbf{v}_f^{n+1} denotes the velocity vector on $(i+1)$ during iteration, and \mathbf{v}_f^i denotes the i th value of \mathbf{v}_f^{n+1} . Then we obtain for $p^{n+1} \nabla \cdot \mathbf{v}_f^{n+1}$:

$$\begin{aligned} p^{n+1} \nabla \cdot \mathbf{v}_f^{n+1} = & \\ -p^{n+1} \frac{1}{a' + b' p^{n+1} |\mathbf{v}_f|^{n+1}} \nabla^2 p^{n+1} - p^{n+1} \nabla \left(\frac{1}{a' + b' p^{n+1} |\mathbf{v}_f|^{n+1}} \right) \cdot \nabla p^{n+1} \approx & \\ -p^i \frac{1}{a' + b' p^i |\mathbf{v}_f|^i} \nabla^2 p^{n+1} - p^i \nabla \left(\frac{1}{a' + b' p^i |\mathbf{v}_f|^i} \right) \cdot \nabla p^{n+1}. & \end{aligned} \quad (5.12)$$

The second term is linearized similarly:

$$\mathbf{v}_f^{n+1} \cdot \nabla p^{n+1} \approx \frac{-\nabla p^i}{a' + b' p^i |\mathbf{v}_f|^i} \cdot \nabla p^{n+1}. \quad (5.13)$$

Re-arranging terms, we obtain the following diffusion equation:

$$\frac{p^{n+1} - p^n}{\Delta t} + \nabla \cdot \left(\frac{-p^i}{a' + b' p^i |\mathbf{v}_f|^i} \nabla p^{n+1} \right) = 0, \quad (5.14)$$

which is one of the standard problems of the SEPRAN package (Segal 1984).

At each time step the following computational procedure is performed:

1. An estimate is made for the pressure p^i . For the first time step we use the linear solution as the first estimate for p^i , while for later time steps p^n is used.
2. Using p^i , $|\mathbf{v}_f^i|$ is obtained via an iteration procedure based on Equation (5.11).
3. The solution p^{n+1} is computed using the finite element approximation.
4. The pressure p^{n+1} provides a new estimate for p^i .
5. Steps 2 and 3 are repeated until convergence is obtained for p^{n+1} .

Fig. 5.10(a) and (b) show the results of the one-dimensional computations for Eindhoven sandstone and Bentheimer sandstone. For Eindhoven sandstone we observe that the predictions using Forchheimer's equation are in agreement with the experimental results. For Bentheimer sandstone the difference between Darcy's law and the Forchheimer's equation is small, because non-linear effects are of minor importance.

5.3.3 Concluding remarks air-filled pores

Using a wide range of permeabilities we observed the transition from wave-like behaviour to diffusion-like behaviour. Due to the high air velocities in the pores, non-linear effects occur. For high permeabilities shock waves are observed in the saturant air. For low permeabilities the experiments can be described by a non-linear diffusion theory based on Forchheimer's equation. Future work should concentrate on non-linear wave propagation in order to understand the shock wave phenomena in case of the high permeabilities. Smeulders *et al.* (1997) have derived non-linear macroscopic mass and momentum conservation laws. Numerical evaluation of their equations is subject of ongoing research.

Chapter 6

Two-dimensional phenomena

Up to now our discussions on wave phenomena in porous materials were limited to the one-dimensional approximation. However, the deviations between the experiments and the theory can, most likely, be attributed to the occurrence of 3-D effects. This was in particular the case for the large gap experiments where also surface waves were observed. First we discuss the surface wave phenomena in general for elastic materials. A flat interface between an semi-infinite elastic solid and a semi-infinite liquid is investigated. Subsequently we follow the approach of Feng and Johnson (1983) in order to extend these computations to a fluid/porous solid interface. Their analysis was limited to the high-frequency limit of Biot's theory, for which the free-field wavenumbers are real-valued and we obtain a lossless medium. In this chapter we extend their results to lossy media, which means that the full Biot theory is used to describe the poroelastic solid.

6.1 Surface waves and elastic solids

An elastic solid is characterized by the so-called Lamé coefficients λ and μ and the density ρ . Using these properties we define the following free-field velocities of the compressional and the transversal waves:

$$c_L = \sqrt{\frac{\lambda + 2\mu}{\rho}}, \quad (6.1)$$

$$c_T = \sqrt{\frac{\mu}{\rho}}. \quad (6.2)$$

Poisson's ratio is defined using the compressional wave velocity c_L and the shear velocity c_T :

$$\nu = \frac{2c_T^2 - c_L^2}{2(c_T^2 + c_L^2)}. \quad (6.3)$$

In vector notation the wave equation can be written as (Achenbach 1973):

$$\mu \nabla^2 \mathbf{u}_s + (\lambda + \mu) \nabla \nabla \cdot \mathbf{u}_s = \rho \frac{\partial^2 \mathbf{u}_s}{\partial t^2}, \quad (6.4)$$

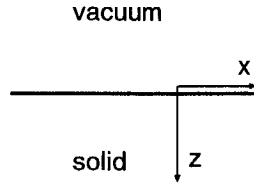


Figure 6.1: *Interface solid/vacuum*

where \mathbf{u}_s is the displacement vector. If we divide both the LHS and the RHS by the density ρ we observe that the wave equation is uniquely characterized by the shear velocity c_T and the Poisson's ratio ν .

In order to solve the wave propagation problem it is useful to define a decomposition of the displacement vector in scalar and vector potentials. According to Miklowitz (1978), Lamé states that every displacement vector field of the form

$$\mathbf{u}_s = \nabla \varphi_s + \nabla \times \boldsymbol{\psi}_s \quad (6.5)$$

satisfies the Equation (6.4), provided that the scalar potential φ_s is a solution of

$$(\lambda + 2\mu)\nabla^2 \varphi_s - \rho \frac{\partial^2 \varphi_s}{\partial t^2} = 0, \quad (6.6)$$

and the vector potential $\boldsymbol{\psi}_s$ is a solution of

$$\mu \nabla^2 \boldsymbol{\psi}_s - \rho \frac{\partial^2 \boldsymbol{\psi}_s}{\partial t^2} = 0. \quad (6.7)$$

Motions of the compressional waves are related to the scalar potential φ , while the motions due to transversal waves correspond to the vector potential $\boldsymbol{\psi}$. A proof of completeness of this solution is given by Miklowitz (1978).¹

6.1.1 Free surface of an elastic half space

First we consider waves along an interface between a semi-infinite elastic solid and a vacuum (Fig. 6.1). In this two-dimensional case $\partial/\partial y = 0$ and $u_{sy} = 0$, so only the second component of $\boldsymbol{\psi}_s$, viz. ψ_{sy} , is of importance. We consider waves which propagate in the positive x -direction. Consequently, we assume the following expressions for the two scalars φ and ψ_{sy} :

$$\varphi_s = A_1 e^{i(\omega t - kx - k_{zc1}z)}, \quad (6.8)$$

¹This decomposition of the displacement vector is similar to the Helmholtz decomposition of a vector field which reads the same as Equation (6.5), together with and additional condition: $\nabla \cdot \boldsymbol{\psi}_s = 0$. However, Lamé's solution satisfies the wave equation even when this last condition is not satisfied. If a new potential $\boldsymbol{\psi}_s = \boldsymbol{\psi}'_s + \nabla g$ is formed, with g a scalar function, it is straightforward to show that the displacement \mathbf{u} is invariant to the change in vector potentials.

$$\psi_{sy} = C_{sh} e^{i(\omega t - kx - k_{zsh}z)}, \quad (6.9)$$

with $\Re(k) > 0$. The wavenumbers in the z -direction are related to the wavenumber in the x -direction and the free-field wave velocities via a complex square root:

$$k_{zcl} = \sqrt{\omega^2/c_L^2 - k^2}, \quad (6.10)$$

$$k_{zsh} = \sqrt{\omega^2/c_T^2 - k^2}. \quad (6.11)$$

This can easily be seen if we substitute the expressions for the potentials in the equations of motion. The finite amplitudes of the potentials for $x \rightarrow \infty$ and $z \rightarrow \infty$ require that

$$\Im m(k) \leq 0, \quad \Im m(k_{zcl}) \leq 0, \quad \Im m(k_{zsh}) \leq 0. \quad (6.12)$$

These conditions are satisfied by choosing the appropriate branch and branch cuts (see Appendix C).

At the interface, the normal and shear stress components vanish and we obtain the following boundary conditions:

$$\tau_{zz} = 0, \quad \tau_{zx} = 0. \quad (6.13)$$

Substituting the expressions for the potentials of the Equations (6.8) and (6.9) in the boundary conditions we obtain a set of equations for the amplitudes A_1 and C_{sh} :

$$\begin{pmatrix} (\lambda + 2\mu)(k_{zcl}^2 + k^2) - 2\mu k^2 & 2\mu k k_{zsh} \\ -2\mu k k_{zcl} & \mu(k_{zsh}^2 - k^2) \end{pmatrix} \begin{pmatrix} A_1 \\ C_{sh} \end{pmatrix} = \begin{pmatrix} 0 \\ 0 \end{pmatrix}. \quad (6.14)$$

For the stress-strain relations in cartesian coordinates the reader is referred to Appendix A. For a non-trivial solution of Equation (6.14) the determinant of the first matrix on the LHS must be zero. After some algebraic manipulation, we can derive an expression for the wave velocity $c = \omega/k$, which is the so-called Rayleigh equation (Achenbach 1973):

$$F(c) = \left(2 - \frac{c^2}{c_T^2}\right)^2 - 4\sqrt{1 - \frac{c^2}{c_L^2}}\sqrt{1 - \frac{c^2}{c_T^2}} = 0. \quad (6.15)$$

In this equation there is no explicit reference to k , which means that the wave velocity which satisfies the Rayleigh equation is frequency independent.² We developed a numerical code to find the zeros of Equation (6.15). This code is based on a Newton-Raphson iteration and comprises a search routine in the complex wavenumber plane. More details are given in Appendix D. We found one wavenumber on the real wavenumber axis, which corresponds to a real phase velocity $c = 0.927c_T$ for $\nu = 0.3$. This wave is called the Rayleigh wave. Achenbach (1973) shows that this is the only root which satisfies the boundary conditions. The wavenumbers k_{zcl} and k_{zsh} are negative-imaginary because $c < c_T < c_L$ and k is real. The potentials show therefore an exponential decaying behaviour in the direction perpendicular to the surface:

$$\varphi_s = A_1 e^{\Im m(k_{zcl})z} e^{i(\omega t - kx)}, \quad (6.16)$$

²This is self-evident for the lossless elastic medium. However, for a lossy porous solid the surface wave velocity is frequency dependent (see Section 6.2.3).

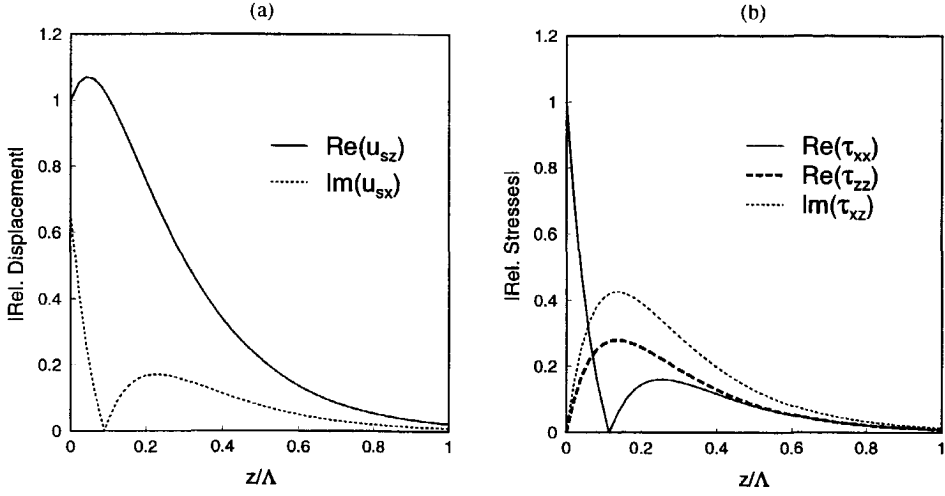


Figure 6.2: Distributions of the relative displacements (a) and stresses (b) for the Rayleigh wave. Displacements are normalized by $u_{sz}|_{z=0}$, the stresses by $\tau_{xx}|_{z=0}$, and the distances from the surface by the wavelength $\Lambda = 2\pi/k$.

and

$$\psi_{sy} = C_{sh} e^{\Im m(k_{zsh})z} e^{i(\omega t - kx)}. \quad (6.17)$$

We can plot the distributions of the stresses and displacements as a function of the distance from the surface. The results for the Rayleigh wave are shown in Fig. 6.2. The displacements in Fig. 6.2(a) are normalized by the displacement $u_{sz}|_{z=0}$ while the stresses in Fig. 6.2(b) are normalized by $\tau_{xx}|_{z=0}$. For the distance from the surface we used the wavelength $\Lambda = 2\pi/k$ as a typical length scale, which leads to frequency-independent distributions. The exponential decay of the stresses and displacements from the surface is typical of surface waves. Furthermore, if we prescribe a real value of τ_{xx} it is observed that τ_{zz} is also real-valued while the shear stress is imaginary-valued. This means that the shear stress is 90° out of phase with the other stress components. The same is valid for the displacement u_{sx} which is 90° out of phase with the displacement u_{sz} . For a further discussion on Rayleigh waves we refer to the work of Viktorov (1967)

6.1.2 Liquid-solid interface

In case of a fluid-loaded elastic halfspace, the situation becomes somewhat different (Fig. 6.3). Introducing a potential φ_w for the water, defined by

$$\mathbf{u}_w = \nabla \varphi_w, \quad (6.18)$$

we may write:

$$\nabla^2 \varphi_w = \frac{1}{c_w^2} \frac{\partial^2 \varphi_w}{\partial t^2}, \quad (6.19)$$

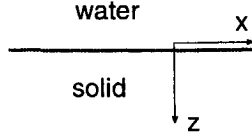


Figure 6.3: Interface solid/liquid

where c_w is the sound velocity in the water. Assuming harmonic variation and plane wave propagation, we write:

$$\varphi_w = A_2 e^{i(\omega t - kx + k_{zw}z)}, \quad (6.20)$$

with

$$k_{zw} = \sqrt{\omega^2/c_w^2 - k^2}. \quad (6.21)$$

Note that for k_{zw} in Equation (6.20) we have chosen a positive sign, contrary to the convention used for the elastic solid. The reason is that in this way a negative imaginary part of the wavenumbers k_{zw} , k_{zcl} and k_{zsh} always corresponds to a damping when moving away from the liquid-solid interface, i.e., for $z \rightarrow -\infty$ in the water, and for $z \rightarrow \infty$ in the solid. For the pressure of the water we can write:

$$p_w = \rho_w \omega^2 \varphi_w. \quad (6.22)$$

The boundary conditions at $z = 0$ for this case are:

$$\begin{aligned} \tau_{zz} &= -p_w, \\ \tau_{xz} &= 0, \\ u_{sz} &= u_{wz}. \end{aligned} \quad (6.23)$$

The relations between the stresses and the potentials are given in Appendix A. By substitution of the potentials in the boundary conditions we obtain the following set of equations:

$$\begin{pmatrix} -(\lambda + 2\mu)\frac{\omega^2}{c_L^2} + 2\mu k^2 & -2\mu k k_{zsh} & \rho_w \omega^2 \\ -2\mu k k_{zcl} & \mu(k_{zsh}^2 - k^2) & 0 \\ ik_{zcl} & ik & ik_{zw} \end{pmatrix} \begin{pmatrix} A_1 \\ C_{sh} \\ A_2 \end{pmatrix} = 0. \quad (6.24)$$

After some algebraic manipulations, we can write the determinant of the matrix explicitly. For a non-trivial solution this determinant must be equal to zero:

$$\theta \frac{c^4}{c_T^4} ik_{zcl} + ik_{zw} \left[\left(2 - \frac{c^2}{c_T^2} \right)^2 - 4 \sqrt{1 - \frac{c^2}{c_L^2}} \sqrt{1 - \frac{c^2}{c_T^2}} \right] = 0, \quad (6.25)$$

where $\theta = \rho_w/\rho_{solid}$ and $c = \omega/k$. Note that for $\theta = 0$ we obtain two solutions. The first one is the sound velocity of water ($k_{zw} = 0$), the second one is the velocity of the Rayleigh wave. For $\theta > 0$ we obtain also two solutions as will be explained below. For a steel/water interface, for example, with $\theta = 0.126$ we found one zero on the real k -axis, with a phase velocity below the sound velocity of the liquid. This wave type is generally called the Stoneley wave as a special case of the surface wave along an interface between two solids. Due to the contributions of J.G. Scholte (1948) some authors refer to this wave as the 'Scholte' wave (Miklowitz 1978, van der Hijden 1984, de Hoop and van der Hijden 1983). The Stoneley wave between two solids exists only for a limited range of elasticity parameters of the solids, while Scholte showed that the surface wave along a solid/liquid interface exists for arbitrary parameters of the solid and the fluid. De Hoop and Van der Hijden (1983) derived that there is only one Stoneley wave along a liquid/solid interface. The distribution of the relative normal stresses, pressures and displacements of the solid and the water are given in Fig. 6.4 for the steel/water interface. For both the liquid and the solid we observe an exponential decay of the stresses and displacements in the direction perpendicular to the surface. The phase velocity of the Stoneley wave, made dimensionless with the sound velocity of the water, is given in Fig. 6.5 as function of the density ratio θ . Note that the Stoneley wave is undamped for the whole range of density ratios. From this graph we observe that for a small density ratio the phase velocity reaches the sound velocity of the water ($k_{zw} = 0$).

The second solution for $\theta > 0$ is the so-called pseudo-Rayleigh wave. There has been a lot of discussion about this wave type (Phinney 1961a, Phinney 1961b, Strick 1959, Ansell 1972, Uberall 1973, Brekhovskikh 1980, de Hoop and van der Hijden 1983, van der Hijden 1984). This wave type is a solution of Equation (6.25) on that part of the Riemann surface where

$$\Im m(k_{zw}) \geq 0, \Im m(k_{zcl}) \leq 0, \text{ and } \Im m(k_{zsh}) \leq 0. \quad (6.26)$$

This means that the amplitude of the potential of the liquid φ_w will increase as we move away from the interface. This fact contradicts our physical intuition, because it results in an infinite amount of energy far away from the surface. However, any result in the space-time domain is obtained only after an integral transformation from the frequency-wavenumber domain. The locations of the branch-cuts (see Appendix C) complicate the definition of closed integration contours in the complex k -plane. These contours are not allowed to pass the branch cuts and thus have to be modified accordingly. The integration can be performed by rewriting it as a set of residue contributions from poles lying on the sheet of integration and branch line integrals arising from integration around the cuts (Ewing *et al.* 1957). According to Phinney (1961b) and Strick (1959) the pseudo-waves are caused by poles of the response which lie on Riemann sheets other than the principal sheet of integration. Due to their proximity to the branch cuts they affect the form of the solution obtained by integration around the cuts, thus generating a contribution to the signal, despite their location on a lower Riemann sheet. Experimentally the pseudo-Rayleigh arrival was observed by Roever (1959), and agreement was found with the modelling of Strick (1959). Van der Hijden (1984) showed the influence of the pseudo-Rayleigh phenomenon on the Green's function (system response) of a fluid/solid interface. The dimensionless phase velocity of the pseudo-Rayleigh wave is given in Fig. 6.6(a) as

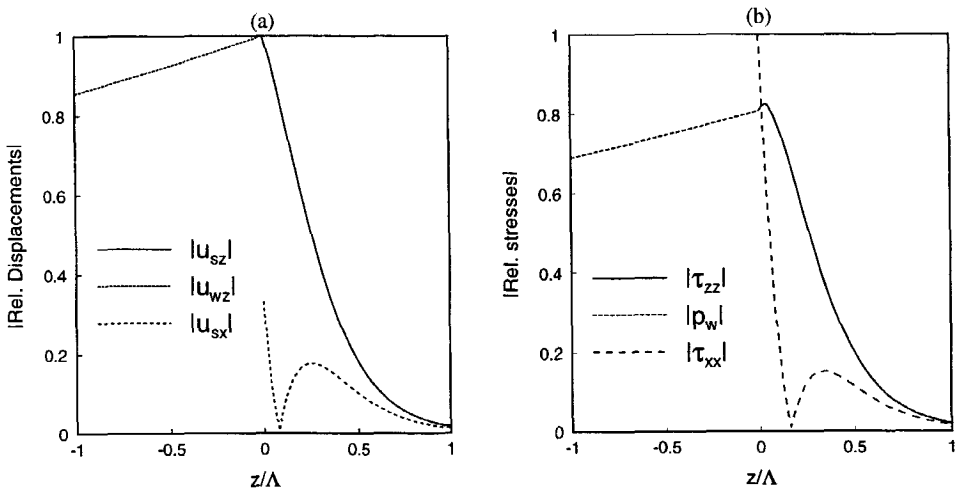


Figure 6.4: Distributions of the relative displacements (a) and normal stresses and pressures (b) for the Stoneley wave. The displacements are normalized using $u_{sz}|_{z=0}$, the stresses and pressures by $\tau_{xx}|_{z=0}$. The distances from the surface are normalized by the wavelength Λ . The calculations were performed for a steel/water interface.

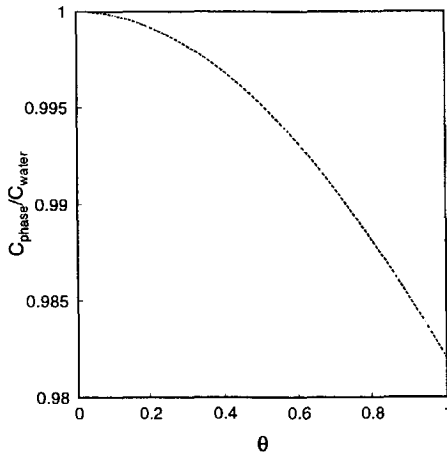


Figure 6.5: Dimensionless phase velocity of the Stoneley wave as function of the density ratio θ .

function of the density ratio while the damping coefficient $\Im m(k)$ is given in Fig. 6.6(b). For the limit $\theta \rightarrow 0$ the phase velocity of the (undamped) Rayleigh wave on an elastic halfspace is reached. For $\theta > 0$ the pseudo-Rayleigh wave is damped in the direction along the interface. This phenomenon is typical of pseudo-surface waves. Note that the true surface wave (Stoneley wave) is undamped. The relative displacements, stresses and pressures for the pseudo-Rayleigh wave are shown in Fig. 6.7, where exponential decay in the solid, and exponential growth in the liquid are observed. The compressional and the shear waves in the solid 'leak' energy into the liquid. Therefore the pseudo-waves are also called 'leaky' waves. This becomes more clear if we sketch the wave fronts in the solid and the fluid as given in Fig. 6.8 (Brekhovskikh 1980). Note that from a mathematical point of view the concept of wave fronts for the pseudo-waves is not applicable (van der Hijden 1984). The waves in the solid and in the fluid travel in the same direction, which can be derived from the behaviour of the complex square roots (Appendix C). The roots for the compressional and shear waves are located in the third quadrant of the k_{zc1} and k_{zsh} planes with the sign conventions $e^{-i(k_{zc1}z)}$ and $e^{-i(k_{zsh}z)}$ for $z > 0$. The root for k_{zw} is located in the first quadrant with the sign convention $e^{i(k_{zw}z)}$ for $z < 0$. The amplitudes are indicated by the line thicknesses.

6.2 Surface waves and porous solids

When the solid half space of Fig. 6.3 is replaced by a porous half space, the situation becomes more complex because of the extra bulk wave, the slow wave, which is typical of porous solids. Feng and Johnson (1983) were the first to consider this configuration. Their results were based on the high-frequency limit of Biot's theory, i.e., they only considered a lossless medium. As in the elastic case, the true surface waves are undamped, while pseudo-waves are damped significantly. In this section we will also consider lossy media. Lauriks *et al.* (1998) considered surface and leaky waves in a lossy porous medium with a motionless frame. In our computations the full Biot theory is used to study the surface and leaky waves. We start with the lossless medium.

6.2.1 Potentials

Following our approach of Chapter 3 we define for the porous solid two scalar potentials for the two compressional wave types and a vector potential for the shear waves. In the two-dimensional configuration with $u_{sy} = 0$ and $\partial/\partial y = 0$ we write:

$$\varphi_{sc1} = A_{1c1} e^{i(\omega t - kx - k_{zc1}z)}, \quad \varphi_{sc2} = A_{1c2} e^{i(\omega t - kx - k_{zc2}z)}, \quad (6.27)$$

and

$$\psi_{sy} = C_{1sh} e^{i(\omega t - kx - k_{zsh}z)}. \quad (6.28)$$

For the water we use the same potential as in the previous case of a solid/liquid interface:

$$\varphi_w = A_2 e^{i(\omega t - kx + k_{zw}z)}. \quad (6.29)$$

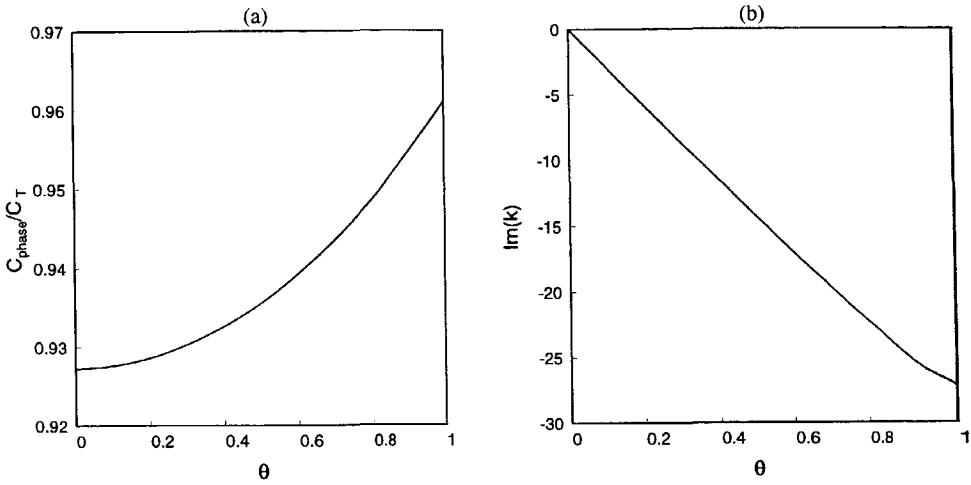


Figure 6.6: Phase velocity (a) and damping (b) of the pseudo-Rayleigh wave as a function of the density ratio θ . The calculations were performed for a solid/water interface.

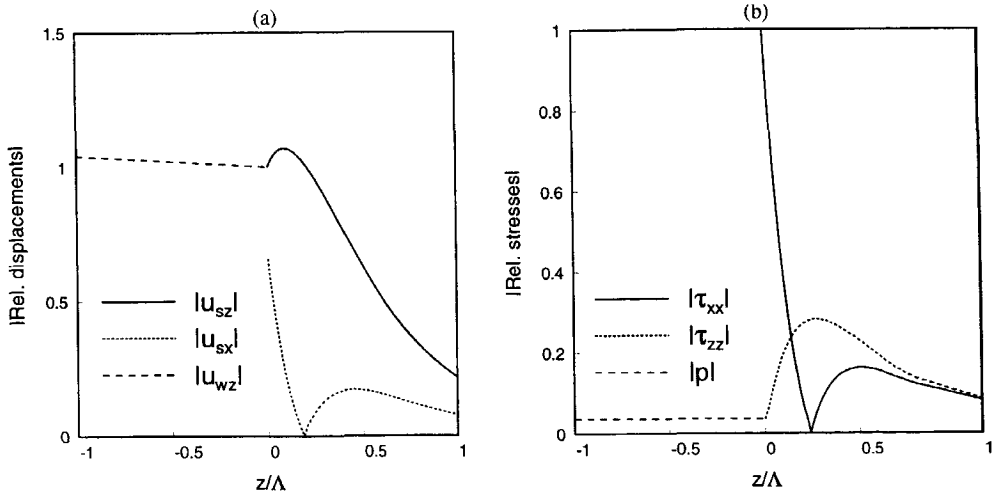


Figure 6.7: Distributions of the relative displacements (a) and normal stresses and pressures (b) for the pseudo-Rayleigh wave. The displacements are normalized using $u_{sz}|_{z=0}$, the stresses and pressures by $\tau_{xx}|_{z=0}$. The distances from the surface are normalized by the wavelength Λ . The calculations were performed for a steel/water interface.

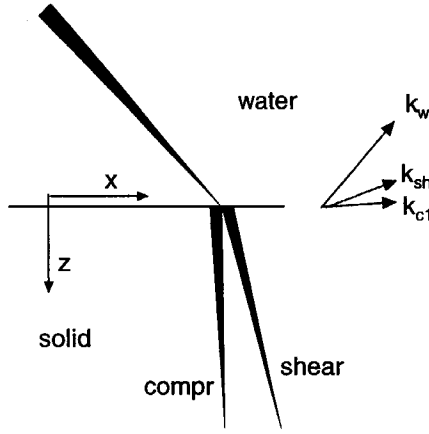


Figure 6.8: Schematic plot of the wave fronts for the pseudo-Rayleigh wave. The wave vectors k_{c1} , k_{sh} , and k_w consist of the x-component k and the z-components k_{zc1} , k_{zsh} and k_{zw} , respectively.

In these equations the wavenumbers in the z-direction are defined using the free-field velocities of the Biot waves:

$$k_{zc1} = \sqrt{\omega^2/c_1^2 - k^2}, \quad k_{zc2} = \sqrt{\omega^2/c_2^2 - k^2}, \quad k_{zsh} = \sqrt{\omega^2/c_{sh}^2 - k^2}, \quad (6.30)$$

and

$$k_{zw} = \sqrt{\omega^2/c_w^2 - k^2}. \quad (6.31)$$

The signs of these square roots are similar to the elastic case (Feng and Johnson 1983) (see also Table 6.1). For true surface waves we take:

$$\Im m(k_{zc1}) \leq 0, \quad \Im m(k_{zc2}) \leq 0, \quad \Im m(k_{zsh}) \leq 0, \quad \Im m(k_{zw}) \leq 0. \quad (6.32)$$

For elastic solids the relations between the potentials and the stresses are given in Appendix A. Assuming incompressible grains we can write $\lambda = (K_b - 2/3G)$ and we can use expressions for the intergranular stresses σ_{zz} and σ_{zx} which are similar to the elastic case:

$$\sigma_{zz} = -(K_b - 2/3G)\nabla^2\varphi_s - 2G\left[\frac{\partial^2\varphi_s}{\partial z^2} + \frac{\partial^2\psi_y}{\partial z\partial x}\right], \quad (6.33)$$

and

$$\sigma_{zx} = -G\left[2\frac{\partial^2\varphi_s}{\partial x\partial z} - \frac{\partial^2\psi_y}{\partial z^2} + \frac{\partial^2\psi_y}{\partial x^2}\right]. \quad (6.34)$$

The scalar potential φ_s is the sum of the potential of the fast wave φ_{c1} and the potential of the slow wave φ_{c2} . Using Equation (2.37) with $e_{kk} = \nabla^2\varphi_{sc1} + \nabla^2\varphi_{sc2}$ and $\epsilon_{kk} =$

$\nabla^2(\beta_{c1}\varphi_{sc1} + \beta_{c2}\varphi_{sc2})$ we can write for the pore pressure p :

$$p = -\frac{\tau}{\phi} = -\frac{K_f}{\phi} \left[((1-\phi) + \beta_{c1}\phi) \nabla^2 \varphi_{sc1} + ((1-\phi) + \beta_{c2}\phi) \nabla^2 \varphi_{sc2} \right]. \quad (6.35)$$

For the solid displacements we can use the expressions of Appendix A with $\varphi = \varphi_{sc1} + \varphi_{sc2}$. For the interface between a porous half-space and a liquid we investigate two sets of boundary conditions, the sealed and the open pore interface.

6.2.2 Lossless porous medium

For the sealed interface the following conditions apply at $z = 0$ (see Chapter 3):

$$\sigma_{zz} + p = p_w, \quad \sigma_{zx} = 0, \quad u_{sz} = u_{fz} = u_{wz}. \quad (6.36)$$

Using these boundary conditions we obtain the following set of equations for the amplitudes of the potentials:

$$\underline{\underline{\mathbf{M}}}(A_{c1} \ A_{c2} \ C_{sh} \ A_2)^T = \underline{\underline{0}}, \quad (6.37)$$

where the matrix $\underline{\underline{\mathbf{M}}}$ contains the following elements:

$$\begin{aligned} M(1, 1) &= \left[(K_b - 2/3G) + \frac{K_f}{\phi} ((1-\phi) + \phi\beta_{c1}) \right] \omega^2/c_1^2 + 2Gk_{zc1}^2, \\ M(1, 2) &= \left[(K_b - 2/3G) + \frac{K_f}{\phi} ((1-\phi) + \phi\beta_{c2}) \right] \omega^2/c_2^2 + 2Gk_{zc2}^2, \\ M(1, 3) &= 2Gk_{zsh}, \\ M(1, 4) &= -\rho_w \omega^2, \end{aligned}$$

$$\begin{aligned} M(2, 1) &= 2kk_{zc1}, \\ M(2, 2) &= 2kk_{zc2}, \\ M(2, 3) &= (-k_{zsh}^2 + k^2), \\ M(2, 4) &= 0, \end{aligned}$$

$$\begin{aligned} M(3, 1) &= -ik_{zc1}, \\ M(3, 2) &= -ik_{zc2}, \\ M(3, 3) &= -ik, \\ M(3, 4) &= -ik_{zw}, \end{aligned}$$

$$\begin{aligned} M(4, 1) &= -\beta_{c1}ik_{zc1}, \\ M(4, 2) &= -\beta_{c2}ik_{zc2}, \\ M(4, 3) &= -\beta_{csh}ik, \\ M(4, 4) &= -ik_{zw}. \end{aligned}$$

The zero's of the determinant of this matrix are determined using our numerical search routine. For this sealed boundary we found one undamped and therefore true surface

wave with a velocity $0.914c_2$ for an interface between water and saturated Bentheimer sandstone, for which the parameters can be found in Appendix E, Table E.1. This new type of surface wave is typical of a porous medium and is present due to the slow compressional wave. Feng and Johnson (1983) were the first to consider this wave type and called it the true Stoneley wave. Experimentally this surface wave was observed by Adler and Nagy (1994). The distributions of the pore pressure and the pressure in the water

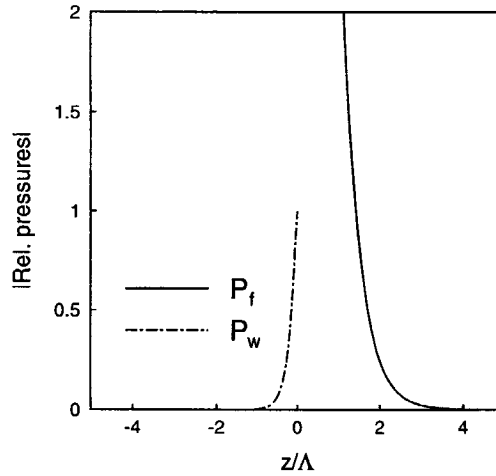


Figure 6.9: Pressure distribution associated with the true Stoneley wave (lossless medium). Pressures are normalized by $p_w|_{z=0}$, and the distances from the surface by the wavelength Λ . The Bentheim/water interface is sealed.

are shown in Fig. 6.9. The pore pressure at the interface differs one order of magnitude with the water pressure at the interface. This is due to the sealing. The pressures show the exponential decay from the surface which is typical of the true surface waves. With the wavelength Λ as a scaling parameter the distribution is frequency-independent.

For a porous medium there exist also pseudo-surface waves. Due to the presence of the slow wave two pseudo-surface waves occur. In agreement with the work of Feng and Johnson (1983), we found a pseudo-surface wave which has a wavenumber k on the Riemann sheet with the following signs:

$$\Im m(k_{zc1}) \leq 0, \Im m(k_{zc2}) \geq 0, \Im m(k_{zcsh}) \leq 0, \Im m(k_{zw}) \geq 0. \quad (6.38)$$

This wave is called the pseudo-Rayleigh wave. Its phase velocity is $0.98c_{sh}$, and therefore comparable with the pseudo-Rayleigh wave for a solid/water interface. The pseudo-Rayleigh wave leaks energy in both the water and the slow compressional wave, and it is damped significantly. The distributions of the pore and water pressure are given in Fig. 6.10. Due to the leakage in both the water and the slow wave the pressures at both sides of the interface increase as we move away from the surface.

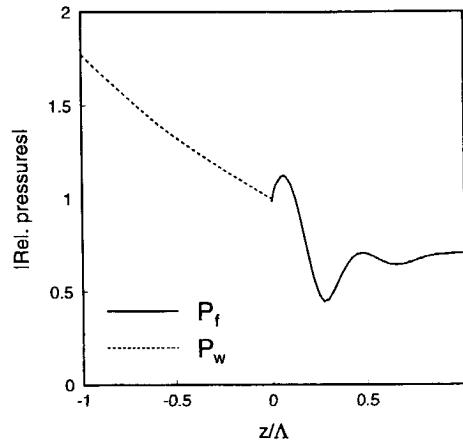


Figure 6.10: Pressure distribution associated with the pseudo-Rayleigh wave (lossless medium). Pressures are normalized by $p_w|_{z=0}$, and the distances from the interface by the wavelength Λ . The Bentheim/water interface is sealed.

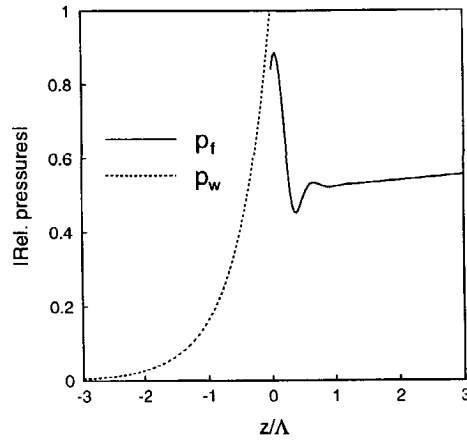


Figure 6.11: Pressure distribution associated with the pseudo-Stoneley wave (lossless medium). Pressures are normalized by $p_w|_{z=0}$, and the distances from the interface by the wavelength Λ . The Bentheim/water interface is sealed.

We found a second pseudo-surface wave with a wavenumber k on the Riemann sheet with the following signs:

$$\Im m(k_{zc1}) \leq 0, \Im m(k_{zc2}) \geq 0, \Im m(k_{zcs}) \leq 0, \Im m(k_{zw}) \leq 0. \quad (6.39)$$

This wave type is called the pseudo-Stoneley wave (Feng and Johnson 1983). Its phase velocity is $0.958c_w$ and therefore comparable with the Stoneley wave for a solid/water interface. However, this pseudo-Stoneley wave is damped significantly, because of its energy leakage into the slow wave. The phase velocity is frequency-independent, while the damping factor $\Im m(k)$ increases as a function of the frequency (see Fig. 6.15(b)). The pressure distribution for the pseudo-Stoneley wave is given in Fig. 6.11. The pore pressure increases slowly as we move away from the interface into the porous solid.

Next, we consider the situation where the pores are not sealed. Then, the following conditions apply at $z = 0$ (see Chapter 3):

$$\sigma_{zz} = 0, p_f = p_w, \sigma_{zx} = 0, \phi u_{sz} + (1 - \phi)u_{fz} = u_{wz}. \quad (6.40)$$

Using these boundary conditions we obtain for the amplitude matrix $\underline{\underline{M}}$ the following elements:

$$\begin{aligned} M(1, 1) &= (K_b - 2/3G)\omega^2/c_1^2 + 2Gk_{zc1}^2, \\ M(1, 2) &= (K_b - 2/3G)\omega^2/c_2^2 + 2Gk_{zc2}^2, \\ M(1, 3) &= 2Gkk_{zsh}, \\ M(1, 4) &= 0, \end{aligned}$$

$$\begin{aligned} M(2, 1) &= 2kk_{zc1}, \\ M(2, 2) &= 2kk_{zc2}, \\ M(2, 3) &= (-k_{zsh}^2 + k^2), \\ M(2, 4) &= 0, \end{aligned}$$

$$\begin{aligned} M(3, 1) &= K_f((1 - \phi) + \phi\beta_{c1})\omega^2/(\phi c_1^2), \\ M(3, 2) &= K_f((1 - \phi) + \phi\beta_{c2})\omega^2/(\phi c_2^2), \\ M(3, 3) &= 0, \\ M(3, 4) &= -\rho_w\omega^2, \end{aligned}$$

$$\begin{aligned} M(4, 1) &= -\phi\beta_{c1}ik_{zc1} - (1 - \phi)ik_{zc1}, \\ M(4, 2) &= -\phi\beta_{c2}ik_{zc2} - (1 - \phi)ik_{zc2}, \\ M(4, 3) &= -\phi\beta_{csh}ik - (1 - \phi)ik, \\ M(4, 4) &= -ik_{zw}. \end{aligned}$$

We found that the pseudo-Rayleigh wave and the pseudo-Stoneley wave still existed, but that the true Stoneley wave on an interface between Bentheimer sandstone and water did no longer exist. This phenomenon is in agreement with the results of Feng and Johnson (1983), who found that the true Stoneley wave exists only for a limited range of parameters of the poroelastic solid and the fluid. Only for sealed conditions the true Stoneley wave exists for arbitrary material properties. This conclusion is confirmed by the experimental results of Adler and Nagy (1994). For the open pore conditions, we found that the phase velocities of the pseudo-Rayleigh and pseudo-Stoneley waves were $0.93c_{sh}$ and $0.97c_w$, respectively.

6.2.3 Lossy media

In case of a lossy poroelastic solid the free-field wavenumbers for the fast, slow, and shear wave become complex-valued, while the free-field wavenumber of the water remains real-valued. This means that both true waves and pseudo-waves are damped. For the lossless medium, we showed in the previous subsection that the true waves were undamped, and that the pseudo waves were damped due to their energy leakage. For a lossy medium the pseudo waves are damped due to a combination of the intrinsic damping of the poroelastic solid and energy leakage. As open pore conditions are applied for our shock tube configuration, we focus in this section on open pore conditions. The true Stoneley wave, however, exists only for the sealed pore condition for our set of rock parameters. Therefore, we apply the sealed pore conditions for the true Stoneley wave. Again, our numerical code is used and the frequency-dependent Biot damping mechanism is incorporated.

In Fig. 6.12(a) the frequency dependence of the phase velocity of the true Stoneley wave is shown, together with the phase velocity of the true Stoneley wave for the lossless medium. The free-field phase velocity of the slow wave is given for comparison. The phase velocities are normalized by the high-frequency limit of the phase velocity of the free-field slow wave. The phase velocity of the true Stoneley wave is lower than the phase velocity of the free-field slow wave over the entire frequency range. Furthermore, we observe that the phase velocity of the true Stoneley wave for the lossy medium is lower than the phase velocity of the true Stoneley wave for the lossless medium. In the high-frequency limit, we found that the velocity of the true Stoneley wave for the lossy medium approaches the velocity of the true Stoneley wave for the lossless medium. In Fig. 6.12(b) the frequency dependence of the damping coefficient of the true Stoneley wave is shown in comparison with the damping of the free-field slow wave. We observe that the damping coefficients of these two waves show the same characteristics. Hence, we conclude that the Biot damping mechanism strongly influences the damping of the true Stoneley wave.

For the pseudo-Rayleigh wave we found two solutions for k that satisfy the boundary conditions. The results for the corresponding phase velocities and damping coefficients are shown in Fig. 6.13. The phase velocities and damping coefficients for the lossless medium are given as a reference. We observe that the phase velocity of one of the two pseudo-Rayleigh waves for the lossy medium converges to the phase velocity of the pseudo-Rayleigh wave for the lossless medium. We studied the k_{zc2} wavenumbers associated with the pseudo-Rayleigh waves, in order to investigate the convergence of these two waves. In the 1-100 kHz frequency range, we found that for the wave indicated by the solid line, k_{zc2} is located in the second quadrant of the k_{zc2} -plane. For the wave indicated by the dashed line, k_{zc2} is located in the fourth quadrant of the k_{zc2} -plane. The k_{zc2} associated with the pseudo-Rayleigh wave for the lossless medium, is located in the first quadrant. In the 1000-10000 kHz frequency range, the results for k_{zc2} are shown in Fig. 6.14.³ We find for the wave indicated by the solid line a transition from the second quadrant of the k_{zc2} -plane to the third quadrant. Therefore, this pseudo-Rayleigh wave is labelled as PR₂₃. For the wave indicated by the dashed line we find a transition from the fourth quadrant to the first quadrant (Fig. 6.14(b)). Consequently, this pseudo-Rayleigh wave is

³Note that Biot's theory does not apply in this frequency range, due to scattering effects. However, the current investigations focus on the mathematical properties of the theory of surface waves in lossy media.

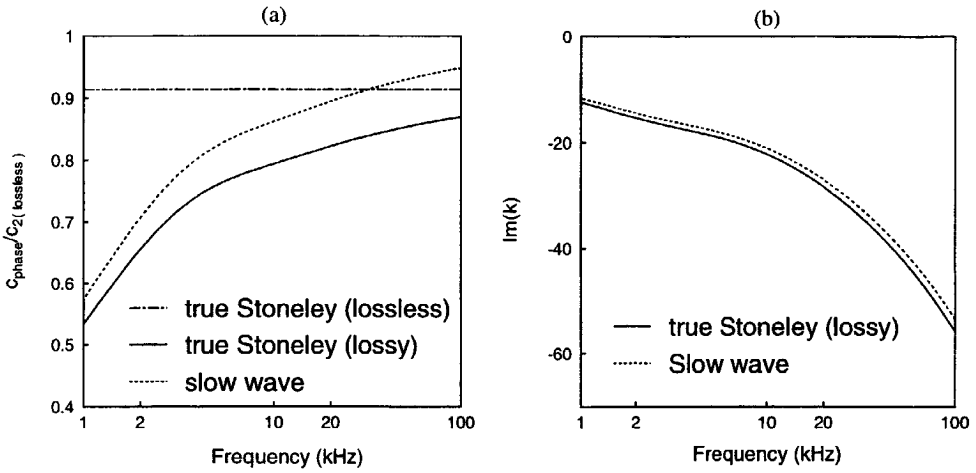


Figure 6.12: Frequency dependence of the phase velocity (a) and damping (b) of the true Stoneley wave for the lossy medium. The solution for the lossless medium is also shown. The Bentheim/water interface is sealed.

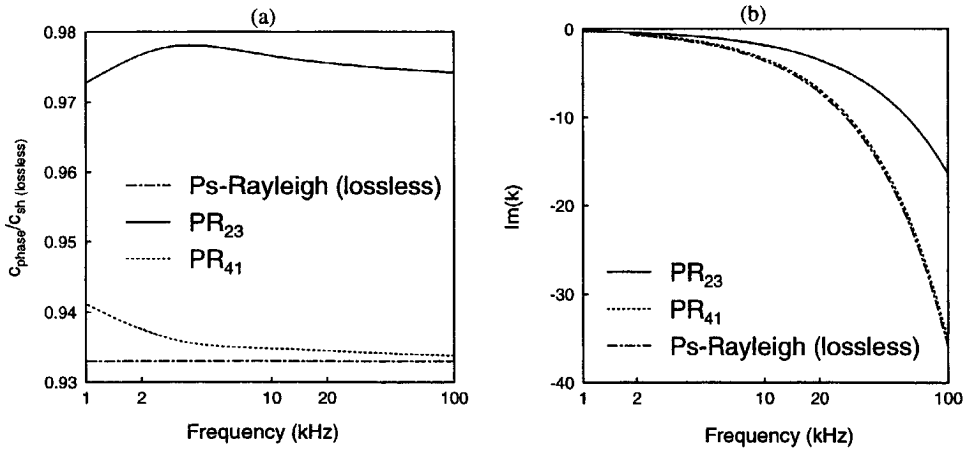


Figure 6.13: Frequency dependence of the phase velocity (a) and damping (b) of the pseudo-Rayleigh wave for the lossy medium. The solution for the lossless medium is also shown. We use open pore conditions for the Bentheim/water interface.

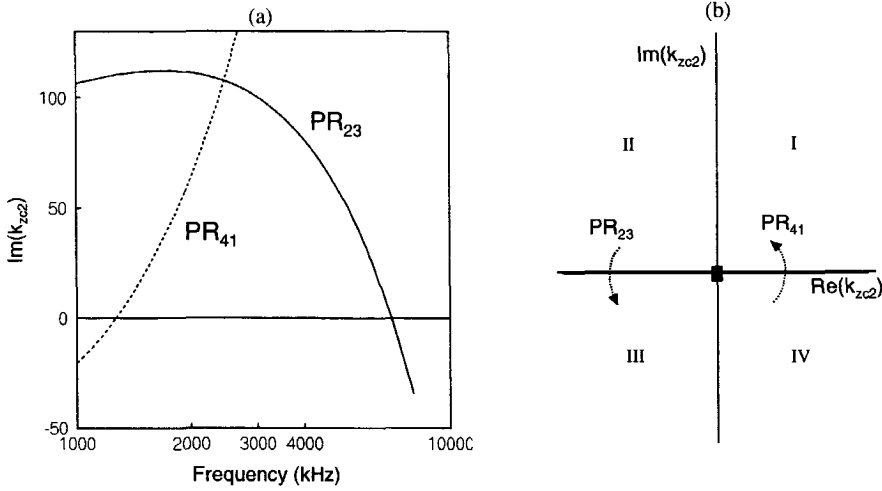


Figure 6.14: Frequency dependence of $\text{Im}(k_{zc2})$ for the pseudo-Rayleigh waves (a). Open pore conditions are used for Benthim/water interface . The complex k_{zc2} plane is given in (b).

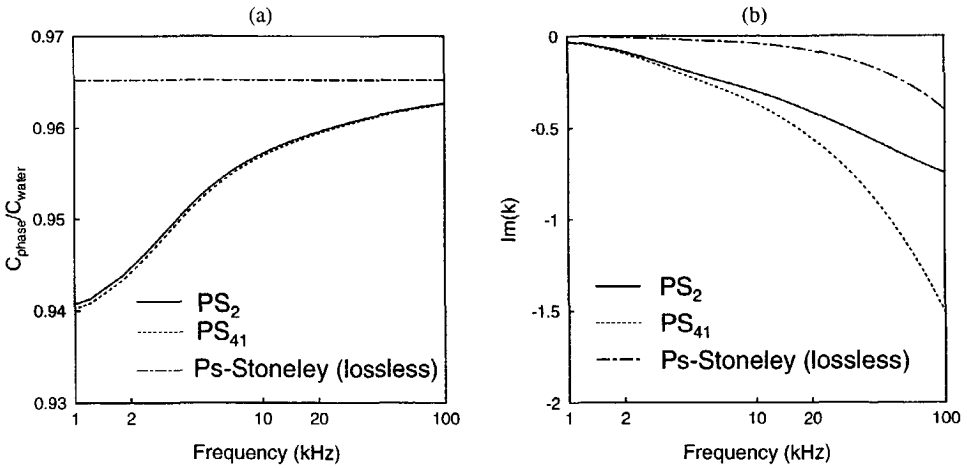


Figure 6.15: Frequency dependence of the phase velocity and damping of the pseudo-Stoneley wave for the lossy medium. The solution for the lossless medium is also shown. Open pore conditions are used for a Benthim/water interface.

labelled as PR_{41} . From this analysis, we conclude that the high-frequency limit of the PR_{41} -wave is equivalent to the pseudo-Rayleigh wave for a lossless medium. The damping of the PR_{41} solution is of the same order as the solution for the lossless medium over the entire frequency range as shown in Fig. 6.13(b). Hence, we conclude that the energy leakage strongly influences the damping of the pseudo-Rayleigh wave. It depends only slightly on the damping of the bulk waves.

For the pseudo-Stoney wave we found also two solutions in the 1-100 kHz frequency range (Fig. 6.15). Again these waves are labelled by the quadrant of k_{zc2} . The pseudo-Stoney wave PS_2 is indicated by the solid line. For wavenumbers k in the fourth quadrant, i.e. for damped waves in the positive x -direction, the corresponding k_{zc2} for this wave is located only in the second quadrant. The pseudo-Stoney wave PS_{41} is indicated by the dashed line. For k in the fourth quadrant, the corresponding k_{zc2} is located in the fourth quadrant of the k_{zc2} -plane at low frequencies. At high frequencies it is located in the first quadrant. The results for the pseudo-Stoney wave for a lossless medium are also given in Fig. 6.15. The phase velocities of the PS_2 -wave and the PS_{41} -wave are nearly equivalent. The damping coefficients, however, differ significantly, but exceed the damping coefficients for the lossless case. Hence, we conclude that both the Biot damping mechanism and the energy leakage contribute to the damping of the pseudo-Stoney wave.

As a summary of the discussion on true and pseudo surface waves Table 6.1 gives an overview of the quadrants of the wavenumbers k_{zc1} , k_{zc2} , and k_{zsh} . The quadrants of the wavenumbers are given for a value of k which is located in the fourth quadrant of the k -plane. The boundary conditions for which the surface waves occur on a Bentheim/water interface are also indicated.

From these discussions it can be concluded that extrapolation of the classical concept of pseudo-waves as developed by Strick (1959) and Phinney (1961b) to lossy media is not straightforward. For a complete description of the pseudo-wave phenomena in lossy media, one needs also to consider the integral transformation from the frequency-wavenumber domain to the time-space domain. This subject is beyond the scope of this thesis and needs to be investigated in the future.

Surface wave type	boundary conditions	quadrant k_{zc1}	quadrant k_{zc2}	quadrant k_{zsh}	quadrant k_{zw}
true Stoneley $c < c_2$ Lossless medium: undamped	sealed	3	3	3	3
pseudo-Stoney $c_2 < c < c_{water}$ Lossless medium: damped	sealed and open pore	3	2 and 4 (LF) \rightarrow 1 (HF)	3	3
pseudo-Rayleigh $c_{water} < c < c_{shear}$ Lossless medium: damped	sealed and open pore	3	2 (LF) \rightarrow 3 (HF) and 4 (LF) \rightarrow 1 (HF)	3	1

Table 6.1: Quadrants of the different wavenumbers, for wavenumbers k which are located in the fourth quadrant. The boundary conditions for which the wave type occurs on a Bentheim/water interface are also indicated.

Chapter 7

Wave modes in elastic cylinders

In this chapter, we discuss the theory of wave modes in elastic solid cylinders. We use this theory to understand the basics of wave propagation in cylindrical configurations. In the next chapter, we combine the theory of wave modes with Biot's theory. Waves in elastic cylinders have been investigated by many authors. The research was started by Pochhammer in 1876, but due to the complexity of the equations it took half a century to obtain computational results. For further details of the historical development we refer to Onoe *et al.* (1962) and Meeker and Meitzler (1964). Experimental data on this subject were provided by Fox *et al.* (1958) and Zemanek (1971). In this chapter we use the system of coordinates as given in Fig. 7.1. Note the difference with the system which we used for flat interfaces, where the z -coordinate is perpendicular to the interface, while now the z -coordinate is parallel to the radial surface of the cylinder. We start with

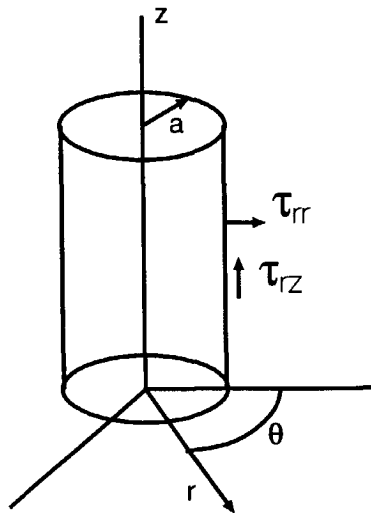


Figure 7.1: Solid elastic cylinder

the derivation of the frequency-wavenumber equation, which is called the Pochhammer equation. Subsequently, we discuss the computational results.

7.1 Pochhammer equation

It appears to be useful for cylindrical configurations to decompose further the vector potential ψ (Miklowitz 1978):

$$\psi = \chi \mathbf{e}_z + \nabla \times (\eta \mathbf{z}), \quad (7.1)$$

where χ and η satisfy

$$\left(\nabla^2 - \frac{1}{c_L^2} \frac{\partial^2}{\partial t^2} \right) \begin{pmatrix} \chi \\ \eta \end{pmatrix} = 0, \quad (7.2)$$

and \mathbf{e}_z is the unit vector along the axial cylindrical coordinate z . Now the scalar potentials φ , χ and η all satisfy a wave equation. We now demonstrate the derivation for the solution of the wave equation for the scalar potential φ . The solutions for the other potentials are similar.

In cylindrical coordinates, a solution for the wave equation can be found by separation of variables. We use a modal harmonic wave propagating in the positive z -direction. The radial and tangential dependence of the potential are modelled by two functions Φ and Θ so that we may write:

$$\varphi = \Phi(r) \Theta(\theta) e^{i(\omega t - kz)}, \quad (7.3)$$

where $\text{Re}(k) > 0$ and $\text{Im}(k) \leq 0$. This expression is substituted in the wave equation for φ :

$$\nabla^2 \varphi - \frac{1}{c_L^2} \frac{\partial^2 \varphi}{\partial t^2} = 0. \quad (7.4)$$

For cylindrical coordinates, as given in Appendix A, we now derive the following equations for Φ and Θ :

$$\frac{d^2 \Phi}{dr^2} + \frac{1}{r} \frac{d\Phi}{dr} + \left(\frac{\omega^2}{c_L^2} - k^2 \right) \Phi - \frac{n^2}{r^2} \Phi = 0, \quad (7.5)$$

and

$$\frac{d^2 \Theta}{d\theta^2} + n^2 \Theta = 0, \quad (7.6)$$

where n is a constant. By substitution of $k_{rc1}^2 = \omega^2/c_L^2 - k^2$ and $\zeta = k_{rc1}r$ in Equation (7.5) we obtain the Bessel equation:

$$\frac{\partial^2 \Phi}{\partial \zeta^2} + \frac{1}{\zeta} \frac{\partial \Phi}{\partial \zeta} + \left(1 - \frac{n^2}{\zeta^2} \right) \Phi = 0. \quad (7.7)$$

The solution of Equation (7.6) is given by:

$$\Theta = e^{\pm i n \theta}. \quad (7.8)$$

Using the condition of continuity for Θ only integer values of n remain. For integer values of n , solutions of the Bessel equation (7.7) are the Bessel functions of the first and the second kind, with argument $k_{rc1}r$. Only Bessel functions of the first kind are taken into account, as the solution for Φ must be finite at $r = 0$. The expression for the scalar potential φ then becomes:

$$\varphi = A_{c1} J_n(k_{rc1}r) e^{i(\omega t - kz)} e^{\pm i n \theta}. \quad (7.9)$$

The solutions for χ and η can be derived in the same way:

$$\chi = B_{c1} J_n(k_{rsh}r) e^{i(\omega t - kz)} e^{\pm i n \theta}, \quad (7.10)$$

$$\eta = C_{sh} J_n(k_{rsh}r) e^{i(\omega t - kz)} e^{\pm i n \theta}, \quad (7.11)$$

where the radial wavenumbers k_{rc1} and k_{rsh} are defined as:

$$k_{rc1} = \sqrt{\frac{\omega^2}{c_L^2} - k^2}, \quad k_{rsh} = \sqrt{\frac{\omega^2}{c_T^2} - k^2}. \quad (7.12)$$

The signs of the square roots are chosen such that $\Im m(k_{rc1}) \leq 0$ and $\Im m(k_{rsh}) \leq 0$. The solutions for the potentials φ , χ , and η show that due to the internal reflections from the radial surface standing wave patterns are formed in the radial direction. In the axial and tangential directions travelling harmonic waves occur.

Due to the normal incidence of waves on the top of the cylinder in our shock tube we only consider axially symmetric waves: $\frac{\partial}{\partial \theta} = 0$, and $u_\theta = 0$. Then, it is sufficient to let $\chi = 0$ and $n = 0$ (see Equation (A.29)). The modal wave propagation is therefore described by the two potentials φ and η in this case:

$$\varphi = A_{c1} J_0(k_{rc1}r) e^{i(\omega t - kz)}, \quad (7.13)$$

$$\eta = C_{sh} J_0(k_{rsh}r) e^{i(\omega t - kz)}. \quad (7.14)$$

The corresponding radial and axial displacements (u_r and u_z) are given in Appendix A. Accordingly, we write:

$$u_r = \frac{\partial \varphi}{\partial r} + \frac{\partial^2 \eta}{\partial z \partial r} = -A_{c1} k_{rc1} J_1(k_{rc1}r) + C_{sh} i k k_{rsh} J_1(k_{rsh}r), \quad (7.15)$$

$$u_z = \frac{\partial \varphi}{\partial z} - \frac{1}{r} \frac{\partial}{\partial r} \left(r \frac{\partial \eta}{\partial r} \right) = -i k A_{c1} J_0(k_{rc1}r) + C_{sh} k_{rsh}^2 J_0(k_{rsh}r). \quad (7.16)$$

Substituting Equations (7.13) and (7.14) in Equations (A.39), (A.41), and (A.43) we can derive that:

$$\begin{aligned} \tau_{rr} = & A_{cl} \left[-\lambda \frac{\omega^2}{c_L^2} J_0(k_{rc1}r) - 2\mu \left(k_{rc1}^2 J_0(k_{rc1}r) - \frac{k_{rc1}}{r} J_1(k_{rc1}r) \right) \right] + \\ & C_{sh} \left[2\mu i k k_{rsh}^2 J_0(k_{rsh}r) - 2\mu i k \frac{k_{rsh}}{r} J_1(k_{rsh}r) \right], \end{aligned} \quad (7.17)$$

$$\tau_{zz} = A_{cl} J_0(k_{rc1}r) \left[-\lambda \frac{\omega^2}{c_L^2} - 2\mu k^2 \right] + C_{sh} J_0(k_{rsh}r) \left[-2\mu i k k_{rsh}^2 \right], \quad (7.18)$$

$$\tau_{rz} = A_{cl} [2ik k_{rc1} J_1(k_{rc1}r)] + C_{sh} [(-k_{rsh}^2 + k^2) k_{rsh} J_1(k_{rsh}r)]. \quad (7.19)$$

It is required that all stresses at $r = a$ vanish:

$$\tau_{rr} = 0, \quad \tau_{r\theta} = 0, \quad \tau_{rz} = 0. \quad (7.20)$$

Due to the axial symmetry the condition $\tau_{r\theta} = 0$ is always satisfied. From Equations (7.17) and (7.19), we obtain for the amplitude coefficients:

$$\underline{\mathbf{M}} (A_{cl} \ C_{sh})^T = \underline{\mathbf{0}}, \quad (7.21)$$

where $\underline{\mathbf{M}} =$

$$\begin{pmatrix} -\frac{1}{2}[k_{rsh}^2 - k^2] J_0(k_{rc1}a) + \frac{k_{rc1}}{a} J_1(k_{rc1}a) & i k k_{rsh}^2 J_0(k_{rsh}a) - \frac{i k k_{rsh}}{a} J_1(k_{rsh}a) \\ 2i k k_{rc1} J_1(k_{rc1}a) & -(k_{rsh}^2 - k^2) k_{rsh} J_1(k_{rsh}a) \end{pmatrix}. \quad (7.22)$$

The requirement that the determinant of coefficients must vanish yields the frequency equation:

$$\begin{aligned} F(\omega, k) = & -\left(\frac{\omega^2}{c_T^2} - 2k^2\right)^2 k_{rsh} J_0(k_{rc1}a) J_1(k_{rsh}a) + \frac{2k_{rc1} k_{rsh}}{a} \left(\frac{\omega^2}{c_T^2}\right) J_1(k_{rsh}a) J_1(k_{rc1}a) \\ & - 4k^2 k_{rsh}^2 k_{rc1} J_1(k_{rc1}a) J_0(k_{rsh}a) = 0. \end{aligned} \quad (7.23)$$

This equation is called the Pochhammer equation. It was first derived by Pochhammer in 1876, and solutions of both damped and undamped waves were given by Onoe *et al.* (1962) and Zemanek *et al.* (1971). We notice that k_{rc1} , $J_0(k_{rc1}r)$ and $J_1(k_{rc1}r)$ only occur in the combinations $k_{rc1}^2 J_0(k_{rc1}r)$ and $k_{rc1} J_1(k_{rc1}r)$. The Besselfunction $J_0(\zeta)$ is the sum of even powers of ζ , while $J_1(\zeta)$ is the sum of odd powers of ζ (see Equation(B.2)). The combinations of wavenumbers and Besselfunctions display therefore only even powers of the radial wavenumber k_{rc1} . This means that discussions on the choice of the sign of the square root in Equation (7.12) can be avoided. The same is valid for the radial wavenumber k_{rsh} .

7.2 Computational results wave modes

As in the case of flat interfaces, we use the numerical code described in Appendix D to determine the zero's of Pochhammer's equation. An important difference with the flat interface computations is the number of zero's at a given frequency. For the flat interface, we found one undamped wave only, but here we find a finite number of undamped waves, and an infinite number of damped waves. These different solutions of the Pochhammer equation are the so-called modes and correspond to the different types of wave motion in the cylinder. Please note that there is a difference with the more general use of the term 'modes' in acoustics, where the 'modes' denote the individual natural resonances of a finite body.

We use two graph types that are well-known in literature (Onoe *et al.* 1962, Zemanek 1971, Achenbach 1973, Miklowitz 1978) to present our solutions. One is for the frequency dependence of the real part of k and the other for the frequency dependence of the imaginary part of k . It is also common to present the former one in a modified way by plotting the phase velocities $\omega/\Re(k)$ versus the frequencies ω . First, we will discuss the results for the undamped modes. Following the conventions of Zemanek (1971), these modes are labelled L modes.

7.2.1 Undamped modes

The results of the calculations are shown in Fig. 7.2(a). On the horizontal axis the real part of the dimensionless wavenumber is shown, while on the vertical axis the dimensionless frequency is given, where a is the radius of the cylinder. Pochhammer's equation is determined uniquely by the variables $\omega a/c_T$, ka , and Poisson's ratio ν (Achenbach 1973). The results are given for $\nu = 0.3$. In Fig. 7.2(b) the same data are presented using the phase velocity of the modes. For reference, we have also given the free-field velocities of the compressional and the shear waves.

In Fig. 7.2 the solutions of the Pochhammer equation in the dashed region ($\omega/c_L < \omega/c_T < \Re(k)$), correspond to surface waves. Considering the square roots given in Equation (7.12), it follows that for $\Im m(k) = 0$ and $\omega/c_L < \omega/c_T < \Re(k)$ the radial wavenumbers k_{rc1} are k_{rsh} are imaginary. Then the Besselfunctions $J_0(i\Im m(k_{rc1})r)$ and $J_0(i\Im m(k_{rsh})r)$ are proportional to $I_0(\Im m(k_{rc1})r)$ and $I_0(\Im m(k_{rsh})r)$, respectively. The latter functions are proportional to exponential functions for large values of r (see Equation (B.11)). Hence, the solutions of the Pochhammer equation in the dashed region correspond to surface waves.

In the high-frequency limit the L1 mode is located in the dashed region, and therefore it is a surface wave. The phase velocity of L1 at high frequencies is equal to the phase velocity of the Rayleigh wave, which was derived in the previous chapter. Because at high frequencies $\Lambda/a \ll 1$, the effect of the curvature of the interface can be neglected. Obviously, this is no longer true for lower frequencies.

We further investigate the physical character of the L1 mode by plotting the radial distributions of the corresponding stresses τ_{rr} , τ_{zz} and τ_{rz} (see Fig. 7.3). Because of the presence of a geometrical length scale in this configuration, we use the radius a of the cylinder as the normalizing parameter. At $\omega a/c_T = 12$ we observe a strong similarity with the stress distributions of the Rayleigh wave as given in Fig. 6.2. For $\omega a/c_T = 0.12$ the

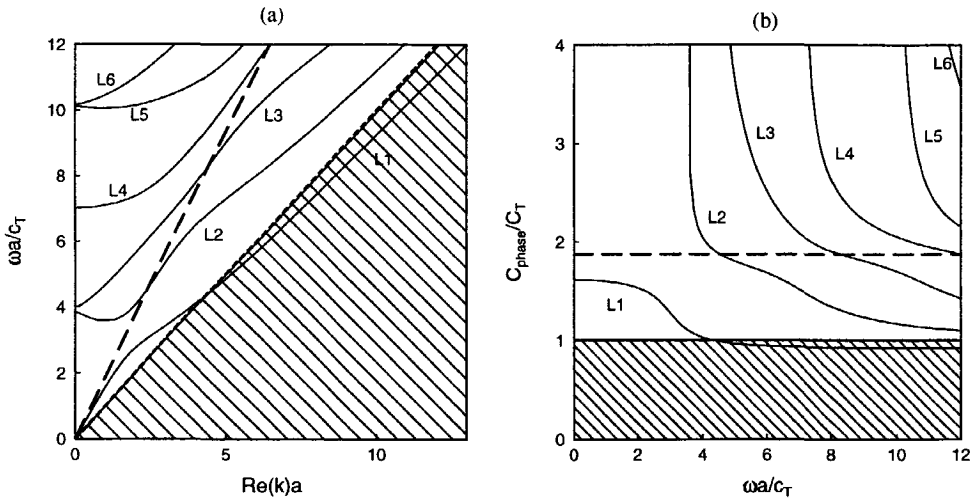


Figure 7.2: Frequency dependence of the $\text{Re}(k)$ (a) and phase velocity (b) of the undamped modes. Note that both graphs represent the same data of an elastic cylinder with $\nu = 0.3$. Dashed line: $\omega = c_L \text{Re}(k)$. Shaded region: $\omega/c_T < \text{Re}(k)$.

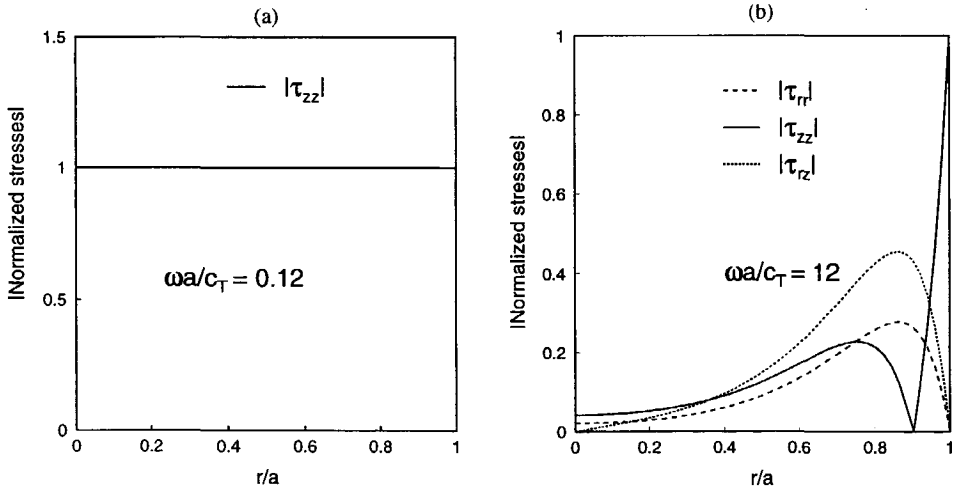


Figure 7.3: Radial distribution of the stress components of mode L1 at $\omega a/c_T = 0.12$ (a) and $\omega a/c_T = 12$ (b). The stress components are normalized using the value of τ_{zz} at $r = a$ at that particular frequency. The radius is normalized by the radius of the cylinder a .

distribution of τ_{zz} is flat. The shear stress τ_{rz} and the radial stress τ_{rr} differ one order in magnitude with the axial stress component τ_{zz} and are therefore not visible in Fig. 7.3(a). The low-frequency limit can thus be characterized by one-dimensional longitudinal stress, contrary to the free-field situation which is characterized by a one-dimensional longitudinal strain. In cartesian coordinates the stress τ_{zz} and ϵ_{zz} are related for the longitudinal stress ($\tau_{xx} = 0$ and $\tau_{yy} = 0$) by

$$\tau_{zz} = E\epsilon_{zz}, \quad (7.24)$$

where E is the Young's modulus:

$$E = \frac{\mu(3\lambda + 2\mu)}{\mu + \lambda}. \quad (7.25)$$

The low-frequency limit of the phase velocity for the L1 mode is equal to $\sqrt{E/\rho}$. It is called the 'bar' velocity, and is often used as an approximate model for thin rods.

The higher-order modes L2,..., L6 are characterized by the high-frequency limit of the phase velocity, which is the free-field shear velocity. At lower frequencies they show a so-called cut-off behaviour. At the cut-off frequencies these modes are non-propagating, which means that the axial wavenumber is equal to zero. This also means that the radial wavenumber is equal to the free-field wavenumber. The cut-off frequencies of the modes can be obtained from Equation (7.23), where $k = 0$:

$$J_1\left(\frac{\omega a}{c_T}\right) \left[\frac{\omega a}{c_T} J_0\left(\frac{\omega a}{c_L}\right) - 2\frac{c_T}{c_L} J_1\left(\frac{\omega a}{c_L}\right) \right] = 0. \quad (7.26)$$

Using this equation two classes of cut-off modes can be discerned. The first one satisfies $J_1(\omega a/c_T) = 0$, while for the second one the term between the square brackets is zero. We found that the L2, L4 and L6 modes belong to the first class, and the L3 and L5 modes to the second. These classes display different physical phenomena as illustrated in the plots of the stress components near the cut-off frequency. Fig. 7.4(a) shows that for the L2 mode τ_{rz} is the dominant stress component. This behaviour is also observed for the L4 mode. When the radial and axial displacements are plotted (Zemanek 1971), it is observed that the axial displacement is dominant. Therefore, this mode class is also called the axial shear mode (Onoe *et al.* 1962, Zemanek 1971). Fig. 7.5(a) gives the radial distributions of the stresses for the L3 mode near the cut-off frequency. In this case τ_{rz} is one order lower than τ_{rr} and τ_{zz} . This difference in order of τ_{rz} is also observed for the L5 mode. Compared to the axial displacement the radial displacement is dominant (Zemanek 1971). The L3 and L5 modes are therefore called the radial modes. At high frequencies this distinction between the mode classes disappears. As an example, the three stress components of L2 are plotted in Fig. 7.4(b) for $\omega a/c_T = 12$. The three stress components are of equal importance for this mode. For the L3 mode the shear stress component τ_{rz} is still small at high frequencies (see Fig. 7.5(b)).

Near the cut-off frequencies several interesting phenomena occur. The phase velocities reach an infinite value. However, it must be noted that the so-called 'group' velocity, which corresponds to the velocity of energy transmission (Miklowitz 1978), remains finite. The group velocity is defined as:

$$c_{gr} = \frac{d\omega}{dk}, \quad (7.27)$$

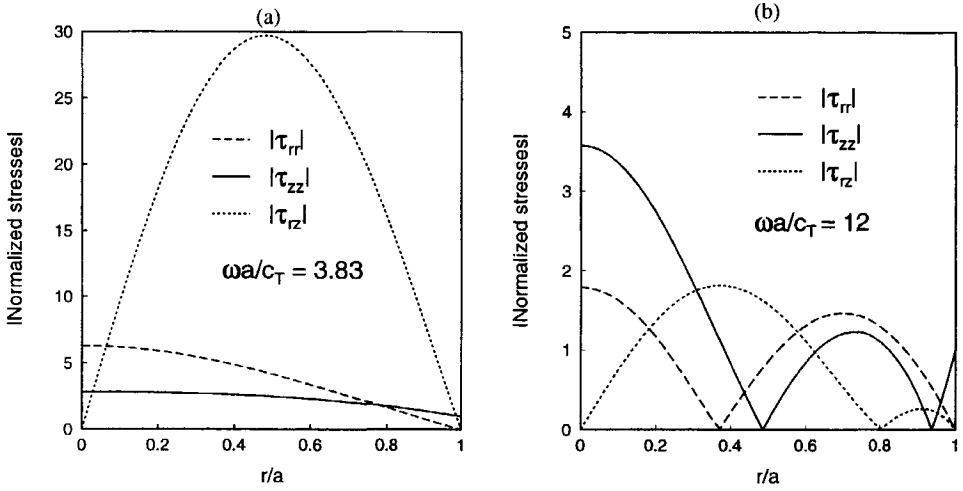


Figure 7.4: Radial distribution of the stress components of mode L2 at $\omega a/c_T = 3.83$ (a) and $\omega a/c_T = 12$ (b). Stresses have been normalized with respect to the axial stress component $\tau_{zz}|_{r=a}$. The radius is normalized by the radius of the cylinder a . Note the different scales on the vertical axes in (a) and (b).

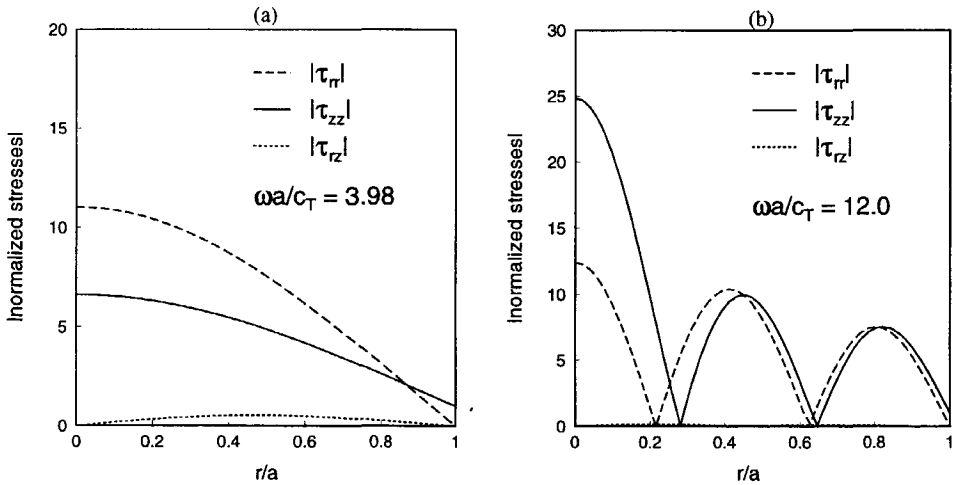


Figure 7.5: Radial distribution of the stress components of mode L3 at $\omega a/c_T = 3.98$ (a) and $\omega a/c_T = 12$ (b). Stresses have been normalized with respect to the axial stress component $\tau_{zz}|_{r=a}$. The radius is normalized by the radius of the cylinder a . Note the different scales on the vertical axes in (a) and (b).

and corresponds to the slope of the curves given in Fig. 7.2(a). It is clear from this graph that the group velocities of the presented modes are lower than the free-field velocity of the compressional wave. Furthermore, we observe that the group velocity of the L2 mode shows an interesting behaviour. Below $\Re(k)a = 1$, the slope of the curve in Fig. 7.2 is negative and corresponds therefore to a negative group velocity while the phase velocity is positive. This means that the energy is transported in the direction opposite to the direction of propagation. For a further discussion on this so-called backward-wave transmission phenomenon the reader is referred to the work of Meitzler (1965).

7.2.2 Damped modes

We now discuss the damped wave modes, for which $\Re(k)a$ and $\Im m(k)a$ are given in Fig. 7.6 as a function of the frequency $\omega a/c_T$. We present these results in one graph, as the $\Re(k)$ -plane and the $\Im m(k)$ -plane are projections of the complex k -plane. As a reference, we also have given the solution for the undamped waves, which are indicated by the solid lines. The solutions for the damped waves are indicated by pairs of dashed lines: one in the $\Re(k)$ -plane, and one in the $\Im m(k)$ -plane. We also have found a mode which does not propagate, i.e., $\Re(k) = 0$. This mode is indicated by the solid-cross line, and labelled Z1. The labels of the damped modes are based on the frequency range for which they exist. The C modes start at a frequency equal to zero, and for higher frequencies, they continue until they join an undamped mode or the Z1 mode. The I modes start at the Z1 mode, and continue until they join the Z2 mode (not shown in Fig. 7.6).

The C, I, and Z modes play an important role for cylinders with finite length (Zemanek 1971). A way to study an impact in the z -direction on a cylinder of finite length is to express the stress condition at the boundary of impact as a sum of the stresses associated with the L, C, I, and Z modes. This method only works if the sum converges and provided that the set of particular modes is complete. At the boundary of impact one can prescribe one single stress component and one single displacement component. This is a set of so-called mixed boundary conditions. For pure boundary conditions one prescribes two stress components. For mixed boundary conditions the impact on a cylinder has been studied by several authors (Skalak 1957, Folk *et al.* 1958, Kaul and McCoy 1964, McKenna and Simpkins 1985, Wilson 1986, Herczynski and Folk 1989). However, for pure boundary conditions it is not known how to solve the impact problem analytically (McKenna and Simpkins 1985, Herczynski and Folk 1989).

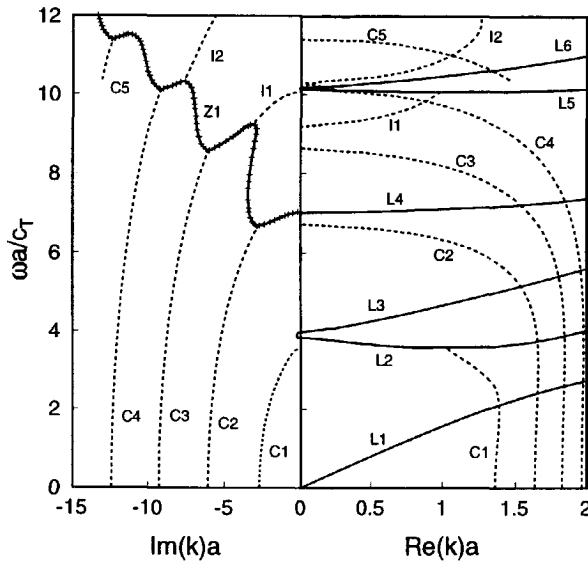


Figure 7.6: Modes of an elastic cylinder in the complex plane. The solid lines correspond to the L modes of Fig. 7.2(a). The pairs of dashed lines correspond to the imaginary and real part of k . The computations were performed for an elastic cylinder with $\nu = 0.3$.

Chapter 8

Wave modes in the shock tube

In this chapter we discuss the application of the wave mode theory to the shock tube configuration. We investigate both the large gap and the small gap configuration for Bentheimer sandstone, which is a fast formation. The influence of permeability and shear modulus on the phase velocities and damping coefficients is studied afterwards. The last topic of the chapter is the modelling of a slow formation. We start with computations where the influence of the wall of the shock tube is neglected.

8.1 Rigid shock tube wall

Wave motion in the porous cylinder is described using the potentials as given in Chapter 3 and the wave mode theory for the elastic cylinder as described in Chapter 6. The eigen vectors φ_{c1} and φ_{c2} in Equation (3.9) satisfy the wave equation with respect to the complex-valued velocities of the fast and slow wave, respectively. The vector potential of the shear wave ψ_s in Equations (3.18) and (3.19) satisfies the wave equation with respect to the (complex-valued) shear wave velocity. The wave motion in the water-filled gap is also described using potentials. The configuration is given in Fig. 8.1. A porous cylinder with a radius a is within a shock tube with inner radius b . Boundary conditions are indicated.

8.1.1 Frequency-wavenumber equation

Similar to Equation (7.13), we can derive for the potentials φ_{c1} and φ_{c2} :

$$\varphi_{sc1} = A_{c1} J_0(k_{rc1} r) e^{i(\omega t - kz)}, \quad (8.1)$$

and

$$\varphi_{sc2} = A_{c2} J_0(k_{rc2} r) e^{i(\omega t - kz)}. \quad (8.2)$$

For the porous cylinder we also apply the decomposition described in Equation (7.1). For the shear wave potential we write (see Equation (7.14)):

$$\eta_{sh} = C_{sh} J_0(k_{rsh} r) e^{i(\omega t - kz)}. \quad (8.3)$$

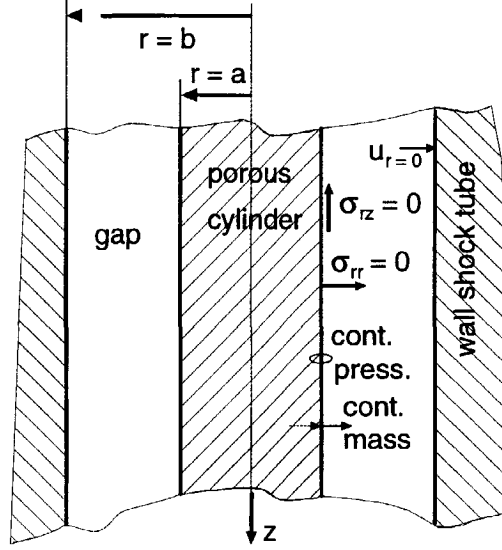


Figure 8.1: Porous cylinder in shock tube

The radial wavenumbers are defined by

$$k_{rc1} = \sqrt{\frac{\omega^2}{c_1^2} - k^2}, \quad k_{rc2} = \sqrt{\frac{\omega^2}{c_2^2} - k^2}, \quad k_{rsh} = \sqrt{\frac{\omega^2}{c_{sh}^2} - k^2}, \quad (8.4)$$

with $\Im m(k_{rc1}) \leq 0$, $\Im m(k_{rc2}) \leq 0$, and $\Im m(k_{rsh}) \leq 0$. As we did in Section 7.1, we write for the solid velocities, omitting the $e^{i(\omega t - kx)}$ dependence:

$$u_{sr} = -A_{c1}k_{rc1}J_1(k_{rc1}r) - A_{c2}k_{rc2}J_1(k_{rc2}r) + C_{sh}ik_{rsh}J_1(k_{rsh}r), \quad (8.5)$$

$$u_{sz} = -ikA_{c1}J_0(k_{rc1}r) - ikA_{c2}J_0(k_{rc2}r) + C_{sh}k_{rsh}^2J_0(k_{rsh}r). \quad (8.6)$$

The fluid displacements are given by

$$u_{fr} = -A_{c1}\beta_{c1}k_{rc1}J_1(k_{rc1}r) - A_{c2}\beta_{c2}k_{rc2}J_1(k_{rc2}r) + C_{sh}\beta_{csh}ik_{rsh}J_1(k_{rsh}r), \quad (8.7)$$

$$u_{fz} = -ik\beta_{c1}A_{c1}J_0(k_{rc1}r) - ik\beta_{c2}A_{c2}J_0(k_{rc2}r) + C_{sh}\beta_{csh}k_{rsh}^2J_0(k_{rsh}r). \quad (8.8)$$

The relations for the intergranular stresses, including the compressibility of the grains, can be derived from Equation (2.16) with $e_{kk} = \nabla^2\varphi_{sc1} + \nabla^2\varphi_{sc2}$ and $\epsilon_{kk} = \nabla^2(\beta_{c1}\varphi_{sc1} + \beta_{c2}\varphi_{sc2})$. Hence, we write for the radial component σ_{rr} with $P = A + 2G$:

$$\sigma_{rr} = - \left[P - 2G - \frac{(1-\phi)Q}{\phi} \right] \nabla^2\varphi_s - \left[Q - \frac{(1-\phi)R}{\phi} \right] \nabla^2\varphi_f - 2G \left[\frac{\partial^2\varphi_s}{\partial r^2} - \frac{\partial^3\eta}{\partial z\partial r^2} \right], \quad (8.9)$$

where $\varphi_s = \varphi_{sc1} + \varphi_{sc2}$ and $\varphi_f = \varphi_{fc1} + \varphi_{fc2}$. Using $\varphi_{fc1} = \beta_{c1}\varphi_{sc1}$ and $\varphi_{fc2} = \beta_{c2}\varphi_{sc2}$ we obtain:

$$\sigma_{rr} = -\Lambda_{c1}\nabla^2\varphi_{sc1} - \Lambda_{c2}\nabla^2\varphi_{sc2} - 2G\left[\frac{\partial^2\varphi_s}{\partial r^2} - \frac{\partial^3\eta_{sh}}{\partial z\partial r^2}\right], \quad (8.10)$$

where

$$\Lambda_{c1} = P - 2G - \frac{(1-\phi)Q}{\phi} + Q\beta_{c1} - \frac{(1-\phi)R\beta_{c1}}{\phi}, \quad (8.11)$$

and

$$\Lambda_{c2} = P - 2G - \frac{(1-\phi)Q}{\phi} + Q\beta_{c2} - \frac{(1-\phi)R\beta_{c2}}{\phi}. \quad (8.12)$$

For the incompressible-grain approximation we simply obtain that $\Lambda_{c1} = \Lambda_{c2} = (K_b - 2/3G)$. We substitute the Equations (8.1), (8.2), and (8.3) in Equation (8.10), and we write:

$$\begin{aligned} \sigma_{rr} = & A_{c1} \left[\Lambda_{c1} \frac{\omega^2}{c_1^2} J_0(k_{rc1}r) + 2G \left(k_{rc1}^2 J_0(k_{rc1}r) - \frac{k_{rc1}}{r} J_1(k_{rc1}r) \right) \right] + \\ & A_{c2} \left[\Lambda_{c2} \frac{\omega^2}{c_2^2} J_0(k_{rc2}r) + 2G \left(k_{rc2}^2 J_0(k_{rc2}r) - \frac{k_{rc2}}{r} J_1(k_{rc2}r) \right) \right] + \\ & C_{sh} \left[-2Gik k_{rsh}^2 J_0(k_{rsh}r) + 2Gik \frac{k_{rsh}}{r} J_1(k_{rsh}r) \right]. \end{aligned} \quad (8.13)$$

For the axial stress component σ_{zz} we can derive that:

$$\begin{aligned} \sigma_{zz} = & A_{c1} J_0(k_{rc1}r) \left[\Lambda_{c1} \frac{\omega^2}{c_1^2} + 2Gk^2 \right] + A_{c2} J_0(k_{rc2}r) \left[\Lambda_{c2} \frac{\omega^2}{c_2^2} + 2Gk^2 \right] + \\ & C_{sh} J_0(k_{rsh}r) \left[2Gik k_{rsh}^2 \right]. \end{aligned} \quad (8.14)$$

For σ_{rz} we obtain:

$$\begin{aligned} \sigma_{rz} = & A_{c1} [-2ikk_{rc1} J_1(k_{rc1}r)] + A_{c2} [-2ikk_{rc2} J_1(k_{rc2}r)] + \\ & C_{sh} [-(k_{rsh}^2 + k^2)k_{rsh} J_1(k_{rsh}r)]. \end{aligned} \quad (8.15)$$

Using Equation (2.15), we can write for the pore pressure:

$$p_p = -\frac{1}{\phi} \left[Q\nabla^2\varphi_s + R\nabla^2\varphi_f \right], \quad (8.16)$$

where $\varphi_s = \varphi_{sc1} + \varphi_{sc2}$, $\varphi_f = \varphi_{fc1} + \varphi_{fc2}$, $\varphi_{fc1} = \beta_{c1}\varphi_{sc1}$, and $\varphi_{fc2} = \beta_{c2}\varphi_{sc2}$. Subsequently, we substitute Equations (8.1) and (8.2) in Equation (8.16), and the pore pressure is given by:

$$p_p = A_{c1} \left[\frac{\omega^2}{c_1^2} \frac{1}{\phi} J_0(k_{rc1}r) (Q + \beta_{c1}R) \right] + A_{c2} \left[\frac{\omega^2}{c_2^2} \frac{1}{\phi} J_0(k_{rc2}r) (Q + \beta_{c2}R) \right]. \quad (8.17)$$

The wave motion in the water-filled gap is described by the wave equation of water. Hence, we can derive the potential of the water-filled gap:

$$\varphi_w = (B_2 Y_0(k_{rw}r) + A_2 J_0(k_{rw}r))e^{i(\omega t - kz)}, \quad (8.18)$$

where the Bessel function of the second kind Y_0 is included, and

$$k_{rw} = \sqrt{\frac{\omega^2}{c_w^2} - k^2}, \quad (8.19)$$

with $\Im m(k_{rw}) \leq 0$. For the pressure in the liquid we write

$$p_w = \rho_w \omega^2 \varphi_w, \quad (8.20)$$

and for the radial water displacement :

$$u_{wr} = \frac{\partial \varphi_w}{\partial r} = -k_{rw} B_w Y_1(k_{rw}r) - k_{rw} A_w J_1(k_{rw}r), \quad (8.21)$$

where the $e^{i(\omega t - kz)}$ dependence has been omitted again. At $r = a$ we apply the open-pore boundary conditions as given in Chapter 3, while at $r = b$ the radial displacement of the water is assumed to be zero. Hence, we obtain the following boundary conditions:

- at $r = a$: $\sigma_{rr} = 0$, $\sigma_{rz} = 0$, $(1 - \phi)u_{sr} + \phi u_{fr} = u_{rw}$, $p = p_w$,
- at $r = b$: $u_{r2} = 0$.

Using the expressions for the displacements and stresses as given previously, we write for the five unknown amplitudes:

$$\underline{\mathbf{M}} (A_{c1} \ A_{c2} \ C_{sh} \ B_w \ A_w)^T = \underline{\mathbf{0}}, \quad (8.22)$$

where

$$M(1, 1) = \Lambda_{c1} \left(\frac{\omega^2}{c_1^2} \right) J_0(k_{rc1}a) + 2G(k_{rc1}(k_{rc1}J_0(k_{rc1}a) - \frac{1}{a}J_1(k_{rc1}a))),$$

$$M(1, 2) = \Lambda_{c2} \left(\frac{\omega^2}{c_2^2} \right) J_0(k_{rc2}a) + 2G(k_{rc2}(k_{rc2}J_0(k_{rc2}a) - \frac{1}{a}J_1(k_{rc2}a))),$$

$$M(1, 3) = -2Gikk_{rsh}(k_{rsh}J_0(k_{rsh}a) - \frac{1}{a}J_1(k_{rsh}a)),$$

$$M(1, 4) = 0,$$

$$M(1, 5) = 0,$$

$$M(2, 1) = -2ikk_{rc1}J_1(k_{rc1}a),$$

$$M(2, 2) = -2ikk_{rc2}J_1(k_{rc2}a),$$

$$M(2, 3) = -k_{rsh}(k^2 - k_{rsh}^2)J_1(k_{rsh}a),$$

$$M(2, 4) = 0,$$

$$M(2, 5) = 0,$$

$$M(3, 1) = ((\phi - 1) - \beta_{c1}\phi)k_{rc1}J_1(k_{rc1}a),$$

$$M(3, 2) = ((\phi - 1) - \beta_{c2}\phi)k_{rc2}J_1(k_{rc2}a),$$

$$M(3, 3) = ((1 - \phi) + \beta_{sh}\phi)ikk_{rsh}J_1(k_{rsh}a),$$

$$M(3, 4) = k_{rw}Y_1(k_{rw}a),$$

$$M(3, 5) = k_{rw}J_1(k_{rw}a),$$

$$M(4, 1) = \frac{1}{\phi} \left(\frac{\omega^2}{c_1^2} \right) J_0(k_{rc1}a)(Q + R\beta_{c1}),$$

$$M(4, 2) = \frac{1}{\phi} \left(\frac{\omega^2}{c_2^2} \right) J_0(k_{rc2}a)(Q + R\beta_{c2}),$$

$$M(4, 3) = 0,$$

$$M(4, 4) = -\rho_w \omega^2 Y_0(k_{rw}a),$$

$$M(4, 5) = -\rho_w \omega^2 J_0(k_{rw}a),$$

$$M(5, 1) = 0,$$

$$M(5, 2) = 0,$$

$$M(5, 3) = 0,$$

$$M(5, 4) = -k_{rw} Y_1(k_{rw}b),$$

$$M(5, 5) = -k_{rw} J_1(k_{rw}b).$$

The matrix elements show only combinations of $J_0(k_{rj}r)$, $k_{rj}^2 J_0(k_{rj}r)$, and $k_{rj} J_1(k_{rj}r)$, where $j = c1, c2, csh$. These combinations are even functions of the corresponding radial wavenumbers and therefore the choice of the Riemann sheet is arbitrary. The Neumann functions $Y_0(x)$ and $Y_1(x)$ are neither an odd nor an even function of x . However, $Y_0(-x)$ can be written as the sum of $Y_0(x)$ and $J_0(x)$ (see Equation(B.5)). Hence, the final result of the potential φ_w as given by Equation (8.18) is not influenced by the sign of k_{rw} , and the choice of the Riemann sheet for the radial wavenumber k_{rw} is arbitrary. The only relevant cut is the branch cut of the functions Y_0 and Y_1 : $|\arg(k_{rw}r)| = \pi$. Passing this cut can be avoided by using $\Im m(k_{rw}) \leq 0$ or $\Im m(k_{rw}) \geq 0$.

8.1.2 Computational results

The computational results were obtained by our Newton-Raphson based search routine, which is described in Appendix D. Some of the modes which we found show similarities with the L, C, and I modes of the elastic cylinders, and consequently these modes are labelled L, C, and I. Furthermore, we found a surface mode, which will be denoted S. Due to the presence of the Biot's slow wave in the porous cylinder an extra class of modes occurs, which is denoted D. Because of the complexity of the complete mode pattern we present the results in separate figures. First, we discuss the L and S modes, which are characterized by a relatively low damping factor. These results are shown in Fig. 8.2, while the results for the C, I, and D modes are shown in Figs. 8.14 and 8.15. The computations were performed for water-saturated Bentheimer sandstone, with a diameter of 70.0 mm, i.e., $a = 0.909b$. The compressibility of the grains was not taken into account. Parameter values are given in Table E.1.

L and S modes

We present the data for the L and S modes in the same way as we did for the elastic case, but for later comparison with our experimental results, we use the frequency instead of

the dimensionless parameter $\omega a/c_T$. In Fig. 8.2(a) we plot the frequency versus the real part of k , while in Fig. 8.2(b) the frequency dependence of the phase velocities is given. We normalized $\Re(k)$ by the inner radius of the shock tube b , while the phase velocities

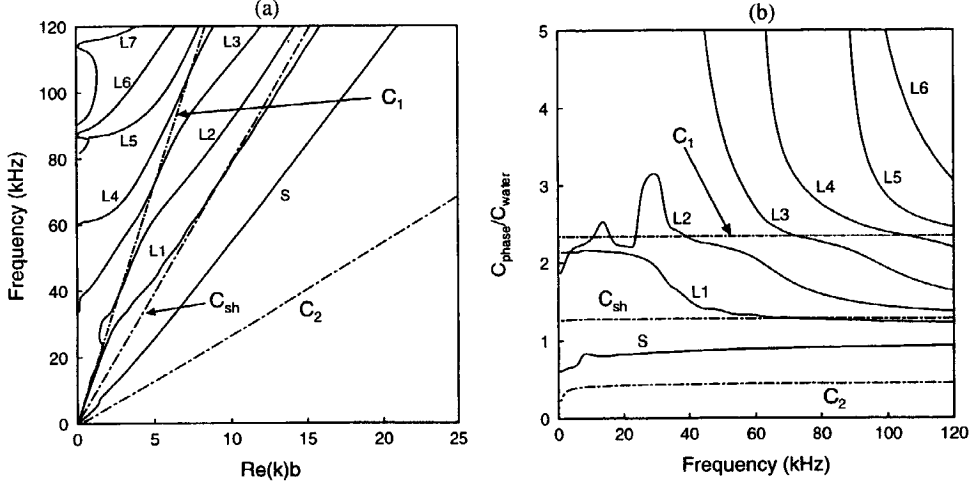


Figure 8.2: Frequency dependence of $\Re(k)$ (a) and the phase velocity (b) for the L and S modes. The wavenumber is normalized by the inner radius of the shock tube b , the phase velocity by the sound velocity of water. The free-field solutions for the fast (C_1), the slow (C_2), and the shear wave (C_{sh}) are also given. The computations are performed for a Bentheimer sandstone cylinder with a diameter of 70.0 mm. Note that the full computational results are presented in three figures. The C and I modes are shown in Fig. 8.14, while the D modes are shown in Fig. 8.15.

are normalized by the sound velocity of water. For comparison, we have also given the free-field solutions for the fast, slow, and shear wave, denoted by C_1 , C_2 , and C_{sh} .

The L_1 and L_2 modes have a finite phase velocity over the entire frequency range, while the higher-order L modes are cut off below a certain frequency. The L modes in Fig. 8.2 show strong similarities with the results of Fig. 7.2, where we observed one mode which propagated over the entire frequency range, while the other modes were cut off below a certain frequency. There is, however, an important difference with the case of elastic cylinders. The L_1 mode for the elastic cylinder is undamped over the entire frequency range, and the higher-order L modes are undamped above the cut-off frequency. Below the cut-off frequency they join the strongly damped C and I modes. For the porous material however, the fast, slow, and shear waves are damped, and consequently, all the L modes are damped over the entire frequency range. The damping coefficients of the L_1 mode over the entire frequency range, and of the higher-order L modes above the cut-off frequency are low, i.e., $\Im m(k)b < 1$. The behaviour of the L_2 mode is somewhat ambiguous, as the phase velocity is limited below 30 kHz (see Fig. 8.2), while the damping coefficient is high.

We now focus on the analysis of the S , L_1 and L_2 modes. For these modes we study the low-frequency and the high-frequency limits of the phase velocities and damping

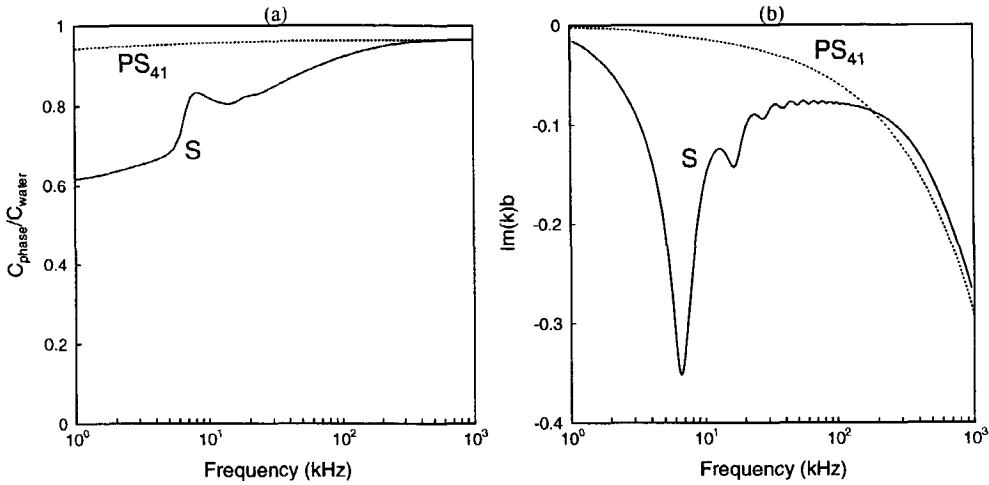


Figure 8.3: Frequency dependence of the phase velocity (a) and damping (b) for the *S* mode in the 1-1000 kHz frequency range. The results for the pseudo-Stoneley wave for a flat interface are also shown. The computations are performed for a Bentheimer sandstone cylinder with a diameter of 70.0 mm. Parameter values are given in Table E.1.

coefficients, as well as the radial distributions of the stresses and pressures. Fig. 8.3 shows the frequency dependence of the phase velocity and the damping coefficient of the *S* mode in the 1-1000 kHz frequency range. In this figure the pseudo-Stoneley wave PS_{41} for a flat interface is also shown. The properties of this wave type are discussed in Chapter 6. From Fig. 8.3 we observe that the *S* mode is equivalent to the pseudo-Stoneley wave in the high-frequency range. Both the phase velocities and the damping coefficients are nearly identical. At high frequencies the wavelength Λ is small, and hence the *S* mode has a small penetration depth, related to both the liquid-filled gap and radius of the cylinder. Thus, the interface of the cylinder can be considered flat. At lower frequencies the *S* mode is influenced by the curvatures of the porous cylinder and of the wall of the shock tube.

The figures 8.4-8.7 show the radial distributions of the stresses and pressures for the *S* mode at several frequencies in the 1-120 kHz frequency range. This frequency range is relevant for our experimental results as will be demonstrated in Chapter 10. The stresses and pressures are normalized by the pore pressures at the radial surface of the porous cylinder $r = a$. From Figs. 8.4 and 8.5 we observe that the typical behaviour of the surface wave is present at 60 and 120 kHz. The pressure oscillations near $r = 0$ are due to the slow wave. As the frequency is lowered, the pressure peak at the wall becomes broader, and the surface wave character disappears. This is illustrated in Fig. 8.6 where bulk type behaviour is dominant. For a frequency of 0.6 kHz, we observe a longitudinal stress situation (Fig. 8.7). This means that there is a uniform distribution of σ_{zz} over the width of the cylinder, and that σ_{rr} becomes zero. Summarizing, we may say that the *S* mode is associated with a surface wave at high frequencies, while it corresponds to a bulk wave type at low frequencies. Note that this is similar to the corresponding mode in a borehole, which is associated with the so-called 'water-hammer' at low frequencies and

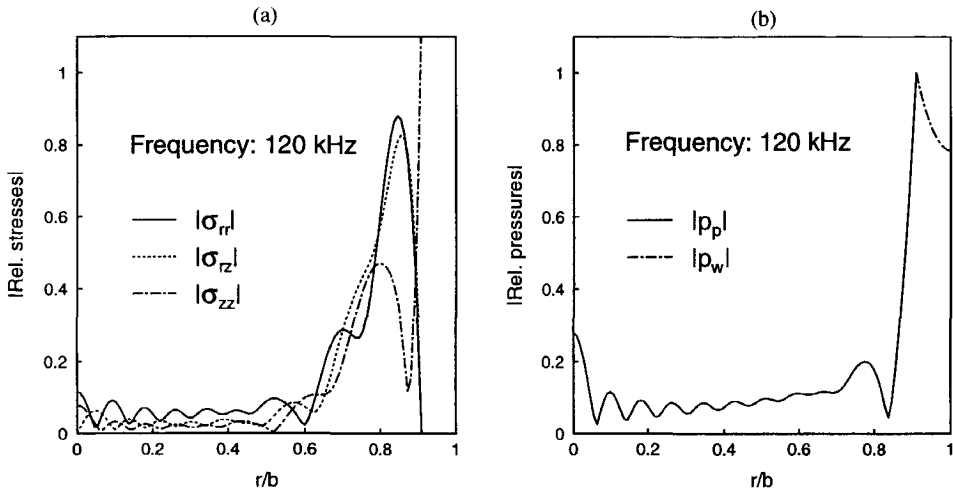


Figure 8.4: Radial distributions of the stresses (a) and pressures (b) for the S mode at 120 kHz. Both the stresses and pressures were normalized by $p_p|_{r=a}$. The calculations were performed for a Benthem cylinder with a diameter of 70.0 mm ($a = 0.909b$). The pores at the boundary were open.

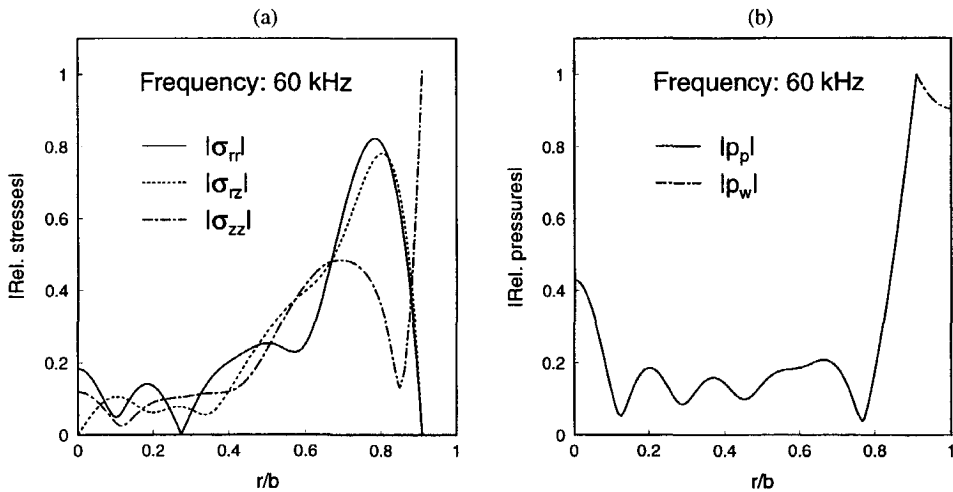


Figure 8.5: Radial distributions of the stresses (a) and pressures (b) for the S mode at 60 kHz. Both the stresses and pressures were normalized by $p_p|_{r=a}$. The calculations were performed for a Benthem cylinder with a diameter of 70.0 mm ($a = 0.909b$). The pores at the boundary were open.

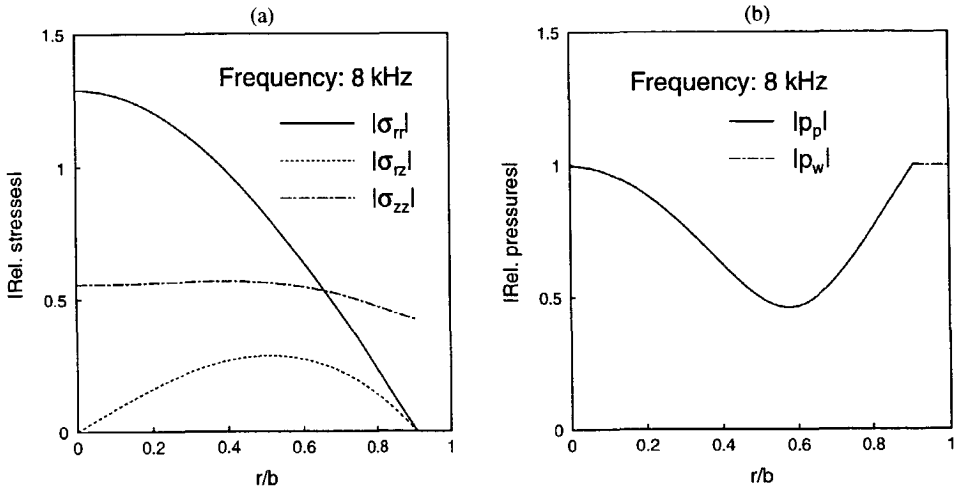


Figure 8.6: Radial distributions of the stresses (a) and pressures (b) for the S mode at 8 kHz. Both the stresses and pressures were normalized by $p_p|_{r=a}$. The calculations were performed for a Benthem cylinder with a diameter of 70.0 mm, ($a = 0.909b$). The pores at the boundary were open.

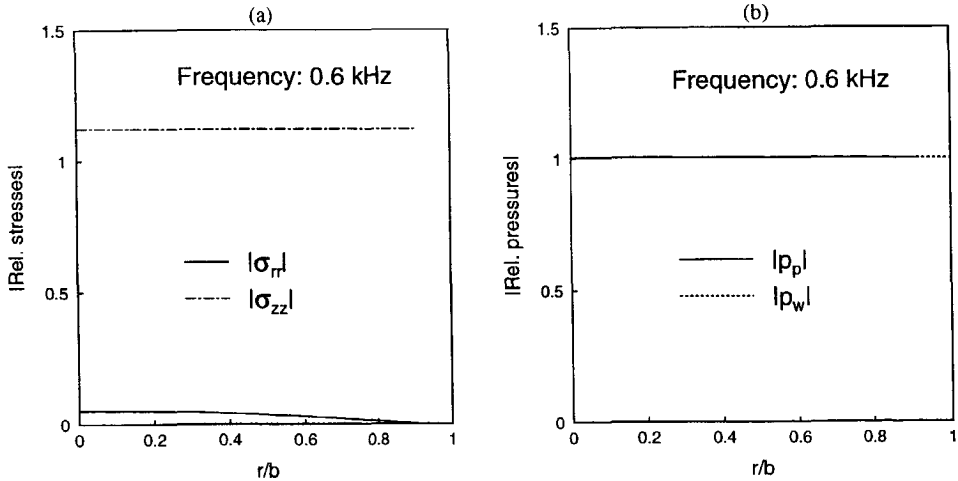


Figure 8.7: Radial distributions of the stresses (a) and pressures (b) for the S mode at 0.6 kHz. Both the stresses and pressures were normalized by $p_p|_{r=a}$. The calculations were performed for a Benthem cylinder with a diameter of 70.0 mm ($a = 0.909b$). The pores at the boundary were open.

with the pseudo-Stoneley wave at high frequencies. Furthermore, we remark that over the entire frequency range, the gap pressures are of the same order as the pore pressures in the porous cylinder.

The phase velocities and the damping coefficients for the L1 mode are shown in Fig. 8.8 in the 1-1000 kHz frequency range. The phase velocity of this wave mode shows similarities with the L1 mode for the elastic case which is shown in Fig. 7.2. At high frequencies, the L1 phase velocity in a poroelastic cylinder in the shock tube reaches the sound velocity of water. This wave is therefore associated with wave motion in the gap. We previously noted that the L1 phase velocity for the elastic case, however, reached for high frequencies the velocity of the Rayleigh wave. In the low-frequency limit, the phase velocity of the L1 mode is somewhat lower than the free-field velocity of the fast wave. For the elastic case the low-frequency limit of the L1 mode was defined as the so-called 'bar' velocity, which was given by $\sqrt{E/\rho}$. The damping coefficient of the L1 mode displays a peculiar behaviour. In the high-frequency limit, the L1 mode is associated with wave motion in the gap. As no intrinsic damping is included for the water, the L1 mode is undamped here. In the low-frequency limit the Biot damping of the fast wave strongly influences the damping of the L1 mode. In between 30 and 500 kHz, a transition occurs from the bulk wave motion in the porous cylinder to bulk wave motion in the gap. Both radial and axial wave motion are important. We observe a number of local maxima and minima in the damping coefficient. The frequencies of the maxima correspond to free-field wavelengths in the water which approximately fit the diameter of the porous cylinder. The Figs. 8.9 and 8.10 show the radial distributions of the stresses and pressures at 120 and 0.6 kHz, respectively. At 120 kHz we observe that the stress components are of equal importance, which is in agreement with our conclusion that both axial and radial wave motion are important in between 30 and 500 kHz. At 0.6 kHz the longitudinal stress situation is reached, which corresponds to bulk wave motion in the porous cylinder.

Fig. 8.11 shows the phase velocity and the damping coefficient of the L2 mode in the 1-1000 kHz frequency range. Above 300 kHz the L2 phase velocity reaches the phase velocity of the free-field shear velocity. At low frequencies the phase velocity remains finite, which is contrary to the behaviour of the L2 mode for the elastic case. The phase velocity of the latter mode becomes infinite. For the poroelastic cylinder, we observe that the damping of the L2 mode is large in the low-frequency limit: $\Im m(k) \approx -6$ (not shown in Fig. 8.11). For the high-frequency limit the damping of the L2 mode is equivalent to the damping of the free-field shear wave. In the intermediate frequency range, a transition occurs from a bulk wave with two-dimensional effects to a one-dimensional shear wave. The Figs. 8.12, and 8.13 show the radial distributions of the stresses and the pressures at 120 and 0.6 kHz, respectively. At 120 kHz we observe that the stress components have amplitudes which are relatively high with respect to the pressure amplitudes. At 0.6 kHz we observe non-uniform stress and pressure distributions, similar to the behaviour of the L2 for the elastic case (Fig. 7.4). The pressure in the gap is negligible at this frequency.

Summarizing the analysis of the S, L1, and L2 modes, we may say that for the S and L1 modes the motion of the water in the gap plays an important role. The gap pressures for these modes are of the same order of magnitude as the stresses and pressures in the porous cylinder. The L2 mode however, is dominated by the motion of the solid matrix and the pore fluid. The same behaviour can be expected for the higher-order wave modes.

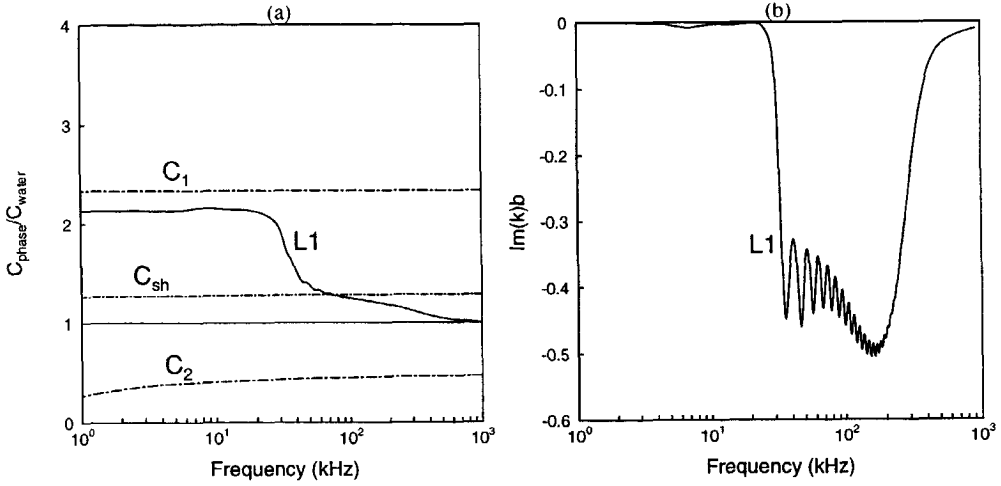


Figure 8.8: Frequency dependence of the phase velocity (a) and damping coefficient (b) for the L1 mode in the 1-1000 kHz frequency range. The results for the phase velocities for the free-field Biot solutions are also given. The computations are performed for a Bentheimer sandstone cylinder with a diameter of 70.0 mm. Parameters are given in Table E.1.

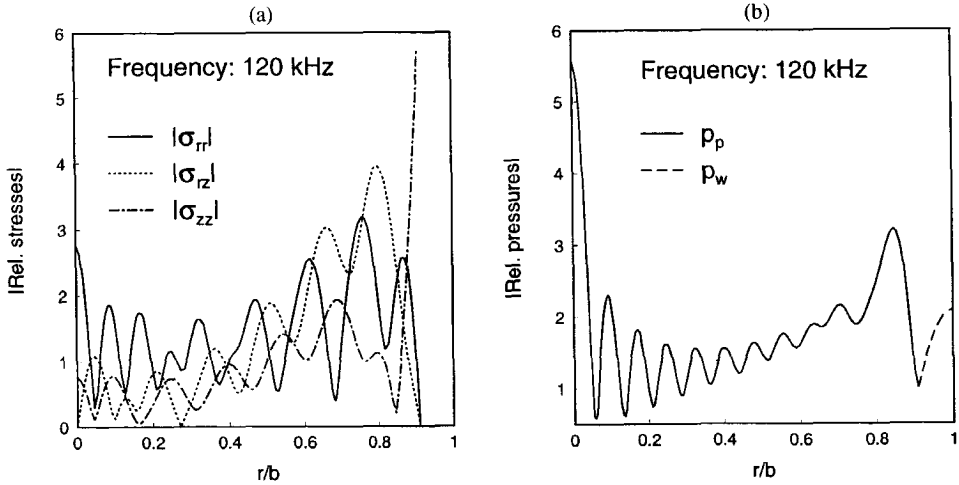


Figure 8.9: Radial distributions of the stresses (a) and pressures (b) for the L1 mode at 120 kHz. Both the stresses and pressures were normalized by $p_p|_{r=a}$. The calculations were performed for a Bentheim cylinder with a diameter of 70.0 mm ($a = 0.909b$). The pores at the boundary were open.

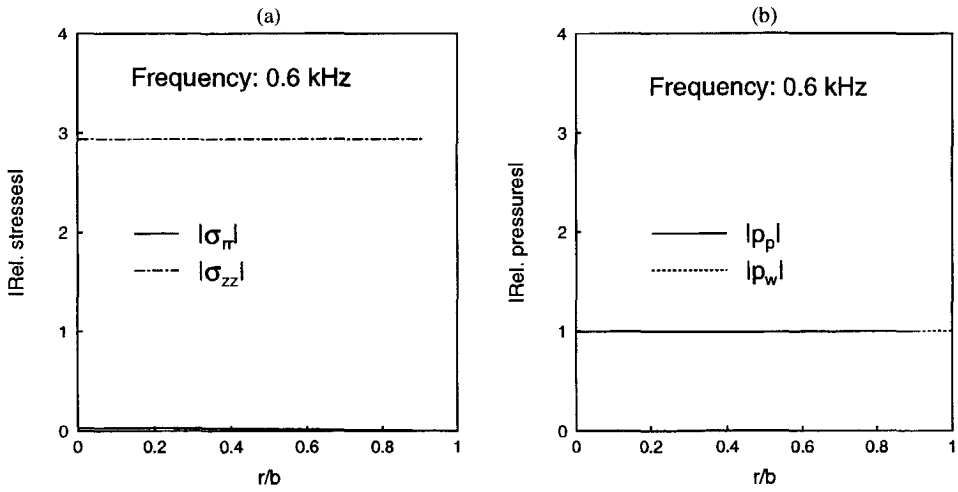


Figure 8.10: Radial distributions of the stresses (a) and pressures (b) for the L1 mode at 0.6 kHz. Both the stresses and pressures were normalized by $p_p|_{r=a}$. The calculations were performed for a Bentheim cylinder with a diameter of 70.0 mm ($a = 0.909b$). The pores at the boundary were open.

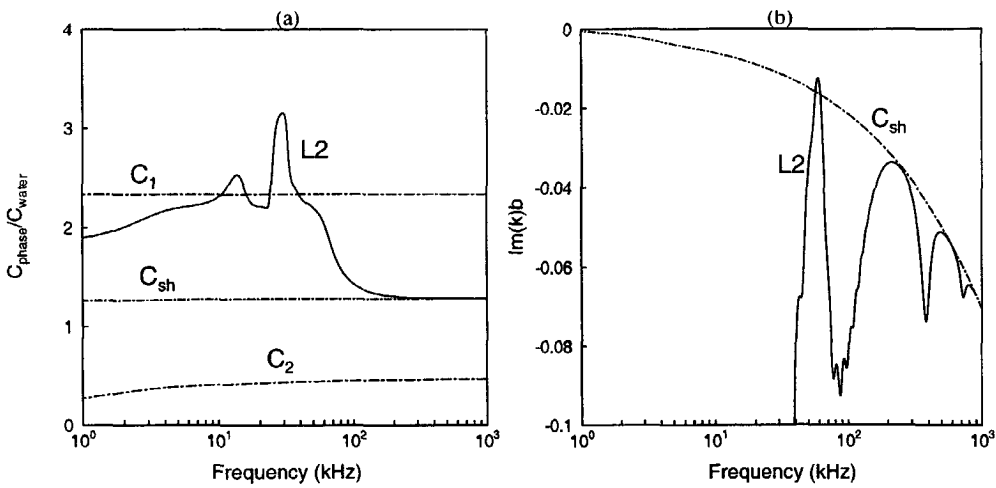


Figure 8.11: Frequency dependence of phase velocity (a) and damping coefficient (b) for the L2 mode. The results for the free-field Biot shear wave are also shown. The computations were performed for a Bentheim cylinder with a diameter of 70.0 mm. The pores at the boundary were open.

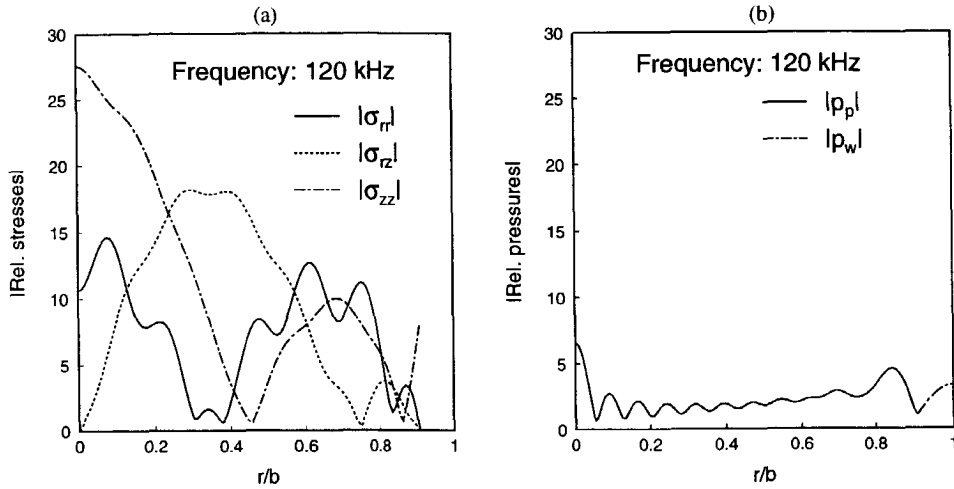


Figure 8.12: Radial distributions of the stresses (a) and pressures (b) for the L2 mode at 120 kHz. Both the stresses and pressures were normalized by $p_p|_{r=a}$. The calculations were performed for a Bentheim cylinder with a diameter of 70.0 mm ($a = 0.909b$). The pores at the boundary were open.

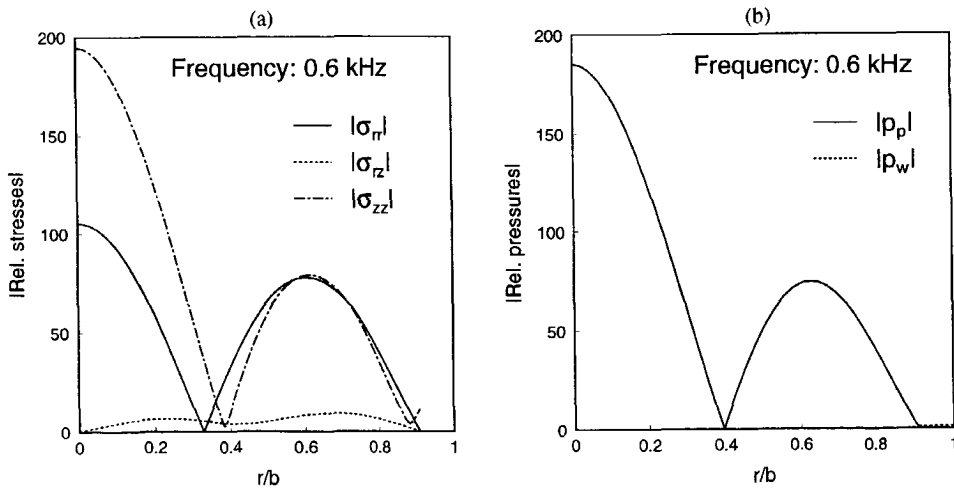


Figure 8.13: Radial distributions of the stresses (a) and pressures (b) for the L2 mode at 0.6 kHz. Both the stresses and pressures were normalized by $p_p|_{r=a}$. The calculations were performed for a Bentheim cylinder with a diameter of 70.0 mm ($a = 0.909b$). The pores at the boundary were open.

C and I modes

Our numerical computations also predict a number of strongly damped modes, which are similar to the damped C and I modes for the elastic case (see Fig. 7.6). Consequently, these modes for the poroelastic cylinder are also labelled C and I. In Fig. 8.14, we present the results in the same way as for the elastic case. The C modes are indicated by the dashed lines, and the I modes are indicated by the solid lines. As a reference, we have given some of the L modes, which are also given in Fig. 8.2. The behaviour of $\Re(k)$ of the C modes for the porous cylinder is somewhat different from the C modes for the elastic case, which have a finite value of $\Re(k)$ at low frequencies. For C modes of the porous cylinder, $\Re(k)$ is zero in the low-frequency limit. The C modes are connected to the I modes via modes in the third quadrant of the k -plane. Those modes have infinite amplitudes for $z \rightarrow \infty$, and hence, we did not show them in Fig. 8.14.

D modes

Up to now we could relate our computational results to the elastic cylinder. For the poroelastic cylinder in the shock tube, however, we found an extra mode type, due to the presence of the slow wave. The occurrence of the slow wave mode type is in agreement with the predictions of Gardner (1962), Liu (1988), and Hsu *et al.* (1997). Gardner gives an expression for the slow wave mode type in the low-frequency limit for a water-saturated porous cylinder in vacuum. Hsu *et al.* present phase velocities and damping coefficients of a slow wave mode for a configuration which is similar to the shock tube (Fig. 1.4(b)). Liu also found slow wave modes, but the configuration was somewhat different (Fig. 1.4(a)). In the following, we denote the slow wave mode by D. The results for the D modes are shown in Fig. 8.15, where the frequency dependence of the real and imaginary parts of k is shown. In this figure the dashed lines indicate the free-field solution for the slow wave. From these results we clearly observe that the D modes have the free-field solution of the slow wave as their high-frequency limit. The damping of these modes is at least as high as the damping of the slow wave and of the same order of magnitude as the damping of the C modes. The radial distributions for the stresses and pressures of the D1 mode are given in Figs. 8.16 and 8.17 for 60 kHz and 0.6 kHz, respectively. For both frequencies, we observe that the pore pressures and the stress components are of the same order of magnitude, while the pressures in the centre of the cylinder are much larger than the gap pressure. This means that the wave motion in the gap is of less importance for the D modes.

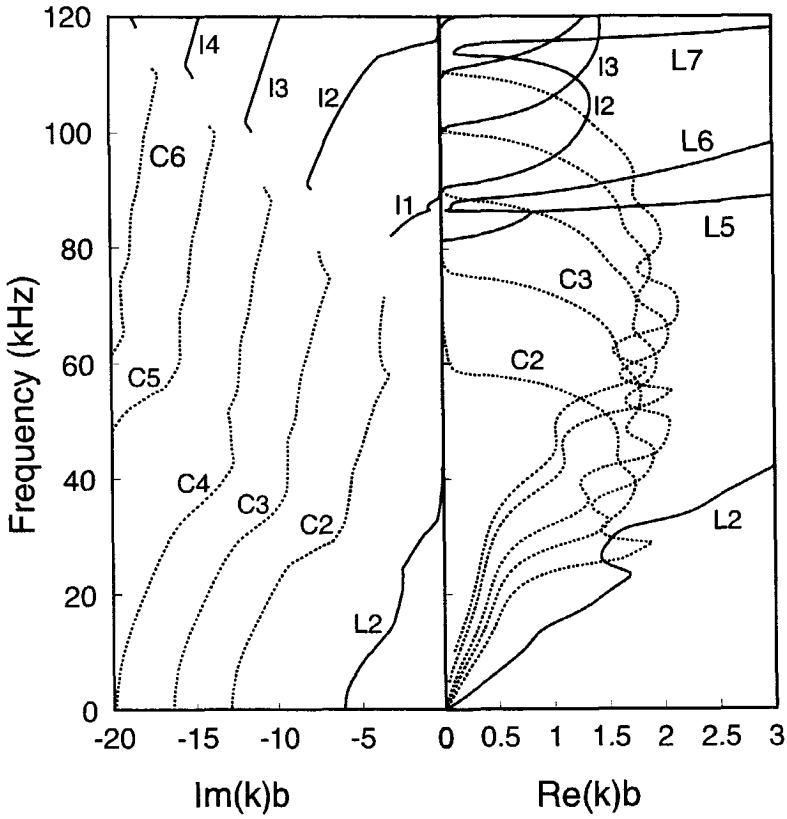


Figure 8.14: Frequency dependence of $\Im m(k)$ and $\Re e(k)$ for the C and I modes. As a reference some L modes are given. The wavenumber is normalized by the inner radius of the shock tube b . The computations were performed for a Benthaim cylinder with a diameter of 70.0 mm. The pores at the boundary were open. Note that the full computational results are presented in three figures. The L and S modes are shown in Fig. 8.2, while the D modes are shown in Fig. 8.15.

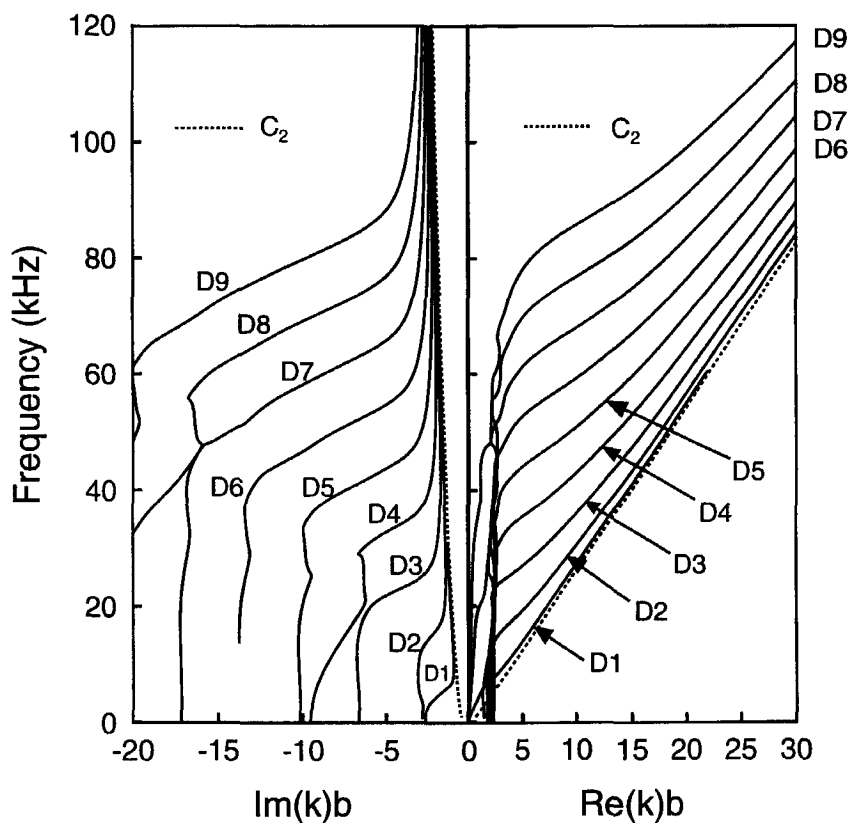


Figure 8.15: Frequency dependence of $\Im m(k)$ and $\Re e(k)$ for the D modes. The wavenumber is normalized by the inner radius of the shock tube b . The computations were performed for a Bentheimer sandstone cylinder with a diameter of 70.0 mm. The pores at the boundary were open. The free-field solution C_2 for the slow wave is indicated by the dashed line. Note that the full computational results are presented in three figures. The L and S modes are shown in Fig. 8.2, while the C and I modes are shown in Fig. 8.14.

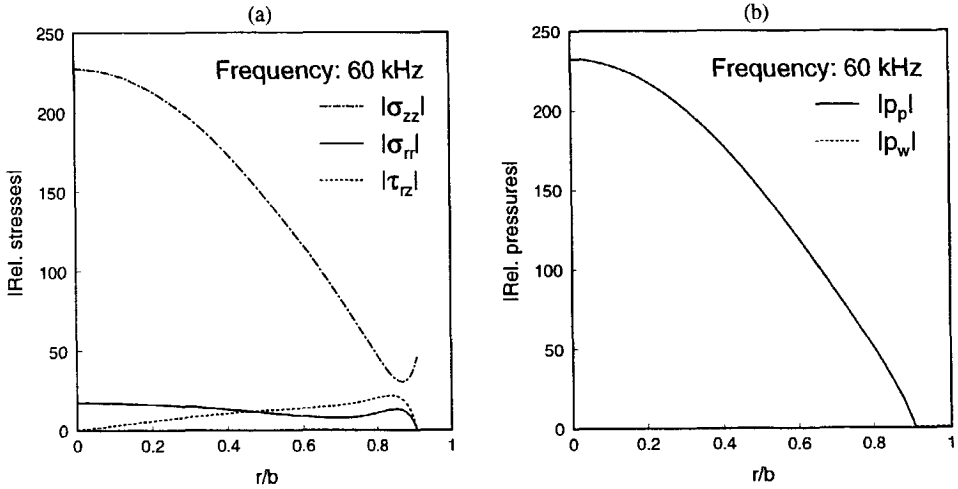


Figure 8.16: Radial distributions of the stresses (a) and pressures (b) for the D1 mode at 60 kHz. Both the stresses and pressures were normalized by $p_p|_{r=a}$. The calculations were performed for a Bentheim cylinder with a diameter of 70.0 mm ($a = 0.909b$). The pores at the boundary were open.

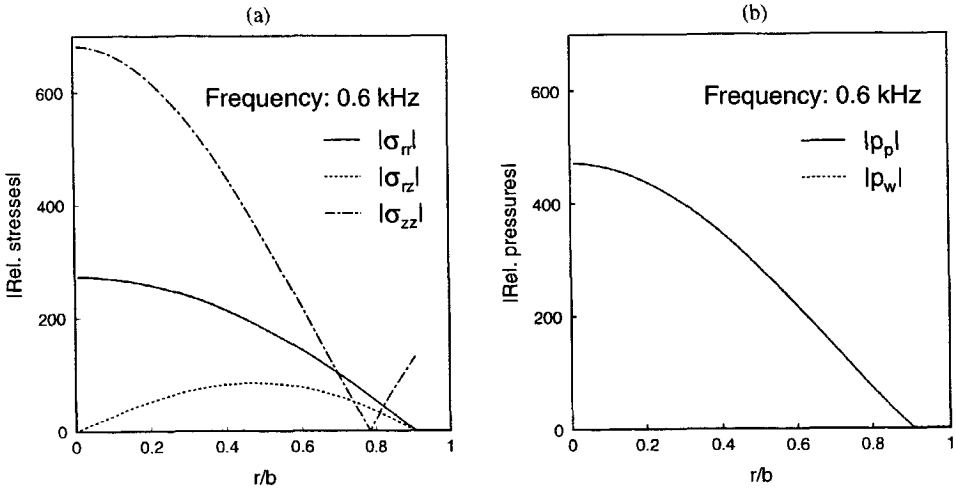


Figure 8.17: Radial distributions of the stresses (a) and pressures (b) for the D1 mode at 0.6 kHz. Both the stresses and pressures were normalized by $p_p|_{r=a}$. The calculations were performed for a Bentheim cylinder with a diameter of 70.0 mm ($a = 0.909b$). The pores at the boundary were open.

8.2 Full modelling fast formation

In this section we discuss the compliance effect of the wall of the shock tube. The configuration for this case is given in Fig. 8.18. The porous cylinder and the water-filled gap

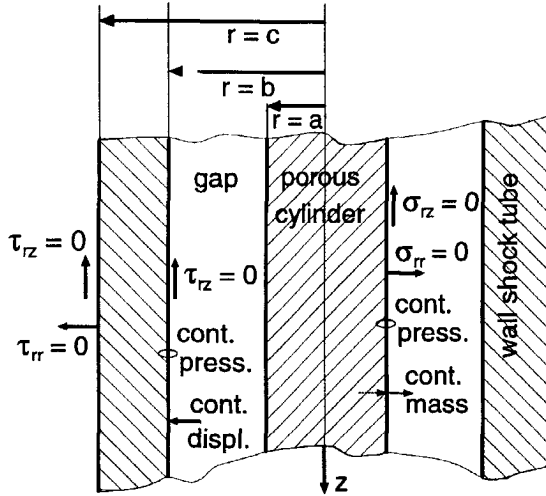


Figure 8.18: Full model of the shock tube.

are described in exactly the same way as in the previous section. For the elastic wall of the shock tube we use two new potentials:

$$\varphi_{st} = B_{st}Y_0(k_{rstc}r) + A_{st}J_0(k_{rstc}r), \quad (8.23)$$

and

$$\eta_{st} = D_{st}Y_0(k_{rstsh}r) + C_{st}J_0(k_{rstsh}r). \quad (8.24)$$

The radial wavenumbers in these expressions are defined by:

$$k_{rstc} = \sqrt{\omega^2/c_L^2 - k^2}, \quad k_{rstsh} = \sqrt{\omega^2/c_T^2 - k^2}, \quad (8.25)$$

with $\Im m(k_{rstc}) \leq 0$ and $\Im m(k_{rstsh}) \leq 0$. The free-field velocities in the shock tube wall of the compressional and the shear wave are given by c_L and c_T respectively. For the boundary conditions at $r = a$ we use the same conditions as in the previous section while at $r = b$ and $r = c$ we use a stress free interface condition. Hence we obtain:

- at $r = a$: $\sigma_{rr} = 0$, $\sigma_{rz} = 0$, $(1 - \phi)u_{sr} + \phi u_{fr} = u_{rw}$, $p = p_w$,
- at $r = b$: $u_{wr} = u_{str}$, $p_w = \tau_{strr}$, $\tau_{strz} = 0$,
- at $r = c$: $\tau_{strr} = 0$, $\tau_{strz} = 0$,

where τ_{strr} and τ_{strz} are the radial and shear stress in the wall of the shock tube. The relations between these stresses and the potentials are given in Appendix A. We obtain a system with nine unknown amplitudes:

$$\underline{\underline{M}} (A_{c1} \ A_{c2} \ C_{sh} \ B_w \ A_w \ B_{st} \ A_{st} \ D_{st} \ C_{st})^T = \underline{0}, \quad (8.26)$$

where

$$M(1, 1) = \Lambda_{c1} \left(\frac{\omega^2}{c_1^2} \right) J_0(k_{rc1}a) + 2G \left(k_{rc1}(k_{rc1}J_0(k_{rc1}a) - \frac{1}{a}J_1(k_{rc1}a)) \right),$$

$$M(1, 2) = \Lambda_{c2} \left(\frac{\omega^2}{c_2^2} \right) J_0(k_{rc2}a) + 2G \left(k_{rc2}(k_{rc2}J_0(k_{rc2}a) - \frac{1}{a}J_1(k_{rc2}a)) \right),$$

$$M(1, 3) = -2Gik_{rsh} \left(k_{rsh}J_0(k_{rsh}a) - \frac{1}{a}J_1(k_{rsh}a) \right),$$

$$M(1, 4) = 0,$$

$$M(1, 5) = 0,$$

$$M(1, 6) = 0,$$

$$M(1, 7) = 0,$$

$$M(1, 8) = 0,$$

$$M(1, 9) = 0,$$

$$M(2, 1) = -2ikk_{rc1}J_1(k_{rc1}a),$$

$$M(2, 2) = -2ikk_{rc2}J_1(k_{rc2}a),$$

$$M(2, 3) = -k_{rsh}(k^2 - k_{rsh}^2)J_1(k_{rsh}a),$$

$$M(2, 4) = 0,$$

$$M(2, 5) = 0,$$

$$M(2, 6) = 0,$$

$$M(2, 7) = 0,$$

$$M(2, 8) = 0,$$

$$M(2, 9) = 0,$$

$$M(3, 1) = ((\phi - 1) - \beta_{c1}\phi) k_{rc1}J_1(k_{rc1}a),$$

$$M(3, 2) = ((\phi - 1) - \beta_{c2}\phi) k_{rc2}J_1(k_{rc2}a),$$

$$M(3, 3) = ((1 - \phi) + \beta_{sh}\phi) ik_{rsh}J_1(k_{rsh}a),$$

$$M(3, 4) = k_{rw}Y_1(k_{rw}a),$$

$$M(3, 5) = k_{rw}J_1(k_{rw}a),$$

$$M(3, 6) = 0,$$

$$M(3, 7) = 0,$$

$$M(3, 8) = 0,$$

$$M(3, 9) = 0,$$

$$M(4, 1) = \frac{1}{\phi} \left(\frac{\omega^2}{c_1^2} \right) J_0(k_{rc1}a)(Q + R\beta_{c1}),$$

$$M(4, 2) = \frac{1}{\phi} \left(\frac{\omega^2}{c_2^2} \right) J_0(k_{rc2}a)(Q + R\beta_{c2}),$$

$$M(4, 3) = 0,$$

$$M(4, 4) = -\rho_w \omega^2 Y_0(k_{rw}a),$$

$$M(4, 5) = -\rho_w \omega^2 J_0(k_{rw}a),$$

$$M(4, 6) = 0,$$

$$M(4, 7) = 0,$$

$$M(4, 8) = 0,$$

$$M(4, 9) = 0,$$

$$M(5, 1) = 0,$$

$$M(5, 2) = 0,$$

$$M(5, 3) = 0,$$

$$M(5, 4) = -k_{rw} Y_1(k_{rw}b),$$

$$M(5, 5) = -k_{rw} J_1(k_{rw}b),$$

$$M(5, 6) = k_{rstc} Y_1(k_{rstc}b),$$

$$M(5, 7) = k_{rstc} J_1(k_{rstc}b),$$

$$M(5, 8) = -k_{rstsh} i k Y_1(k_{rstsh}b),$$

$$M(5, 9) = -k_{rstsh} i k J_1(k_{rstsh}b),$$

$$M(6, 1) = 0,$$

$$M(6, 2) = 0,$$

$$M(6, 3) = 0,$$

$$M(6, 4) = -\rho_w (\omega^2) Y_0(k_{rw}b),$$

$$M(6, 5) = -\rho_w (\omega^2) J_0(k_{rw}b),$$

$$M(6, 6) = -(\lambda_{st} + 2\mu_{st})(k_{rstc}^2) - \lambda_{st} k^2 Y_0(k_{rstc}b) + 2\mu_{st} k_{rstc} Y_1(k_{rstc}b)/b,$$

$$M(6, 7) = -(\lambda_{st} + 2\mu_{st})(k_{rstc}^2) - \lambda_{st} k^2 J_0(k_{rstc}b) + 2\mu_{st} k_{rstc} J_1(k_{rstc}b)/b,$$

$$M(6, 8) = 2\mu_{st} i k (k_{rstc}^2) Y_0(k_{rstsh}b) - 2\mu_{st} i k k_{rstsh} Y_1(k_{rstsh}b)/b,$$

$$M(6, 9) = 2\mu_{st} i k (k_{rstc}^2) J_0(k_{rstsh}b) - 2\mu_{st} i k k_{rstsh} J_1(k_{rstsh}b)/b,$$

$$M(7, 1) = 0,$$

$$M(7, 2) = 0,$$

$$M(7, 3) = 0,$$

$$M(7, 4) = 0,$$

$$M(7, 5) = 0,$$

$$M(7, 6) = 2i k k_{rstc} Y_1(k_{rstc}b),$$

$$M(7, 7) = 2i k k_{rstc} J_1(k_{rstc}b),$$

$$M(7, 8) = -(k_{rstsh}^2 - k^2) k_{rstsh} Y_1(k_{rstsh}b),$$

$$M(7, 9) = -(k_{rstsh}^2 - k^2) k_{rstsh} J_1(k_{rstsh}b),$$

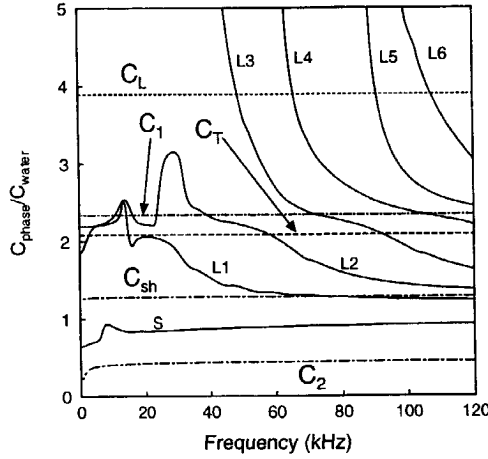


Figure 8.19: Frequency dependence of the phase velocities of the L and S modes. In these computations the elasticity of the wall is included. The free-field velocities of the three Biot waves, and the free field velocities of steel are given. The latter ones are indicated by C_L and C_T for the compressional and shear wave respectively. The computations are performed for a Bentheimer sandstone cylinder with a diameter of 70.0 mm, i.e., $a = 0.909b$ and $c = 1.62b$.

$$\begin{aligned}
 M(8,1) &= 0, \\
 M(8,2) &= 0, \\
 M(8,3) &= 0, \\
 M(8,4) &= 0, \\
 M(8,5) &= 0, \\
 M(8,6) &= -(\lambda_{st} + 2\mu_{st})(k_{rstc}^2 - \lambda_{st}k^2)Y_0(k_{rstc}c) + 2\mu_{st}k_{rstc}Y_1(k_{rstc}c)/c, \\
 M(8,7) &= -(\lambda_{st} + 2\mu_{st})(k_{rstc}^2 - \lambda_{st}k^2)J_0(k_{rstc}c) + 2\mu_{st}k_{rstc}J_1(k_{rstc}c)/c, \\
 M(8,8) &= 2\mu_{st}ik(k_{rstc}^2)Y_0(k_{rstsh}c) - 2\mu_{st}ikk_{rstsh}Y_1(k_{rstsh}c)/c, \\
 M(8,9) &= 2\mu_{st}ik(k_{rstc}^2)J_0(k_{rstsh}c) - 2\mu_{st}ikk_{rstsh}J_1(k_{rstsh}c)/c,
 \end{aligned}$$

$$\begin{aligned}
 M(9,1) &= 0, \\
 M(9,2) &= 0, \\
 M(9,3) &= 0, \\
 M(9,4) &= 0, \\
 M(9,5) &= 0, \\
 M(9,6) &= 2ikk_{rstc}Y_1(k_{rstc}c), \\
 M(9,7) &= 2ikk_{rstc}J_1(k_{rstc}c), \\
 M(9,8) &= -(k_{rstsh}^2 - k^2)k_{rstsh}Y_1(k_{rstsh}c), \\
 M(9,9) &= -(k_{rstsh}^2 - k^2)k_{rstsh}J_1(k_{rstsh}c).
 \end{aligned}$$

We have performed computations for a Bentheim cylinder with a diameter of 70.0 mm. The outer diameter of the shock tube is 125 mm, and we used the literature values of steel for the free-field velocities of the compressional and the shear wave in the wall of the shock tube: $c_L = 5790$ m/s and $c_T = 3100$ m/s (CRC 1973).

The computational results for the phase velocities of the L and S modes are shown in Fig. 8.19. We have also given the free-field velocities of the three Biot waves, as well as the free-field velocities of the steel. If we compare the wave modes with the data of the rigid wall case (Fig. 8.2), we observe that the L1 and the S mode are influenced by the compliance effects of the wall, especially at low frequencies. For the S mode, the phase velocities are larger, and for the L1 mode we observe an oscillation in the phase velocity. This is also illustrated by the plots of the radial distributions of the radial displacements. For the porous cylinder we show the property $|\phi u_{fr} + (1 - \phi)u_{sr}|$, which is identical to $|u_{wr}|$ at $r = b$. Fig. 8.20 shows the results for the S mode at 13.5 and 120 kHz. At 13.5 kHz the displacement of the wall is significant and the rigid wall approximation is not valid. At 120 kHz the effect is much less important. For the L1 mode the compliance effect of the wall at 13.5 kHz is even more prominent. Fig. 8.21(a) shows that the radial displacements of the wall are larger than the radial displacements of the porous cylinder. At 120 kHz the radial displacements of the wall of the shock tube are small however, and the influence of the elasticity of the tube wall on the phase velocity of the L1 mode is small (see Fig. 8.21(b)). The higher-order modes L2, L3, etc. are slightly influenced, which is in agreement with our previous observation that the higher order modes are primarily related to wave motion in the porous cylinder. Computations for the D modes yield that the rigid wall approximation is accurate for this mode type also.

Please note that in this configuration also tube wave modes occur which are primarily related to wave motion in the wall of the shock tube. We did not investigate these modes, as we are primarily interested in wave motion of the porous cylinder and the water-filled gap. Moreover, these tube wave modes are not generated effectively in our experiments.

8.3 Parameter study

In this section we study the influence of geometrical and material properties on phase velocities and damping coefficients of the several wave modes. First, we take into account the compressibility-effects of the grains. Subsequently, we pay attention to the influence of the gap width on the L, S and D modes. This topic is relevant from a theoretical point of view, but it is also important for studying the effects of the diameter variations in a borehole, as well as the influence of a logging tool on different wave modes. As discussed in Chapter 1, borehole wave modes are used for shear modulus and permeability evaluation. The shear and permeability effects for the borehole configuration were studied by Schmitt *et al.* (1988a, 1988b). In this section, we discuss the permeability and shear effects for the shock tube configuration.

8.3.1 Compressible grains

For the rigid grain approximation we used the expressions of the Equations (2.33), (2.34) and (2.35), and we substituted $\Lambda_{c1} = \Lambda_{c2} = (K_b - 2G/3)$ in Equation (8.13). For compressible grains, however, Equations (8.11) and (8.12) are used. In the full expressions for P, Q, and R, we use the literature value for the bulk modulus of quartz $K_s = 36.5$ GPa, (CRC 1973).

In Fig. 8.22(a), we plot the free-field velocities of the three Biot waves for compressible

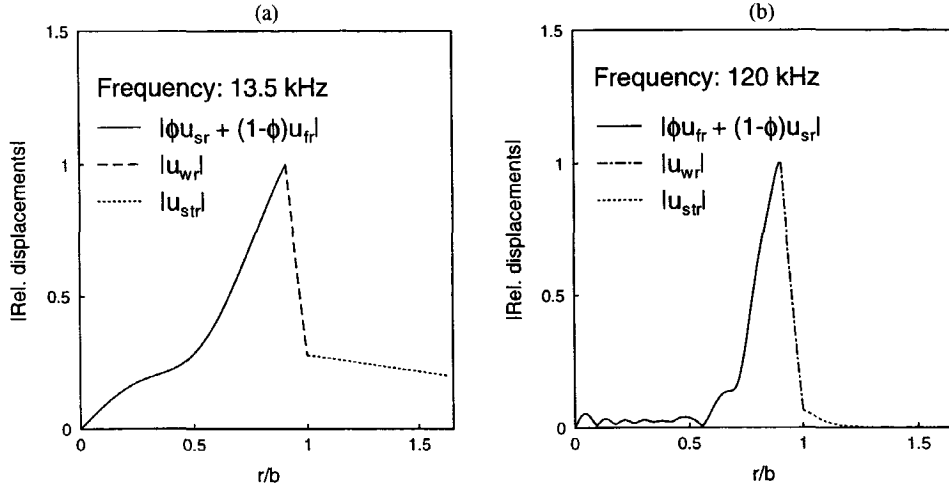


Figure 8.20: Radial distributions of the displacements for the S mode at 13.5 kHz (a) and 120 kHz (b). The displacements are normalized by the radial displacement of the water in the gap. For the porous cylinder the property $|\phi u_{sr} + (1-\phi)u_{fr}|$ is given. Note the continuity at $r = a$. The calculations were performed for a Benthem cylinder with a diameter of 70.0 mm., i.e., $a = 0.909b$ and $c = 1.62b$.

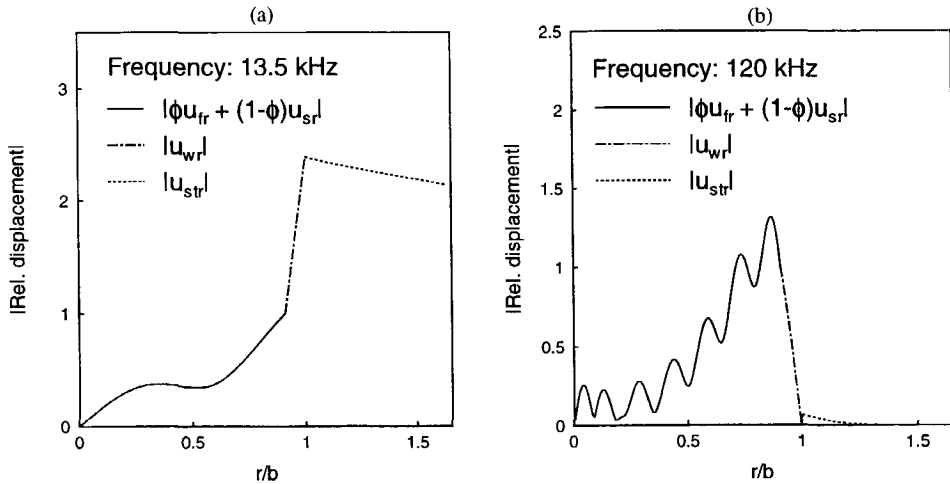


Figure 8.21: Radial distributions of the displacements for the L1 mode at 13.5 kHz (a) and 120 kHz (b). The displacements are normalized by the radial displacement of the water in the gap. For the porous cylinder the property $|\phi u_{sr} + (1-\phi)u_{fr}|$ is given. Note the continuity at $r = a$. The calculations were performed for a Benthem cylinder with a diameter of 70.0 mm., i.e., $a = 0.909b$ and $c = 1.62b$.

and incompressible grains. Also, the compressional and shear velocities of the wall of the shock tube are given. The solutions for compressible grains are indicated by the solid lines, while the solutions for the incompressible grains are indicated by the dashed lines. The compressibility of the grains influences the free-field velocity of the fast wave so that it becomes nearly equal to the free-field shear wave velocity of the wall. The shear wave of the porous material is not influenced by the compressibility of the grains, and the slow wave is only slightly influenced. In Fig. 8.22(b) the phase velocities for the L and S wave modes including the compressibility of the grains are indicated by the solid lines, while the results for the rigid grains are indicated by the dashed lines. Note that the results for the rigid grains are also given in Fig. 8.19. The compressibility of the grains strongly influences the higher-order L modes, while the S mode and the L1 mode are slightly influenced. Due to large decrease of the free-field velocity of the fast wave, the phase velocities of the higher-order L modes are lower for the compressible grains.

8.3.2 Gap effects

We performed computations for a smaller gap width ($a/b = 0.998$). Results are given in Fig. 8.23. The computations include the compressibility of the grains as well as the elasticity of the wall. We observed the existence of a new mode type, denoted M. This mode type shows similar behaviour as the L modes. The M mode is also cut off below a certain frequency, but this wave mode has the fast wave velocity, instead of the shear wave velocity as its high-frequency limit. In the 1-120 kHz frequency range, we found only one M mode, for which the phase velocity is given in Fig. 8.23(a). The M modes are also observed for the slow formation as we discuss in Section 8.3.5.

L and D modes

For this small gap width we observe that over a large frequency range the L1 mode has a phase velocity which is equal to the free-field velocity of the fast wave. Fig. 8.23(b) shows that the damping coefficient of the L1 mode becomes very high for certain frequencies. For reference the damping of the free-field C_1 wave is also given. Fig. 8.24 shows the radial distributions of the stresses and pressures at 120 kHz. From these plots we observe that the axial stress component σ_{zz} is dominant, while the pressure distribution is oscillatory around an approximately uniform average. The radial stress component in the wall of the shock tube is of the same magnitude as the pore pressure. Further insight can be obtained by plotting the radial distributions of the axial and radial displacements. The results are given in Fig. 8.25, from which we can conclude that the axial displacements are dominant. Furthermore, we observe from Fig. 8.25(b) that the radial displacement of the wall of the shock tube is of the same order as the radial displacements in the porous cylinder. Indeed, the rigid wall approximation would have been not applicable, even at high frequencies. We recall that for the large gap the rigid wall approximation was accurate at high frequencies, but it failed at low frequencies.

Changing the gap width does not alter the shape of the higher-order mode curves, but does influence the location in the frequency-wavenumber plane. For example, the cut-off frequencies for the small gap configuration are much larger than the cut-off frequencies for the large gap configuration.

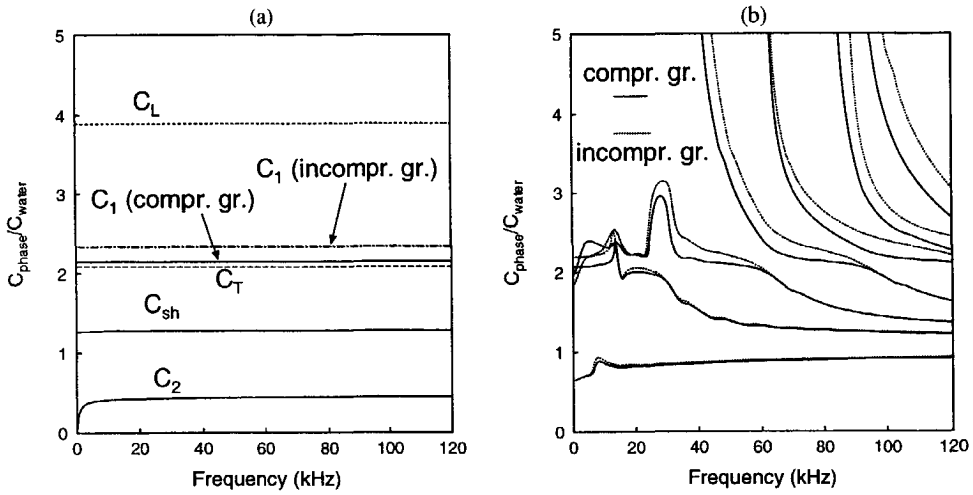


Figure 8.22: Frequency dependence of the free-field velocities (a) and the phase velocities of the L and S modes (b). The solid lines indicate the computations including the compressibility of the grains. The dashed lines indicated the computations without the compressibility of the grains. The computations are performed for a Bentheim cylinder with a diameter of 70.0 mm., i.e., $a = 0.909b$, and $c = 1.62b$.

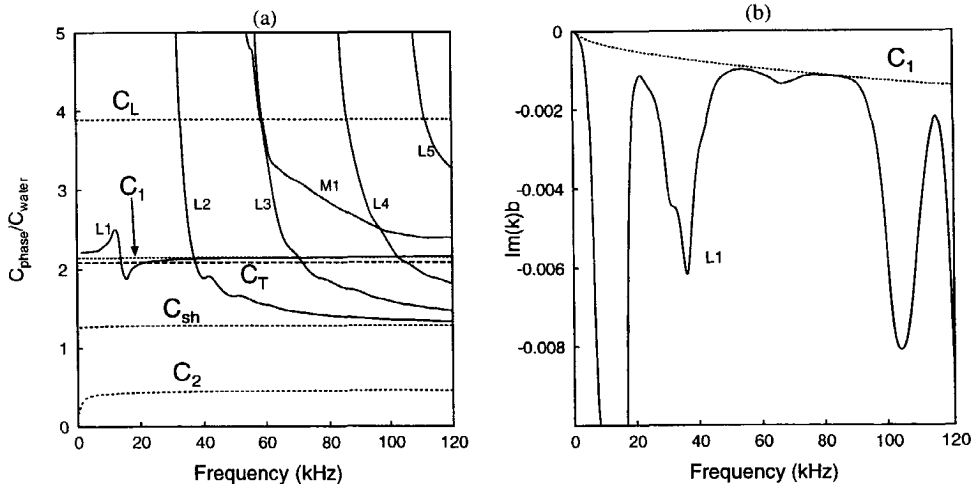


Figure 8.23: Frequency dependence of the phase velocities (a) and damping coefficients (b) for L and M modes. The free-field velocities of the three Biot waves and the compressional and shear velocities of the steel wall are also shown. For the damping only the L1 mode is shown, together with the free-field damping coefficient of the fast wave. The calculations were performed for Bentheimer sandstone with a diameter of 76.85 mm., i.e., $a/b = 0.998$ and $c/b = 1.62$. The compressibility of the grains was included.

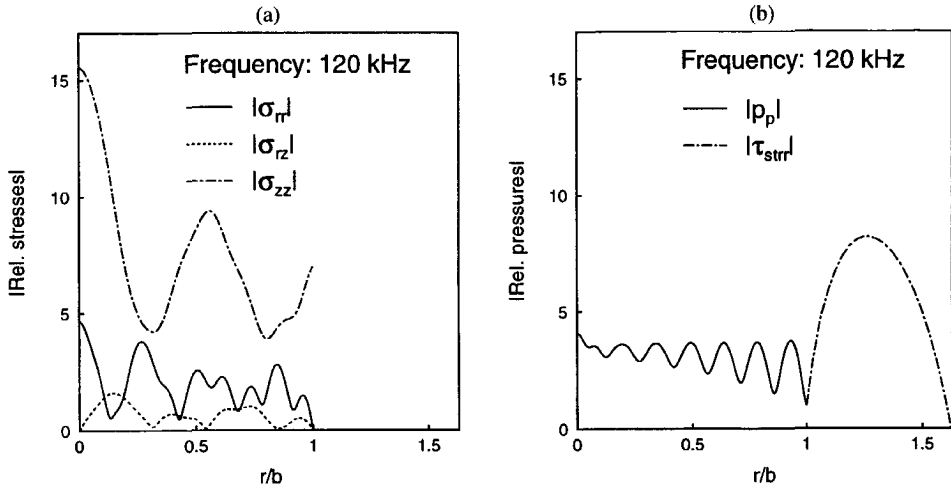


Figure 8.24: Radial distributions of the stresses (a) and pressures (b) for the L1 mode at 120 kHz. Both the stresses and pressures were normalized by $p_p|_{r=a}$. The calculations were performed for Bentheimer sandstone with $a/b = 0.998$ and $c/b = 1.62$. The water-filled gap is not visible in this figure.

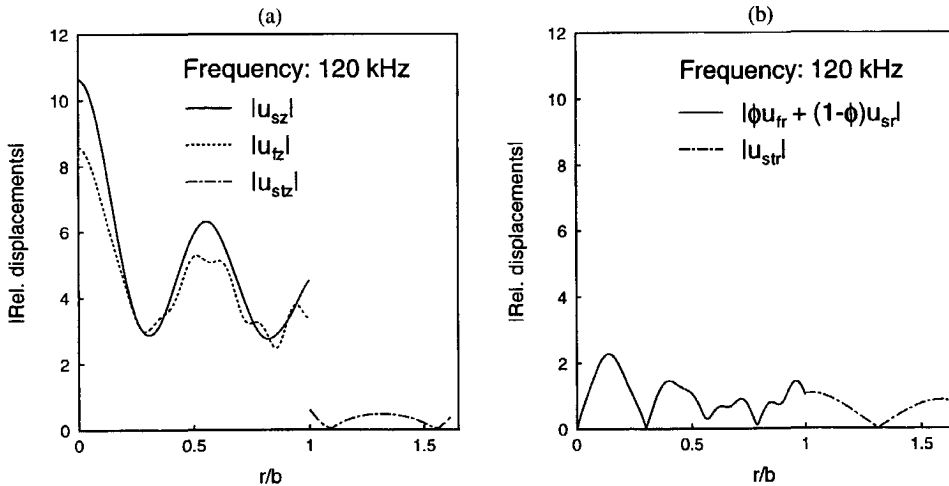


Figure 8.25: Radial distributions of the axial displacements (a) and radial displacements (b) for the L1 mode at 120 kHz. The displacements were normalized by the radial displacement in the gap at $r = a$. For the porous cylinder the property $|\phi u_{fr} + (1-\phi)u_{sr}|$ is shown. The calculations were performed for Bentheimer sandstone with $a/b = 0.998$ and $c/b = 1.62$. The water-filled gap is not visible in this figure.

Fig. 8.26 shows the phase velocities and damping coefficients of the D modes. The character of the D modes is not sensitive to a change in gap width. We observe that the D1 mode is equivalent to the solution for the free-field slow wave over nearly the entire frequency range.

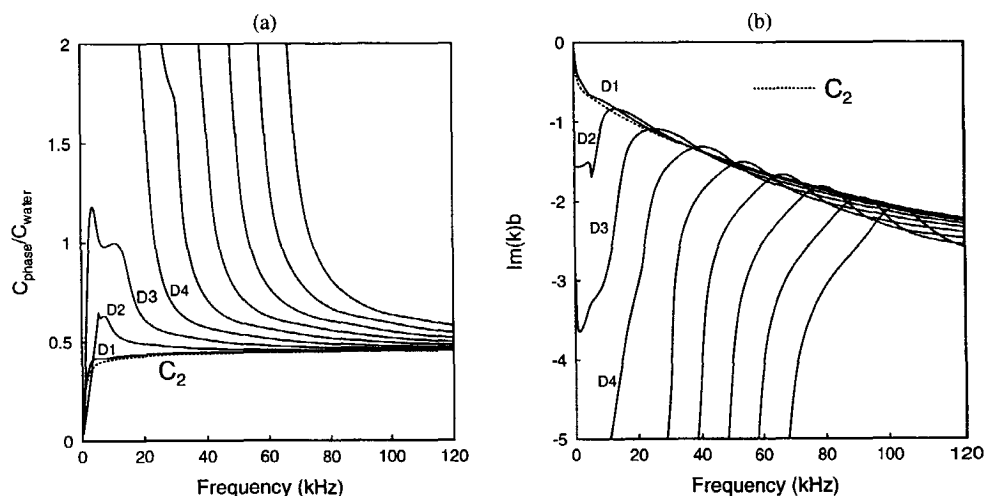


Figure 8.26: Frequency dependence of the phase velocity (a) and damping coefficient (b) for the D modes. The free-field velocities and damping coefficients of slow wave are also shown. The calculations were performed for Bentheimer sandstone with a diameter of 76.85 mm, i.e., $a/b = 0.998$ and $c/b = 1.62$.

S modes

For the small gap configuration $a/b = 0.998$, the S mode did not appear in our computations. It is therefore interesting to investigate the behaviour of the S mode for a decreasing gap width. Fig. 8.27 shows the phase velocity and the damping coefficient for the S mode for different diameters of the Bentheim porous cylinder. The inner diameter of the shock tube is kept constant (77.0 mm). From these plots we observe that for a decrease of the gap width the phase velocity of the S mode decreases and the damping coefficient increases. Detailed computations showed that the local maxima in the damping coefficients occur for those frequencies where the phase velocity of one of the D modes is equal to the phase velocity of the S mode. Hence, there is an interaction between the S mode and the D modes. For very small gap widths (diameters 76.6 and 76.7 mm), the S mode joins one of the D modes at a certain frequency, and below this frequency the S mode does not exist. For the diameter of 76.85 mm, the S mode does not exist in the 1-120 kHz frequency range. A possible explanation is that the radial motions of the fluid and the solid are suppressed by the presence of the wall of the shock tube.

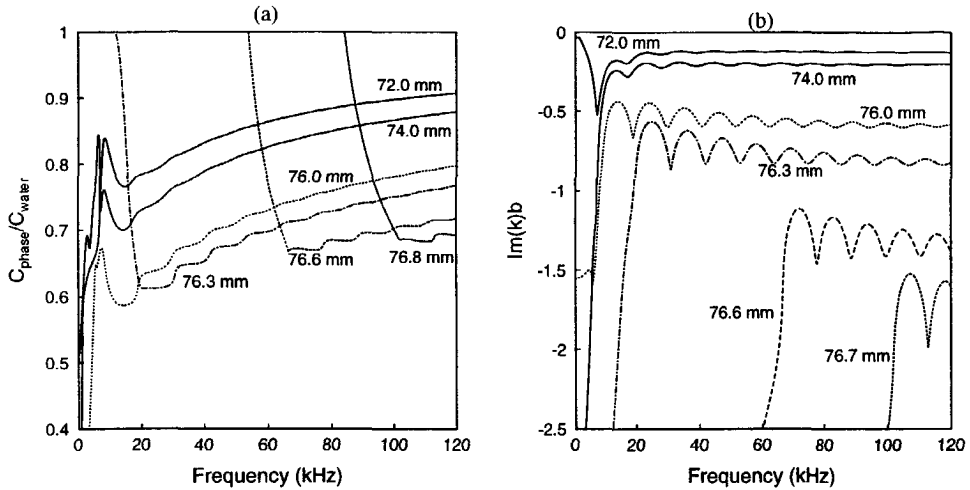


Figure 8.27: Frequency dependence of the phase velocity (a) and damping (b) for the S mode. Results are given for several diameters of a Bentheimer sandstone cylinder. The inner diameter of the shock tube is 77.0 mm.

8.3.3 Permeability effects

We performed computations to study permeability effects for the large gap configuration: $a = 0.099b$. As reference parameters, we used the parameters of Bentheimer sandstone as given in Table E.1. The permeability was varied by two orders of magnitude with respect to the reference permeability k_{ref} . As an illustration, we first discuss the permeability effects for the free-field Biot waves and for the pseudo-Stoneley wave in the flat-interface configuration. The phase velocities and damping coefficients of the fast, the slow, and the shear wave are given in Fig. 8.28. Please note that the absolute values of the damping coefficients are shown on a logarithmic scale. The permeability strongly influences the damping coefficients of all the wave types. The velocities of the fast and shear wave are weakly sensitive to permeability changes. The slow wave phase velocity, however, is strongly influenced by the permeability changes.

Fig. 8.29 gives for the flat-interface configuration the phase velocities and the damping coefficients for the pseudo-Stoneley wave PS_{41} at 120 kHz. The properties of this wave were discussed in Chapter 6. Parameter values are given in Table E.1. The phase velocity shows a weak dependence on the permeability. The damping of the pseudo-Stoneley wave shows the same characteristics as the damping of the fast and the shear wave in Fig. 8.28.

We now discuss the permeability effects in the shock tube configuration. In Fig. 8.30 the results of the S mode are given for different permeabilities. At low frequencies the phase velocity increases as the permeability decreases. At higher frequencies the reverse situation is obtained. These phenomena are in agreement with the results of Schmitt *et al.* (1988a) for the Stoneley mode in a permeable borehole. The damping coefficients of the S mode are strongly influenced by the permeability changes. We notice that the shape of the curve can change dramatically. For the L1 mode we observe from Fig. 8.31 that

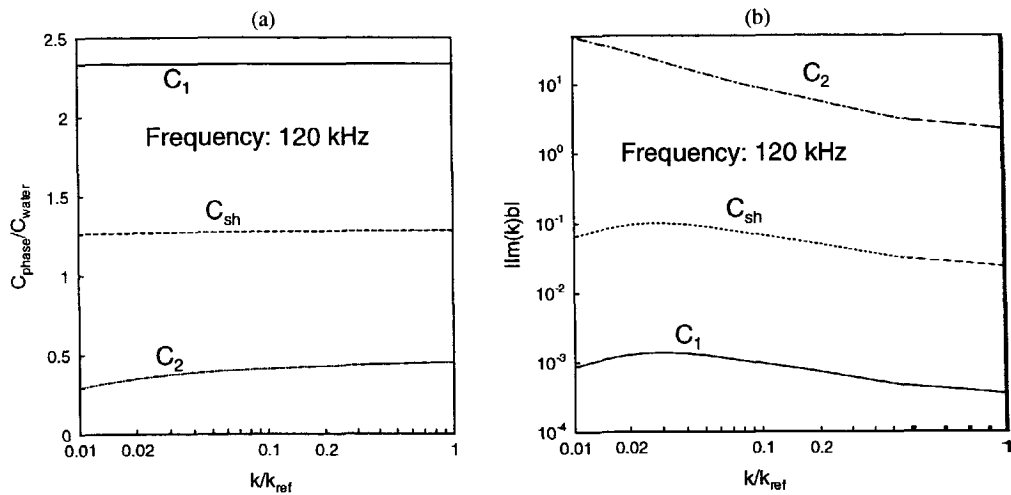


Figure 8.28: Permeability dependence of the phase velocity (a) and damping coefficients (b) for the free-field fast, slow and shear waves at 120 kHz. Note that the absolute value *of the* damping coefficient is shown on a logarithmic scale. Parameter values are given in Table E.1.

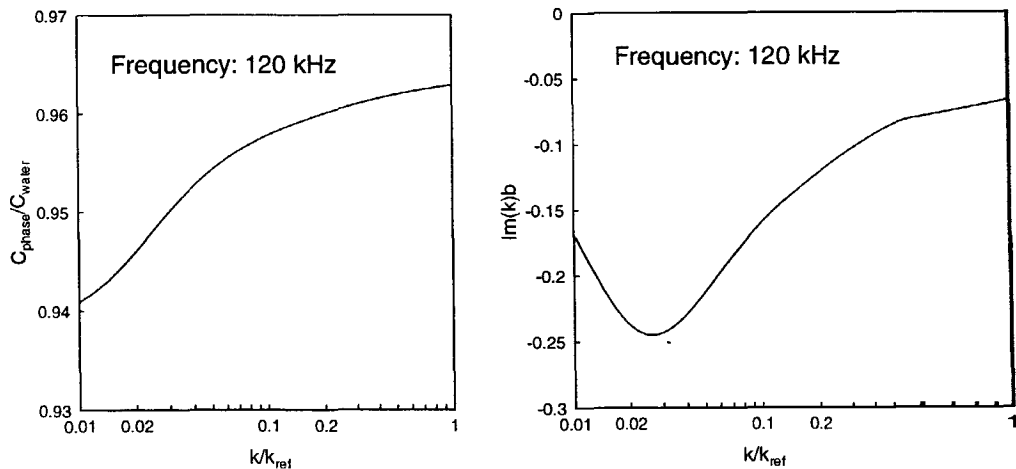


Figure 8.29: Permeability dependence of the phase velocity (a) and damping (b) for the Pseudo-Stoneley mode PS_{11} . Parameter values are given in Table E.1.

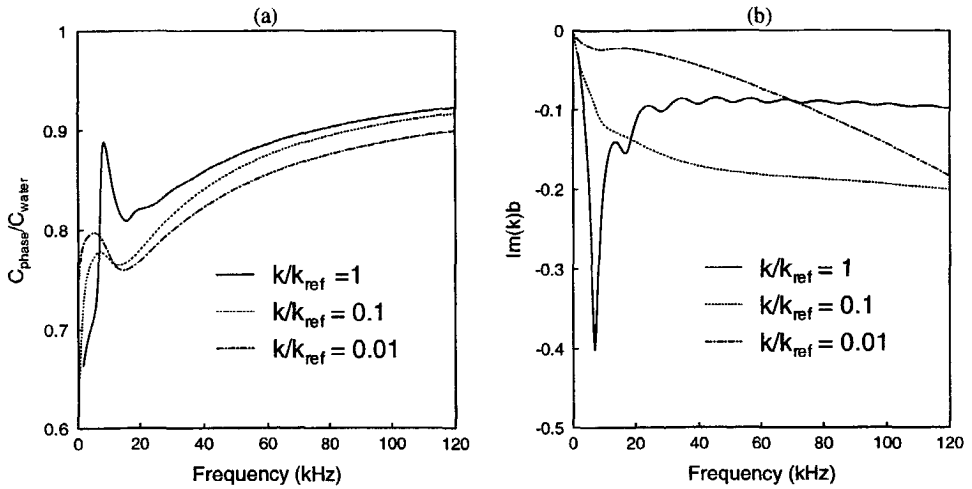


Figure 8.30: Frequency dependence of the phase velocity (a) and damping (b) for the S mode. Parameters are given in Table E.1. Computations include the compressibility of the grains and the elasticity of the wall. $a/b = 0.909$ and $c/b = 1.62$.

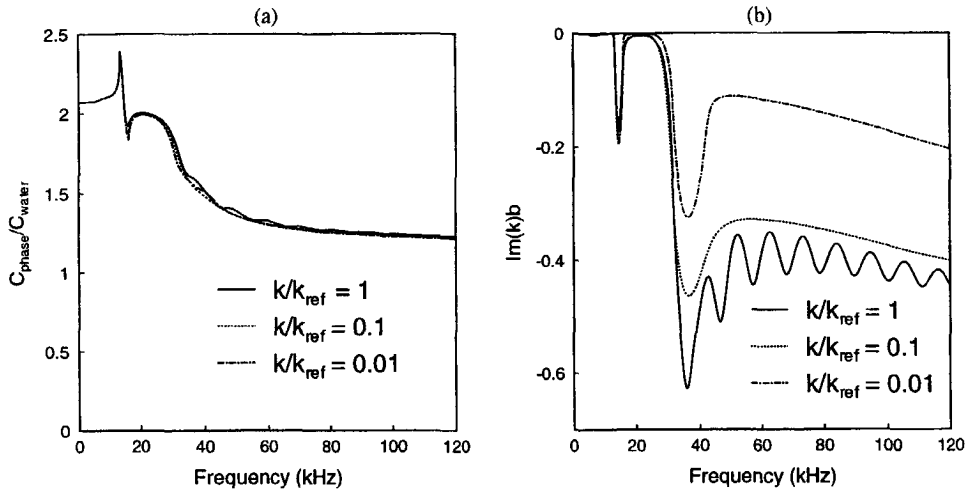


Figure 8.31: Frequency dependence of the phase velocity (a) and damping (b) for the L1 mode. Parameters are given in Table E.1. Computations include the compressibility of the grains and the elasticity of the wall. $a/b = 0.909b$ and $c/b = 1.62$.

the influence of the permeability on the phase velocity can be neglected. The damping coefficients, however decrease for a decreasing permeability.

Summarizing, we may say that the phase velocities of the S and L1 mode are weakly sensitive to permeability changes, especially at high frequencies. The damping coefficients, however, are strongly influenced by permeability changes. Winkler *et al.* (1989) found similar phenomena for a borehole configuration. From the discussion as given above we can conclude that the permeability dependence of the S and L1 mode have generally the same characteristics as the borehole wave modes.

8.3.4 Shear effects

We studied the influence of the shear modulus on the phase velocities of the L and S modes. In Fig. 8.32 the solid lines represent the results for $G = 0.7G_{ref}$, while the dashed lines correspond to the results for the reference parameters given in Table E.1. The computations were performed for a Bentheim cylinder with a diameter of 70.0 mm. In Fig. 8.32(a) the free-field velocities are shown, while in Fig. 8.32(b) the phase velocities of the L and S modes are given. The character of the L and S modes is insensitive to changes of the shear modulus. Quantitatively, the phase velocities decrease when the shear modulus is decreased. The damping coefficients are weakly sensitive to changes in the shear modulus. From Figs. 8.32 and 8.22 we observe that shear effects and compressibility effects are similar.

8.3.5 Slow formation

Up to now, our parameter studies were limited to the Bentheimer sandstone. This is usually called a fast formation. This means that the free-field velocity of the shear wave is higher than the water velocity. To study a slow formation we used the parameters given in Table E.3 (N5B). Fig. 8.33 shows the results of the wave mode computations for this rock type in the 1-150 kHz frequency range. Significant experimental data could be obtained in the high-frequency regime for this formation (see Fig. 10.16). The free-field velocities of the three Biot waves are also given. Similar to the Bentheim case, we observe S, L, M, and D modes. In the following, we give a short analysis of the character of the S, L1 and L2 mode.

As can be observed from Fig. 8.33(a), at high frequencies the S mode has a lower phase velocity than the phase velocity of the free-field slow wave. This means that this wave mode corresponds to the true Stoneley wave. The properties of this wave type were discussed in Chapter 6. For low frequencies the S mode has a velocity in between the shear wave velocity and the slow wave velocity. In this frequency range bulk wave phenomena are present.

The shape of the L1 mode in Fig. 8.33 is different from the L1 Bentheim mode, but nevertheless this mode has the same behaviour at high and low frequencies as the L1 Bentheim mode. At high frequencies, its phase velocity reaches the water velocity and the L1 mode is primarily based on wave motion in the gap. The phase velocity at low frequencies is nearly equivalent to the fast wave velocity. The L2 mode is characterized by the high-frequency limit of the phase velocity and the cut-off frequency. At high frequencies, the L2 phase velocity reaches the shear velocity.

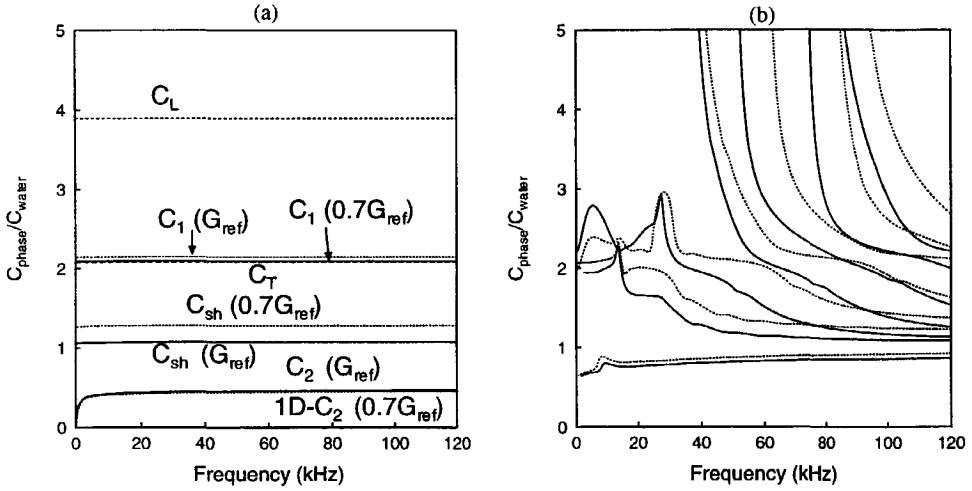


Figure 8.32: Frequency dependence of the free-field velocities (a) and the phase velocities of the L and S modes (b). The solid lines indicate the computations with $G = 0.7G_{\text{ref}}$. The dashed lines indicate the computations $G = G_{\text{ref}}$. In the computations the elasticity of the wall is included, as well as the compressibility of the grains. The computations are performed for Bentheimer sandstone cylinder with a diameter of 70.0 mm, i.e., $a/b = 0.909$ and $c/b = 1.62$. As reference parameters, we used the values of Table E.1.

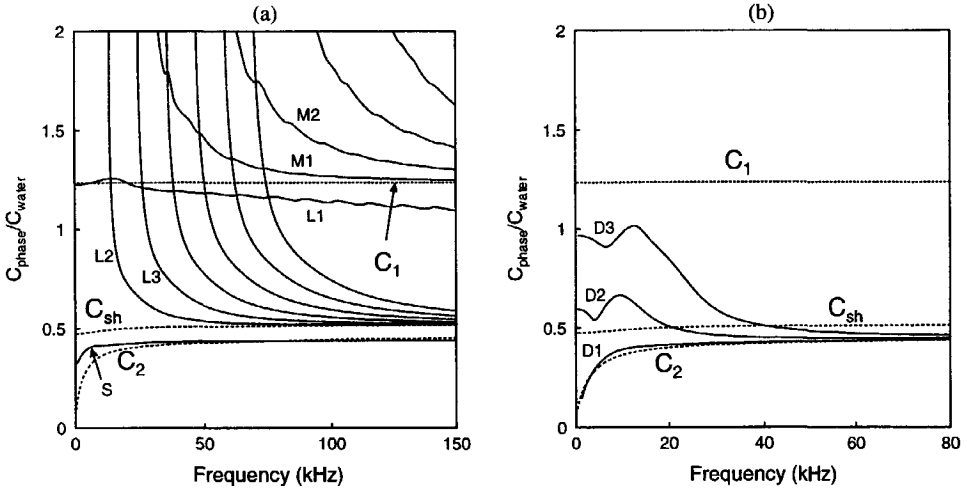


Figure 8.33: Frequency dependence of the phase velocities of the L, M, and S modes (a) and the D modes (b). In the computations the elasticity of the wall is included, as well as the compressibility of the grains. The computations are performed for the N5b cylinder with a diameter of 70.0 mm, i.e., $a/b = 0.909$ and $c/b = 1.62$.

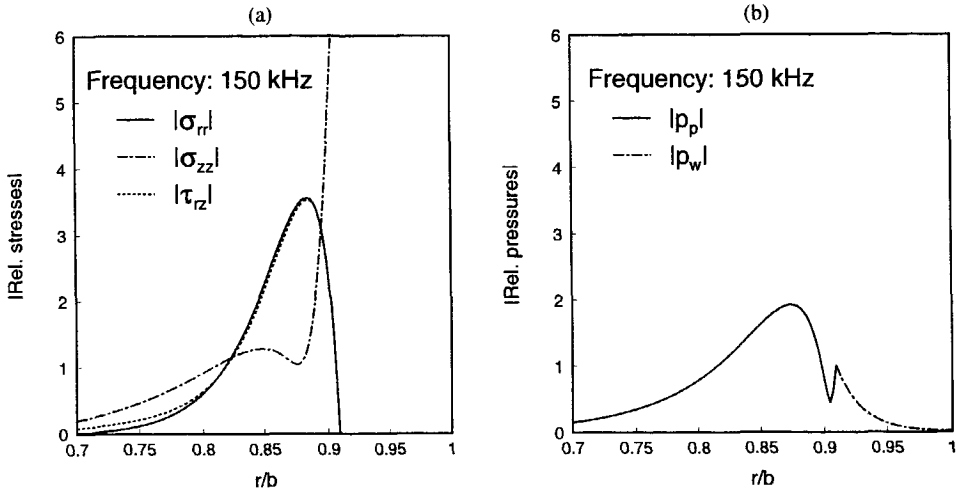


Figure 8.34: Radial distributions of the stresses (a) and pressures (b) for the S mode at 150 kHz. Both the stresses and pressures were normalized by $p_p|_{r=a}$. In the computations the elasticity of the wall is included, as well as the compressibility of the grains. The computations were performed for the N5b cylinder with a diameter of 70.0 mm, i.e., $a/b = 0.909$ and $c/b = 1.62$.

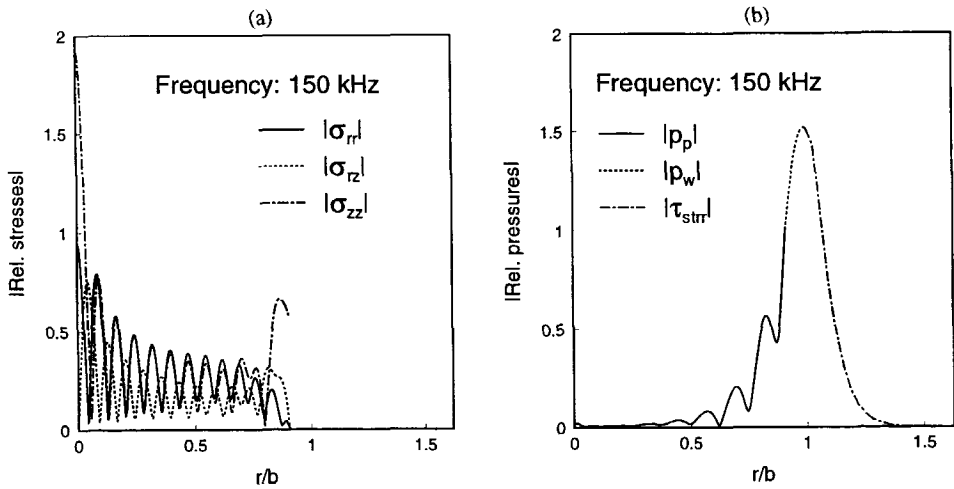


Figure 8.35: Radial distributions of the stresses (a) and pressures (b) for the L1 mode at 150 kHz. Both the stresses and pressures were normalized by $p_p|_{r=a}$. In the computations the elasticity of the wall is included, as well as the compressibility of the grains. The computations are performed for the N5b cylinder with $a/b = 0.909$ and $c/b = 1.62$.

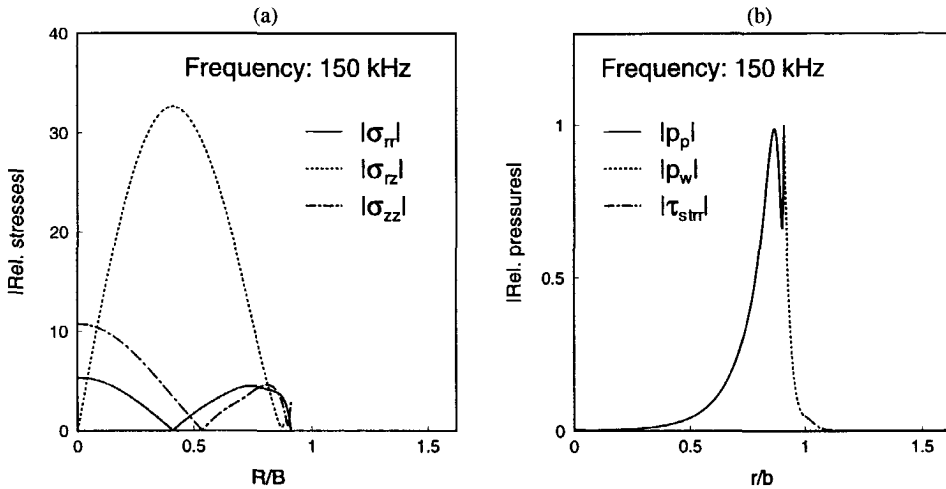


Figure 8.36: Radial distributions of the stresses (a) and pressures (b) for the L2 mode at 150 kHz. Both the stresses and pressures were normalized by $p_p|_{r=a}$. Note the different scales in Fig. (a) and (b). In the computations the elasticity of the wall is included, as well as the compressibility of the grains. The computations are performed for the N5b cylinder with $a/b = 0.909$ and $c/b = 1.62$.

The radial distributions of the stresses and pressures are given for the S mode in Fig. 8.34. These plots clearly show the exponential decay away from the surface for both stresses and pressures. Note that the pressure amplitude at $r = b$ is small at 150 kHz.

In Fig. 8.35 the radial distributions of the stresses and pressures are given for the L1 mode. The stresses are oscillatory around an approximately uniform average. The maximum pressure occurs in the water-filled gap, while the pressures in the center of the cylinder are very small. For the L2 mode the radial distributions of the stresses and pressures are given in Fig. 8.36.

The shear stress component σ_{rz} is dominant over the pressure and the other stress component σ_{zz} and σ_{rr} . This is in agreement with the phase velocity of L2 mode, which is equal to the shear velocity.

8.4 Summary

As a summary we give the main points of this chapter:

1. The theory of wave modes has been applied to the porous cylinder in the shock tube. The so-called L modes are equivalent to the ones in a solid elastic cylinder. These modes are characterized by cut-off frequencies and their phase velocities in the high-frequency limit which are equal to the shear velocity.
2. A surface mode S occurs at the interface between a porous cylinder and a relatively large water-filled gap. At high frequencies this wave corresponds to the pseudo-

Stoneley wave in case of a Bentheimer sandstone cylinder, which is a fast formation. For one specific synthetic slow formation, we found that this wave corresponds to the true Stoneley wave.

3. We investigated the permeability effects and the shear effects on the phase velocities and damping coefficients of the S mode and L1 mode. The surface mode S is sensitive to both the permeability and the shear velocity. This conclusion is valid both for our shock tube set-up and also for the borehole configuration.
4. Extra bulk wave modes, the D modes, occur due to the presence of the Biot slow wave. The damping of the higher-order D modes is at least as high as the damping of the Biot slow wave itself.
5. We investigated the influence of the compressibility of the grains on the phase velocities of the L and S modes. We found that the higher-order L modes are sensitive to the compressibility of the grains.
6. We studied the gap effects on the phase velocities and damping coefficients of the L, S, and D modes. We found that for the small gap configuration one of the L modes is equivalent to the free-field solution for the fast wave over nearly the entire frequency range. One of the D modes is identical to the free-field solution of the slow wave. The phase velocities and damping coefficients of the S mode are strongly sensitive to the dimensions of the gap. The S mode does not exist at lower frequencies for a very small gap width.
7. The elasticity of the wall of the shock tube influences the wave modes in the lower frequency range in case of a large gap. For a small gap the compliance effects of the wall are important over the entire frequency range.

Chapter 9

Prony's method

It is very attractive to consider Biot's theory in the frequency domain. The transition from the dominance of viscous effects to the dominance of inertia effects, marked by the roll-over frequency ω_c , strongly influences the phase velocities and damping coefficients of the waves. Moreover, the two-dimensional modelling as described in Chapter 8 is carried out in the frequency domain. Therefore it is important to convert the experimental data from the time domain to the frequency domain.

There are several methods to estimate the wavenumbers of the different wave modes in a time-recorded pressure signal. For an overview of a number of (classical) spectral estimation methods, the reader is referred to the work of Kay and Marple (1981) and Marple (1987). Schoenberg *et al.* (1981) used Fourier transforms both in time and in space for their borehole measurements, but they observed a poor resolution in the spatial domain. They tried to improve their results by using a Maximum Likelihood Method (MLM) but were not quite successful. A better performance of the MLM was obtained by Hsu and Baggeroer (1986). However, this technique is computationally intensive. A technique which is reported to perform as well as the MLM while requiring less computational effort is the one by Prony (Lang and McClellan 1980, Lang *et al.* 1987, Tufts and Kumaresan 1982). In 1795, Gaspard Riche, Baron de Prony, assumed that laws governing expansion of various gases could be represented by sums of damped exponentials (Marple 1987). The modern least square version of the exponential modelling method has evolved significantly from Prony's original procedure. Tjhuis (1987) provides results of Prony's method for electromagnetic fields. Lang (1987) applied Prony's method to estimate phase velocities from arrays of sonic logging waveforms. Several other papers also reported the successful use of Prony's method in geophysics and solid mechanics, also in the presence of noise (Winkler *et al.* 1989, Ellefsen *et al.* 1989, Plona *et al.* 1992, Grosh and Williams 1993, Vollman *et al.* 1997, Hsu *et al.* 1997).

Ellefsen *et al.* (1993) presented their so-called homomorphic processing method which shows a better performance than Prony's method. However, it can only be used for a single wave mode. One of the advantages of Prony's technique is that it enables us to analyse a number of modes which are not separated in time. This is especially important in the case of our shock tube, where several wave modes add up to constitute the total pressure signal. Prony's method can be used as a first guess in the parametric estimation method of Hsu and Emmersoy (1992). Their method, however, is computationally intensive. For

these reasons, we use Prony's method for the processing of our data.

The approach of this chapter is as follows. First, we explain the basics of Prony's method as described by Hildebrand (1956). Subsequently, we discuss the extended versions which account for noise.

9.1 Noiseless signals

We apply Prony's method by transforming the pressure signals to the frequency domain using FFT. Then we assume a finite number (say M) of travelling harmonic waves and we write:

$$\hat{p}(\omega, x) = \bar{p}_1 e^{-ik_1 x} + \bar{p}_2 e^{-ik_2 x} + \dots + \bar{p}_M e^{-ik_M x}. \quad (9.1)$$

This means that at any position $(n-1)\Delta x$ ($n = 1, \dots, N$), the pressure $\hat{p}(\omega, n)$ can be written in terms of the pressure components $\bar{p}_1, \bar{p}_2, \dots, \bar{p}_M$:

$$\hat{p}(\omega, n) = \bar{p}_1 e^{-ik_1(n-1)\Delta x} + \bar{p}_2 e^{-ik_2(n-1)\Delta x} + \dots + \bar{p}_M e^{-ik_M(n-1)\Delta x}. \quad (9.2)$$

By substitution of

$$z_j = e^{-ik_j \Delta x}, \quad j = 1, \dots, M, \quad (9.3)$$

we can write for a given frequency ω :

$$\hat{p}(n) = \bar{p}_1 z_1^{(n-1)} + \bar{p}_2 z_2^{(n-1)} + \dots + \bar{p}_M z_M^{(n-1)}. \quad (9.4)$$

Written in this way it is possible to determine at a given frequency ω the values of $\bar{p}_1, \bar{p}_2, \dots, \bar{p}_M$ and the values of z_1, z_2, \dots, z_M . If the number of pressure signals N is at least two times the number of wave components M the system can be solved. However, this is not straightforward because of the powers of z . To overcome these problems Prony's method uses the so-called Linear Prediction techniques (Makhoul 1975). We illustrate these techniques assuming two travelling waves. For the extended versions which account for noise the general expressions are given in Section 9.2.

In the linear prediction techniques the pressure values on $n\Delta x$ are predicted using the values on $(n-1)\Delta x$ and $(n-2)\Delta x$. Using Equation (9.4) we can write ($M=2$):

$$\begin{aligned} a_0 \hat{p}(n) + a_1 \hat{p}(n-1) + a_2 \hat{p}(n-2) &= a_0 (\bar{p}_1 z_1^{n-1} + \bar{p}_2 z_2^{n-1}) \\ &+ a_1 (\bar{p}_1 z_1^{n-2} + \bar{p}_2 z_2^{n-2}) \\ &+ a_2 (\bar{p}_1 z_1^{n-3} + \bar{p}_2 z_2^{n-3}). \end{aligned} \quad (9.5)$$

By re-arranging we obtain:

$$\begin{aligned} a_0 \hat{p}(n) + a_1 \hat{p}(n-1) + a_2 \hat{p}(n-2) &= \bar{p}_1 z_1^{n-3} (a_0 z_1^2 + a_1 z_1 + a_2) \\ &+ \bar{p}_2 z_2^{n-3} (a_0 z_2^2 + a_1 z_2 + a_2). \end{aligned} \quad (9.6)$$

Up to now, a_0 , a_1 , and a_2 were still arbitrary. Let us choose a_0 , a_1 , and a_2 such that z_1 and z_2 are the roots of the equation

$$a_0 z^2 + a_1 z + a_2 = 0. \quad (9.7)$$

Subsequently, we can write with $a_0 = 1$:

$$-\hat{p}(n) = a_1 \hat{p}(n-1) + a_2 \hat{p}(n-2). \quad (9.8)$$

The same can be done for the pressure value recorded at $(n-1)\Delta x$:

$$-\hat{p}(n-1) = a_1 \hat{p}(n-2) + a_2 \hat{p}(n-3). \quad (9.9)$$

In this way we need four pressure values to determine the coefficients of the polynomial a_1 and a_2 . Once the coefficients of the polynomial are known it is straightforward to determine z_1 and z_2 , the zero's of the polynomial. Then Equation (9.3) can be used in its inverse form to determine the real and imaginary parts of the wavenumbers k_1 and k_2 :

$$\Im m(k) = \frac{\ln|z|}{\Delta x}, \quad (9.10)$$

$$\Re e(k) = -\frac{\arg(z)}{\Delta x}. \quad (9.11)$$

By the property $-\pi < \arg(z) < \pi$ we obtain a condition for the value of Δx :

$$|\Re e(k)\Delta x| < \pi. \quad (9.12)$$

In the case of a negligible amount of noise this method works very well as illustrated in the following example. We take

$$\hat{p}(x) = e^x + 2e^{2x} \quad (9.13)$$

as a function to generate four pressure values \hat{p}_1 , \hat{p}_2 , \hat{p}_3 and \hat{p}_4 . This means that $\Im m(k_1) = 1$ and $\Im m(k_2) = 2$, and that $\bar{p}_1 = 1$, and $\bar{p}_2 = 2$. For $\Delta x = 1$ we obtain the following values:

$\hat{p}(1)$	$x = 0$	3
$\hat{p}(2)$	$x = 1$	17.496
$\hat{p}(3)$	$x = 2$	116.585
$\hat{p}(4)$	$x = 3$	826.943

The rounding-off errors introduce a very small amount of noise. Using the forward prediction as explained above the following polynomial can be derived:

$$z^2 - 10.106z + 20.077 = 0. \quad (9.14)$$

The zero's of this equation are $z_2 = 7.3886$ and $z_1 = 2.7174$, which give $\Im m(k_2) = 1.9999$ and $\Im m(k_1) = 0.9997$. The real parts of k_1 and k_2 are equal to zero. In this case 4 pressure values are sufficient to reconstruct the wavenumbers.

The influence of a larger amount of noise can be investigated using the truncated values of the pressures:

$\hat{p}(1)$	$x = 0$	3
$\hat{p}(2)$	$x = 1$	17
$\hat{p}(3)$	$x = 2$	116
$\hat{p}(4)$	$x = 3$	826

These values give the following polynomial:

$$z^2 - 8.576z + 9.93 = 0. \quad (9.15)$$

We obtain bad results for reconstruction of the wavenumbers: $\Im m(k_2) = 1.97$ and $\Im m(k_1) = 0.322$. This example clearly shows the sensitivity to noise of the original version of Prony's method.

9.2 Least squares Prony's methods

To account for noisy signals extended versions were developed, which is necessary for the application of Prony's method in experiments. In the original Prony's method the number of spatial measurements N is equal to $2M$, where M is the number of wave components in the data. Using a number of equations for the linear prediction coefficients larger than the number of unknowns, a problem is stated which can be solved by the so-called least squares approximation (LS). This approach was already proposed by Hildebrand (1956), who improved the performance of Prony's method in the presence of noise.

However, a more efficient measure to account for noise is obtained by application of the method of overdetermination, in combination with the LS method (Tufts and Kumaresan 1982, Braun and Ram 1987, Grosh and Williams 1993). The recorded signals in the presence of noise can be written as follows:

$$\hat{p}(n) = \sum_{j=1}^M \tilde{p}_j z_j^{(n-1)} + w(n), \quad (9.16)$$

where $w(n)$ is the noise function. In the method of overdetermination the noise function is then written as a sum of additional wave components so that we obtain:

$$\hat{p}(n) = \sum_{j=1}^M \tilde{p}_j z_j^{(n-1)} + \sum_{j=M+1}^L \tilde{p}_j z_j^{(n-1)}. \quad (9.17)$$

The characteristic polynomial, a generalized version of Equation (9.7), determines the roots more accurately, but also includes noise roots:

$$\Phi(z) = \prod_{i=1}^M (z - z_j) \prod_{i=M+1}^L (z - z_j) = \sum_{i=0}^L a_i z^{L-i}, \quad (9.18)$$

with $a_0 = 1$.

The procedure described in Section 9.1 can be generalized from two roots to L roots. The coefficients a_j are related to the pressure values $\hat{p}(n)$ by a set of linear equations (see Equations (9.8) and (9.9)). In matrix form, we write:

$$\mathbf{B}\mathbf{a} = \mathbf{g}, \quad (9.19)$$

where

$$\mathbf{B} = \begin{pmatrix} \hat{p}(L) & \hat{p}(L-1) & \dots & \hat{p}(1) \\ \hat{p}(L+1) & \hat{p}(L) & \dots & \hat{p}(2) \\ \vdots & \vdots & \ddots & \vdots \\ \hat{p}(N-1) & \hat{p}(N-2) & \dots & \hat{p}(N-L) \end{pmatrix}, \quad (9.20)$$

and

$$\mathbf{a} = \begin{pmatrix} a_1 & a_2 & \dots & a_L \end{pmatrix}^T, \quad (9.21)$$

$$\mathbf{g} = \begin{pmatrix} -\hat{p}(L+1) & -\hat{p}(L+2) & \dots & -\hat{p}(N) \end{pmatrix}^T. \quad (9.22)$$

This system of L unknowns and $(N-L)$ equations can be solved using the LS approximation. Once the coefficients of the characteristic polynomial have been found it is straightforward to find the L solutions of Equation (9.18). We used the Nag Fortran Library routine C02AFF (Group 1995) to determine the roots of the complex polynomial. The wavenumbers follow from the inversions as given by the Equations (9.10) and (9.11). Subsequently it is possible to determine the amplitudes \tilde{p} of the different wave components. Again by the LS approximation we can solve the following set of equations:

$$\begin{pmatrix} 1 & 1 & \dots & 1 \\ z_1^1 & z_2^1 & \dots & z_L^1 \\ z_1^2 & z_2^2 & \dots & z_L^2 \\ \vdots & \vdots & \ddots & \vdots \\ z_1^{(N-1)} & z_2^{(N-1)} & \dots & z_L^{(N-1)} \end{pmatrix} \begin{pmatrix} \tilde{p}_1 \\ \tilde{p}_2 \\ \vdots \\ \tilde{p}_L \end{pmatrix} = \begin{pmatrix} \hat{p}(1) \\ \hat{p}(2) \\ \vdots \\ \hat{p}(N) \end{pmatrix}. \quad (9.23)$$

The total procedure gives in this way the wavenumbers and the amplitudes of the model given in Equation (9.17). However, a practical implementation of the overdetermination requires the answers on the following questions:

- What is the number M of wave components in the data ?
- What is the necessary extent of overdetermination $(L - M)$?
- How can the true poles be distinguished from the noisy poles ?

Before discussing these questions we treat the solution of the LS problem, which is not trivial because of the overdetermination. The followed approach provides also some tools to determine the number of wave components present in the data.

9.2.1 Singular value decomposition

As the number of wave components M is a priori unknown, the principle of overdetermination has to be applied in both the noisy and the noise less case, i.e., $L > M$. In the absence of noise, the rank r of matrix \mathbf{B} , is equal to the number of wave components M . If the system is overdetermined, and the amount of noise is zero, the matrix \mathbf{B} is

called rank deficient. Then the standard LS techniques which use the normal equations fail (Bjoerck 1996). In case of the presence of a small amount of noise the matrix \mathbf{B} is not exactly rank deficient. For the general case we write therefore:

$$M \leq r \leq L. \quad (9.24)$$

Following Marple (1987), Braun and Ram (1987), and Grosh and Williams (1993) we solve the LS problem using singular value decompositions (SVD). The vector space of $m \times n$ complex matrices is designated by $\mathbf{C}^{m \times n}$ and the vector space of $m \times n$ real matrices by $\mathbf{R}^{m \times n}$. The SVD of matrix $\mathbf{B} \in \mathbf{C}^{(N-L) \times L}$ is (Bjoerck 1996):

$$\mathbf{B} = \mathbf{U} \mathbf{\Sigma} \mathbf{V}^H, \quad (9.25)$$

where $\mathbf{\Sigma} \in \mathbf{R}^{(N-L) \times L}$, $\mathbf{U} \in \mathbf{C}^{(N-L) \times (N-L)}$ and $\mathbf{V} \in \mathbf{C}^{L \times L}$. The superscript H denotes the conjugate transposition: $\mathbf{V}_{ij}^H = \mathbf{V}_{ji}^*$. The matrix $\mathbf{\Sigma}$ contains the so-called singular values of matrix \mathbf{B} . For $(N-L) \geq L$ we write:

$$\mathbf{\Sigma} = \begin{pmatrix} \mathbf{\Sigma}_1 & 0 \\ 0 & \mathbf{\Sigma}_2 \\ 0 & 0 \end{pmatrix}, \quad (9.26)$$

where $\mathbf{\Sigma}_1 = \text{diag}(\sigma_1, \sigma_2, \dots, \sigma_M)$ and $\mathbf{\Sigma}_2 = \text{diag}(\sigma_{M+1}, \sigma_{M+2}, \dots, \sigma_L)$. The singular values are denoted by σ_1 and $\sigma_2 \dots$ etc., and are sorted in descending order ($\sigma_1 \geq \sigma_2 \geq \dots \geq 0$). The matrices \mathbf{U} and \mathbf{V} are unitary matrices which means that $\mathbf{U} \mathbf{U}^H = \mathbf{I}$. The first L columns of the matrices \mathbf{U} and \mathbf{V} are the left-hand and right-hand singular vectors of \mathbf{B} :

$$\begin{aligned} \mathbf{B} \mathbf{v}_i &= \sigma_i \mathbf{u}_i, \\ \mathbf{B}^H \mathbf{u}_i &= \sigma_i \mathbf{v}_i, \end{aligned} \quad (9.27)$$

where $i = 1, \dots, L$. Please note that σ_i is a scalar, and that we do not apply the Einstein convention here. The i -th columns of \mathbf{U} and \mathbf{V} are denoted by \mathbf{u}_i and \mathbf{v}_i respectively. In the noise less case the problem is exactly rank-deficient ($r = M, L > M$) and the elements of $\mathbf{\Sigma}_2$ are equal to zero. If a very small amount of noise is introduced the problem is not exactly rank-deficient, $M \leq r \leq L$ and the elements of $\mathbf{\Sigma}_2$ are non-zero. However, it can be imagined that the elements of $\mathbf{\Sigma}_2$ are small related to the elements of $\mathbf{\Sigma}_1$. Then we can define a so-called break point between the singular values, which is defined by a large change in magnitude between two subsequent singular values i.e. $\sigma_{i+1}/\sigma_i < \epsilon$, where ϵ is the maximum noise-induced variation in the matrix. Another definition of the break point is the first σ_i for which

$$\frac{\sigma_i}{\sigma_{max}} < \epsilon, \quad (9.28)$$

where σ_{max} is the largest singular value. For high signal-to-noise ratios (SNR's) it is therefore possible to obtain a first estimate of the number of wave components M by the number of i for which the break point occurs (Braun and Ram 1987, Grosh and Williams 1993). If the SNR decreases, the break point will be ill-defined and the determination of M becomes complicated.

The rank deficient LS problem has an infinite number of solutions. In order to obtain a unique solution, the minimum norm solution can be used. This solution constrains the length of the solution vector, \mathbf{a}_{LS} , to be the minimum. The resulting solution is (Bjoerck 1996)

$$\mathbf{a}_{LS} = \mathbf{V} \begin{pmatrix} \Sigma_{r1} & 0 & 0 \\ 0 & \Sigma_{r2} & 0 \end{pmatrix} \mathbf{U}^H \mathbf{g} = \mathbf{B}^\# \mathbf{g}, \quad (9.29)$$

where $\Sigma_{r1} = \text{diag}(1/\sigma_1, 1/\sigma_2, \dots, 1/\sigma_M)$. For the exact rank deficient case the elements of Σ_{r2} are equal to zero, otherwise $\Sigma_{r2} = \text{diag}(1/\sigma_{M+1}, 1/\sigma_{M+2}, \dots, 1/\sigma_L)$. The matrix $\mathbf{B}^\#$ is called the pseudo-inverse of matrix \mathbf{B} (Bjoerck 1996).

In this way the SVD can be used to solve the rank-deficient problem as stated by Equation (9.19). In case of high SNR's it is also possible to determine the true number of exponents which are present in the data. There are several ways to determine the SVD of a matrix (Bjoerck 1996). We used the Nag Fortran Library Routine F02XEF to determine the SVD of matrix \mathbf{B} .

9.2.2 Implementation

For a practical implementation of Prony's technique in case of an overdetermined system, we first have to determine first the number of wave components M . Subsequently, we have to choose the necessary extent of overdetermination $(L - M)$. The last step of the procedure is the determination of the roots which correspond to the signal roots. Braun and Ram (1987) propose the following techniques for the first two steps. A rough estimate of the number M has to be made on physical grounds, after which a value of L is chosen which is larger than M . Subsequently the SVD is used and the singular values are evaluated by definition of the break point criterion of Equation (9.28). Note that the definition of the value of ϵ can be problematic in case of real experiments. If none of the singular values satisfies this criterion the number of L is increased until a break point is found. In this way an approximation of M is obtained. In order to determine the necessary extent of overdetermination $(L - M)$ the number of L is increased further. The results for the wavenumbers are evaluated now. If at least M wavenumbers remain unaltered in the k -plane for increasing L , the extent of overdetermination $(L - M)$ is large enough. Braun and Ram (1987) found the following range for L :

$$1.5M < L < 3M. \quad (9.30)$$

It is important to realize that this range of values is derived empirically from synthetic data with white noise. No guarantees are given that it works for real experiments with non-white noise. Furthermore the SVD technique with the break point method only works for high SNR's. For low SNR's the value of M can only be estimated roughly. We come back to these methods in the discussion of our experimental results. Once the extent of overdetermination $(L - M)$ is known, it is possible to discriminate between the true and the noisy poles. This can be done by the following approaches (Braun and Ram 1987, Lang *et al.* 1987):

1. By repetition of the experiment the noise in the signals will be varied. Therefore the noisy poles will move in the complex k -plane, while the true poles remain, approximately, at the same positions. A clustering algorithm can be used to determine the

moving poles, which are the noisy poles, and the true poles. A criterion must be used to define the conditions for which a pole can be labelled as a moving pole.

2. Starting from the necessary extent of overdetermination the value of L can be increased. The noisy poles are perturbed again, while the true poles remain at the same positions in the complex k -plane. Again a clustering algorithm can be used to determine the true poles.
3. Option 1 can be simulated by the introduction of arbitrary perturbations on the elements of matrix Σ_{r2} . After calculating the SVD of matrix \mathbf{B} , we simulate a number of experiments by perturbation of $\sigma_{M+1} \dots \sigma_L$. Therefore this method is called the perturbation method. Those poles which cluster within a fixed area are the true poles.
4. Power editing of the data. Wave components with an amplitude \tilde{p}_j which fall below a certain threshold, based on the LS approximation error, are assumed to be noisy poles. The drawback of this method is that true poles with a small amplitude are removed.

Grosh and Williams (1993) used the perturbation method as described in option 3, in addition to criteria on physical grounds. Poles which correspond to unrealistic damping factors and/or phase velocities are identified as noisy poles. Braun and Ram (1987), and also Grosh and Williams (1993) applied their techniques to synthetic data, where white noise was added, and obtained good results. However, in experimental data the situation can become more complex, a fact which is also recognized by Grosh and Williams. Furthermore, we want to perform the editing at a large range of frequencies, while procedures as described above have to be performed at each frequency. This will enlarge the computational effort. Ellefsen *et al.* (1989) windowed out the signal of the wave of interest already in the time domain, which reduces the number of waves in the processing. In their experiments the noise data were deleted manually.

In the next chapter we discuss our experimental technique. We apply option 2 for the processing of our experimental results. As the number of recorded pressure signals is limited, we also apply a modified version of option 2. Instead of taking two values for L , we then use two values for Δx .

9.2.3 Forward and backward prediction

For slightly damped or undamped waves it is possible use the so-called backward prediction in addition to the forward prediction as given in Equation (9.20). In forward prediction $\hat{p}(N)$ is predicted based on the values of $\hat{p}(N-1)$, $\hat{p}(N-2)$, ..., $\hat{p}(N-L)$. In the backward prediction the method is performed the other way around. The pressure value $\hat{p}(1)$ is predicted based on the values $\hat{p}(2)$, $\hat{p}(3)$, ..., $\hat{p}(L+1)$. For undamped waves the linear predictor coefficients for the backward prediction are the complex conjugate values of the coefficients for the forward prediction (Marple 1987, Haykin 1985), so that

we can write (Tufts and Kumaresan 1982):

$$\mathbf{B} = \begin{pmatrix} \hat{p}(L) & \hat{p}(L-1) & \dots & \hat{p}(1) \\ \hat{p}(L+1) & \hat{p}(L) & \dots & \hat{p}(2) \\ \vdots & \vdots & \ddots & \vdots \\ \hat{p}(N-1) & \hat{p}(N-2) & \dots & \hat{p}(N-L) \\ \hat{p}^*(2) & \hat{p}^*(3) & \dots & \hat{p}^*(L+1) \\ \hat{p}^*(3) & \hat{p}^*(4) & \dots & \hat{p}^*(L+2) \\ \vdots & \vdots & \ddots & \vdots \\ \hat{p}^*(N-L+1) & \hat{p}^*(N-L+2) & \dots & \hat{p}^*(N) \end{pmatrix}, \quad (9.31)$$

and

$$\mathbf{a} = \begin{pmatrix} a_1 & a_2 & \dots & a_L \end{pmatrix}^T, \quad (9.32)$$

and

$$\mathbf{g} = \begin{pmatrix} -\hat{p}(L+1) & -\hat{p}(L+2) & \dots & -\hat{p}(N) & -\hat{p}^*(1) & -\hat{p}^*(2) & \dots & -\hat{p}^*(N-L) \end{pmatrix}^T. \quad (9.33)$$

Similar to the single use of forward prediction the system of equations can be solved using singular value decomposition. Note that for this case $\mathbf{B} \in \mathbb{C}^{2(N-L) \times L}$. For an elaborate discussion on the choice of the model order L we refer to Tufts and Kumaresan (1982). They suggest a value of L equal to $3N/4$ for the forward-backward prediction. For these values of L and N the system given by Equation (9.19) is underdetermined. Such a system has an infinite number of solutions and SVD can be used to obtain the minimum norm solution (Golub and Loan 1989). Again we remark that the analysis of Tufts and Kumaresan (1982) is based on synthetic signals.

9.3 Discussion and conclusions

In this chapter we discussed the main properties of Prony's technique. Using this technique it is possible to determine the wavenumbers of the different modes which are present in pressure signals. The wave modes need not to be separated in the time domain. This is especially advantageous in our shock tube experiments. To account for noise, extra wave components are added to the system. The total number of wave components which is needed, is discussed by several authors (Tufts and Kumaresan 1982, Braun and Ram 1987, Grosh and Williams 1993). They developed also sophisticated techniques in order to separate the true poles from the noisy poles. These procedures have to be carried out at a large number of frequencies, which gives a considerable amount of the computational effort. Moreover, these techniques are limited to experiments with high signal-to-noise ratios.

Chapter 10

Experimental results in the frequency domain

In this chapter the results of Prony's technique applied to the shock tube experiments are discussed. From the treatment of Prony's method in the previous chapter it has become clear that a large number of pressure signals at equidistant axial positions is needed. As we have only a limited number of pressure gauges available, the shock tube was modified so that we could record this large number of pressure signals by repeating the wave experiment. We present reflection measurements that serve as a test procedure for the application of Prony's method. It is shown that our experimental technique can be used to determine the frequency dependence of phase velocities in a broad frequency range. As an additional result of these test measurements we obtained the frequency dependence of the reflection coefficient. The last section is used to discuss the results of experiments on porous cylinders. Phase velocities and damping coefficients of bulk and surface waves are presented in a broad frequency range.

10.1 Modification of the conventional shock tube

In order to record a large number of pressure signals at equidistant positions the shock tube had to be modified. In the conventional measurements as described in Chapter 5, only three signals at 5 cm spacing could be recorded, while for the application of Prony's technique a number in the range of 20-40 is indispensable. Furthermore, the distance between two spatial samples has to be small (0.5 - 1 cm) in order to satisfy the condition $\Re(k)\Delta x < \pi$. We have developed a new part of the set-up to overcome these problems. The bottom section of the shock tube (Fig. 10.1) is designed so that the position of the porous sample in the shock tube can be varied with respect to the pressure gauges. By rotation of the screw gear, drawn in Fig 10.1, the piston pushes the porous cylinder in the upward direction with a system inaccuracy of a tenth of a millimeter. The position of the porous cylinder is measured electronically.

In this way a large number of equidistant pressure signals can be recorded by combining the experiments. The experimental procedure is organized as follows. A shock-tube run as described in Chapter 5 is performed. The pressure transducers are mounted as drawn in Fig. 5.1. The first pressure transducer P1 is mounted in the wall of the shock tube above the porous sample. The transducers P2, P3, and P4 are mounted in the wall of the shock tube along the porous sample. Then three pressure signals are recorded for $\Delta x = 5$

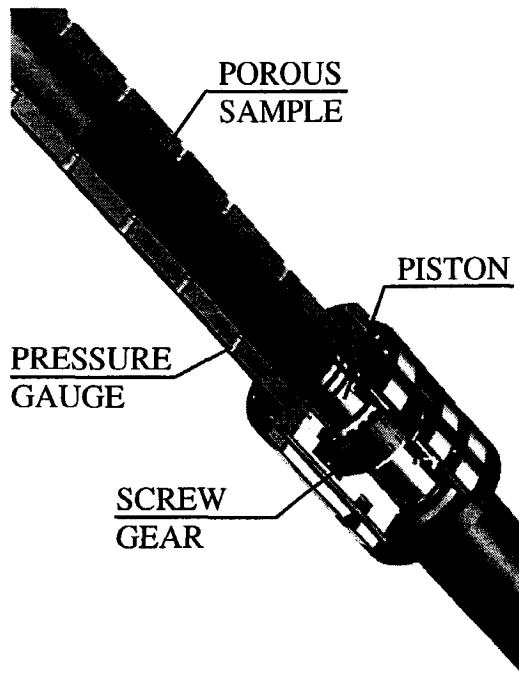


Figure 10.1: *Porous sample in test section of the shock tube.*

cm by P2, P3, and P4, while the transducer P1 is used as a reference. Subsequently, the sample is moved upwards over a distance of 0.5 cm. Then again a wave experiment is carried out and three more pressure signals are recorded. This procedure is repeated 10 times, which results in a record of 30 pressure signals 0.5 cm apart. Instead of the 0.5 cm we also used $\Delta x = 0.25$ cm in our experiments.

In the final result, measurements of several shock-tube runs are incorporated. This means that the repeatability of the experiments must be sufficiently high. It is observed that the signal shape reproduces quite well, but the amplitude of the signal displays some variation. Another complicating factor is that the time axis varies in each experiment. The data-acquisition is triggered at P1, while the distance between the top of the sample and P1 decreases when the porous cylinder is displaced in the upward direction. Furthermore, the 30 pressure signals are not sorted properly, and distributed over 10 files. In the first experiment, $P(t, 1)$, $P(t, 11)$ and $P(t, 21)$ are recorded, in the last experiment $P(t, 10)$, $P(t, 20)$ and $P(t, 30)$. For these reasons a FORTRAN computer code has been written which performs the following operations:

- The pressure signal P_1 is used to determine the zero of the time axis. The average of the arrival times of the step wave and the reflection from the top of the sample (indicated by the arrows in Fig. 10.2(a)), yields the arrival time $t = 0$ of the step wave at the top of the sample. In this way a unique time scale for the experiments is defined.
- Corrections are made for the offset of the pressure transducers. Subsequently, the amplitude of the incident wave is determined. The pressure signals P_1 , P_2 , P_3 , and P_4 are normalized on this amplitude.
- The pressure signals are ordered as $P(t, 1), P(t, 2), \dots, P(t, 30)$.

The output of these manipulations is considered as the output of 30 pressure transducers 0.5 cm apart at a single shock-tube run. An example is given in Fig. 10.3, where 8 signals are displayed for $\Delta x = 0.5$ cm. This graph also shows that the signal shape reproduces quite well. The pressure signals were recorded with a sample frequency of 2 MHz.

However, the signals generated by the step wave are non-periodic signals. Therefore, a part of the signal has to be windowed out (see Fig. 10.2(b)), which is used for the generation of a periodic signal as is drawn in Fig. 10.4. The first part of the signal in Fig. 10.4 corresponds to the window in Fig. 10.2. The end value of the signal within the window is used to fill the remaining data points in a 2048 record. Subsequently, we take for the second 2048 points the mirrored values of the first ones. In this way the end value of the period is equal to its begin value and we have obtained a continuous periodic signal. For the determination of the length of the window we used two methods. In the first case, a time interval is chosen such that the reflection from the bottom of the shock tube is windowed out as is drawn in Fig. 10.2. The length of this time interval is equal for all the spatial measurements $P(t, 1), P(t, 2), \dots, P(t, 30)$. In the second case, we applied a window such that all phase velocities which are lower than a certain threshold value are outside the window. Due to the different positions of $P_1(t), P_2(t), \dots, P_{30}(t)$, the lengths of the windows are different for every pressure signal.

10.2 Reflection measurements

Experiments were carried out in a reflection configuration. In this case the pressure transducers P_1, P_2, P_3 and P_4 are all mounted in the wall of the shock tube above the porous cylinder. In this way the reflection coefficient and the phase velocities of the incident and reflected waves can be determined. These experiments also provide a test for the application of Prony's method. Four pressure measurements 5 cm apart were obtained in each shock-tube run. We performed the shock tube experiments using $\Delta x = 0.5$ cm. Pressure signal $P(t, 1)$ was recorded 24 cm above the sample. The pressure signals display the behaviour of the P_1 signal as shown in Fig. 10.2(a). For the length of the window a constant time interval for all pressure signals was chosen. The length of the window was determined by the condition that reflections from the bottom must be outside the interval. In this way we have to do with a number of wave components that is a priori known ($M = 2$), as only the incident step wave and its reflection from the top of the sample are taken into account. Subsequently, Prony's analysis is carried out at each frequency as described in Chapter 9.

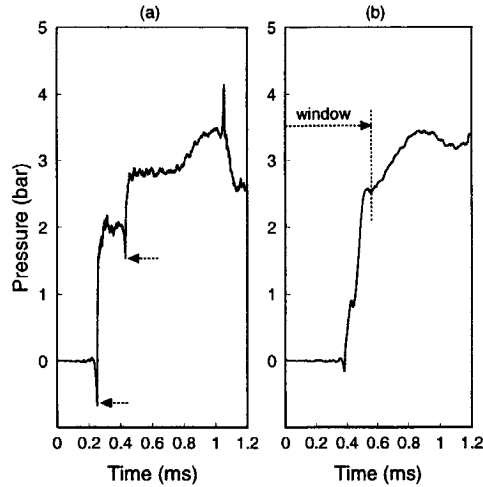


Figure 10.2: Pressure signals recorded at P1 (a) and P4 (b). The arrows indicate the arrival and reflection times which are used for the definition of $t = t_0$, where t_0 is the moment of arrival of the step wave at the top of the sample. The window indicated in (b) is used to construct a periodic signal (see Fig.10.4). The measurements were performed on Bentheimer sandstone. Sample diameter: 70.0 mm.

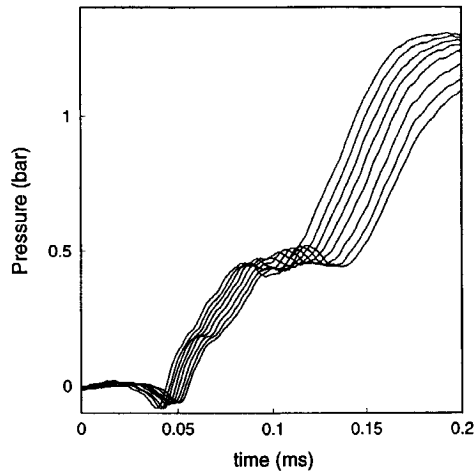


Figure 10.3: Pressure signals for a Bentheim sample at equidistant axial positions. Sample diameter 70.0 mm. $\Delta x = 0.5$ cm.

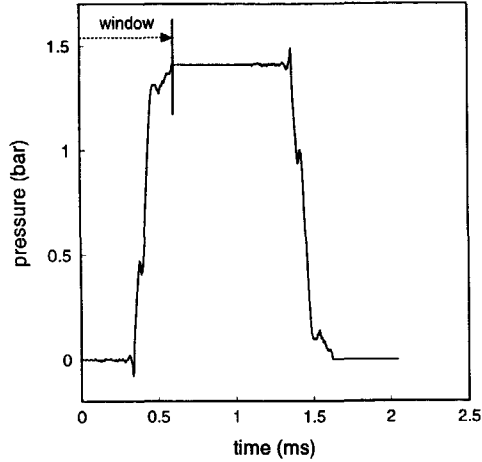


Figure 10.4: Input signal for Fast Fourier Transform.

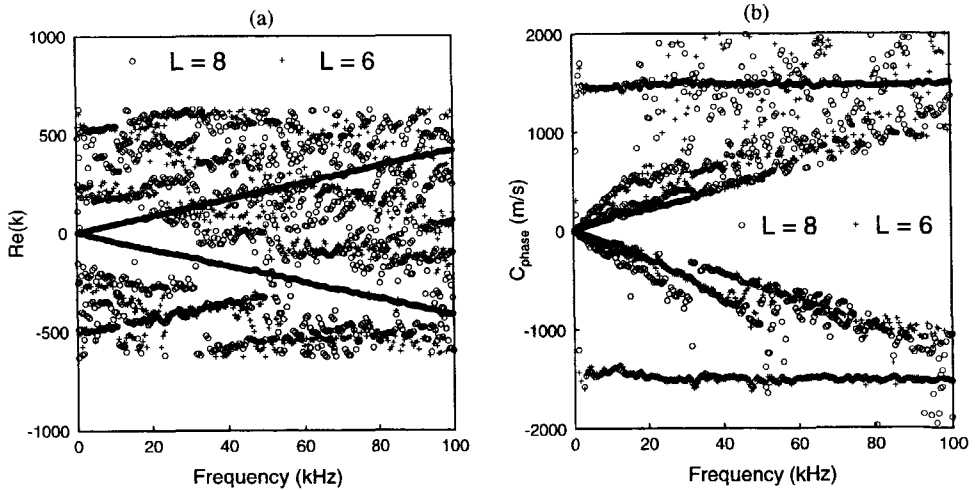


Figure 10.5: Prony analysis of the reflection experiment. Both the real parts of the wavenumber (a) and the phase velocities (b) are plotted. Noisy poles are included. L is the number of wave components in Prony's technique. The number of pressure signals N is 40.

10.2.1 Phase velocities

The results for the real parts of the wavenumbers are shown in Fig. 10.5(a). In Fig. 10.5(b) the results for the phase velocities are shown. For both variables the results are plotted for $L = 6$ and $L = 8$. As mentioned earlier, $L > M$ is used to compensate for the noise in the recordings. Because of the occurrence of both incident and reflected waves, we used the forward-backward linear prediction technique as described in Chapter 9. In Fig. 10.5(a), two straight lines appear in the form of a 90 degrees rotated V-shape, corresponding to the incident step wave and its reflection from the top of the sample. Both waves appear as horizontal lines in Fig. 10.5(b). The other data points are wave components which account for the noise. The band of wavenumbers which is found corresponds to the requirement that $\Re(k)\Delta x < \pi$.

Editing process

Using these results we demonstrate the editing process of the spurious wavenumbers as discussed in the previous chapter. As the number of wave components is a priori known as $M = 2$, we have to find the extent of overdetermination ($L - M$), in order to remove the noisy wavenumbers. This is done by increasing the number of wave components L until Prony's solution does not show any significant changes with respect to the two straight lines. This is the case for $L = 8$. Using a much larger number for L as suggested by Tufts and Kumarasan (1982) appears not to be useful. The number $L = 8$ is larger than indicated by Braun and Ram (1987), who suggested a maximum $L = 6$ for $M = 2$. This is an indication that the values given by other authors are of limited use for our case.

The same is more or less valid for the application of the editing techniques which are used to remove the noisy wavenumbers. One of these techniques is based on the singular values procedure as discussed in Section 9.2.2, option 3. As an illustration, Fig. 10.6(a) shows the frequency dependence of the singular values of the data matrix \mathbf{B} (see Section 9.2.1). At frequencies below 30 kHz, the singular values of the true poles are clearly indicated by the two upper lines, while the singular values of the noisy poles form a cloud of points. However, above this frequency the distinction between true and noisy poles becomes ambiguous. For the application of the break point criterion of Equation (9.28), one would have to vary the threshold level at every frequency, which seems to be rather complicated. For this reason the determination of the true number of poles based on the singular values procedure (Option 3, section 9.2.2) is not quite accurate.

Another possibility is editing on the basis of amplitudes of the wave components (Option 4, section 9.2.2). The amplitudes of the wave components can be determined once the wavenumbers are known (see Equation (9.23)). The results are shown in Fig. 10.6(b). At high frequencies the amplitudes become small and of the same order of magnitude as the noise for the reflected wave. This problem will become worse in case of the experiments on the porous cylinders (see Fig. 10.11(b)). Therefore one cannot neglect those amplitudes below a certain threshold, because the true poles will also be omitted.

For option 1 of Section 9.2.2, it is necessary to perform two shock-tube runs at each spatial position, and therefore we did not try this option. We found that option 2 works quite well. In this technique, the wavenumbers are plotted for different L -values. The true poles remain at the same position, while the noisy poles move. In the frequency-

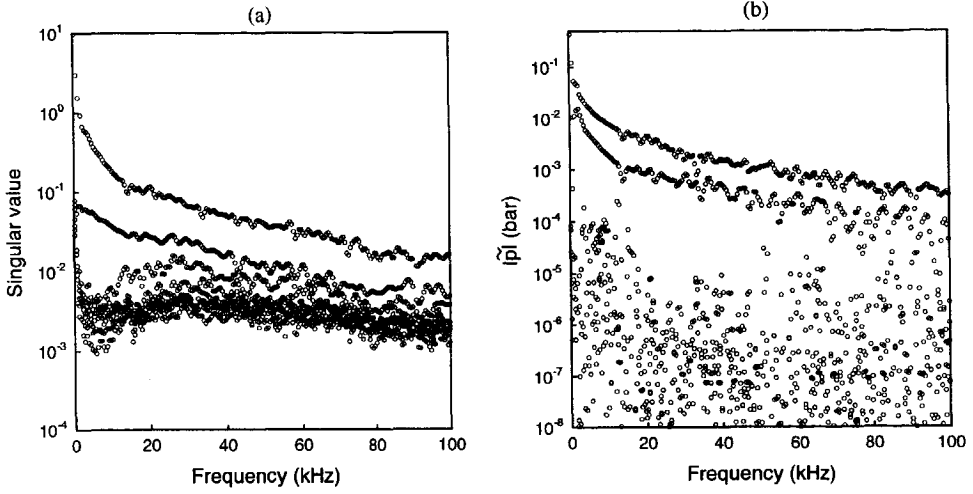


Figure 10.6: Frequency dependence of the singular values (a) and the amplitudes (b). Forward-backward prediction, $L = 8$, $N = 40$.

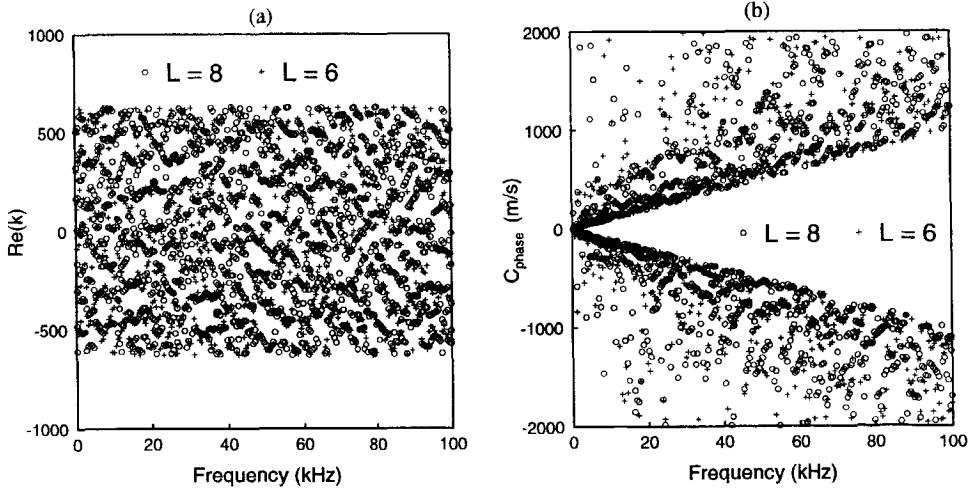


Figure 10.7: Prony analysis of the reflection experiment using Gaussian noise as input signal. The standard deviation of the noise is equal to 0.15, while the average value is equal to zero. Both the real part of the wavenumber (a) and phase velocity (b) are plotted. The number of pressure signals $N = 40$.

wavenumber plane (Fig. 10.5(a)), the true poles line up to wave modes, and the noisy poles form clouds of points. However, some points coincide and suggest the presence of a mode. Therefore still additional criteria are needed. An important criterion is the phase velocity of the modes which are presented in Fig. 10.5(b). Here the question arises whether the non-horizontal lines that are visible in this figure also represent physical wave modes. To solve this problem, we tested the Prony approach using synthetic Gaussian noise having a standard deviation of 0.15 and an average value of zero. The results are shown in Fig. 10.7. We observe the same non-horizontal lines as in Fig. 10.5(b), which thus can be attributed to the noise in the signal. Removing these poles from Fig. 10.5 we finally arrive at Fig. 10.8. The obtained phase velocities show good agreement with the predicted values. The small decrease of the experimental phase velocity below 20 kHz can be explained by the deviation from the one-dimensional approach. This phenomenon was also observed by Laffeur and Shields (1995) in a water-filled aluminum tube.

10.2.2 Reflection coefficients

The ratio between the amplitudes of the incoming and reflected waves determines the reflection coefficient. The two upper lines of Fig. 10.6(b) can therefore be used to determine the reflection coefficient as a function of the frequency. The experiments were performed using sample N6b, for which the parameters are given in Table E.3. The diameter of the sample was 76.9 mm. At high frequencies the oscillations of the lines in Fig. 10.6(b) are quite large and the results for the reflection coefficients are unsatisfactory. Most likely, these oscillations are due to the small signal-to-noise ratio. In order to suppress the amount of noise we re-derive the amplitudes of Fig. 10.6(b) using the frequency independent theoretical wavenumbers for the z -values of Equation (9.23). The results of Prony's analysis with $L = 2$ are shown in Fig. 10.9. If we compare Fig. 10.9(a) to the upper lines of Fig. 10.6(b), it is clear that the performance of Prony's method has improved. In Fig. 10.9 the solid line indicates the computations based on the 1-D Biot theory. Despite the oscillations, the measurements show a reasonable agreement between the measured reflection coefficient and the one-dimensional computations based on Biot's theory. Note that all the physical parameters were determined in independent laboratory experiments. The significant non-oscillatory deviation from the one-dimensional theory in the 5-30 kHz frequency range is probably due to compliance effects of the wall of the shock tube (see chapter 8).

10.3 Transmission experiments

In this section we discuss the results for the transmission experiments. As mentioned in Chapter 5, we consider two cases for the diameter of the sample. In the first case a diameter of 70.0 mm is chosen. This means that the sample-to-tube surface ratio is 0.826, and a relatively large water-filled gap exists between the cylinder surface of the sample and the shock tube wall. Experiments in this configuration are called the large gap experiments. In the second case we use a diameter close to the inner diameter of the test section: 76.9 mm. This means that the sample-to-tube surface ratio is 0.997. Experiments in this configuration are called the small gap experiments. The pressure

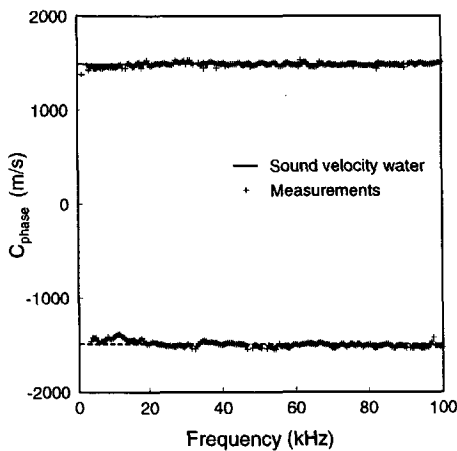


Figure 10.8: Comparison between experiment and theory for the phase velocity of the incident and reflected wave.

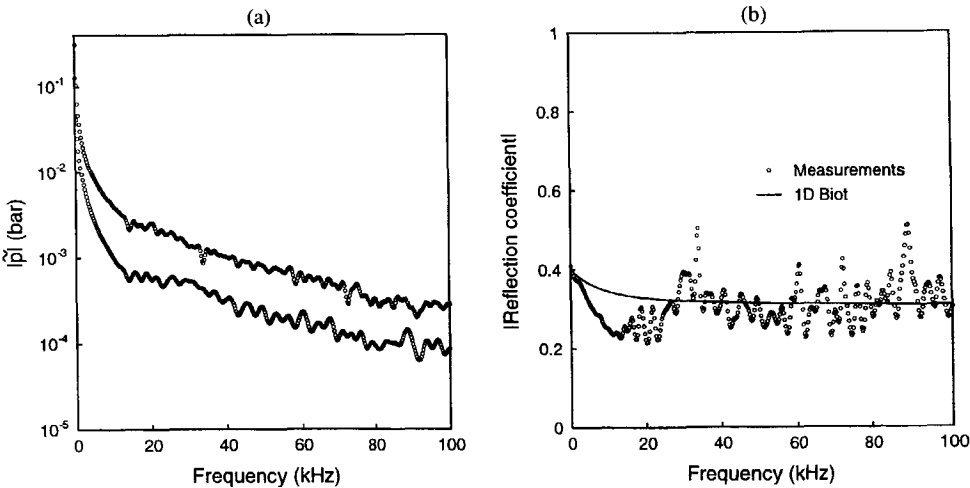


Figure 10.9: Experimental results for the amplitudes of the incident and reflected waves (a) using theoretical wavenumbers in Prony's technique. The corresponding reflection coefficients are given in (b). The solid line indicates the computational results based on the 1D Biot theory. We used sample N6b with a diameter of 76.9 mm. The rock properties are given in Table E.3.

transducers are mounted for both cases in the same configuration as for the conventional shock tube experiments (see Fig. 5.1). The first transducer P1 is mounted in the wall of the shock tube above the porous sample. The transducers P2, P3, and P4 are mounted in the wall along the porous sample. Some results in the time domain are discussed in Chapter 5 for both large and small gap experiments. Here, we focus on the frequency domain. First, we demonstrate the editing process for the transmission experiment, which is somewhat different from that of the reflection measurements. Here, we deal with forward prediction, and we use a variable length for the time window. Subsequently, we compare the experimental results with the wave mode calculations. This is done for Bentheimer sandstone for the large and the small gap experiments. We discuss the large gap experiment for the synthetic rock sample N5b in the last subsection.

10.3.1 Editing the large gap experiment for Bentheimer sandstone

Fig. 10.2 shows an example of the recorded pressure signals in the time domain for a large gap experiment. For this experiment the length of the window is chosen such that the part of the signal with a phase velocity lower than 0.6 times the water velocity is windowed out. Using this variable window we obtained the smallest amount of scatter for the higher order modes. Note that the length of the window at each spatial position is different. An additional benefit of this windowing is that the reflections from the bottom are windowed out. The wave modes of interest now travel in one direction, so that only forward linear prediction was applied. The experiments were carried out with $\Delta x = 0.25$ cm and a record length of 60 signals. Now, it is also possible to construct an array of pressure signals with $\Delta x = 0.5$ cm or $\Delta x = 0.75$ cm. For the record of $\Delta x = 0.5$ cm we obtain 30 pressure signals, while for $\Delta x = 0.75$ cm, 20 signals remain. The results, presented in Fig 10.10, are obtained from two separate processing procedures using $\Delta x = 0.5$ cm, and $\Delta x = 0.75$ cm, respectively. No editing has taken place in Fig. 10.10(a). In Fig. 10.10(b) only positive values are shown for the phase velocities.

As mentioned in Chapter 9 we first have to determine the number of wave modes M which are present in the data. Subsequently, the extent of overdetermination ($L - M$) has to be chosen, after which the true poles must be separated from the noisy poles. In Fig. 10.11(a), we show the singular values of the data matrix \mathbf{B} (see Section 9.2.1). The distinction, between the singular values is ambiguous, especially at higher frequencies, and therefore, the singular value procedure to determine the true wave modes (see Chapter 9) is not applicable. In Fig. 10.11(b) we show the amplitudes of the wave modes. The distinction between the amplitudes is also ambiguous, and therefore the power-editing method also cannot be used to determine the true wave modes. We conclude therefore, that the editing methods as presented by different authors (Lang *et al.* 1987, Braun and Ram 1987, Grosh and Williams 1993) are not applicable to our case.

If we take into account that phase velocities which are within the window, i.e., wave modes with a phase velocity above 0.6 times the water velocity, we obtain that M is 3 or 4. As we need M for the estimation of the extent of overdetermination ($L - M$), we can only obtain a rough approximation for L . We have taken the number of L as large as possible for the case of $\Delta x = 0.75$ cm. As we have only 20 pressure signals available ($N = 20$), the maximum number to satisfy the condition $N \geq 2L$ is $L = 10$. For $\Delta x = 0.5$ cm we used $L = 11$. For the removal of the noisy poles we use a modified version of option 2 (see

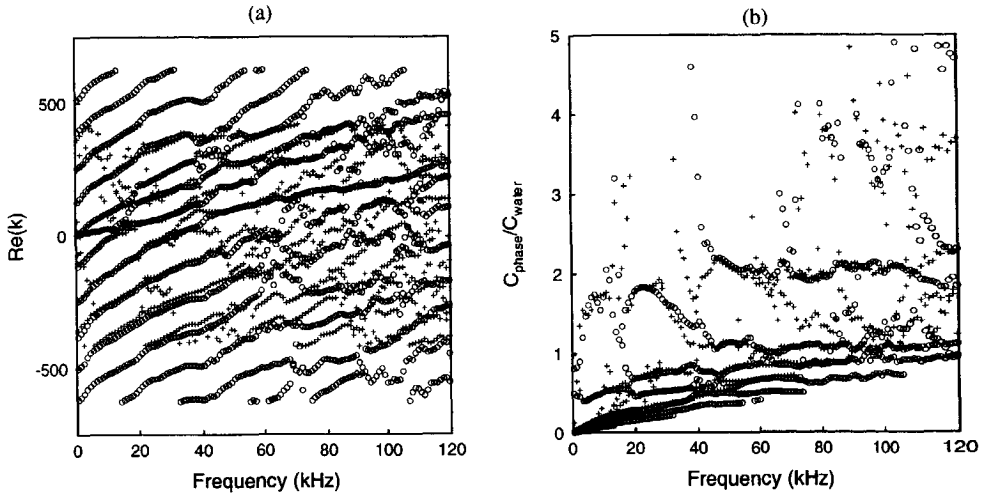


Figure 10.10: Prony analysis of the transmission experiment. Both the real part of the wavenumber (a) and the phase velocity (b) are plotted. \circ : $L = 11$, $\Delta x = 0.5$ cm and $+$: $L = 10$, $\Delta x = 0.75$ cm. We used Bentheimer sandstone with a diameter of 70.0 mm.

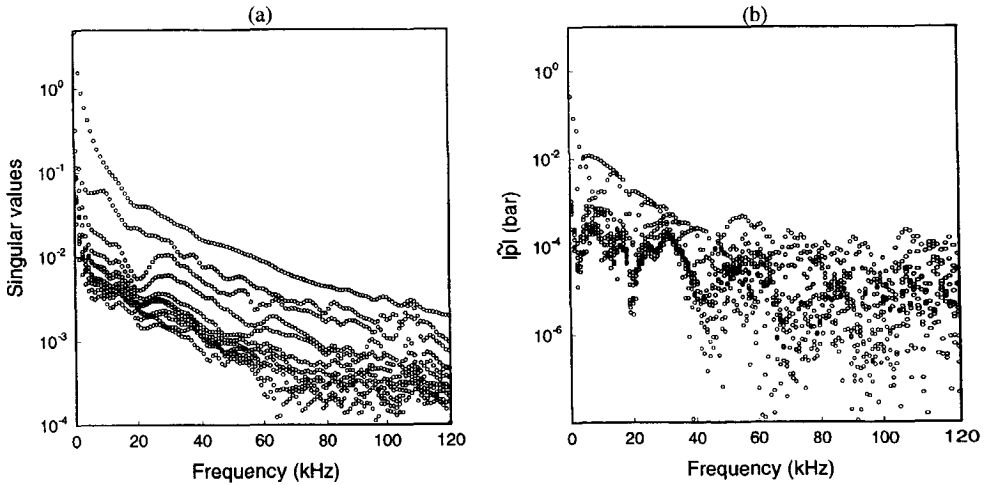


Figure 10.11: Frequency dependence of the singular values (a) and amplitudes of the wave modes (b). Forward prediction is applied, using $L = 11$ and $N = 30$. $\Delta x = 0.5$ cm.

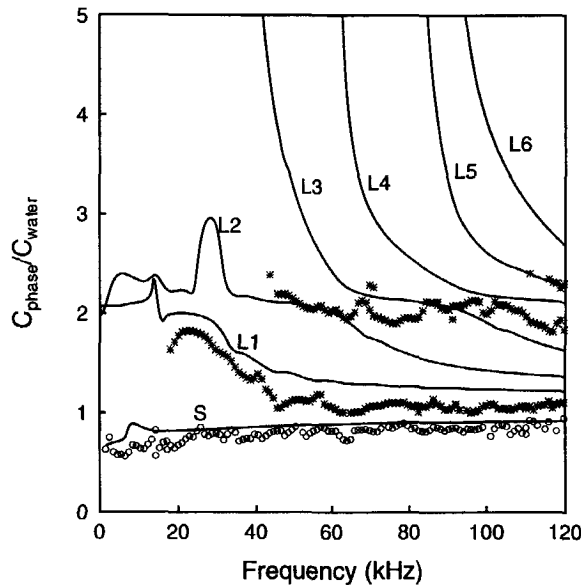


Figure 10.12: Comparison between experiments and theory for parameters which were determined in independent laboratory experiments. Solid lines: wave mode computations. \circ : experiments with a cylinder which was sealed at the top surface. $*$: experiments with open pores at the top surface. We used a Bentheimer sandstone cylinder with a diameter of 70.0 mm.

Section 9.2.2). Instead of taking two values for L , we used two values for Δx . The output of the processing with $\Delta x = 0.5$ cm and $\Delta x = 0.75$ cm can be considered as the results of two separate experiments. Those points which do not 'line-up' and form 'clouds' of points correspond to noisy poles in any case. At frequencies above 60 kHz we observe in Fig. 10.10(a) clouds of points, which consequently correspond to noisy poles. Below this frequency several points line up and therefore suggest the presence of physical wave modes. However, not all of these modes are physical wave modes indeed. The modes with a negative real part of the wavenumbers are removed, as only wave modes with positive phase velocities are within the window. In Fig. 10.10(b) we observe the same non-horizontal lines as in the synthetic white noise experiment of Fig. 10.7(b). They correspond to phase velocities which are outside the time-window which we have chosen for the input of Prony's method. Therefore, we remove in the output of Prony's method the wavenumbers with a phase velocity below 0.6 times the water velocity. Finally, we arrive at the data indicated by the asterixes in Fig. 10.12. We have shown the data for $L = 11$ and $\Delta x = 0.5$ cm. The data in Fig. 10.12 indicated by the open symbols are also observed in Fig. 10.10(b) for the frequencies above 60 kHz.

10.3.2 Comparison with theory

We now compare the edited experimental results with the wave mode computations given in Chapter 8. In Fig. 10.12 the solid lines indicate the computations for the Bentheimer sandstone cylinder with a diameter of 70.0 mm. The computations include the compressibility of the grains, as well as the elasticity of the wall. We determined the physical parameters in independent laboratory experiments. The data values represented by the circles in Fig. 10.12 are taken from an experiment with a porous cylinder which was sealed at the top surface. We used a two-component coating (Araldit SW 404) as a sealing. The asterixes in Fig. 10.12 represent the data taken from an experiment with open pores at the top surface.

The data indicated by the asterixes show two different lines. The lower line is in agreement with the L1 mode. Below 20 kHz the data points were omitted, as the scatter in the data was high. A strong decrease of the phase velocity of the L1 mode in between 25 and 50 kHz is observed in the experimental results, as well as an asymptotic behaviour above 50 kHz. The upper line of the asterixes in Fig. 10.12 is difficult to explain, but clearly can be attributed to the higher-order wave phenomena. In Chapter 8 we noted that these modes generate relatively low pressure amplitudes in the gap. Hence, they are difficult to be detected.

The data represented by circles in Fig. 10.12 are in agreement with the S mode predictions over the entire frequency range. The S mode corresponds to the pseudo-Stoneley wave in the high-frequency limit and is a bulk wave in the low-frequency limit. We found that the sealing at the top surface of the cylinder enhances the excitation of the S mode.

The results of Fig. 10.12 show that we are able to excitate multiple wave modes in one experiment over a broad frequency range. This is noteworthy, as most experimental setups are able to excitate either one wave mode over a broad frequency range, or multiple wave modes in a limited frequency range (see Chapter 1).

Fig. 10.13 shows the corresponding imaginary parts of the wavenumbers. Again these plots results from a combination of 60 pressure signals, from which the noise has been removed in the output of Prony's method. The scatter in these measurements, however, is large. Only the results for the L1 mode suggest qualitative agreement between 30 and 40 kHz. Ellefsen *et al.* (1993) and Hsu *et al.* (1997) also report large bias in the attenuation coefficient in the presence of noise. For higher SNR's the scatter in the damping coefficients decreases as will be shown later.

10.3.3 Small gap experiments for Bentheimer sandstone

Experiments were performed for Bentheimer sandstone using the small gap configuration. We observed two wave modes in the experimental results. For a clear comparison with the theory the results are presented in two separate figures. Figs. 10.14 display the mode with the highest phase velocity. The data were processed using $\Delta x = 0.5$ cm. As for the large gap experiment, the length of the window was chosen such that $c_{\text{phase}}/c_{\text{water}} > 0.6$. The experimental data show an acceptable agreement with the L1 mode. The scatter of the damping coefficients is large, and the experiments and theory differ one order in magnitude.

The results for the second mode are shown in Figs. 10.15. The data were processed

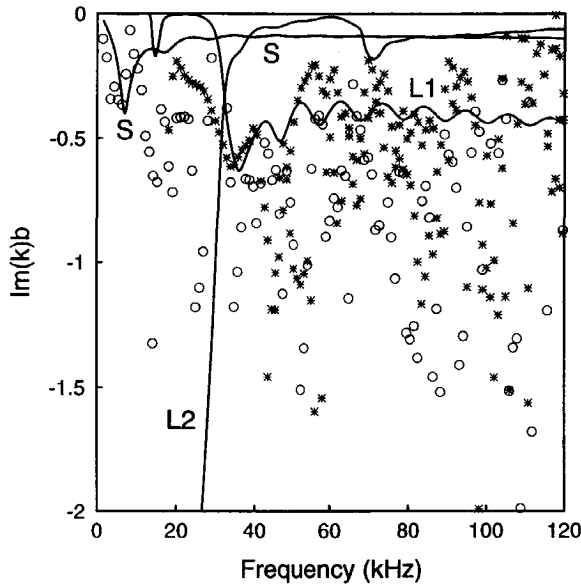


Figure 10.13: Comparison between experiment and theory for the damping coefficient. Solid lines: wave mode computations. \circ : experiments with a cylinder which was sealed at the top surface. $*$: experiments with open pores at the top surface. We used a Bentheimer sandstone cylinder with a diameter of 70.0 mm.

using $\Delta x = 0.25$ cm. For this case the length of the window was constant for every spatial measurement. It was chosen such that reflections from the bottom were windowed out. Most likely, the experimental wave mode as given in Fig. 10.15 can be attributed to the D modes. These modes have the free-field slow wave velocity as their high-frequency limit, as explained in Chapter 8. The experiments show only one mode in Fig. 10.15(a), while a number of theoretical D modes exist in this frequency range. A possible explanation is that Prony's technique only finds the most dominant amplitudes. Similar phenomena were reported by Plona *et al.* (1992) and Hsu *et al.* (1997). The experimental damping coefficients in Fig. 10.15(b) show the same trend as the theoretical attenuation data.

10.3.4 Large gap experiments for synthetic rock

Experiments were carried out for the synthetic rock sample N5b. The parameters are given in Table E.3, Appendix E. The corresponding shear velocity is lower than the water velocity, and hence this rock sample is a so-called slow formation.

The results of the wave mode computations for this rock type are given by the solid lines in Fig. 10.16. As explained in Chapter 8 the L1 mode is based on the wave motion in the gap between the porous cylinder and the shock tube wall at high frequencies. At low frequencies it is based on longitudinal wave motion in the shock tube. The S mode for this slow formation corresponds to a so-called true surface wave at high frequencies.

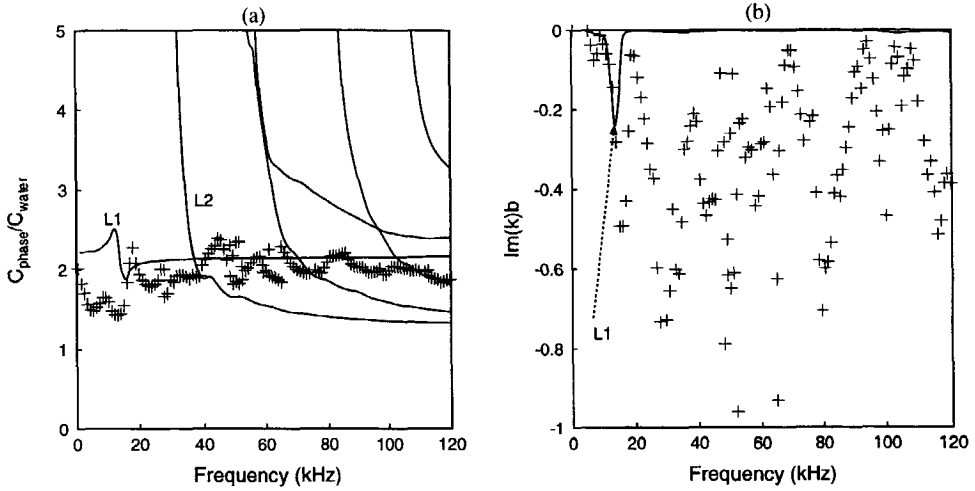


Figure 10.14: Comparison between experiment and theory for the small gap experiment. Both the results for the phase velocities (a) and damping (b) are shown. The damping coefficients are scaled by the inner radius of the shock tube b . We used a Bentheimer sandstone cylinder with a diameter of 76.8 mm. Note that the results of the experiment are presented using two separate figures: Fig. 10.14 and Fig. 10.15.

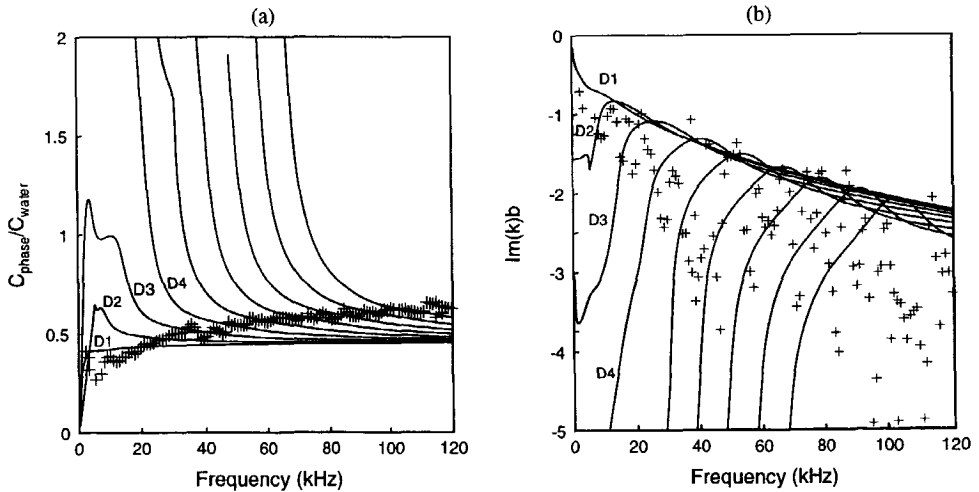


Figure 10.15: Comparison between experiment and theory for the small gap experiment. Both the results for the phase velocities (a) and damping (b) are shown. The damping coefficients are scaled by the inner radius of the shock tube b . We used a Bentheimer sandstone cylinder with a diameter of 76.8 mm. Note that the results of this experiment are presented using two separate figures: Fig. 10.14 and Fig. 10.15.

The phase velocity is lower than the slow wave velocity. At low frequencies the S mode related to bulk wave motion.

The experimental results in the frequency domain show one dominant wave mode over the entire frequency range with a slightly decreasing phase velocity (Fig. 10.16(a)). For this experiment the smallest amount of scatter was obtained for a sample which was

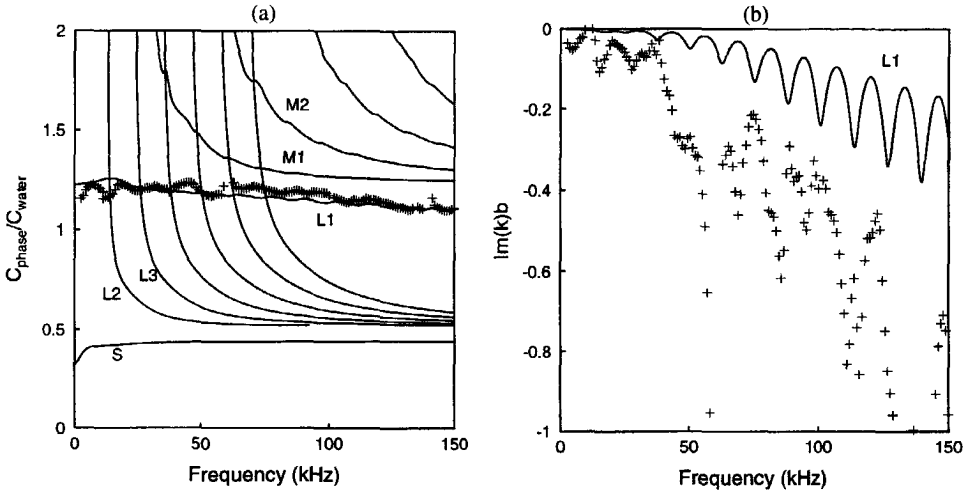


Figure 10.16: Comparison between experiments and theory for synthetic rock N5b. The theoretical results for the phase velocities (a) are given for the L, M and S modes. For the damping (b) the L1 mode is shown. The lines indicate the theory. The damping coefficients are scaled by the inner radius of the shock tube b . The diameter of the sample was 70 mm.

sealed at the top surface. The time window was chosen such that $c_{\text{phase}}/c_{\text{water}} > 0.5$. For the processing in Prony's method we used $N = 30$, $\Delta x = 0.5$ cm, and $L = 11$. The experimental wave mode is in excellent agreement with the theoretical predictions for the L1 mode. Note that these predictions are based on parameters which have been determined in independent laboratory experiments. The amplitude of the surface wave was too small to be detected using Prony's method. This is consistent with the modelling of the S mode. Fig. 8.34 shows that the relative amplitude of the gap pressure is small.

We obtained reasonable results for the damping coefficients, most likely due to the high SNR. Experiments and the theory show the same trend and the orders of the magnitudes are also in agreement (see Fig. 10.16(b)).

10.4 Discussion and conclusions

By a unique modification of a conventional shock tube configuration data recorded in the time domain could be converted to the frequency domain using Prony's technique. Several methods for the editing process of the spurious wavenumbers in Prony's method have been discussed. We found that processing of two records of pressure signals with different values for the spatial sampling distance works best. Furthermore, we used a synthetic white noise

signal to investigate the influence of noise on Prony's method. Phase velocities, damping coefficients and reflection coefficients could be measured in the 1-120 kHz frequency range.

For a synthetic rock sample agreement was found for the reflection coefficient with one-dimensional calculations based on Biot's theory. In Bentheimer sandstone the pseudo-Stoneley wave has been observed in case of the large gap experiment. In this large gap experiment we have also recorded a wave mode which is, at high-frequencies, based on wave motion in the water-filled gap. Furthermore, we observed wave modes which could be related to higher-order wave phenomena. It is difficult to obtain results for higher-order wave modes, due to the small pressure amplitude in the gap. For the synthetic rock sample N5b, we have recorded one wave mode in the large gap configuration. This wave mode is based on wave motion in the water-filled gap.

Experiments were carried out for the small gap configuration using Bentheimer sandstone. We found a wave mode, which most likely can be attributed to the D modes, which have a direct relation with the slow wave. This is a confirmation of the existence of the slow compressional wave in natural rock.

The experimental results have been compared to the computational results, which were discussed in Chapter 8. The computations were based on independent parameters, which were determined using dry samples. The compressibility of the grains was taken into account. For the compressibility of the grains literature values were used. For both Bentheimer sandstone and the synthetic rock N5b, the theoretical predictions for the phase velocities were in agreement with the measurements.

We have also determined the damping coefficients of the wave modes. Due to the large amount of scatter in the damping coefficients, the comparison with the theoretical results is complicated. For the synthetic rock sample, qualitative agreement with the predictions has been found.

Chapter 11

Conclusions

1. A shock tube was used to generate acoustic bulk and surface waves in poroelastic materials. The pores of the materials were filled with either air or water. The size of the gap between the porous cylinder and the wall of the shock tube determined which wave modes were generated. For a large gap surface waves were generated. For a small one the fast and the slow compressional wave were detected.
2. For air-filled pores the transition from wave-like behaviour to diffusion-like behaviour of the slow compressional wave was demonstrated. For very high permeabilities (> 500 Darcy) the shock wave character was preserved and could be detected at the end of the sample. For lower permeabilities the diffusion effect dominated. The non-linear diffusion was described by Forchheimer's equation.
3. For water-saturated pores wave-like behaviour is prominent. Computations based on a one-dimensional version of Biot's theory were carried out. Good agreement was observed with the experimental results in the time domain, provided that the gap between the porous sample and the shock tube wall was small.
4. Wyllie's equation was used to determine the velocity for a given porosity. The corresponding impedance poorly correlated with reflection coefficients that were derived from the experiments. For the velocity the correlation was reasonable.
5. For a large size of the gap between the cylinder and the shock tube two-dimensional effects played an important role. The theory of surface waves on flat interfaces and the theory of waveguides in cylinders are both important to understand the wave phenomena in the shock tube configuration.
6. We considered surface waves on an interface between an elastic solid and a liquid. Following Feng and Johnson (1983), this analysis was extended to an interface between a lossless poroelastic solid and a liquid. We included the full Biot theory and obtained a better description of the attenuation of surface waves.
7. The theory of waveguides in elastic and poro-elastic solid cylinders was investigated. Some of the wave modes that occur in the porous cylinder in the shock tube are equivalent to the ones in solid elastic cylinders. These modes are characterized by

a low-frequency cut-off and the high-frequency limit of the phase velocity, which is equal to the shear velocity. In our shock tube configuration also modes occurred which have the fast wave velocity as their high-frequency limit.

8. A surface mode occurs on the interface between the porous cylinder and a relatively large water-filled gap. This wave is related to the pseudo-Stoneley wave in case of a Bentheimer sandstone cylinder, which is a fast formation. For one set of properties for a slow formation, it corresponds to the true Stoneley wave.
9. An extra bulk wave mode type occurs due to the presence of the slow Biot wave. The damping of the higher-order slow wave modes is at least as high as the damping of the free-field slow wave.
10. The surface mode in the shock tube configuration is sensitive to both the permeability and the shear velocity. Because this sensitivity also applies to the surface mode in a borehole configuration, this conclusion can have important implications for the analysis of permeability estimation from acoustic logging data.
11. A screw gear unit was used to change the position of the porous cylinder in the shock tube. Performing multiple shock tube runs it was possible to obtain the equivalence of a large series of pressure transducers at equidistant positions. This modification of the shock tube configuration enables the determination of phase velocities, damping and reflection coefficients in the 1-120 kHz frequency range.
12. A least-squares version of Prony's method was used to perform the transformation of a series of time-recorded signals to the frequency domain. We evaluated editing methods suggested in literature to remove spurious wave modes in Prony's method. It was demonstrated that modified versions of these editing techniques could effectively be used in our experiments.
13. The surface mode was detected in the shock tube from 1 to 120 kHz on Bentheimer sandstone. This was to our knowledge the first time that this mode was recorded in a shock tube on porous material in such a broad frequency range. The velocity of this mode agreed well with the velocity derived from the full modelling of the shock tube with a wide gap between the cylinder and the tube wall. The comparison between the experiments and theory was based on parameters which were determined independently on core samples.
14. The modelled and measured phase velocities of the lowest-order bulk mode agreed for both fast and slow formations. For high Signal-to-Noise ratio's it is possible to obtain damping coefficients. Qualitative agreement between experimental and theoretical attenuation data was found for synthetic rock.

Appendix A

Basic relations cartesian and cylindrical coordinates

In this appendix relations between potentials, displacements and stresses are given for cartesian and cylindrical coordinates. They can also be found in standard textbooks (Achenbach 1973, Miklowitz 1978). The following decomposition for the displacements is used:

$$\mathbf{u} = \nabla\varphi + \nabla \times \boldsymbol{\psi}. \quad (\text{A.1})$$

A.1 Cartesian coordinaters

We obtain for cartesian coordinates:

$$u_x = \frac{\partial\varphi}{\partial x} + \frac{\partial\psi_z}{\partial y} - \frac{\partial\psi_y}{\partial z}, \quad (\text{A.2})$$

$$u_y = \frac{\partial\varphi}{\partial y} - \frac{\partial\psi_z}{\partial x} + \frac{\partial\psi_x}{\partial z}, \quad (\text{A.3})$$

$$u_z = \frac{\partial\varphi}{\partial z} + \frac{\partial\psi_y}{\partial x} - \frac{\partial\psi_x}{\partial y}. \quad (\text{A.4})$$

The strain-displacement relations in cartesian coordinates read as follows:

$$\epsilon_x = \frac{\partial u_x}{\partial x}, \quad \epsilon_y = \frac{\partial u_y}{\partial y}, \quad \epsilon_z = \frac{\partial u_z}{\partial z}, \quad (\text{A.5})$$

$$2\epsilon_{xy} = 2\epsilon_{yx} = \frac{\partial u_x}{\partial y} + \frac{\partial u_y}{\partial x}, \quad (\text{A.6})$$

$$2\epsilon_{yz} = 2\epsilon_{zy} = \frac{\partial u_y}{\partial z} + \frac{\partial u_z}{\partial y}, \quad (\text{A.7})$$

$$2\epsilon_{zx} = 2\epsilon_{xz} = \frac{\partial u_z}{\partial x} + \frac{\partial u_x}{\partial z}. \quad (\text{A.8})$$

For the stress-displacement relations Hook's law applies:

$$\tau_{xx} = \lambda \left(\frac{\partial u_x}{\partial x} + \frac{\partial u_y}{\partial y} + \frac{\partial u_z}{\partial z} \right) + 2\mu \frac{\partial u_x}{\partial x}, \quad (\text{A.9})$$

$$\tau_{yy} = \lambda \left(\frac{\partial u_x}{\partial x} + \frac{\partial u_y}{\partial y} + \frac{\partial u_z}{\partial z} \right) + 2\mu \frac{\partial u_y}{\partial y}, \quad (\text{A.10})$$

$$\tau_{zz} = \lambda \left(\frac{\partial u_x}{\partial x} + \frac{\partial u_y}{\partial y} + \frac{\partial u_z}{\partial z} \right) + 2\mu \frac{\partial u_z}{\partial z}, \quad (\text{A.11})$$

$$\tau_{xy} = \tau_{yx} = \mu \left(\frac{\partial u_x}{\partial y} + \frac{\partial u_y}{\partial x} \right), \quad (\text{A.12})$$

$$\tau_{yz} = \tau_{zy} = \mu \left(\frac{\partial u_y}{\partial z} + \frac{\partial u_z}{\partial y} \right), \quad (\text{A.13})$$

$$\tau_{zx} = \tau_{xz} = \mu \left(\frac{\partial u_z}{\partial x} + \frac{\partial u_x}{\partial z} \right). \quad (\text{A.14})$$

Using the decomposition in potentials we obtain:

$$\tau_{xx} = \lambda \nabla^2 \varphi + 2\mu \left[\frac{\partial^2 \varphi}{\partial x^2} + \frac{\partial}{\partial x} \left(\frac{\partial \psi_z}{\partial y} - \frac{\partial \psi_y}{\partial z} \right) \right], \quad (\text{A.15})$$

$$\tau_{yy} = \lambda \nabla^2 \varphi + 2\mu \left[\frac{\partial^2 \varphi}{\partial y^2} - \frac{\partial}{\partial y} \left(\frac{\partial \psi_z}{\partial x} - \frac{\partial \psi_x}{\partial z} \right) \right], \quad (\text{A.16})$$

$$\tau_{zz} = \lambda \nabla^2 \varphi + 2\mu \left[\frac{\partial^2 \varphi}{\partial z^2} + \frac{\partial}{\partial z} \left(\frac{\partial \psi_y}{\partial x} - \frac{\partial \psi_x}{\partial y} \right) \right], \quad (\text{A.17})$$

$$\tau_{xy} = \mu \left[2 \frac{\partial^2 \varphi}{\partial x \partial y} + \frac{\partial}{\partial y} \left(\frac{\partial \psi_z}{\partial y} - \frac{\partial \psi_y}{\partial z} \right) - \frac{\partial}{\partial x} \left(\frac{\partial \psi_z}{\partial x} - \frac{\partial \psi_x}{\partial z} \right) \right], \quad (\text{A.18})$$

$$\tau_{yz} = \mu \left[2 \frac{\partial^2 \varphi}{\partial y \partial z} - \frac{\partial}{\partial z} \left(\frac{\partial \psi_z}{\partial x} - \frac{\partial \psi_x}{\partial z} \right) + \frac{\partial}{\partial y} \left(\frac{\partial \psi_y}{\partial x} - \frac{\partial \psi_x}{\partial y} \right) \right], \quad (\text{A.19})$$

$$\tau_{zx} = \mu \left[2 \frac{\partial^2 \varphi}{\partial x \partial z} + \frac{\partial}{\partial z} \left(\frac{\partial \psi_z}{\partial y} - \frac{\partial \psi_y}{\partial z} \right) + \frac{\partial}{\partial x} \left(\frac{\partial \psi_y}{\partial x} - \frac{\partial \psi_x}{\partial y} \right) \right]. \quad (\text{A.20})$$

The stress-strain relations are of the form:

$$\tau_{rr} = \lambda \left(\frac{\partial u_r}{\partial r} + \frac{u_r}{r} + \frac{1}{r} \frac{\partial u_\theta}{\partial \theta} + \frac{\partial u_z}{\partial z} \right) + 2\mu \frac{\partial u_r}{\partial r}, \quad (\text{A.33})$$

$$\tau_{\theta\theta} = \lambda \left(\frac{\partial u_r}{\partial r} + \frac{u_r}{r} + \frac{1}{r} \frac{\partial u_\theta}{\partial \theta} + \frac{\partial u_z}{\partial z} \right) + 2\mu \left[\frac{u_r}{r} + \frac{1}{r} \frac{\partial u_\theta}{\partial \theta} \right], \quad (\text{A.34})$$

$$\tau_{zz} = \lambda \left(\frac{\partial u_r}{\partial r} + \frac{u_r}{r} + \frac{1}{r} \frac{\partial u_\theta}{\partial \theta} + \frac{\partial u_z}{\partial z} \right) + 2\mu \frac{\partial u_z}{\partial z}, \quad (\text{A.35})$$

$$\tau_{r\theta} = \mu \left(\frac{\partial u_\theta}{\partial r} - \frac{u_\theta}{r} + \frac{1}{r} \frac{\partial u_r}{\partial \theta} \right), \quad (\text{A.36})$$

$$\tau_{\theta z} = \mu \left(\frac{1}{r} \frac{\partial u_z}{\partial \theta} + \frac{\partial u_\theta}{\partial z} \right), \quad (\text{A.37})$$

$$\tau_{zr} = \mu \left(\frac{\partial u_r}{\partial z} + \frac{\partial u_z}{\partial r} \right). \quad (\text{A.38})$$

The relations between the stress components and the potentials φ and η are given here for the axi-symmetric case, so $\partial/\partial\theta = 0$ and $u_\theta = 0$.

$$\tau_{rr} = \lambda \nabla^2 \varphi + 2\mu \left[\frac{\partial^2 \varphi}{\partial r^2} - \frac{\partial^3 \eta}{\partial z \partial r^2} \right], \quad (\text{A.39})$$

$$\tau_{\theta\theta} = \lambda \nabla^2 \varphi + 2\mu \left[\frac{1}{r} \frac{\partial \varphi}{\partial r} + \frac{1}{r} \frac{\partial^2 \eta}{\partial z \partial r} \right], \quad (\text{A.40})$$

$$\tau_{zz} = \lambda \nabla^2 \varphi + 2\mu \left[\frac{\partial^2 \varphi}{\partial z^2} - \frac{\partial^3 \eta}{\partial r^2 \partial z} - \frac{1}{r} \frac{\partial^2 \eta}{\partial r \partial z} \right], \quad (\text{A.41})$$

$$\tau_{r\theta} = \tau_{\theta z} = 0, \quad (\text{A.42})$$

$$\tau_{zr} = \mu \left[2 \frac{\partial^2 \varphi}{\partial z \partial r} + \frac{\partial^3 \eta}{\partial z^2 \partial r} - \frac{\partial}{\partial r} \left(\frac{\partial}{\partial r} \left(r \frac{\partial \eta}{\partial r} \right) \right) \right]. \quad (\text{A.43})$$

A.2 Cylindrical coordinates

The displacement components in the r , θ and z directions are denoted by u_r , u_θ and u_z , respectively. The Laplacian in cylindrical coordinates is defined as:

$$\nabla^2 = \frac{\partial^2}{\partial r^2} + \frac{1}{r} \frac{\partial}{\partial r} + \frac{1}{r^2} \frac{\partial^2}{\partial \theta^2} + \frac{\partial^2}{\partial z^2}. \quad (\text{A.21})$$

The Laplacian of a vector can be calculated using the vector identity

$$\nabla^2 \psi = \nabla(\nabla \cdot \psi) - \nabla \times \nabla \times \psi, \quad (\text{A.22})$$

where

$$\nabla \cdot \psi = \frac{\partial \psi_z}{\partial z} + \frac{\partial(\psi_r r)}{\partial r} + \frac{1}{r} \frac{\partial \psi_\theta}{\partial \theta}. \quad (\text{A.23})$$

The relations between the displacement components and the potentials are given by:

$$u_r = \frac{\partial \varphi}{\partial r} + \frac{1}{r} \frac{\partial \psi_z}{\partial \theta} - \frac{\partial \psi_\theta}{\partial z}, \quad (\text{A.24})$$

$$u_\theta = \frac{1}{r} \frac{\partial \varphi}{\partial \theta} + \frac{\partial \psi_r}{\partial z} - \frac{\partial \psi_z}{\partial r}, \quad (\text{A.25})$$

$$u_z = \frac{\partial \varphi}{\partial z} + \frac{1}{r} \frac{\partial(\psi_\theta r)}{\partial r} - \frac{1}{r} \frac{\partial \psi_r}{\partial \theta}. \quad (\text{A.26})$$

For cylindrical coordinates the following decomposition for the vector potential is used:

$$\psi = \chi \mathbf{e}_z + \nabla \times (\eta \mathbf{z}). \quad (\text{A.27})$$

where \mathbf{e}_z is the unit vector in the z -direction. Then we can write:

$$u_r = \frac{\partial \varphi}{\partial r} + \frac{1}{r} \frac{\partial \chi}{\partial \theta} + \frac{\partial^2 \eta}{\partial z \partial r}, \quad (\text{A.28})$$

$$u_\theta = \frac{1}{r} \frac{\partial \varphi}{\partial \theta} - \frac{\partial \chi}{\partial r} + \frac{1}{r} \frac{\partial^2 \eta}{\partial z \partial \theta}, \quad (\text{A.29})$$

$$u_z = \frac{\partial \varphi}{\partial z} - \frac{1}{r} \frac{\partial}{\partial r} \left(r \frac{\partial \eta}{\partial r} \right) - \frac{1}{r^2} \frac{\partial^2 \eta}{\partial \theta^2}. \quad (\text{A.30})$$

In cylindrical coordinates the strain-displacement relations are given by

$$\epsilon_r = \frac{\partial u_r}{\partial r}, \quad \epsilon_\theta = \frac{u_r}{r} + \frac{1}{r} \frac{\partial u_\theta}{\partial \theta}, \quad \epsilon_z = \frac{\partial u_z}{\partial z}, \quad (\text{A.31})$$

$$2\epsilon_{r\theta} = \frac{\partial u_\theta}{\partial r} - \frac{u_\theta}{r} + \frac{1}{r} \frac{\partial u_r}{\partial \theta}, \quad 2\epsilon_{\theta z} = \frac{1}{r} \frac{\partial u_z}{\partial \theta} + \frac{\partial u_\theta}{\partial z}, \quad 2\epsilon_{zr} = \frac{\partial u_r}{\partial z} + \frac{\partial u_z}{\partial r}. \quad (\text{A.32})$$

Appendix B

Bessel functions

In this appendix we show a few aspects of the Bessel functions which are used in this thesis. For further details we refer to Abramowitz and Stegun (1964). Bessel functions are solutions of Bessel's equation:

$$\frac{d^2 y}{dx^2} + \frac{1}{x} \frac{dy}{dx} + \left(1 - \frac{n^2}{x^2}\right)y = 0, \quad (\text{B.1})$$

where x , y , and n are complex-valued in the general case. For integer values of n two independent solutions for y exist. The first one, $J_n(x)$, is called the Bessel function of the first kind of order n . It can be expressed by the following power series:

$$J_n(x) = \sum_{m=0}^{\infty} \frac{(-1)^m \left(\frac{x}{2}\right)^{2m+n}}{m!(m+n)!}. \quad (\text{B.2})$$

A second independent solution $Y_n(x)$ is the Bessel function of the second kind of order n . This function is denoted as the Neumann function. The following power series apply:

$$Y_n(x) = \frac{2}{\pi} J_n(x) \log(x/2) + x^{-n} \sum_{m=0}^{n-1} \alpha_m x^{2m} + x^n \sum_{m=0}^{\infty} \beta_m x^{2m}, \quad (\text{B.3})$$

where α_m and β_m are real-valued constants. Expressions for α_m and β_m are given by Abramowitz and Stegun (1964). Y_n is singular in $x = 0$ with branch cut $|\arg(x)| = \pi$. For the argument $-x$ it can be derived that:

$$J_n(-x) = (-1)^n J_n(x) \quad (\text{B.4})$$

and

$$Y_n(-x) = \begin{cases} (-1)^n (Y_n(x) - 2iJ_n(x)) & \text{if } \arg(x) \in (0, \pi], \\ (-1)^n (Y_n(x) + 2iJ_n(x)) & \text{if } \arg(x) \in (-\pi, 0]. \end{cases} \quad (\text{B.5})$$

For $|x| \rightarrow \infty$, the two solutions can be written as:

$$\lim_{|x| \rightarrow \infty} J_n(x) \sim \sqrt{\frac{2}{\pi x}} \cos\left(x - \left(n + \frac{1}{2}\right)\frac{\pi}{2}\right), \quad (\text{B.6})$$

$$\lim_{|x| \rightarrow \infty} Y_n(x) \sim \sqrt{\frac{2}{\pi x}} \sin \left(x - \left(n + \frac{1}{2} \right) \frac{\pi}{2} \right). \quad (\text{B.7})$$

Other common independent sets of solutions are the Hankel functions, which are labelled using the superscripts (1) and (2):

$$\begin{aligned} H_n^{(1)}(x) &= J_n(x) + iY_n(x), \\ H_n^{(2)}(x) &= J_n(x) - iY_n(x). \end{aligned} \quad (\text{B.8})$$

For the asymptotic behaviour of $H_n^{(2)}$ we can write:

$$\lim_{|x| \rightarrow \infty} H_n^{(2)} \sim \sqrt{\frac{2}{\pi x}} \exp \left(-i \left(x - \left(n + \frac{1}{2} \right) \frac{\pi}{2} \right) \right). \quad (\text{B.9})$$

Note that the Hankel functions are singular in $x = 0$ and the branch cut is defined by $|\arg(x)| = \pi$. For Bessel functions with purely imaginary arguments, it is appropriate to use the modified Bessel functions. The so-called modified Bessel function of the first kind is defined as:

$$I_n(x) = i^{-n} J_n(ix). \quad (\text{B.10})$$

If $|\arg(x)| < (\pi/2)$, we can write for the asymptotic behaviour of $I_n(x)$:

$$\lim_{|x| \rightarrow \infty} I_n(x) \sim \sqrt{\frac{2}{\pi x}} e^x. \quad (\text{B.11})$$

For the derivatives of the Bessel functions, the following relations are valid:

$$\frac{d}{dx}(J_n(\lambda x)) = \frac{1}{2} \lambda (J_{n-1}(\lambda x) - J_{n+1}(\lambda x)), \quad (\text{B.12})$$

where λ is a complex-valued constant. The function $J_{n+1}(x)$ is related to $J_n(x)$ and $J_{n-1}(x)$ via:

$$J_{n+1}(\lambda x) = \frac{2n}{\lambda x} J_n(\lambda x) - J_{n-1}(\lambda x). \quad (\text{B.13})$$

Hence, we can write for the derivatives:

$$\frac{d}{dx}(J_n(\lambda x)) = \lambda J_{n-1}(\lambda x) - \frac{n}{x} J_n(\lambda x). \quad (\text{B.14})$$

For J_0 the expression is

$$\frac{d}{dx} J_0(\lambda x) = -\lambda J_1(\lambda x). \quad (\text{B.15})$$

Appendix C

Riemann sheets

In multi-dimensional configurations the components of the wave vector are related to each other as well as to the free-field wavenumbers via a square root which can be complex-valued. By choosing the appropriate branch and branch cuts we obtain a single-valued square root function. We illustrate the choice of the branch and branch cuts for the shear wavenumbers. The square roots for the other wavenumbers are treated in a similar way. For a flat interface between a solid and a fluid we write the potential ψ_y (see Chapter 6):

$$\psi_y = A_1 e^{i(\omega t - kx - k_{zsh}z)}, \quad (C.1)$$

where

$$k_{zsh} = \pm \sqrt{\omega^2/c_T^2 - k^2}. \quad (C.2)$$

As in Chapter 6, we have chosen the x-axis parallel to the interface and z-axis perpendicular to the interface. The sign of the square root is chosen such that ψ_y remains finite for $z \rightarrow \infty$. Splitting the wavenumber in a real and an imaginary part we can derive that

$$\Im m(k_{zsh}) \leq 0 \quad (C.3)$$

must be satisfied. For the so-called 'leaky' waves (see Chapter 6) the opposite sign is used. In order to avoid confusion, we only consider the case of $\Im m(k)_{zsh} \leq 0$ in this Appendix. The line $\Im m(k_{zsh}) = 0$ divides the two sets of solutions of the square root. In the complex k -plane this line is called the branch cut. Via this branch cut, the k -planes corresponding to the positive and the negative square roots are connected. The different k -planes are also called Riemann sheets. Together they form the Riemann surface. Following the approach of Ewing *et al.* (1957), we investigate the position of the branch cuts. We start with the following relation

$$k_{zsh}^2 = k_{sh}^2 - k^2, \quad (C.4)$$

where $k_{sh} = \omega/c_T$. We assume k_{sh} to be complex. Splitting the real and the imaginary parts of Equation (C.4), we obtain two relationships to determine the branch cuts:

$$\Re e^2(k_{zsh}) - \Im m^2(k_{zsh}) = \Re e^2(k_{sh}) - \Im m^2(k_{sh}) - \Re e^2(k) + \Im m^2(k), \quad (C.5)$$

$$\Re(k_{zsh})\Im(k_{zsh}) = \Im(k_{sh})\Re(k_{sh}) - \Re(k)\Im(k). \quad (C.6)$$

The branch cut $\Im(k_{zsh}) = 0$ is substituted in these expressions and from Equation (C.5) it follows that:

$$\Re^2(k) - \Im^2(k) < \Re^2(k_{sh}) - \Im^2(k_{sh}). \quad (C.7)$$

From Equation (C.6), we obtain:

$$\Im(k) = \frac{\Re(k_{sh})\Im(k_{sh})}{\Re(k)}. \quad (C.8)$$

In Fig. C.1(a), we have drawn the complex k -plane. The solid lines indicate the branch cuts and correspond to those parts of the hyperbola defined by Equation (C.8) which satisfy Equation (C.7). In Fig. C.2 we have drawn the complex k_{zsh} -plane. The branch cut $\Im(k_{zsh}) = 0$ is indicated by the solid line. The dashed curve defined by $\Re(k_{zsh}) = 0$ in Fig. C.2 corresponds to the dashed part of the hyperbolic curve in Fig. C.1(a). The solid and the dashed lines intersect a special point of interest where $k_{zsh} = 0$. In that case $k = k_{sh}$. These points are the so-called branch points.

We now investigate which quadrants of the k_{zsh} -plane correspond to values of k in the fourth quadrant of the k -plane. We are interested in the fourth quadrant of the k -plane, as it represents damped waves in the positive x -direction. In Equations (C.5) and (C.6), we substitute values of k which are located in the dashed region of Fig. C.1(a). Then, we find that the corresponding values of k_{zsh} are located in the dashed region of Fig. C.2. If we substitute in the same equations values of k located in the blank region of the fourth quadrant of Fig. C.1(a), we find corresponding k_{zsh} -values in the fourth quadrant of the k_{zsh} -plane. Hence, we conclude that for damped waves which propagate in the positive x -direction, the sign of $\Re(k_{zsh})$ can either be positive or negative.

If there is no intrinsic damping, we can write: $\Im(k_{sh}) = 0$. Using Equations (C.5) and (C.6) and $\Im(k_{zsh}) = 0$, we obtain for the branch cut:

$$\Re^2(k_{sh}) > \Re^2(k) - \Im^2(k), \quad (C.9)$$

and

$$\Re(k)\Im(k) = 0. \quad (C.10)$$

Hence,

$$\Re(k) = 0 \vee \Im(k) = 0. \quad (C.11)$$

If $\Im(k) = 0$, we find from Equation (C.9):

$$\Re^2(k) < \Re^2(k_{sh}). \quad (C.12)$$

In Fig. C.1(b), again the complex k -plane is given. The line BOA indicates the values of k which satisfy Equation (C.12).

If $\Re(k) = 0$, we obtain

$$\Re^2(k_{sh}) > -\Im^2(k). \quad (C.13)$$

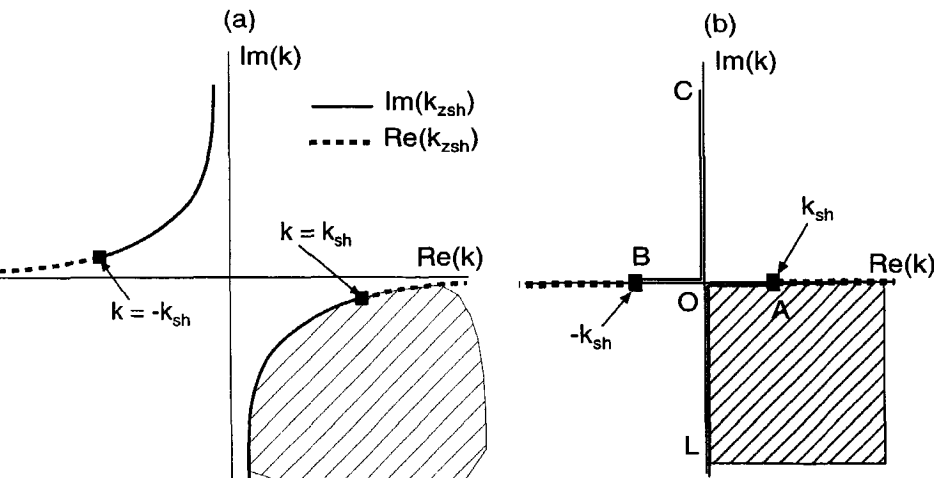


Figure C.1: Branch cuts in the complex k -plane for free field wavenumbers which are complex-valued (a) and real-valued (b)

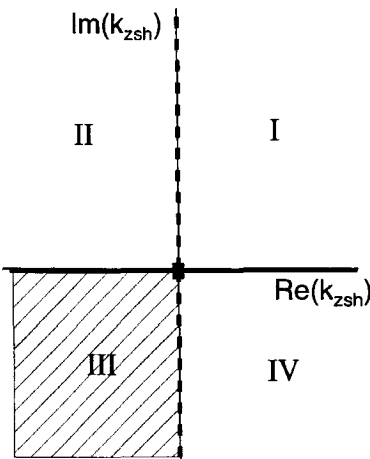


Figure C.2: Complex k_{zsh} -plane. The solid line $\text{Im}(k_{zsh}) = 0$ corresponds to the branch cuts in the Fig. C.1. The dashed line $\text{Re}(k_{zsh}) = 0$ corresponds to the dashed lines in Fig. C.1. The dashed regions corresponds to the dashed regions in Fig. C.1.

This relation is satisfied for all k . From Equations (C.12) and (C.13), we find that part of the real k -axis is a branch cut and the entire imaginary k -axis is a branch cut also. The branch cuts only are independent if they pass through a branch point (Ewing *et al.* 1957). Therefore, we use AOL and BOC as the branch cuts in the complex k -plane (see Fig. C.1(b)). The solid and dashed lines in Fig. C.1(b) correspond to the solid and dashed lines in Fig. C.2. From these graphs it is also clear that values of k on the dashed line correspond to a completely imaginary value of k_{zsh} , which is typical for a surface wave. Similar to Fig. C.1(a), the dashed region in Fig. C.1(b) corresponds to the dashed region in Fig. C.2. For the undamped case, the sign of $\Re(k_{zsh})$ is negative for damped waves propagating in the positive x -direction.

For the liquid-loaded porous halfspace we obtain a combination of branch cuts for real-valued and complex-valued free field velocities. A schematic drawing of the branch cuts for this system is given in Fig. C.3. Note that the positions of these branch cuts are a function of the frequency, due to the frequency-dependence of the Biot velocities.

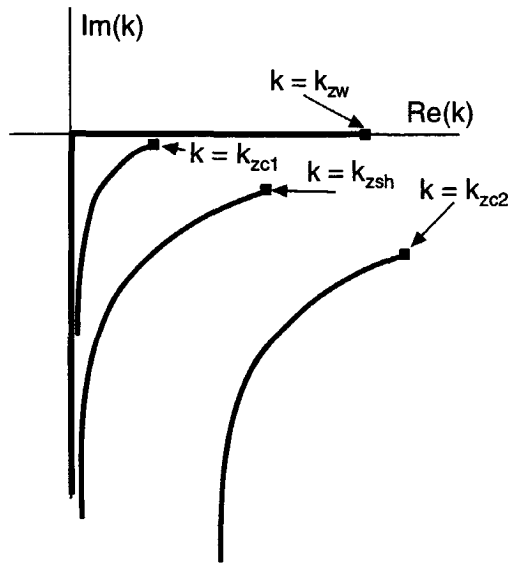


Figure C.3: Branch cuts in the complex k -plane for a liquid-loaded porous halfspace.

Appendix D

Zero-search routines

In this appendix we discuss the zero-search methods which have been used to determine the zero's of the dispersion relations $F(\omega, k) = 0$, where k is the complex wavenumber, and ω is the frequency. The following two methods have been used:

1. Plotting phase contour lines
2. Newton-Raphson iteration

D.1 Phase contour lines

When the absolute value of a complex number is equal to zero, the phase is not defined. Plotting the phase contour lines of F in the complex k -plane at fixed ω , these contour lines will intersect when $F(k, \omega) = 0$. An example of such a contour plot is given in Fig. D.1. We used Pochhammer's equation for $\omega a/c_T = 1.6$ (see Chapter 7). Four zero's occur in this plot. One of the zero's (near $\text{Re}(k)a \approx 1$) only has a real part. This corresponds to an undamped wave. The other zero's correspond to damped waves. It must be remarked that the resolution of the contour plots must be high related to distance between two zero's, otherwise the zero cannot be detected. This method will yield only qualitative results. When studying the frequency dependence of the wave modes this method is far from efficient and can only be used as a first orientation with respect to the existing wave types.

D.2 Newton-Raphson iteration

A more efficient method, yielding also quantitative results, is based on the well known Newton-Raphson method. We implement the Newton-Raphson method in the following way. At a given frequency ω , we start at an arbitrary value of k_i in the complex k -plane. The next value k_{i+1} , at the same frequency ω , is determined using:

$$k_{i+1} = k_i - \frac{F(k_i)}{\frac{dF}{dk_i}(k_i)} \quad (\text{D.1})$$

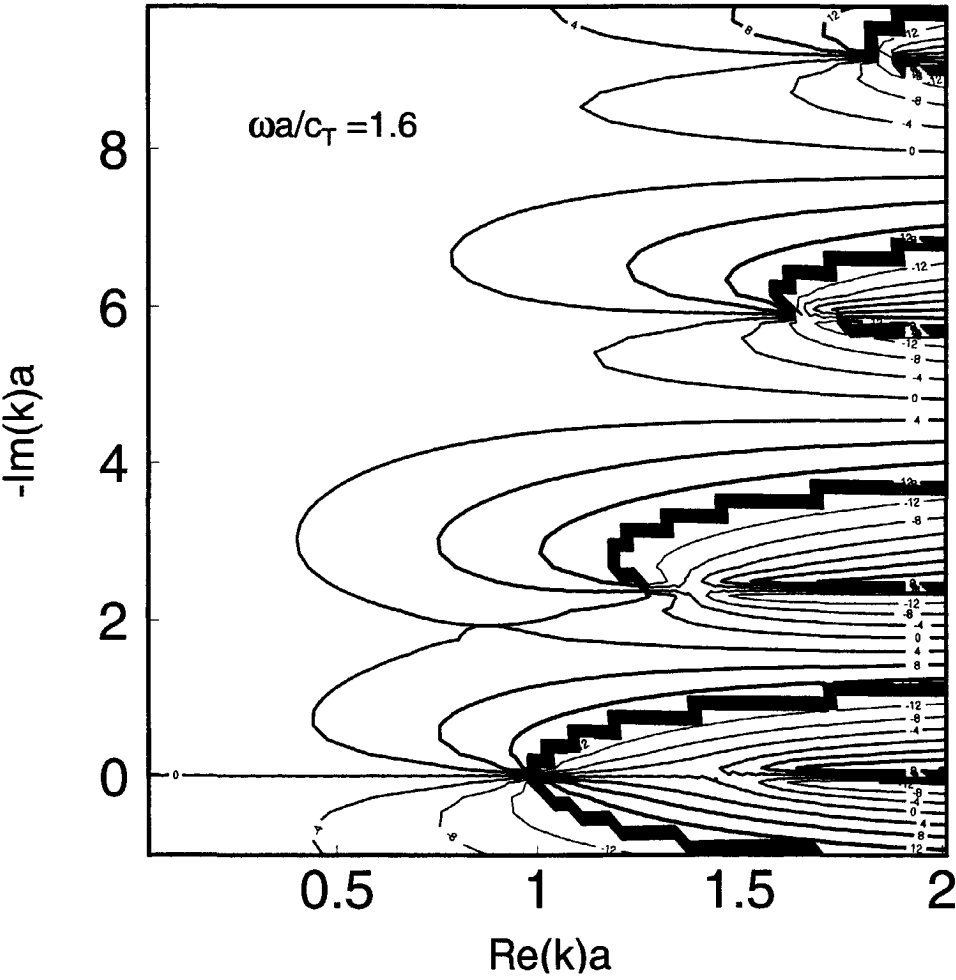


Figure D.1: Contour plot of the phase of F for the case of an elastic cylinder, with $\nu = 0.3$. $\omega a/c_T = 1.6$, where a is the radius of the cylinder. The line thickness is a measure for the number of coinciding curves.

The derivative dF/dk_i can be determined analytically, but due to the complexity of F in case of the full shock tube configuration we use a second-order numerical method:

$$\frac{dF}{dk_i}(k_i) = \frac{F(k_i + dk) - F(k_i - dk)}{2dk_i} + \mathcal{O}(dk_i^2). \quad (\text{D.2})$$

In order to improve the accuracy of the determination of dF/dk , we determined this derivative in three different directions in the complex k -plane. Please note that for an analytic function the derivative in the complex plane is insensitive to the direction of the derivative. As a convergence criterion we use:

$$\frac{|k_{i+1} - k_i|}{|k_{i+1}|} < \epsilon \bigwedge \frac{|k_{i+1} - k_{i-1}|}{|k_{i+1}|} < \epsilon, \quad (\text{D.3})$$

where $\epsilon = 10^{-5}$.

The effect of the choice for dk_i is investigated using the following test function:

$$F(k) = (k - p)^3, \quad (\text{D.4})$$

where $\Re(p) = 1$ and $\Im(p) = -1$. Both $F(k)$ and the first two derivatives are zero at $k = p$, and hence this function can be considered as being a worst case. We used $\Re(k_1) = 0.0$ and $\Im(k_1) = 0.0$. Table D.2 gives the results of the numerical search routine for different values of $|dk|$. The number of iterations n is given for which the convergence criterion Equation (D.3) was satisfied. The last two columns of Table D.2 indicate the final results $\Re(k_n)$ and $\Im(k_n)$. From Table D.2, we conclude that our

$ dk $	number of iterations n	$\Re(k_n)$	$\Im(k_n)$
0.5	483	0.991	-1.00
0.25	310	0.994	-1.00
0.125	202	0.996	-1.00

Table D.1: Computational results Newton-Raphson iteration for different values of dk . The number of iterations is given for which the convergence criterion Equation (D.3) is satisfied. We have also given the final results $\Re(k_n)$ and $\Im(k_n)$.

numerical search routine performs quite well even for large values of $|dk|$ with respect to $|k|$. The best results are obtained if $|dk|$ is much smaller than $|k|$.

It is possible that the derivative of F can be discontinuous at the so-called branch cuts. This will cause an error in the determination of the derivative. In our numerical code, we included a procedure to check whether a branch cut was passed or not. If a branch cut was passed, $|dk|$ was automatically decreased so that this was no longer the case. Another computational problem is that the values of F may become very large. To overcome this problem, we used a normalization procedure such that $|F| < 10^{20}$. The final results of the numerical search routine were insensitive to the normalization procedure.

To find the a priori unknown positions of all values of k , we divide the complex k -plane in a number of blocks as illustrated in Fig. D.2. We start the iteration in a first block. If the iteration procedure does not converge within 100 steps or has moved out of the block after 100 steps, we stop the procedure and re-start it in the next block.

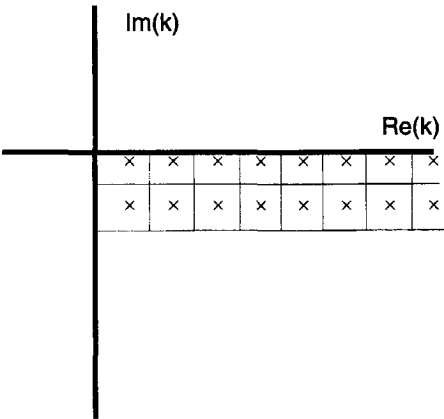


Figure D.2: Initial locations of k for the Newton-Raphson procedure.

Appendix E

Parameters of porous samples.

The properties of the porous samples were determined in independent laboratory experiments. We used three series of samples: natural Bentheimer sandstone and two series of synthetic samples. The latter two series are indicated by N and G. The N-series consist of sintered crushed glass and were manufactured by COSS (Poland). The G series consist of Al_2O_3 and were manufactured by Gimex (Geldermalsen, The Netherlands). The natural Bentheimer sandstone samples were prepared by Schols en 't Hart (Delft, The Netherlands) and Shell International Exploration and Production Laboratory (Rijswijk, The Netherlands).

E.1 Porosity and grain density

Porosities of all porous samples were measured using the standard two-weight (dry and buoyant) method. The dry weight G_0 is measured first, and subsequently, the buoyant weight G_1 of the same sample is determined. Using G_0 and G_1 , the density of the solid ρ_s and the porosity can be obtained:

$$\rho_s = \frac{G_0}{G_0 - G_1} \rho_w, \quad (E.1)$$

and

$$\phi = \frac{G_1 - G_0 + \rho_w g V_b}{\rho_w g V_b}, \quad (E.2)$$

where ρ_w is the water density, V_b is the bulk volume of the sample and g the gravity constant.

E.2 Permeability

The steady-state permeability constant k_0 and the second Forchheimer coefficient (see Section 5.3) are determined using an integrated form of Forchheimer's equation. The permeability constants are determined using dry samples. It is assumed that the same

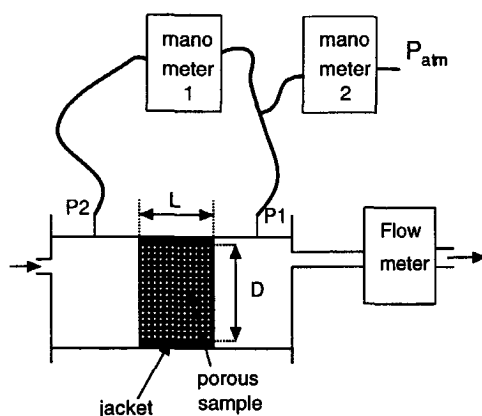


Figure E.1: Set-up for the permeability measurements.

parameters apply for water-saturated samples. The Forchheimer equation reads as follows:

$$\frac{\partial p}{\partial x} = -\frac{\phi \eta v}{k_0} - \phi^2 \rho v^2 b \quad (\text{E.3})$$

where v is the average velocity in the pores, η the dynamic fluid viscosity, and ρ the fluid density. The permeability coefficients are determined by measuring both the volumetric flow rate and the pressure drop. The set-up is shown in Fig. E.1. The pressure difference $P_2 - P_1$ is measured with manometer 1 and the pressure difference $P_1 - P_{\text{atm}}$ is measured using manometer 2, where P_{atm} is the atmospheric pressure. Highly sensitive water manometers (v. Essen, Betz micromanometer, 500 mm) were used for small pressure differences. For higher pressures, we used a water U-tube and also mechanical pressure meters (Wallace and Tiernan). We measured the volume flow rate using a gasmeter (Schlumberger Industries, Meterfabriek) for low flow rates, while for higher flow rates a Rota meter (Q1.1000) was applied. A jacket is applied to prevent leakage of air along the porous sample. In this way a one-dimensional flow is obtained in the sample. The Forchheimer equation as given in Equation (E.3) is related to the measured quantities in the following way. The average velocity v in the pores is related to the measured volume flow rate, which is written as a mass flow rate Q_m in order to avoid pressure effects:

$$v = \frac{Q_m}{\rho A \phi}, \quad (\text{E.4})$$

where $A = \pi D^2/4$, with D the diameter of the sample. The density of the air can be related to the pressure p by

$$\rho = \frac{p}{RT}, \quad (\text{E.5})$$

where R is the specific gas constant and T the temperature. Integrating along the length L of the porous sample we obtain:

$$\frac{p_2^2 - p_1^2}{2RTL\eta Q_m/A} = \frac{1}{k_0} + \frac{b}{\eta} Q_m/A. \quad (\text{E.6})$$

Plotting the LHS of this equation versus Q_m/A yields k_0 from the intercept with the vertical axis and yields b from the slope of the curve. As an example, the results for Eindhoven Sandstone are given in Fig. E.2. For the higher mass flow rates Forchheimer's equation is in good agreement with the experimental results. For the lower range we observe a significant deviation from the theory. Forchheimers equation essentially is an empirical model, and for lower velocities in the pores the validity is not quite clear. For a discussion on this subject we refer to Firdaouss *et al.* (1997).

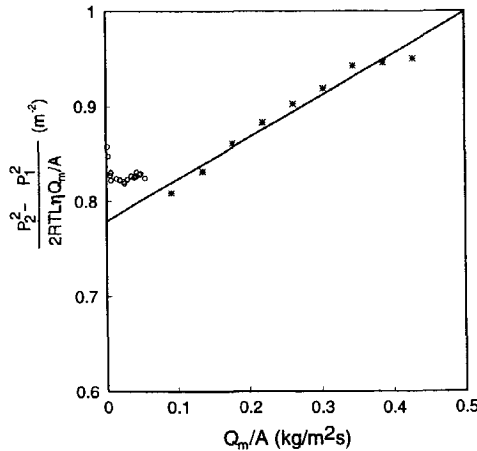


Figure E.2: Experimental results of the permeability measurements for Eindhoven Sandstone. On the horizontal axis, the mass flowrate is given, while on the vertical axis the LHS of Equation (E.6) is given. \circ : flowrates measured using Schlumberger gasmeter, $*$: flowrates measured using Rota meter Q1.1000.

E.3 Tortuosity

The tortuosity was determined in an electrical resistivity experiment. The analogy between the acceleration of an inviscid incompressible fluid within a rigid porous medium, and the electric current density within an electrolyte filled porous insulator, was first demonstrated by Brown (1980). We can write for the tortuosity α_∞ :

$$\frac{\alpha_\infty}{\phi} = \frac{R_s}{R_f}, \quad (\text{E.7})$$

with R_f as the intrinsic resistivity of the electrolyte in Ωm and R_s as the intrinsic resistivity of the porous sample in Ωm . The ratio α_∞/ϕ is also known as the formation factor F . This relation was verified experimentally by Johnson *et al.* (1982). Our set-up is shown in Fig. E.3. A storage vessel is filled with a 0.08 KCl water solution and subsequently

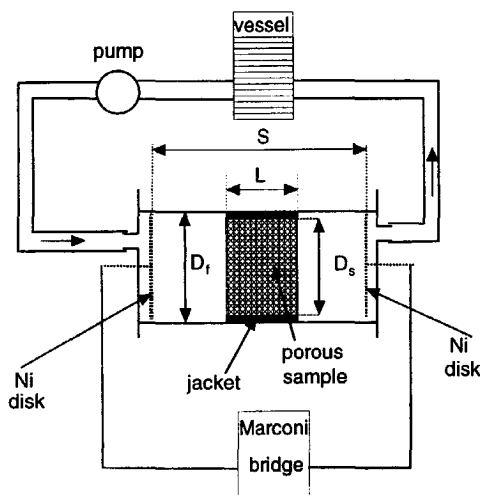


Figure E.3: Set-up for the tortuosity measurements.

the porous sample is slowly saturated with this solution. The pump is used to keep the solution homogenous. A jacket is applied in order to avoid leakage along the sample. Furthermore, it is assumed that the conductivity of the matrix can be neglected. The distance S between two Ni-electrodes can be varied. The length of the porous sample is denoted by L . The resistivities R_f and R_s are measured in the following way. Using a resistance bridge (Marconi Universal Bridge TF2700), the resistance in Ω of the system with length S between the two Ni-electrodes is measured. We apply a.c. with a 1000 Hz frequency in order to avoid electrolysis. Subsequently, the electrodes are displaced and we measure the resistance again. This is repeated for decreasing values of S and we plot the resistance versus $S - L$. An example of the results is given in Fig. E.4. The intercept of the first order fit gives the resistance r_s in Ω of the porous sample with length L . The slope of the curve gives the resistance of the electrolyte per mm (r_f/L). The intrinsic resistivity of the porous insulator is obtained by:

$$R_s = \frac{r_s \pi D_s^2}{4L}, \quad (\text{E.8})$$

where D_s is the diameter of the porous sample. The intrinsic resistivity of the electrolyte follows from:

$$R_f = \frac{r_f \pi D_f^2}{4L}, \quad (\text{E.9})$$

where D_f is the inner diameter of the perspex tube (see Fig. E.4). For this specific case we obtain for the formation factor F a value of 3.86. Using the porosity $\phi = 0.48$ we arrive at $\alpha_\infty = 1.85$ for the tortuosity.

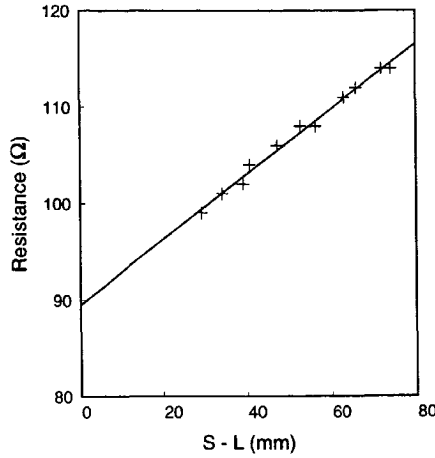


Figure E.4: Experimental data resistivity measurements sample N4. The resistance is plotted versus $S - L$.

E.4 Elastic parameters

For air-saturated porous materials the velocities of the fast and shear wave only depend on the solid properties. For the high-frequency limite we can write from Equation (3.3.2) using $\rho_f = 0$:

$$c_1 = \sqrt{\frac{K_p}{(1 - \phi)\rho_s}}, \quad (\text{E.10})$$

and

$$c_{sh} = \sqrt{\frac{G}{(1 - \phi)\rho_s}}. \quad (\text{E.11})$$

These velocities are deduced from acoustic transmission experiments. In a water-filled tank a dry sample of porous material is enclosed in a thin impermeable jacket. The experimental configuration is shown in Fig. E.5. In this set-up a short duration pulse is sent through the sample and recorded by the receiver. The porous sample can be mounted in various positions in between the transducers. For details of this set-up we refer to Kelder (1998). We perform two experiments for each porous sample. First, we record the transmitted signal for normal incidence ($\alpha = 0^\circ$). Subsequently, an experiment for oblique incidence is carried out ($\alpha \approx 20^\circ$). Fig. E.6(a) shows the recorded signal for $\alpha = 0^\circ$. For this case only the fast compressional wave and the internal reflection of this wave in the sample is recorded. The first arrival is denoted by T_{c1} and the arrival of the reflection is denoted by T_{rc1} . Using these arrival times, we determine the velocity of the fast wave c_1 . For oblique incidence the shear wave is also generated. Fig. E.6(b) shows the arrival of the fast wave T_{c1o} , followed by the arrival of the shear wave T_{csh} . We use T_{c1o} , T_{csh} , and c_1 to determine the velocity of the shear wave c_{sh} in the dry material.

Another method for the determination of the fast wave velocity in dry samples is the use of a concrete tester (SIMAC- CSI-ctt4). In that case the piezo-electric transducers are brought in good mechanical contact with the dry sample and the transit time of an acoustic pulse is measured. In order to enhance the acoustic coupling between the transducers and the porous sample a mixture of glycerine and quartz powder was applied. Fig. E.7 gives a comparison between the data for different samples of the concrete tester and the water tank. We found that the difference between the two measurements was within 100 m/s.

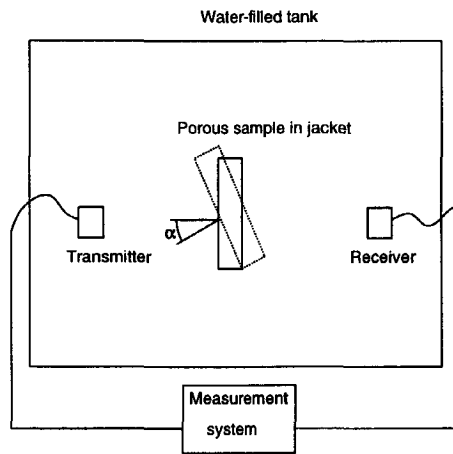


Figure E.5: Set-up for experiments on dry samples.

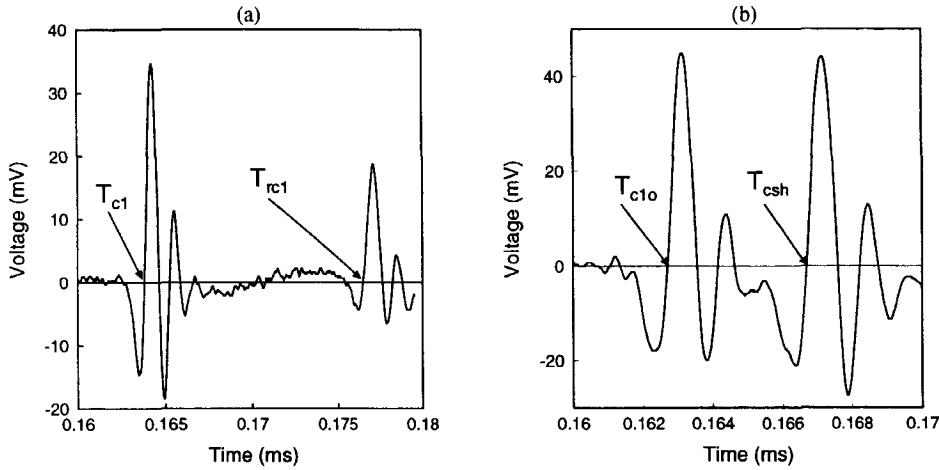


Figure E.6: Recorded signals at the receiver in the water tank. The signals are given for two configurations. For the first case (a) $\alpha = 0^\circ$ and for the second case (b) $\alpha = 22^\circ$.

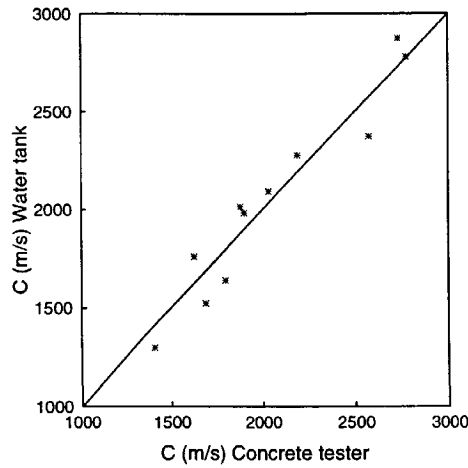


Figure E.7: Comparison between data for different samples of the water tank and the concrete tester.

E.5 Parameters

We now give the parameters which we used in our computations, and subsequently, we give the properties for the samples which were used for shock tube experiments.

air-filled pores:	
density of air ρ_f (kg/m ³)	1.205
speed of sound (m/s)	343
viscosity of air (10^{-5} kgm ⁻¹ s ⁻¹)	1.81
water-saturated rock:	
density of water ρ_w (kg/m ³)	998
dynamic viscosity of water η (Pa.s)	10^{-3}
water bulk modulus K_f (GPa)	2.2
rock properties:	
density of the solid ρ_s (10^3 kg/m ³)	2.62
porosity (%)	0.22
permeability k_0 (10^{-12} m ²)	2.73
tortuosity	2.9
constrained modulus K_p (GPa)	17
shear modulus G (GPa)	8.0
bulk modulus of the grains K_s (GPa)	36.5

Table E.1: Parameter values used in computations. The rock parameters correspond to the parameter set of Bentheimer sandstone 1 in Table E.3. For the bulk modulus of the grains we use the literature value for quartz (CRC 1973).

Sample name	diameter (mm)	length (mm)
Eindhoven sandstone	73.2 \pm 0.1	152.5 \pm 0.1
Bentheimer sandstone 1	70.0 and 76.9 \pm 0.1	400 \pm 0.2
Bentheimer sandstone 2	74.7 \pm 0.1	20.5 \pm 0.1
N1B	75.8 \pm 0.1	400 \pm 0.2
N2	76.5 \pm 0.1	400 \pm 0.2
N3	76.8 \pm 0.1	400 \pm 0.2
N4	76.8 \pm 0.1	400 \pm 0.2
N4B	76.8 \pm 0.1	400 \pm 0.2
N5	76.5 \pm 0.1	400 \pm 0.2
N5B	70.0 \pm 0.1	400 \pm 0.2
N6B	76.8 \pm 0.1	400 \pm 0.2
G50A	76.8 \pm 0.1	200 \pm 0.2
G30B	76.8 \pm 0.1	200 \pm 0.2
G40A	75.8 \pm 0.1	200 \pm 0.2
G20B	76.8 \pm 0.1	200 \pm 0.2

Table E.2: Measured lengths and diameters of the porous samples.

Sample name	solid density ρ_s (kg/m ³)	porosity ϕ (-)	permeability k_0 (10 ⁻¹² m ²)	second Forchheimer coefficient b (10 ⁴ m ⁻¹)	tortuosity α_∞ (-)	constrained modulus K_p (GPa)	shear modulus G (GPa)
Eindhoven sandstone	2.46 ± 0.05	0.35 ± 0.01	122 ± 8	7.5 ± 0.1	2.1 ± 0.1	9.6 ± 0.9	(-)
Bentheimer sandstone 1	2.62 ± 0.04	0.22 ± 0.01	2.73 ± 0.2	(-)	2.9 ± 0.1	17 ± 2	8.0 ± 0.8
Bentheimer sandstone 2	2.63 ± 0.04	0.23 ± 0.01	3.7 ± 0.2	500 ± 0.1	2.4 ± 0.1	16 ± 2	7.0 ± 0.7
N1B	2.51 ± 0.04	0.57 ± 0.01	216 ± 15	(-)	1.6 ± 0.1	1.5 ± 0.1	(-)
N2	2.55 ± 0.04	0.48 ± 0.01	71 ± 4	(-)	1.8 ± 0.1	4.2 ± 0.4	1.6 ± 0.1
N3	2.49 ± 0.04	0.51 ± 0.01	82 ± 5	(-)	1.6 ± 0.1	3.5 ± 0.3	1.4 ± 0.1
N4	2.56 ± 0.04	0.48 ± 0.01	20 ± 1	(-)	1.8 ± 0.1	6.4 ± 0.6	2.9 ± 0.2
N4B	2.55 ± 0.04	0.46 ± 0.01	20 ± 1	(-)	2.0 ± 0.1	9.1 ± 0.9	3.3 ± 0.3
N5	2.59 ± 0.04	0.52 ± 0.01	3.2 ± 0.2	(-)	1.7 ± 0.1	2.5 ± 0.2	0.88 ± 0.09
N5B	2.57 ± 0.04	0.52 ± 0.01	3.4 ± 0.2	(-)	1.7 ± 0.1	2.1 ± 0.2	0.88 ± 0.09
N6B	2.59 ± 0.04	0.53 ± 0.01	2.9 ± 0.2	(-)	1.7 ± 0.1	3.7 ± 0.3	1.3 ± 0.1
G50A	3.14 ± 0.06	0.58 ± 0.01	(3.45 ± 0.2) 10 ⁻⁴		2.0 ± 0.1	4.8 ± 0.4	2.0 ± 0.2
G30B	3.1 ± 0.06	0.56 ± 0.01	(3.9 ± 0.2) 10 ⁻³	(-)	3.1 ± 0.2	5.9 ± 0.6	2.4 ± 0.2
G40A	3.21 ± 0.06	0.53 ± 0.01	(6.1 ± 0.02) 10 ⁻³	(-)	2.53 ± 0.2	6.6 ± 0.6	2.6 ± 0.2
G20B	3.06 ± 0.06	0.52 ± 0.01	(-)	(-)	(-)	6.2 ± 0.6	(-)

Table E.3: Measured rock properties porous samples.

Bibliography

- ABRAMOWITZ, M., & I.A. STEGUN. 1964. *Handbook of Mathematical Functions*. Dover Publications, Inc., New York.
- ACHENBACH, J. D. 1973. *Wave propagation in elastic solids*. North-Holland publishing Company.
- ADLER, L., & P.B. NAGY. 1994. Measurements of acoustic surface waves on fluid-filled porous rocks. *J. Geophysical Research* **99**:17863–17869.
- ALLARD, J. F. 1993. *Propagation of sound in porous media*. Elsevier Science.
- ALLARD, J.F., M. HENRY, J. TIZIANEL, L. KELDERS, & W. LAURIKS. 1998. Sound propagation in air saturated random packings of beads. *J. Acoust. Soc. Am.* **104**:2004–2007.
- ANSELL, J.H. 1972. The roots of the stoneley wave equation for solid-liquid interfaces. *Pure Appl. Geophysics* **94**:172–188.
- ATTENBOROUGH, K. 1987. On the acoustic slow wave in air-filled granular media. *J. Acoust. Soc. Am.* **81**:93–102.
- BARDOT, A., B. BROUARD, & J.F. ALLARD. 1996. Frame decoupling at low frequency in thin porous layers saturated by air. *J. Acous. Soc. Am.* **79**:8223–8229.
- BERRYMAN, J. G. 1981. Elastic wave propagation in fluid-saturated porous media. *J. Acous. Soc. Am.* **69**:416–424.
- BERRYMAN, J. G. 1983. Dispersion of extensional waves in fluid-saturated porous cylinders at ultrasonic frequencies. *J. Acous. Soc. Am.* **74**:1805–1812.
- BIOT, M. A. 1941. General theory of three-dimensional consolidation. *J. Appl. Physics* **12**:155–164.
- BIOT, M. A. 1955. Theory of elasticity and consolidation for a porous anisotropic solid. *J. Appl. Physics* **26**:182–185.
- BIOT, M. A. 1956a. Theory of propagation of elastic waves in a fluid-saturated porous solid i. low-frequency range. *J. Acous. Soc. Am.* **28**:168–178.
- BIOT, M. A. 1956b. Theory of propagation of elastic waves in a fluid-saturated porous solid ii. higher frequency range. *J. Acous. Soc. Am.* **28**:179–191.

- BIOT, M. A., & D. G. WILLIS. 1957. The elastic coefficients of the theory of consolidation. *J. Appl. Mech.* **24**:594-601.
- BJOERCK, A. 1996. *Numerical methods for least square problems*. SIAM.
- BOURBIÉ, TH., O. COUSSY, & B. ZINSZNER. 1987. *Acoustics of porous media*. Gulf publishing company.
- BRAUN, S., & Y.M. RAM. 1987. Determination of structural modes via the prony model: System order and noise induced poles. *J. Acous. Soc. Am.* **81**:1447-1459.
- BREKHOVSKIKH, L.M. 1980. *Waves in layered media*. Academic Press.
- BROWN, R.J. 1980. Connection between formation factor for electrical resistivity and fluid-solid coupling factor in biot's equations for acoustic waves in fluid-filled porous media. *Geophysics* **45**:1269-1275.
- BURNS, D.R. 1988. Viscous fluid effects on guided wave propagation in a borehole. *J. Acoust. Soc. Am.* **83**:463-469.
- BURNS, D.R., & C.H. CHENG. 1987. Inversion of borehole guided wave amplitudes for formation shear wave attenuation values. *J. Geophys. Research* **92**:12713-12725.
- BURNS, D.R., C.H. CHENG, D.P. SCHMITT, & M.N. TOKSÖZ. 1988. Permeability estimation from full waveform acoustic logging data. *The Log Analyst* 112-122.
- BURRIDGE, R., & J.B. KELLER. 1983. Poroelasticity equations derived from microstructure. *J. Acous. Soc. Am.* **70**:1140-1146.
- CARSLAW, H.S., & J.C. JAEGER. 1986. *Conduction of heat in solids*. Clarendon Press.
- CHANDLER, R.N. 1981. Transient streaming potential measurements on fluid-saturated porous structures: An experimental verification of biot's slow wave in the quasi-static limit. *J. Acous. Soc. Am.* **70**:116-121.
- CHANDLER, R.N., & D.L. JOHNSON. 1981. The equivalence of quasistatic flow in fluid-saturated porous media and biot's slow wave in the limit of zero frequency. *J. Appl. Phys.* **52**:3391-3395.
- CHANG, S.K., H.L. LIU, & D.L. JOHNSON. 1988. Low-frequency tube waves in permeable rocks. *Geophysics* **53**:519-527.
- CHENG, C.H., Z. JINZHONG, & D.R. BURNS. 1987. Effects of in-situ permeability on the propagation of stoneley (tube) waves in a borehole. *Geophysics* **52**:1279-1289.
- CRC Press. 1973. *Handbook of Chemistry and Physics*.
- CUVELIER, C., G. SEGAL, & A.A. VAN STEENHOVEN. 1986. *Finite element methods and Navier-Stokes equations*. Reidel.
- DAVIES, J. L. 1988. *Wave propagation in solids and fluids*. Springer-Verlag, New-York.

- DE HOOP, A. T., & J.H.M.T. VAN DER HIJDEN. 1983. Generation of acoustic waves by an impulsive line source in a fluid/solid configuration with a plane boundary. *J. Acoust. Soc. Am.* **74**:333-342.
- DERESIEWICZ, H. 1960. The effect of boundaries on wave propagation in a liquid-filled porous solid: I. reflection of plane waves at a free plane boundary (non-dissipative case). *Bull. Seism. Soc. Am.* **50**:599-607.
- DERESIEWICZ, H., & R. SKALAK. 1963. On uniqueness in dynamic poroelasticity. *Bull. Seism. Soc. Am.* **53**:783-788.
- DUNN, K-J. 1986. Acoustic attenuation in fluid-saturated porous cylinders at low frequencies. *J. Acous. Soc. Am.* **79**:1709-1721.
- DUNN, K-J. 1987. Sample boundary effect in acoustic attenuation of fluid-saturated porous cylinders. *J. Acous. Soc. Am.* **81**:1259-1266.
- ELLEFSSEN, K.J., D.R. BURNS, & C.H. CHENG. 1993. Homomorphic processing of the tube wave generated during acoustic logging. *Geophysics* **58**:1400-1407.
- ELLEFSSEN, K.J., C.H. CHENG, & K.M. TUBMAN. 1989. Estimating phase velocity and attenuation of guided waves in acoustic logging data. *Geophysics* **54**:1054-1059.
- ELLIS, D.V. 1987. *Well logging for Earth Scientists*. Elsevier Science Publishers.
- EWING, W.M., W.S. JARDETZKY, & F. PRESS. 1957. *Elastic waves in layered media*. McGraw-Hill.
- FENG, S., & D.L. JOHNSON. 1983. High-frequency acoustic properties of a fluid/porous solid interface. *J. Acous. Soc. Am.* **74**:906-924.
- FIRDAOUSS, M., J-L GUERMOND, & P. L QUÉRÉ. 1997. Nonlinear corrections to darcy's law at low reynolds numbers. *J. Fluid Mech.* **343**:331-350.
- FOLK, R., G. FOX, C.A. SHOOK, & C.W. CURTIS. 1958. Elastic strain produced by sudden application of pressure to one end of a cylindrical bar i. theory. *J. Acous. Soc. Am.* **30**:552-558.
- FOX, G., & C.W. CURTIS. 1958. Elastic strain produced by sudden application of pressure to one end of a cylindrical bar ii. experimental observations. *J. Acous. Soc. Am.* **30**:559-563.
- GARDNER, G.H.F. 1962. Extensional waves in fluid-saturated porous cylinders. *J. Acoust. Soc. Am.* **34**:36-40.
- GASSMANN, F. 1951. Elastic waves through a packing of spheres. *Geophysics* **16**:673-685.
- GEERTSMA, J., & D.C. SMIT. 1961. Some aspects of elastic wave propagation in fluid-saturated porous solids. *Geophysics* **26**:169-181.

- GOLUB, G.H., & C.F. VAN LOAN. 1989. *Matrix Computations*. The Johns Hopkins University Press.
- GROSH, K., & E.G. WILLIAMS. 1993. Complex wave-number decomposition of structural vibrations. *J. Acoust. Soc. Am.* **93**:836-848.
- GROUP, NUMERICAL ALGORITHM. 1995. *NAG Fortran Library Manual*. NAG Ltd Wilkinson House.
- HANNOURA, A.A., & F.J. BAREND. 1981. Non-darcy flow; a state of the art. In *Proceedings of Euromech*.
- HAYKIN, S. 1985. Radar array processing for angle of arrival estimation. In S. HAYKIN (ED.), *Array signal processing*, Prentice-Hall processing series, 194-292. Prentice-Hall, New Jersey.
- HERCZYNSKI, A., & R.T. FOLK. 1989. Orthogonality condition for the pochhammer-chree modes. *Quart. J. Mech. appl. Math.* **42**:524-536.
- HILDEBRAND, F.B. 1956. *Introduction to numerical analysis*. McGraw-Hill book Company.
- HÖLSCHER, P. 1995. *Dynamical response of saturated and dry soils*. PhD thesis, Delft University of Technology.
- HSU, C-J, S. KOSTEK, & D.L. JOHNSON. 1997. Tube waves and mandrel modes: Experiment and theory. *J. Acoust. Soc. Am.* **102**:3277-3289.
- HSU, K., & A.B. BAGGEROER. 1986. Application of the maximum-likelihood method (mlm) for sonic velocity logging. *Geophysics* **51**:780-787.
- HSU, K., & C. ESMERSOY. 1992. Parametric estimation of phase and group slownesses from sonic logging waveforms. *Geophysics* **57**:978-985.
- HSUI, A.T., & M.N. TOKÖZ. 1986. Application of an acoustic model to determine in situ permeability of a borehole. *J. Acoust. Soc. Am.* **79**:2055-2059.
- JOHNSON, D.L. 1980. Equivalence between fourth sound in liquid he ii at low temperatures and the biot slow wave in consolidated porous media. *Appl. Phys. Lett.* **37**:1065-1067.
- JOHNSON, D.L., D.L. HEMMICK, & H. KOJIMA. 1994. Probing porous media with first and second sound. i. dynamic permeability. *J. Appl. Phys.* **76**:104-114.
- JOHNSON, D.L., J. KOPLIK, & R. DASHEN. 1987. Theory of dynamic permeability and tortuosity in fluid-saturated porous media. *J. Fluid. Mech.* **176**:379-402.
- JOHNSON, D.L., & S. KOSTEK. 1995. A limitation of the biot-gardner theory of extensional waves in fluid-saturated porous cylinders. *J. Acoust. Soc. Am.* **97**:741-744.

- JOHNSON, D.L., & T.J. PLONA. 1986. Recent developments in the acoustic properties of porous media. In *Frontiers of physical acoustics*. North Holland Publishing Company, Amsterdam.
- JOHNSON, D.L., & T.J. PLONA. 1994. Probing porous media with first and second sound. ii. acoustic properties of water-saturated porous media. *J. Appl. Phys.* **76**:115-125.
- JOHNSON, D.L., T.J. PLONA, C. SCALA, F. PASIERB, & H. KOJIMA. 1982. Tortuosity and acoustic slow waves. *Phys. Rev. Letters* **49**:1840-11844.
- JONG, G. DE JOSSELIN DE. 1956. Wat gebeurt er in de grond tijdens het heien ? *De ingenieur* **25**:b77-b88.
- KAUL, R.K., & J.J. MCCOY. 1964. Propagation of axisymmetric waves in a circular semiinfinite elastic rod. *J. Acoust. Soc. Am.* **36**:653-660.
- KAY, S.M., & S.L. MARPLE. 1981. Spectrum analysis - a modern perspective. *Proc. of IEEE* **69**:1380-1419.
- KELDER, O. 1998. *Frequency-dependent wave propagation in water-saturated porous media*. PhD thesis, Delft University of Technology.
- LAFLEUR, L. D., & F.D. SHIELDS. 1995. Low-frequency propagation modes in a liquid-filled elastic tube waveguide. *J. Acoust. Soc. Am.* **97**:1435-1445.
- LANG, S.W., A. L. KURKJIAN, J.H. MCCLELLAN, C.F. MORRIS, & T.W. PARKS. 1987. Estimating slowness dispersion from arrays of sonic logging waveforms. *Geophysics* **52**:530-544.
- LANG, S.W., & J.H. MCCLELLAN. 1980. Frequency estimation with maximum entropy spectral estimators. *IEEE Transactions ASSP* **28**:716-724.
- LAURIKS, W., L. KELDERS, & J-F. ALLARD. 1998. Surface waves and leaky waves above a porous layer. *Wave motion* **28**:59-67.
- LIU, H.L. 1988. Borehole modes in a cylindrical fluid-saturated permeable medium. *J. Acous. Soc. Am.* **84**:424-431.
- LIU, H.L., & D.L. JOHNSON. 1997. Effects of an elastic membrane on tube waves in permeable formations. *J. Acous. Soc. Am.* **101**:3322-3329.
- LOVE, A.E.H. 1944. *A treatise on the mathematical theory of elasticity*. Cambridge University Press.
- MAKHOUL, J. 1975. Linear prediction: A tutorial review. *Proc. of IEEE* **63**:561-580.
- MARPLE, S.L. 1987. *Digital spectral analysis: with applications*. Prentice-Hall.
- McKENNA, J., & P.G. SIMPKINS. 1985. Modal solutions, symmetry properties, and orthogonality conditions for elastic waves in cylinders. *J. Acoust. Soc. Am.* **78**:1675-1683.

- MEEKER, T.R., & A.H. MEITZLER. 1964. Guided wave propagation in elongated cylinders and plates. In W.P. MASON (ED.), *Physical acoustics*, Vol. 1, 111-167. Academic Press.
- MEITZLER, A.H. 1965. Backward-wave transmission of stress pulses in elastic cylinders and plates. *J. Acoust. Soc. Am.* **38**:835-842.
- MIKLOWITZ, J. 1978. *The theory of elastic waves and waveguides*. North-Holland publishing Company.
- NAGY, P.B., & L. ADLER. 1990. Slow wave propagation in air-filled porous materials and natural rocks. *Appl. Phys. Lett.* **56**:2504-2506.
- NAKORYAKOV, V.E., V.V. KUZNETSOV, & V.E. DONTSOV. 1989. Pressure waves in saturated porous media. *Int. J. Multiphase Flow* **15**:857-875.
- ONOE, M., H.D. MCNIVEN, & R.D. MINDLIN. 1962. Dispersion of axially symmetric waves in elastic rods. *J. Appl. Mechanics* **29**:729-734.
- PAILLET, F.L., & C.H. CHENG. 1991. *Acoustic waves in boreholes- the theory and application of acoustic full-waveform logs*. CRC Press.
- PAILLET, F.L., C.H. CHENG, & W.D. PENNINGTON. 1992. Acoustic-waveform logging - advances in theory and application. *The Log Analyst* 239-258.
- PHINNEY, R.A. 1961a. Leaking modes in the crustal waveguide part 1 the ocean pl wave. *J. Geophysical Research* **66**:1445-1469.
- PHINNEY, R.A. 1961b. Propagation of leaking interface waves. *Bull. Seism. Soc. of Am.* **51**:527-555.
- PLONA, T.J. 1980. Observation of a second bulk compressional wave in a porous medium at ultrasonic frequencies. *Appl. Phys. Lett.* **36**:259-261.
- PLONA, T.J., B.K. SINHA, S. KOSTEK, & S-K CHANG. 1992. Axisymmetric wave propagation in fluid-loaded cylindrical shells ii: theory versus experiment. *J. Acous. Soc. Am.* **92**:1132-1143.
- ROEVER, W.L., & T.F. VINING. 1959. Propagation of elastic wave motion from an impulsive source along a fluid/solid interface. *Philos. Trans. R. Soc. London, Ser. A* **251**:455-465.
- ROSENBAUM, J.H. 1974. Synthetic microseismograms: Logging in porous formations. *Geophysics* **39**:14-32.
- SCHMITT, D.P., M. BOUCHON, & G. BONNET. 1988a. Full-wave synthetic acoustic logs in radially semiinfinite saturated porous media. *Geophysics* **53**:807-823.
- SCHMITT, D.P., Y. ZHU, & C.H. CHENG. 1988b. Shear wave logging in semi-infinite saturated porous formations. *J. Acous. Soc. Am.* **84**:2230-2244.

- SCHOENBERG, M., T. MARZETTA, J. ARON, & R.P. PORTER. 1981. Space-time dependence of acoustic waves in a borehole. *J. Acous. Soc. Am.* **70**:1496-1507.
- SCHOLTE, J.G. 1948. On the large displacements commonly regarded as caused by Love waves and similar dispersive surface waves. *Proc. K. Ned. Akad. Wet.* **51**:533-543, 624-649, 828-835, 969-976.
- SEGAL, G. 1984. *Sepran Manual*. Ingenieursbureau Sepra.
- SKALAK, R. 1957. Longitudinal impact of a semi-infinite circular elastic bar. *J. Appl. Mechanics* **24**:59-64.
- SMEULDERS, D.M.J. 1992. *On wave propagation in saturated and partially saturated porous media*. PhD thesis, Eindhoven University of Technology.
- SMEULDERS, D.M.J., R.L.G.M. EGGELS, & M.E.H. VAN DONGEN. 1992. Dynamic permeability: reformulation of theory and new experimental and numerical data. *J. Fluid Mech.* **245**:211-227.
- SMEULDERS, D.M.J., & M.E.H. VAN DONGEN. 1997. Wave propagation in porous media containing a dilute gas-liquid mixture: theory and experiments. *J. Fluid Mech.* **343**:351-373.
- SMEULDERS, D.M.J., M.E.H. VAN DONGEN, & C.J. WISSE. 1997. Acoustic slow wave transition in air-saturated porous media. In *Proc. 21st International Symposium on Shock waves*.
- SMEULDERS, D.M.J., R.R. VAN HASSEL, & M.E.H. VAN DONGEN. 1994. Similarity of sharp-edged porous media. *Int. J. Engng. Sci.* **32**:979-990.
- SNIEKERS, R.W.J.M., D.M.J. SMEULDERS, M.E.H. VAN DONGEN, & H. VAN DER KOGEL. 1989. Pressure wave propagation in a partially water-saturated porous medium. *J. Appl. Phys.* **66**:4522-4524.
- STOLL, R.D. 1974. Acoustic waves in saturated sediments. In L.D. HAMPTON (ED.), *Physics of sound in marine sediments*. Plenum.
- STRICK, E. 1959. Propagation of elastic wave motion from an impulsive source along a fluid/solid interface. *Philos. Trans. R. Soc. London, Ser. A* **251**:465-523.
- TANG, X.M. 1993. Waveform inversion of seismic velocities and attenuation from low-frequency waves in cylindrical bars. *Geophysics* **58**:1525-1531.
- TANG, X.M. 1998. Simultaneous inversion of shear wave anisotropy parameters from multiple component dipole acoustic array. In *Expanded abstracts EAGE, 59th Conference and Technical Exhibition*.
- TANG, X.M., & C.H. CHENG. 1996. Fast inversion of formation permeability from Stoneley wave logs using a simplified Biot-Rosenbaum model. *Geophysics* **61**:639-645.

- TANG, X.M., C.H. CHENG, & M.N. TOKSÖZ. 1991. Dynamic permeability and borehole stoneley waves: A simplified biot-rosenbaum model. *J. Acous. Soc. Am.* **90**:1632-1646.
- TANG, X.M., E.C. REITER, & D.R. BURNS. 1995. A dispersive-wave processing technique for estimating formation shear velocity from dipole and stoneley waveforms. *Geophysics* **60**:19-28.
- TIJHUIS, A.G. 1987. *Electromagnetic inverse profiling; theory and numerical implementation*. PhD thesis, Delft University of Technology.
- TUFTS, D.W., & R. KUMARESAN. 1982. Estimation of frequencies of multiple sinusoids: Making linear prediction perform like maximum likelihood. *Proc. IEEE* **9**:975-989.
- UBERALL, H. 1973. Surface waves in acoustics. In W.P. MASON (ED.), *Physical acoustics*, Vol. 10, 1-60. Academic Press.
- VAN DER GRINTEN, J.G., M.E.H. VAN DONGEN, & H. VAN DER KOGEL. 1985. A shock tube technique for studying pore pressure propagation in a dry and water-saturated porous medium. *J. Appl. Phys.* **58**:2937-2942.
- VAN DER GRINTEN, J.G., M.E.H. VAN DONGEN, & H. VAN DER KOGEL. 1987. Strain and pore pressure propagation in a water-saturated porous medium. *J. Appl. Phys.* **62**:4682-4687.
- VAN DER HIJDEN, J.H.M.T. 1984. Quantitative analysis of the pseudo-rayleigh phenomenon. *J. Acoust. Soc. Am.* **74**:1041-1047.
- VAN DONGEN, M.E.H., D.M.J. SMEULDERS, T. KITAMURA, & K. TAKAYAMA. 1995. On wave phenomena in permeable foam. *Acustica* **81**:63-70.
- VERRUIJT, A. 1982. The theory of consolidation. In J. BEAR & M. Y. CORAPCIOGLU (EDS.), *Fundamentals of transport phenomena in porous media*, Vol. 82 of *NATO ASI Series*, 351-368. Martinus Nijhoff Publishers.
- VIKTOROV, I.A. 1967. *Rayleigh and Lamb waves*. Plenum press New York.
- VOLLMAN, J., R. BREU, & J. DUAL. 1997. High-resolution analysis of the complex wave spectrum in a cylindrical shell containing a viscoelastic medium. part ii. experimental results versus theory. *J. Acous. Soc. Am.* **93**:909-920.
- WHITE, J.E. 1983. *Underground sound-Application of seismic waves*. Elsevier Science.
- WILLIAMS, D.M., J. ZEMANEK, F.A. ANGONA, C.L. DENIS, & R.L. CALDWELL. 1984. The long space acoustic logging tool. In *Trans. SPLWA Ann. Loggin Symp.* **25th**.
- WILSON, D.K., J.D. MCINTOSH, & R.F. LAMBERT. 1988. Forchheimer-type nonlinearities for high-intensity propagation of pure tones in air-saturated porous media. *J. Acoust. Soc. Am.* **84**:350-359.

- WILSON, L.O. 1986. The response of a semi-infinite fiber to a pulse applied asymmetrically to its end. *J. Acous. Soc. Am.* **79**:1798-1810.
- WINKLER, K.W., H-S LIU, & D.L. JOHNSON. 1989. Permeability and borehole stoneley waves: Comparison between experiment and theory. *J. Acous. Soc. Am.* **54**:66-75.
- WISSE, C.J., D.M.J. SMEULDERS, & M.E.H. VAN DONGEN. 1998. Shock tube measurements on water-saturated porous cylinders. In *Proc. Biot Conference on poromechanics*.
- WYLLIE, M.R.J., A.R. GREGORY, & G.H.F. GARDNER. 1958. An experimental investigation of factors affecting elastic wave velocities in porous media. *Geophysics* **23**:459-493.
- WYLLIE, M.R.J., A.R. GREGORY, & L.W. GARDNER. 1956. Elastic wave velocities in heterogenous and porous media. *Geophysics* **21**:41-70.
- ZEMANEK, J. 1971. An experimental and theoretical investigation of elastic wave propagation in a cylinder. *J. Acous. Soc. Am.* **51**:265-283.

Dankwoord

Na het schrijven van een groot aantal bladzijden wetenschappelijke tekst hier een persoonlijk woord van dank aan allen die de afgelopen vier jaar hebben bijgedragen aan de totstandkoming van dit proefschrift.

Dit proefschrift is het resultaat van een voorbeeldige samenwerking tussen twee universiteiten: de Technische Universiteit Delft en de Technische Universiteit Eindhoven. Als zijnde promovendus van de (sub)Faculteit Technische Aardwetenschappen (voorheen Mijnbouwkunde) van de eerstgenoemde universiteit heb ik ruim vier jaar de Brabantse gastvrijheid ondervonden van de vakgroep Transportfysica, sectie Gasdynamica. Dit boekje staat officieel op naam van de TU Delft, de TU Eindhoven echter heeft minstens zoveel bijgedragen aan het welslagen van het onderzoek. Hiervoor hartelijk dank.

David Smeulders van de TU Delft heeft als directe begeleider vele uurtjes gespendeerd om alle bladzijden van dit proefschrift door te ploegen en van commentaar te voorzien. De opmerking dat sommige passages een sprookjesachtig karakter hadden, heb ik uiteraard opgevat als een compliment. Deze passages zijn er uitgeknipt (helaas voor de lieve lezertjes). Aan de bladzijden van dit proefschrift gingen minstens evenzovele uren van discussie vooraf over diverse uitgeprinte figuren.

Mijn eerste promotor Max Peeters heeft er voor gezorgd dat de link van het onderzoek met de 'echte' boorgatmetingen steeds up-to-date bleven. Tevens heeft zijn commentaar de leesbaarheid van verscheidene delen van dit proefschrift vergroot. Mijn tweede promotor Rini van Dongen was elke keer weer bereid om tijd te investeren in dit onderzoek. Even binnelopen was voldoende voor een hoop bruikbare ideeën. Verder is hij in staat om op sympathieke wijze je duidelijk te maken als er iets niet klopt, dan wel slecht opgeschreven is.

Ondersteuning op theoretisch gebied heb ik gekregen van Dr. Frans van de Vosse van de TUE met betrekking tot Sepran. Dr. Sjoerd Rienstra van de faculteit Wiskunde en Informatica (TUE) heeft me attent gemaakt op de problematiek van de complexe wortels en vertakkingsneden. Verder was hij bereid in de commissie zitting te nemen, evenals Prof. Fokkema, en Prof. Barends. Mede door hun suggesties naar aanleiding van het conceptproefschrift is dit manuscript tot stand gekomen. Prof. Allard van l'Université du Maine in Frankrijk heeft het conceptproefschrift van commentaar voorzien, maar was helaas niet in de gelegenheid om de promotie bij te wonen. Prof. van Kruijsdijk was bereid om als reservelid op te treden.

Een onderzoek met een belangrijke experimentele poot heeft groot belang bij goede technische ondersteuning. Die is de afgelopen vier jaar in ruime mate aanwezig geweest. De eerste twee jaar heeft Marieke van Hilten veel energie gestopt in het wederopbouw van de schokbuis, het bepalen van parameters, het bakken van nieuwe monsters en het voorbereiden en uitvoeren van schokbuisexperimenten, het tekenen in AutoCad en nog veel meer. De 'oogstperiode' vond, zoals gewoonlijk bij een promotieonderzoek, plaats in

de laatste twee jaar. De resultaten van al de inspanningen zijn nu te lezen in dit boekje. Joachim Tempelaars heeft de laatste twee jaar van de technische ondersteuning voor zijn rekening genomen. Een brandweerman, tevens directeur van een onderneming-in-wording, vermomd als technicus. Hij bleek ontzettend handig te zijn. Zonder de verstelbare bodemsectie was het experimentele deel van dit proefschrift een heel stuk magerder uitgevallen. De flitsende 3D AutoCad-plaatjes (zie omslag) doen de grenzen van de realiteit vervagen. Voor verdere technische ondersteuning hebben Eep van Voorthuizen, Jan Willems, Harm Jager en Louis Wasser gezorgd. Mijn 'buurmannen' Ad Holten en Herman Koolmees hebben, naast technische ondersteuning, de laatste anderhalf jaar gezorgd voor de aanwezigheid van boeiende achtergrondgeluiden. Karel Heller en André Hoving van de TU Delft hebben tijdens mijn spaarzame verblijven in Delft de nodige technische ondersteuning verleend.

Birgitt Hepp heeft met haar stage een bijdrage geleverd aan de bepaling van de gesteenteparameters. Mijn verblijf in Eindhoven werd verder veraangenaamd door de aanwezigheid van mijn collegapromovendi. Ik heb ze één keer vermoeid met het spelen op het orgel van de TU. Ze vonden het nog boeiend ook. Tijdens het tafeltennissen ben ik overigens afgehaakt wegens chronisch gebrek aan talent. De secretaresses Anita Peeters en Brigitte van de Wijdeven voorzagen de lunchgesprekken van andere onderwerpen dan computers, wetenschap en aanverwante artikelen.

Van mijn ouders, broers en schoonzussen heb ik morele ondersteuning ontvangen. Het is moeilijk uit te leggen hoe je over een buis met een stuk steen een boek van 200 pagina's kan schrijven. Het is dan toch gelukt, maar de inhoud ervan is voor een leek volkomen onbegrijpelijk. De gedachte van Pascal dat de gehele zichtbare wereld slechts een onwaarneembaar streepje is in de schoot van de natuur, is voldoende excuus om een ander boek ter hand te nemen.

Curriculum vitae

1970	geboren te Mariekerke
1982-1986	HAVO Voetsiusscholengemeenschap Goes
1986-1988	VWO Christelijke Scholengemeenschap Walcheren
1988-1994	Werktuigbouwkunde Technische Universiteit Delft
1994-1998	Assistent-in-Opleiding TU Delft / TU Eindhoven